

# UC Berkeley

## UC Berkeley Electronic Theses and Dissertations

### Title

Hybrid Switched-Capacitor Power Converters: Fundamental Limits and Design Techniques

### Permalink

<https://escholarship.org/uc/item/5s36b083>

### Author

Ye, Zichao

### Publication Date

2020

Peer reviewed|Thesis/dissertation

Hybrid Switched-Capacitor Power Converters: Fundamental Limits and Design Techniques

by

Zichao Ye

A dissertation submitted in partial satisfaction of the

requirements for the degree of

Doctor of Philosophy

in

Engineering — Electrical Engineering and Computer Sciences

in the

Graduate Division

of the

University of California, Berkeley

Committee in charge:

Associate Professor Robert C.N. Pilawa-Podgurski, Chair

Professor Seth R. Sanders

Professor Kristofer Pister

Associate Professor Jason T. Stauth

Fall 2020

Hybrid Switched-Capacitor Power Converters: Fundamental Limits and Design Techniques

Copyright © 2020

by

Zichao Ye

## Abstract

Hybrid Switched-Capacitor Power Converters: Fundamental Limits and Design Techniques

by

Zichao Ye

Doctor of Philosophy in Engineering — Electrical Engineering and Computer Sciences

University of California, Berkeley

Associate Professor Robert C.N. Pilawa-Podgurski, Chair

In this dissertation, we develop and explore very-high-performance power conversion systems for emerging applications that require high efficiency and high power density simultaneously, such as large-scale data center power delivery and mobile computing on portable and wearable electronics.

This work focuses on a topological effort to drastically improve the performance of existing power electronics. In particular, a hybrid approach is adopted, in which both inductors and capacitors are used in the voltage conversion and power transfer process. Compared to conventional switched-capacitor (SC) converters, the augmenting inductors can greatly reduce or eliminate the capacitor charge sharing loss, and thus improve the energy utilization of the capacitors without sacrificing efficiency. This process is called soft-charging operation. In combination with other potential advantages such as soft switching and voltage regulation, hybrid SC converters show promise in the development of future high-performance power electronics systems.

This dissertation explores hybrid SC converters from three main aspects: fundamental limits and topology comparisons, practical circuit implementation challenges, and high-performance hardware demonstrations. We start by analyzing the reactive power processed by the passive components of hybrid SC converters operating in resonant mode. This analysis is applied to express and optimize the total passive component volume of resonant switched-capacitor (ReSC) converters. To compare different ReSC topologies, a normalized passive volume parameter is proposed for simple and fair comparison. This normalized passive volume parameter, along with a normalized switch stress parameter (based on switch VA ratings), can be used to visualize and compare the passive and active component utilizations among different topologies, offering a framework to compare the relative performance of different topologies.

The large number of floating switches and flying capacitors pose great challenges in practical



circuit implementations. Several bootstrap and charge-pump based techniques are developed to provide gate drive power to the floating switches in a compact and efficient manner. Compared to conventional isolated dc/dc power supply chips, the proposed circuits have a simple structure and operating principle, and can be implemented with a small number of diodes, capacitors, and LDOs, leading to less occupied board area and lower implementation cost. Another crucial practical challenge is flying capacitor voltage balancing. In unbalanced operation, capacitor voltages deviate from their nominal values, potentially resulting in system failure. We experimentally investigate the origins of the voltage imbalance in practical implementations of flying capacitor multilevel (FCML) converters and present corresponding solutions. It is found that an FCML converter with an even number of levels has significantly better capacitor balancing than one with an odd number of levels, due to better inherent immunity to circuit non-idealities.

With the theoretical analysis tools and the practical circuit techniques developed above, a number of high-performance discrete hardware prototypes are designed in the context of 48 V power delivery architecture for modern data centers. Based on a novel cascaded resonant topology, a 48-to-12 V, 4-to-1 fixed-ratio, intermediate bus converter is built with 99% peak efficiency and 2500 W/in<sup>3</sup> power density. To further increase the conversion ratio without increasing circuit complexity, the concept of multi-phase operation is introduced, along with a 6-to-1 cascaded series-parallel topology and an 8-to-1 multi-resonant-doubler topology. In addition to fixed-ratio ReSC converters, a regulated multi-level binary hybrid converter for direct 48 V to 1–2 V point-of-load applications is also developed. All of the hardware prototypes achieve the best in-class efficiency and power density simultaneously, reflecting the great potential of hybrid and resonant switched-capacitor converters for future power conversion systems.

*To my family*

# Contents

<b>Contents</b>	<b>ii</b>
<b>List of Figures</b>	<b>iv</b>
<b>List of Tables</b>	<b>x</b>
<b>1 Introduction</b>	<b>1</b>
1.1 Introduction . . . . .	1
1.2 Organization of Thesis . . . . .	2
<b>2 Fundamentals of Hybrid and Resonant Switched-Capacitor Converters</b>	<b>4</b>
2.1 Limitations of Conventional Topologies . . . . .	4
2.2 Soft-Charging Operation . . . . .	10
2.3 PWM Regulated Mode vs. Fixed-Ratio Mode . . . . .	11
2.4 Inductor Placement Strategy . . . . .	14
<b>3 Modeling and Comparison of Passive Component Volume</b>	<b>18</b>
3.1 Background and Motivation . . . . .	18
3.2 Analysis of Basic 2-to-1 Resonant Switched-Capacitor Converter . . . . .	20
3.3 Design Guidelines and Comparisons with Other Solutions . . . . .	25
3.4 Generalized Analysis . . . . .	35
3.5 Resonant SC Topology Comparison . . . . .	41
3.6 Comparison of Regulated Hybrid Converters . . . . .	45
3.7 Chapter Summary . . . . .	51
<b>4 Capacitor Voltage Balancing of Flying Capacitor Multilevel Converters</b>	<b>52</b>
4.1 Background and Motivation . . . . .	52
4.2 Operating Principle of FCML Converters . . . . .	54
4.3 Imbalance Caused by Source Impedance . . . . .	55
4.4 Imbalance Caused by Gate Driver Delay and Uneven Switch Resistance . . . . .	70
4.5 Chapter Summary . . . . .	76
<b>5 Circuit Techniques for Powering Floating Gate Drivers</b>	<b>77</b>

5.1	Background and Motivation . . . . .	77
5.2	Bootstrap at Deadtime . . . . .	81
5.3	Cascaded Bootstrap with LDOs . . . . .	86
5.4	Double Charge Pump . . . . .	90
5.5	Gate-Driven Charge Pump . . . . .	91
5.6	Cascaded Synchronous Bootstrap . . . . .	94
5.7	Implementation Examples . . . . .	96
5.8	Design Considerations . . . . .	103
5.9	Chapter Summary . . . . .	104
<b>6</b>	<b>Cascaded Resonant Switched-Capacitor Converter</b>	<b>106</b>
6.1	Background and Motivation . . . . .	106
6.2	Overview of Data Center Power Delivery Architecture . . . . .	108
6.3	Cascaded Resonant Converter . . . . .	110
6.4	Design Guidelines and Experimental Results . . . . .	114
6.5	Zero Voltage Switching Technique . . . . .	120
6.6	Cascading and Interleaving Strategies . . . . .	128
6.7	Chapter Summary . . . . .	131
<b>7</b>	<b>Multi-Resonant Switched-Capacitor Converter</b>	<b>133</b>
7.1	Background and Motivation . . . . .	133
7.2	Theoretical Performance Limit of SC converters . . . . .	135
7.3	Generation and Synthesis of Multi-Phase Topologies . . . . .	137
7.4	8-to-1 Multi-Resonant-Doubler Converter . . . . .	139
7.5	6-to-1 Cascaded Series-Parallel Converter . . . . .	147
7.6	Alternative Topology Variations . . . . .	151
7.7	Chapter Summary . . . . .	154
<b>8</b>	<b>Multi-Level Binary Hybrid Switched-Capacitor Converter</b>	<b>156</b>
8.1	Background and Motivation . . . . .	156
8.2	Proposed Topology . . . . .	157
8.3	Hardware Design and Experimental Results . . . . .	161
8.4	Alternative Topology Variation . . . . .	166
8.5	Chapter Summary . . . . .	168
<b>9</b>	<b>Future Work</b>	<b>171</b>
<b>10</b>	<b>Conclusions</b>	<b>176</b>
	<b>Bibliography</b>	<b>178</b>

# List of Figures

1.1	Performance summary of the hybrid and resonant SC converter prototypes presented in this dissertation. . . . .	3
2.1	Schematic drawing of a buck converter. . . . .	5
2.2	A high-performance GaN-based 48-to-12 V buck converter [1]. . . . .	5
2.3	Schematic drawing of a 2-to-1 SC converter. . . . .	6
2.4	A high-performance 48-to-24 V switched-capacitor converter [8]. . . . .	7
2.5	Pure SC converter: ideal circuit model, output impedance vs. switching frequency, origin of capacitor charge sharing loss (capacitor charging current at SSL and FSL). . . . .	8
2.6	Soft-charging operation with ideal current load. . . . .	10
2.7	Schematic drawing of a three-level buck converter / 2-to-1 ReSC converter. . . . .	11
2.8	Key operating waveforms and circuit states of a three-level buck converter at duty ratio $> 0.5$ . . . . .	12
2.9	Key operating waveforms and circuit states of a 2-to-1 resonant SC converter. . . . .	13
2.10	2-to-1 SC converter with different augmenting inductor locations. . . . .	14
2.11	Output impedance with respect to inductor location. . . . .	15
2.12	Inductor current at different locations and frequencies. . . . .	15
2.13	Effect of duty ratio on rms current and output impedance. . . . .	17
3.1	Schematic drawing of a 2-to-1 resonant switched-capacitor converter and its two operating states. . . . .	20
3.2	Current, voltage, and power waveforms of the flying capacitor and the resonant inductor in a 2-to-1 ReSC converter. . . . .	21
3.3	The effects of flying capacitor voltage ripple on capacitor volume, inductor volume and overall volume for a 2-to-1 ReSC converter (assuming $\rho_{E,C}/\rho_{E,L} = 100$ ). . . . .	24
3.4	Given fixed output power and switching frequency, the 2-to-1 ReSC converter can always achieve the same minimum total passive component volume. But the optimum capacitance (and inductance) allocation depends on the magnitude of the load resistance. Parameters for the plot: $P_{\text{out}} = 100$ W, $f_{\text{sw}} = 100$ kHz, $\rho_{E,C} = 0.1$ J/cm <sup>3</sup> , $\rho_{E,C}/\rho_{E,L} = 100$ . . . . .	25
3.5	The optimum volume ratio between capacitor and inductor with respect to their energy density ratio. . . . .	26

3.6	Output impedance of 2-to-1 Pure SC and ReSC converters vs. frequency. . . . .	28
3.7	Relative passive component volume comparison between 2-to-1 pure SC converter and 2-to-1 ReSC converter (assuming converter series resistance $R_{\text{FSL}} = 5 \text{ m}\Omega$ ). . . . .	30
3.8	Relative passive component volume comparison between 2-to-1 pure SC converter and 2-to-1 ReSC converter with respect to converter efficiency. . . . .	31
3.9	Photograph of the hardware prototype for passive component volume and efficiency comparisons. . . . .	32
3.10	Measured 48-to-24 V efficiency ( $f_{\text{sw}} = 100 \text{ kHz}$ ). . . . .	34
3.11	Required passive component volume to achieve the efficiency performance shown in Fig. 3.10. . . . .	35
3.12	N-to-1 resonant series-parallel converters with different inductor locations. . . . .	39
3.13	Minimized total passive volume of N-to-1 resonant series-parallel converters with different inductor locations (normalized to the 2-to-1 case). . . . .	41
3.14	4-to-1 resonant switched-capacitor converter topologies. . . . .	43
3.15	Normalized passive volume (assuming $\rho_{E,C}/\rho_{E,L} = 100$ ). Lower is better. . . . .	44
3.16	Normalized switch stress. Lower is better. . . . .	45
3.17	4-to-1 ReSC topology comparison. . . . .	46
3.18	Schematic drawings of two example regulated hybrid converters. . . . .	47
3.19	Circuit operating states of a three-level buck converter at $D < 0.5$ . . . . .	47
3.20	Circuit operating states of a three-level buck converter at $D > 0.5$ . . . . .	48
3.21	Reactive power processed by the passive components of a three-level buck converter. . . . .	48
3.22	Average power processed by the passive components in hybrid converters. . . . .	49
4.1	Schematic drawing of a five-level FCML buck converter. . . . .	54
4.2	PWM, switch node voltage, and inductor current waveforms of a five-level FCML buck converter at $\frac{1}{2} < D < \frac{3}{4}$ . . . . .	55
4.3	Schematic drawing of the configurable 3/4/5-level FCML buck converter prototype. There is a source impedance $Z_{\text{in}}$ between the input voltage source $V_{\text{DC}}$ and the actual converter input $V_{\text{in}}$ . The magnitude of the input voltage ripple $\Delta V_{\text{in}}$ is determined by the low-ESR low-ESL input capacitor. . . . .	56
4.4	Photograph of the configurable 3/4/5-level FCML buck converter prototype. . . . .	56
4.5	Measured input voltage ripple of a three-level FCML converter. . . . .	57
4.6	Measured flying capacitor voltage of a three-level FCML converter. . . . .	58
4.7	The flying capacitor voltage of a three-level FCML converter will increase in the presence of input voltage ripple. . . . .	59
4.8	Measured flying capacitor voltage variations ( $C_{\text{in}} = 13 \mu\text{F}$ , $I_{\text{out}} = 4 \text{ A}$ ). . . . .	61
4.9	Simulated step response of the flying capacitor voltages using the proposed models ( $\Delta V_{\text{in}}$ is the input). . . . .	63
4.10	Capacitor voltage variation of a four-level FCML converter under the influence of input voltage ripple. . . . .	64
4.11	The flying capacitor voltages of a four-level FCML converter can stabilize themselves in the presence of input voltage ripple. . . . .	65

4.12	Measured flying capacitor voltages of a four-level FCML converter ( $C_{in} = 13 \mu\text{F}$ ).	66
4.13	Measured flying capacitor voltages of a five-level FCML converter. . . . .	67
4.14	Measured $C_1$ voltage of five-level FCML converter. . . . .	68
4.15	Six possible circuit configurations that can generate the $\frac{1}{2}V_{in}$ voltage level in a five-level FCML converter. PSPWM utilizes the first four states. . . . .	68
4.16	Measured LM5113 gate driver propagation delay (from gate driver input to output).	71
4.17	Schematic drawing of a three-level FCML buck converter. . . . .	72
4.18	The effects of gate signal delay mismatch on capacitor balancing for a three-level FCML converter. . . . .	72
4.19	Schematic drawing of a cascaded bootstrap circuit. . . . .	73
4.20	Measured effect of gate delay mismatch on capacitor voltage (three-level, $C_{in} = 65 \mu\text{F}$ , $D = 0.25$ ). . . . .	73
4.21	Measured flying capacitor voltage of a three-level FCML converter ( $C_{in} = 65 \mu\text{F}$ ).	74
4.22	The effect of input ripple on capacitor balancing at light-load condition of a three-level converter with $D > 0.5$ . . . . .	75
4.23	Switching cell design. . . . .	76
5.1	Schematic drawing of a cascaded bootstrap circuit on a four-level FCML buck converter. . . . .	79
5.2	Inductor current flow in a two-level buck converter during deadtime. . . . .	81
5.3	Simulated cascaded bootstrap circuit during deadtime ( $V_{pwr} = 5 \text{ V}$ , $V_{Dbody} = 2 \text{ V}$ , $V_{Dboot} = 0.6 \text{ V}$ ). . . . .	83
5.4	Additional circuitry to observe the overcharge effect of bootstrap operation at deadtime. . . . .	84
5.5	Voltage on cascaded bootstrap capacitors. . . . .	85
5.6	Schematic drawing of a cascaded bootstrap circuit with LDOs on a string of series-connected switches. . . . .	86
5.7	Simulated cascaded bootstrap voltages of a six-level FCML converter under different operating conditions ( $f_{ac} = 60 \text{ Hz}$ , $f_{sw} = 120 \text{ kHz}$ , $V_{pwr} = 16 \text{ V}$ , $C_{boot} = 20 \mu\text{F}$ , switch: GS61004B[95], GD: Si827x[96], diode: $V_f = 0.6 \text{ V}$ , $R_{on} = 5 \Omega$ ). . . . .	89
5.8	Schematic drawing of a double charge pump circuit. . . . .	90
5.9	Schematic drawing of a gate-driven charge pump circuit. . . . .	91
5.10	Different ways to connect gate-driven charge pump. . . . .	92
5.11	Turn-on behavior of EPC 2016C GaN switch with gate-driven charge pump connected (simulation parameters: $R_{up} = 1 \Omega$ , $R_G = R_p = 10 \Omega$ , $C_L = C_H = C_{pump} = 1 \mu\text{F}$ , $V_{C_L} = 5 \text{ V}$ ). . . . .	93
5.12	Schematic drawing of a synchronous bootstrap circuit. . . . .	94
5.13	Key switching waveform of the synchronous bootstrap circuit. . . . .	95
5.14	Measured cascaded synchronous bootstrap voltages on a seven-level FCML buck converter at no-load condition (switch: EPC2001C, $f_{sw} = 140 \text{ kHz}$ ). . . . .	95
5.15	Proposed gate drive power supply methods for a seven-level FCML converter. . . . .	96
5.16	Calculated efficiency of the proposed gate drive power supply circuit. . . . .	97

5.17	Power module (switching cell) design with proposed gate drive power supply circuit.	97
5.18	Comparison of the hardware prototype with [99].	98
5.19	Measured double charge pump operation.	99
5.20	Measured gate-driven charge pump operation.	100
5.21	An example gate drive circuit for a 4-to-1 Dickson converter.	101
5.22	An example gate drive circuit for a 4-to-1 series-parallel converter.	102
5.23	Block diagram of a proposed gate driver IC with built-in LDO and self-oscillatory inverter for cascaded bootstrap and gate-driven charge pump operations.	102
5.24	Powering a four-level FCML converter with the proposed gate driver IC.	103
6.1	An example data center power delivery system from line to point-of-loads.	108
6.2	Comparison of different approaches to convert 48 V down to 1–2 V.	109
6.3	Schematic drawing of a cascaded resonant converter.	110
6.4	Simulated inductor/capacitor current at first stage.	111
6.5	Schematic drawing of a two-phase interleaved cascaded resonant converter.	112
6.6	Minimize $C_{\text{mid}}$ with interleaved design.	112
6.7	Comparison of various ReSC converters at a conversion ratio of 4-to-1.	113
6.8	Output impedance plot for cascaded resonant converter.	114
6.9	Photograph of the hardware prototype (two-phase interleaved).	116
6.10	Annotated photograph of the converter (one phase). Dimensions: 1.38×0.46×0.22 inch (3.5×1.17×0.56 cm).	117
6.11	Measured 36 V to 9 V efficiency ( $f_{\text{sw}} = 91$ kHz).	118
6.12	Measured 48 V to 12 V efficiency ( $f_{\text{sw}} = 100$ kHz).	118
6.13	Measured 60 V to 15 V efficiency ( $f_{\text{sw}} = 111$ kHz).	119
6.14	Thermal performance with fan cooling only ( $V_{\text{in}} = 48$ V, $I_{\text{out}} = 60$ A).	119
6.15	The interleaved inductor currents at the first stage.	120
6.16	The inductor currents of the two stages (one phase).	120
6.17	Transient response of 10 A to 30 A load step.	121
6.18	Control signals for different modes of operation.	121
6.19	Zero voltage switching operation on cascaded resonant converter.	122
6.20	Detailed view at the ZVS switching moment.	123
6.21	Effect of deadtime on the turn-on of low-side switch ( $L = 180$ nH, $C_{\text{oss,tot}} = 1.5$ nF).	124
6.22	Achieving complete ZVS at light load with the optimum deadtime.	125
6.23	$I_L$ and $V_{\text{sw}}$ under ZVS.	125
6.24	ZVS turn-on of $S_{1A}$ .	126
6.25	ZVS turn-on of $S_{2B}$ .	126
6.26	Comparison of measured 48-to-12 V power stage efficiency.	127
6.27	ZVS efficiency including gate drive loss.	127
6.28	Loss breakdown of the prototype in ZVS mode.	128
6.29	Comparison of full-load efficiency and power density of state-of-the-art commercial products and previously published research.	129



6.30	An alternative 12-switch design of the cascaded resonant converter with single first-stage. . . . .	130
6.31	Cascading 2-to-1 ReSC with two-phase interleaved switched-tank converters (STC). . . . .	131
6.32	Cascading 2-to-1 ReSC with four-phase interleaved series-parallel converters. . . . .	132
7.1	The maximum voltage gain in two-phase SC converters follows the Fibonacci sequence. . . . .	134
7.2	Exponential growth of voltage gain with voltage doublers. . . . .	135
7.3	Achieving different conversion ratios with the same fundamental structure. . . . .	138
7.4	Schematic drawing of the 8-to-1 multi-resonant-doubler converter with device ratings and control signals labeled. . . . .	139
7.5	Inductor and capacitor current waveforms, control signals, and equivalent circuits of the 8-to-1 multi-resonant-doubler converter. . . . .	140
7.6	Photograph of the converter prototype. Dimensions: $1.38 \times 0.46 \times 0.22$ inch ( $3.5 \times 1.17 \times 0.55$ cm). . . . .	142
7.7	Waveform of inductor current and switch node voltage. . . . .	144
7.8	Load-step from 10 A to 40 A at 48 to 6 V. . . . .	144
7.9	Measured 40 V to 5 V efficiency ( $f_{sw} = 70$ kHz). . . . .	145
7.10	Measured 48 V to 6 V efficiency ( $f_{sw} = 70$ kHz). . . . .	145
7.11	Measured 60 V to 7.5 V efficiency ( $f_{sw} = 78$ kHz). . . . .	146
7.12	Thermal performance with fan cooling only ( $V_{in} = 48$ V, $I_{out} = 40$ A). . . . .	146
7.13	Load regulation ( $V_{in} = 48$ V, $V_{out} = 6$ V). . . . .	147
7.14	Parallel operation of MRD converters to optimize the utilization of the flying capacitors and the associated switches. . . . .	148
7.15	Schematic drawing of the 6-to-1 cascaded series-parallel converter with device ratings and control signals labeled. . . . .	148
7.16	Inductor and capacitor current waveforms, control signals, and equivalent circuits of the 6-to-1 cascaded series-parallel converter. . . . .	149
7.17	Theoretical performance comparison of various ReSC converters and buck converter at 6-to-1 conversion ratio. . . . .	150
7.18	Inductor current and switch node voltage of the cascaded series-parallel converter. . . . .	150
7.19	Measured 48 V to 8 V efficiency of the cascaded series-parallel converter ( $f_{sw} = 68$ kHz). . . . .	151
7.20	Fundamental building block of the multi-phase resonant SC converter. . . . .	152
7.21	Schematic drawing of an 8-to-1 cascaded series-parallel converter (three-phase). . . . .	152
7.22	Inductor and capacitor current waveforms, control signals, and equivalent circuits of the 8-to-1 cascaded series-parallel converter. . . . .	153
7.23	Schematic drawing of a 10-to-1 cascaded series-parallel converter (three-phase). . . . .	153
7.24	Inductor and capacitor current waveforms, control signals, and equivalent circuits of the 10-to-1 cascaded series-parallel converter. . . . .	154
7.25	Schematic drawing of a 12-to-1 cascaded doubler series-parallel converter (four-phase). . . . .	154

7.26	Inductor and capacitor current waveforms, control signals, and equivalent circuits of the 12-to-1 cascaded doubler series-parallel converter. . . . .	155
8.1	Schematic drawing of the proposed MLB-PoL converter. The device voltage ratings are labeled in red and the operating phases of the switches are labeled in blue. . . . .	158
8.2	Voltage, current and PWM waveforms of the proposed MLB-PoL converter and equivalent circuit models. . . . .	159
8.3	Photograph of the prototype. Dimensions: $1.14 \times 0.72 \times 0.39$ inch ( $2.9 \times 1.84 \times 1.01$ cm). . . . .	162
8.4	Balanced interleaved inductor currents ( $V_{\text{out}} = 2$ V, $I_{\text{out}} = 20$ A). . . . .	164
8.5	Flying capacitor voltages at $V_{\text{out}} = 2$ V and $I_{\text{out}} = 20$ A. . . . .	164
8.6	Measured power stage efficiency from 48 V to 2.5–1.0 V. . . . .	165
8.7	Measured efficiency at various output voltages. . . . .	166
8.8	Thermal performance at equilibrium with 110 CFM fan cooling only ( $V_{\text{out}} = 2.0$ V, $I_{\text{out}} = 65$ A). . . . .	168
8.9	Schematic drawing of a proposed multi-phase hybrid converter with a 6-to-1 SC stage and three interleaved output inductors. The device voltage ratings are labeled in red and the operating phases of the switches are labeled in blue. . . . .	169
8.10	Voltage, current, PWM waveforms, and equivalent circuit models of the proposed hybrid SC converter with a 6-to-1 SC stage. . . . .	170

# List of Tables

2.1	Comparison of three-level buck converter and 2-to-1 ReSC converter . . . . .	14
2.2	Comparison of different inductor placement strategies . . . . .	17
3.1	Key converter operating parameters . . . . .	33
3.2	Main component listing of the hardware prototype . . . . .	34
3.3	Comparison between calculation and experiment . . . . .	35
3.4	Key parameters of N-to-1 series-parallel converter . . . . .	41
4.1	Four-level converter system parameters . . . . .	62
4.2	Five-level converter system parameters . . . . .	62
5.1	Measured voltage on cascaded bootstrap capacitors with 1 A load current and different deadtimes . . . . .	86
5.2	Measured gate drive power supply voltages of the seven-level FCML converter (at $250 V_{DC}$ to $100 V_{DC}$ ) . . . . .	99
5.3	Comparison with the state of the art solution . . . . .	100
5.4	Key characteristics of the five proposed methods . . . . .	104
6.1	Main component listing of the cascaded resonant converter . . . . .	116
6.2	Comparison of this work and existing non-isolated intermediate bus converters .	129
7.1	Maximum attainable conversion ratios . . . . .	136
7.2	Comparison of component number of 8-to-1 SC converters . . . . .	141
7.3	Comparison of passive and active component utilization of 8-to-1 SC converters	141
7.4	Key prototype parameters of the MRD converter . . . . .	143
7.5	Main component listing of the MRD converter . . . . .	143
7.6	Comparison of this work and existing high-step-down bus converters . . . . .	147
8.1	Voltage rating and operating frequency of the main active and passive components	160
8.2	Comparison of the voltage conversion strategies of selected hybrid converters at 48 V to 2 V conversion . . . . .	161
8.3	Main component listing of the prototype . . . . .	163
8.4	Key parameters of the prototype . . . . .	163

8.5	Summary of measured efficiency and power density results at various output voltages . . . . .	167
8.6	Comparison of this work and existing hybrid SC works . . . . .	167
8.7	Comparison of this work and existing commercial products . . . . .	168

## Acknowledgments

The completion of this dissertation is an important milestone in my life as it marks the closure of my graduate school journey. The young adulthood years are of singular importance and I have no regrets having spent them with a world class engineering research group. I am sincerely thankful for the many great people I have met on my journey; their mentorship, support, love, and care are the driving force that keeps me going and makes me want to better myself.

My first thank you goes to my adviser, Professor Robert Pilawa, for bringing me into his research group and for his guidance over the past six years. To this day, I have no idea how a personal statement put together in one night got his attention and marvel at how quickly I made the decision to study power electronics immediately following our first meeting in which he showed me some cool circuit boards. It was a great decision, and I could not have asked for a better adviser. I am incredibly grateful to Robert for providing me unlimited trust, freedom, and support which is everything a Ph.D. student could hope for in an adviser. Robert is a pioneer researcher of hybrid switched-capacitor technologies and brought me into this most promising field of power electronics and has guided me through cutting edge research that has a tangible impact on society. He has shown me, by example, what it means to be an enthusiastic researcher, presenter, and visionary leader. His engineering and research acumen aside, he has taught me to be a better thinker, investigator, and innovator. To quote Sir Isaac Newton: “If I have seen further, it is only because I have had the opportunity to stand on the shoulders of these giants.” Robert has always encouraged me to “think outside the box,” challenge prevailing thought, and look to the future. Thank you, Robert, for helping me become a more capable person and for giving me the tools to overcome the challenges that lie on the road ahead. I will forever treasure our association.

I would like to thank my committee members Professors Seth Sanders, Kristofer Pister, and Jason Stauth for their valuable suggestions and guidance throughout the course of this work. In particular, the passive component modeling work in Chapter 3 would not have been possible without the inspiration I received from Professor Sanders through our fascinating discussion on the fundamental limits of direct and indirect power in power converters. I am also grateful for the outstanding power and energy faculty of University of Illinois at Urbana-Champaign (UIUC), especially Professor Pete Sauer who served as my undergraduate adviser and sparked my first interest in power and Professor Philip Krein who taught my first power electronics class and laboratory. I much admire their dedication and humility which have deeply influenced my approach to research and life.

Thank you to all fellow members of the Pilawa group, past and present: Yutian Lei, Shibin Qin, Christopher Barth, Enver Candan, Andrew Stillwell, Ben Macy, Joseph Liu, Pourya Assem, Derek Heeger, Zitao Liao, Derek Chou, Thomas Foulkes, Yizhe Zhang, Nathan Pallo, Nathan Brooks, Pei Han Ng, Samantha Coday, Maggie Blackwell, Rose Abramson, Kelly Fernandez, Joseph Schaadt, Logan Horowitz, Yicheng Zhu, Rahul Iyer, Yong-Long Syu, Ting Ge, Nathan Ellis, Raya Mahony, and many more. The last six years would not be the same without their company and I hope our paths cross again in the future. A special thank you

to Yutian and Shibin, my big brothers and role models. I am greatly indebted for the strong push they gave me at start of my graduate studies. I appreciate their wisdom, humor, and the hotwok lunch boxes we had together. Yutian's leading work on hybrid switched capacitors set a high bar for me to leap and has been the driving force behind my pursuit of excellence to this day. I also wish to thank Joseph and Pourya for being supportive peers throughout our journey. We started together in the same year and now we are finishing together. The classes we took, the circuits we drew, the snacks we shared, and the seasons we had in the sun are sure to be wonderful memories I will cherish forever. A special thanks to Zitao, the best artist among all the engineers I know, and probably the best engineer amongst all artists! Many of the figures and photos in my papers and slides would not look as good as they do without his advice and help. Moreover, Zitao and his wife Yun Hao had been with me throughout the many highs and lows of graduate school. Their presence and support were indispensable for me in navigating through the difficulties of 2020 due to COVID-19 and I cannot overstate my gratitude. Many thanks to Rose for working on multiple projects with me. Her coding and soldering were instrumental in achieving many of the records we broke together. She also provided English editing help for many of our publications. Heartfelt thanks to Nathan Pallo for building and operating a well-equipped group laboratory, and to Maggie and Sam for making birthday cakes and desserts for everyone in the group. Each of you went out of your way to make my graduate life more memorable and I am incredibly thankful for it.

It has been a privilege to work alongside some incredibly talented researchers in power electronics. I would like to thank Dr. Pradeep Shenoy for providing invaluable guidance in the early stages of my graduate study. I appreciate the inspiring bi-weekly discussions with Professor Minjie Chen and his group. I am grateful to Professor Hanh-Phuc Le for offering me the rare opportunity to present my work at the renowned IEEE PELS webinar as a graduate student. I am also thankful to Professor Jason Stauth and his group for their excellent and inspiring work in the hybrid switched-capacitor field. It was a great honor to be part of this brilliant society and to work with them in pushing the boundaries of high-performance power converters.

I want to thank the staff of EECS at Berkeley and the staff of ECE at UIUC. They played a huge role in this long journey. Special thanks to Shirley Salanio for always being so responsive and helpful in fielding every question, request, and petition. I will always remember her warm smile and friendly greetings. Thank you, Robin Smith and Joyce Mast, for managing the events and all the expenses for the power and energy group of UIUC. Being under your conscientious care made me feel I was part of a big, happy family. I would also like to acknowledge the funding and material support we received from our industry partners including Texas Instruments, Intel, Infineon, and the Advanced Research Projects Agency-Energy (ARPA-E).

Finally, and most significantly, I would like to express my deepest gratitude to my family to whom I dedicate this thesis. To my mother, Li Hui: it is because of you that I have been able to start and finish this long journey to the completion of my Ph.D. Your unconditional love and continual encouragement have given me optimism and the positive attitude neces-

sary to face life's challenges. Your unwavering trust and support have enabled me to follow my heart and pursue my dreams. Your rigorous approach towards research and your position as professor influenced me from an early age and seeded my academic potential. I cannot express the full extent of my gratitude to my Aunt Shelly and Uncle Vern for providing me a warm and loving second home in the United States. The unparalleled view of Lake Michigan and the indefatigable "Blue Dragon" have refueled my gas tank every year and allowed me to keep going. Thanks to Shelly for always making herself a simple phone call away whenever I need her support. Her wisdom, vision, and love have led me through dark times more than once. Lastly, thanks to my father, Ye Qiang, now in heaven: I wish to share all my accomplishments with you and make you proud.

# Chapter 1

## Introduction

### 1.1 Introduction

Power converters are electrical energy processing circuits to convert and control energy flow between different voltage domains and magnitudes. Similar to the blood circulatory system in the human body, power converters manage and deliver the requisite electrical energy in computer systems, personal electronics, automobiles, and just about every possible application of electricity. The most desirable features of power converters are high reliability, high energy efficiency, high power density, and low cost.

Thanks to continued research and development in the past decades, switch-mode power supplies with two alternating voltage levels (such as buck and boost converters) have become prevalent, offering high reliability and low cost. However, a variety of applications have recently emerged with very challenging design requirements that conventional technologies cannot meet. For instance, in space- and thermally-constrained smartphone systems, the conventional buck-based battery chargers cannot support the demand of faster charging speed, owing to their limited efficiency performance. In datacenter and telecommunication systems, the explosive growth of information processing and the associated energy consumption require innovative power delivery architecture and technology with better efficiency and power density.

Due to the fundamental structure of conventional two-level designs, trends toward higher efficiency and power density have reached the point that further improvement becomes increasingly difficult. It is therefore important to rethink the whole problem and come up with new solutions which could achieve a drastic performance improvement. This dissertation focuses on a topological effort to more efficiently utilize the active and passive devices, through a hybrid switched-capacitor/inductor approach. By introducing more switches, the system can have more than two voltage levels (as in the conventional structures). This allows for the use of high-energy-density capacitors in the voltage conversion process and thus reduces the size and loss of the inductive elements. These inductive elements in turn softly charge/discharge the capacitors, reducing the capacitor charge sharing loss.



We believe that increasing the system complexity can offer many advantages and is oftentimes necessary to improve performance. However, it should be done in appropriate ways, which requires a good understanding of both the fundamental limits and the practical design techniques. In this work, we analyze the theoretical benefits of hybrid and resonant switched-capacitor converters, address the important circuit implementation challenges, and design hardware prototypes with cutting-edge performance.

## 1.2 Organization of Thesis

Chapter 2 starts with the fundamental limitations of conventional switched-inductor and switched-capacitor converters and details the attractive benefits of hybrid resonant switched-capacitor converters. The concept of soft-charging operation is reviewed, together with different possible operating modes including fixed-ratio resonant mode and PWM regulated mode. The characteristics of different inductor augmenting strategies are also discussed.

Chapter 3 presents a new technique to calculate the passive component volume of hybrid resonant switched-capacitor converters, based on the fundamental processed reactive energy. Combining with the switch stress parameter (switch VA ratings), a framework to showcase the relative performance of different topologies is created, which can be used to visualize and compare the utilization of passive and active components.

Several important challenges in the practical implementation of high-performance hybrid switched-capacitor converters are addressed in Chapters 4 and 5. In Chapter 4, a number of bootstrap and charge pump based circuit techniques are developed to power the large number of floating gate drivers in these topologies, in a compact and efficient manner. In Chapter 5, the origins of flying capacitor voltage imbalance in practical flying capacitor multilevel converter designs are investigated experimentally. The presence of non-ideal source impedance and gate signal delay mismatch are found to have non-negligible impacts on capacitor balancing, and even-level designs are proved to have stronger inherent immunity to such nonidealities than odd-level designs.

With the above theoretical and practical knowledge, a number of very high-performance discrete prototypes are designed for emerging datacenter power delivery applications in Chapters 6 through 8. Following a brief overview of different datacenter power delivery architectures, Chapter 6 presents a 48 V to 12 V intermediate bus converter design based on a novel cascaded resonant topology, with 99.0% peak efficiency and 2500 W/in<sup>3</sup> power density. The main performance-enhancing features in this design - the two-phase interleaving concept and the zero-voltage-switching control technique - can also be applied to other resonant switched-capacitor topologies.

Chapter 7 further explores the use of resonant SC converters as intermediate bus converters with high conversion ratios, as recent research suggests that a 4 - 6 V intermediate bus voltage could provide the best overall system efficiency. A major challenge in implementing these converters at high conversion ratios is the large number of circuit components. To address this challenge, we introduce a multi-operating-phase concept to greatly reduce the

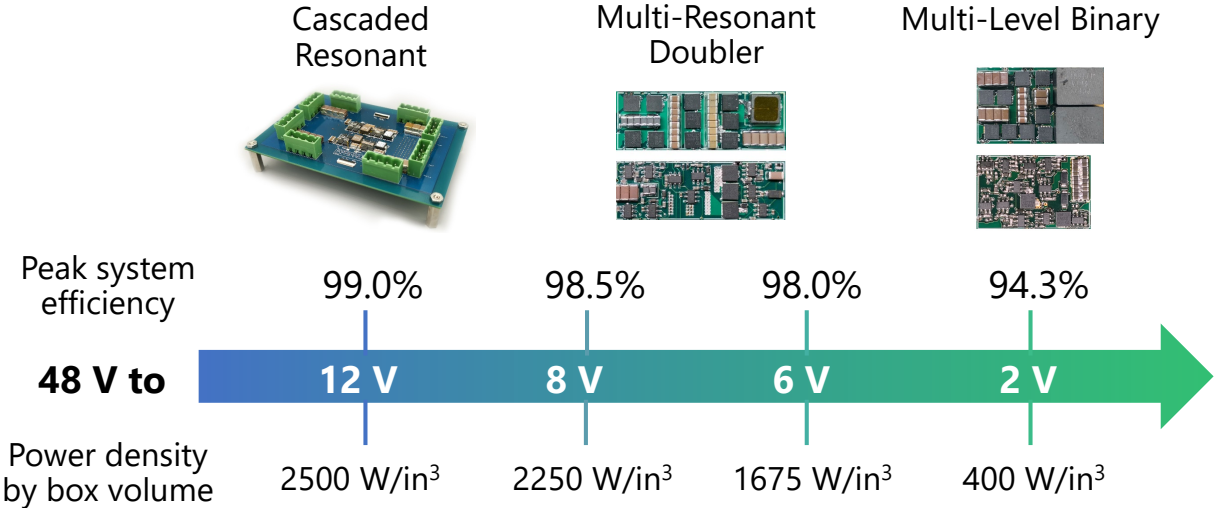


Figure 1.1: Performance summary of the hybrid and resonant SC converter prototypes presented in this dissertation.

circuit complexity and present a family of multi-phase resonant SC topologies. A 48 V to 6 V multi-resonant-doubler converter is presented with 98.0% peak efficiency and 1675 W/in<sup>3</sup> power density.

Chapter 8 extends the multi-operating-phase concept from fixed-ratio resonant SC converters to regulated hybrid SC converters. A multi-level doubler topology with merged 8-to-1 SC stage and two-phase interleaved buck stage is proposed for direct 48 V to point-of-load applications. Its prototype achieves 95.1% peak efficiency from 48 V to 2V, with near 400 W/in<sup>3</sup> power density, demonstrating one of the best in-class performance. Fig. 1.1 summarizes the performance of the three hardware prototypes presented in Chapters 6 through 8.

Chapter 9 discusses some present challenges and suggests areas for future work. Finally, conclusions are given in Chapter 10.

## Chapter 2

# Fundamentals of Hybrid and Resonant Switched-Capacitor Converters

This chapter first highlights the fundamental limitations of conventional switched-inductor and switched-capacitor (SC) power converters, and then motivates the unique characteristics of hybrid and resonant SC converters. The concept of soft-charging operation is reviewed, followed by different modes of operation to achieve soft-charging. A three-level buck converter and a 2-to-1 resonant SC converter are introduced as examples. The pros and cons of different inductor augmenting strategies are also discussed.

## 2.1 Limitations of Conventional Topologies

### Switched-Inductor Converters

A commonly used switched-mode dc/dc power converter is a buck converter, and its circuit schematic is shown in Fig. 2.1. It can achieve voltage step-down with two switches and one inductor, by switching between two circuit states. In State 1,  $S_{1A}$  is on and  $S_{1B}$  is off, so that the switch node voltage  $V_{sw}$  sees the input voltage  $V_{in}$  and the inductor current ramps up. In State 2,  $S_{1A}$  turns off and  $S_{1B}$  turns on. Then,  $V_{sw}$  is pulled to ground and the inductor current ramps down. Through inductor volt-second analysis, it can be derived that  $V_{out} = DV_{in}$ , where  $D$  is the duty ratio defined as the time of State 1 over the total time of the two states. The reactive energy that needs to be processed in the inductor per switching cycle is  $E_L = \frac{(1-D)P_{out}}{f_{sw}}$ , where  $P_{out}$  is the output power and  $f_{sw}$  is the switching frequency. More details about the processed reactive energy of passive components are presented in Chapter 3.

There is an inherent trade-off between achievable efficiency and power density in power converter designs. Since the passive components (e.g. inductors) oftentimes contribute a

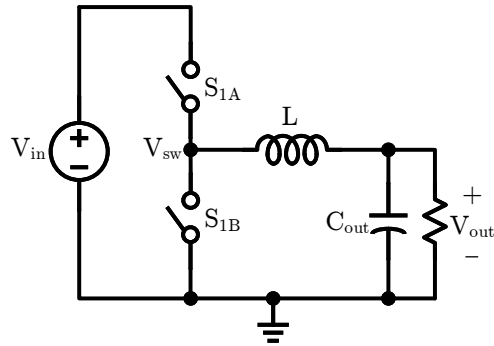


Figure 2.1: Schematic drawing of a buck converter.

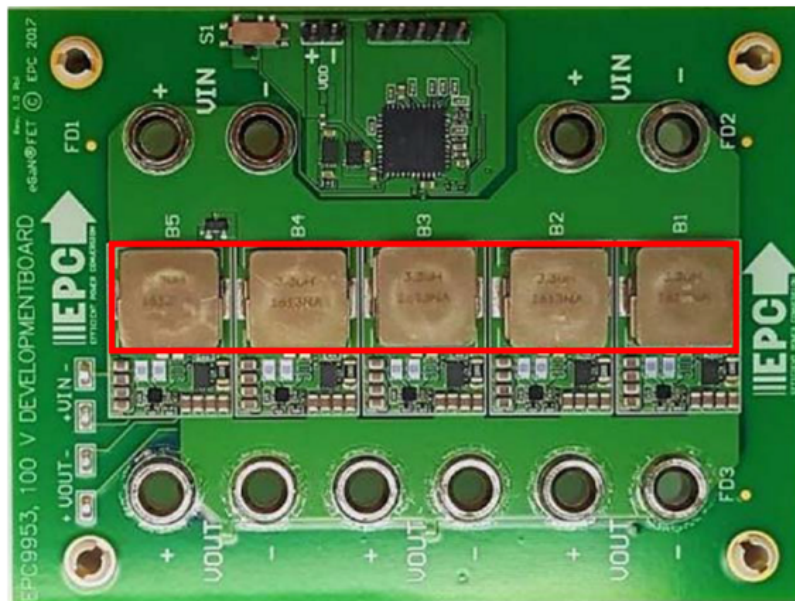


Figure 2.2: A high-performance GaN-based 48-to-12 V buck converter [1].

great portion to the overall volume, it is desirable to reduce their stored energy and therefore physical size by operating at a high switching frequency. However, this will inevitably result in an increase of semiconductor switching loss, magnetic core loss and ac winding loss, as well as other frequency-dependent losses.

The work in [1] reports a highly optimized GaN-based buck converter design for 48-to-12 V data center applications. Owing to the relatively poor energy density of inductors, the converter is designed to operate at 500 kHz. It achieves 96% efficiency and 1000 W/in<sup>3</sup> power density. However, as can be seen in Fig. 2.2, the inductors dominate the size of the overall

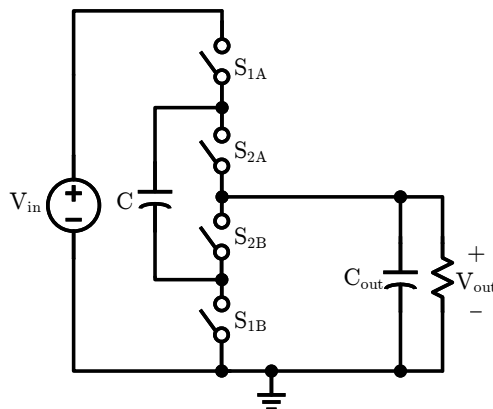


Figure 2.3: Schematic drawing of a 2-to-1 SC converter.

solution. It is difficult to further improve the power density without sacrificing the efficiency, regardless of the advancement of semiconductor technology. On the other hand, the room for efficiency improvement by operating at a lower switching frequency is also limited. Owing to the various loss mechanisms of inductors, it is very challenging to design a buck converter with greater than 98% efficiency for 48-to-12 V conversion, even at a relatively low frequency of 100 to 200 kHz.

## Switched-Capacitor Converters

In comparison to inductors, capacitors are known to have much higher energy densities (e.g., up to 100x-1000x higher) [2], [3]. Specifically, multilayer ceramic capacitors (MLCCs), with their high energy density (comparable to electrolytic capacitors) and low dissipation factor (typically less than 5%), are suitable candidates for energy transfer in power converters. Converters that use only capacitors in the energy conversion process are called switched-capacitor (SC) converters [4]–[6].

The schematic drawing of a basic 2-to-1 SC converter is shown in Fig. 2.3. In the first half switching cycle, switch  $S_{1A}$  and  $S_{2B}$  are on, and the series combination of flying capacitor  $C$  and the output is charged by the input voltage source. In the second half switching cycle,  $S_{2A}$  and  $S_{1B}$  are on. The input is disconnected and the output is powered by the flying capacitor. Through capacitor “charge multiplier vector” analysis [7], it can be found that the flying capacitor voltage and the output voltage are fixed at  $V_C = V_{out} = \frac{1}{2}V_{in}$  for the no-load condition. Thanks to the additional voltage level ( $\frac{1}{2}V_{in}$ ) provided by the flying capacitor, the voltage that needs to be blocked by each switch is only  $\frac{1}{2}V_{in}$ . This allows for the use of low-voltage switches as compared to the conventional two-level switched-inductor converters (e.g., buck converters), in which the switches need to block the full high-level voltage in the system.

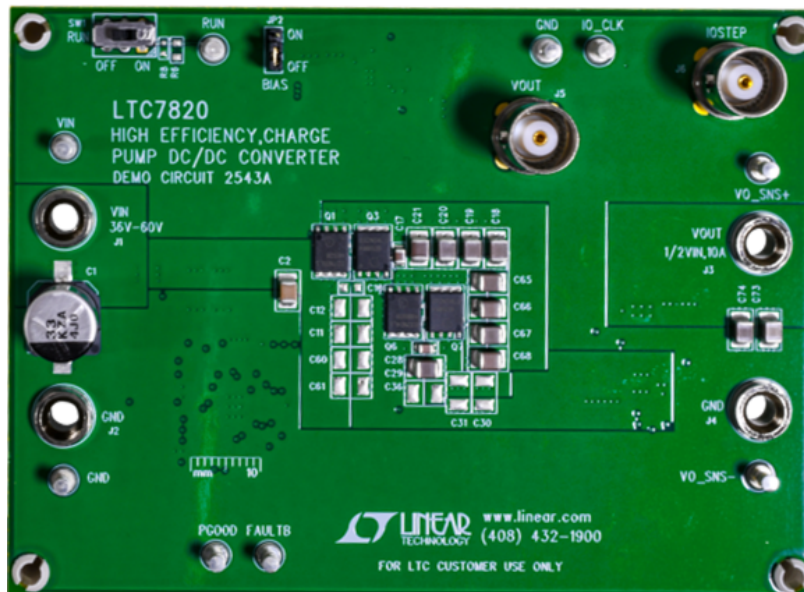


Figure 2.4: A high-performance 48-to-24 V switched-capacitor converter [8].

Historically, SC converters are most commonly used as low-power fully integrated converters, due to the fact that SC topologies can achieve lower switch stress at high conversion ratios and capacitors are easier to be integrated on-chip than inductors [9], [10]. In the past, they were less favored for discrete applications ( $> 10$  W) because of the lack of lossless regulation capability, and the efficiency and electromagnetic interference (EMI) challenges associated with charge sharing loss. Recently, there has been a trend to use SC converters for high-power performance-driven applications, where the stringent efficiency and power density requirements cannot be achieved by inductor-based converters. In these applications, the voltage regulation requirement is not as important. Fig. 2.4 shows the photograph of a commercially available 48-to-24 V, 20 A SC converter [8]. It demonstrates up to 99% efficiency and  $4000 \text{ W/in}^3$  power density, along with rugged start-up and protection features.

However, regardless of the dedicated design, this SC converter still suffers from the fundamental loss mechanism in pure capacitor-based converters: capacitor charge sharing loss (also known as charge redistribution loss). Here, we briefly review the origin and effects of this loss.

Fig. 2.5 shows the generic SC converter model as well as the output impedance curve with respect to the switching frequency. The generic SC model [11] consists of an ideal transformer and an output impedance  $R_{\text{out}}$ . The ideal transformer represents the nominal conversion ratio of the converter. The output impedance  $R_{\text{out}}$  incorporates both the conduction loss of the converter as well as the capacitor charge sharing loss, and is a good indication of the efficiency performance of the converter. This impedance is usually plotted against the

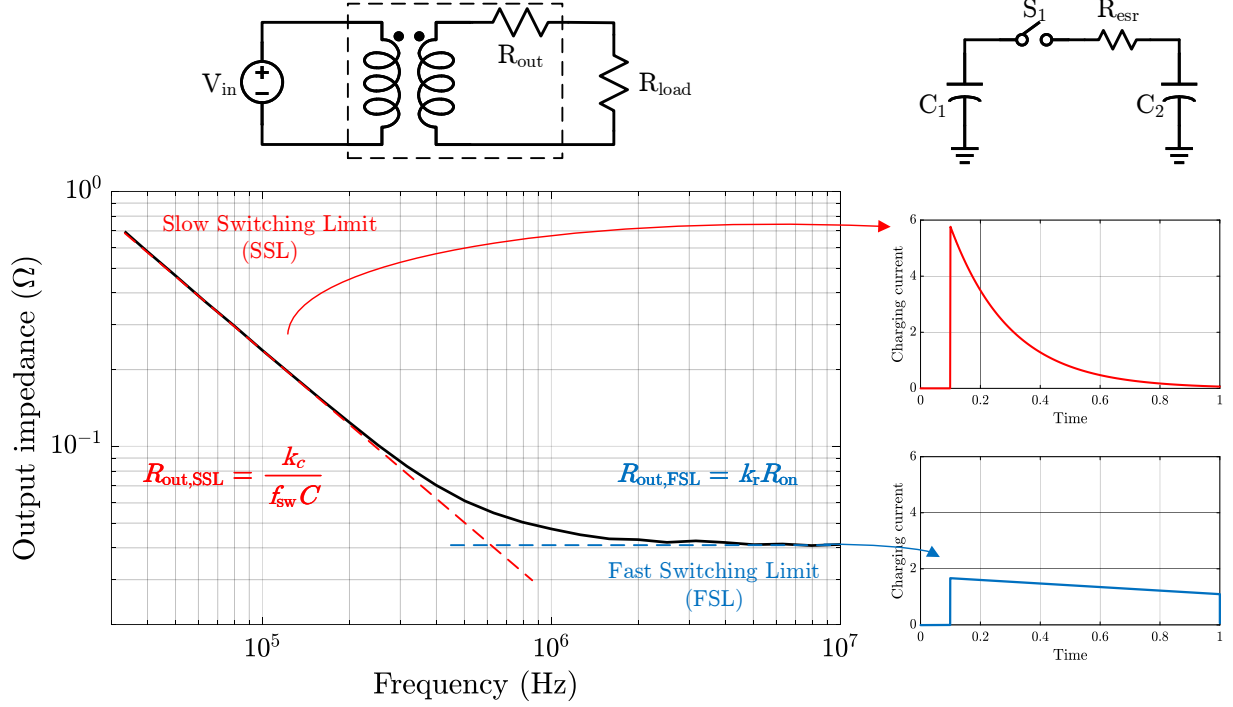


Figure 2.5: Pure SC converter: ideal circuit model, output impedance vs. switching frequency, origin of capacitor charge sharing loss (capacitor charging current at SSL and FSL).

switching frequency to reveal the characteristics of the SC converters. It can be seen that there are two asymptotic operating regions: the fast switching limit (FSL) and the slow switching limit (SSL) [4], [5], [7], [12], [13]. The FSL represents the lowest achievable output impedance of a SC converter. It occurs at high switching frequencies where the capacitor charge transfer is incomplete and the charging current is nearly constant per switching cycle. In this case, the dominating loss is the conduction loss due to the series resistance in the converter (e.g., switch resistance, flying capacitor ESR, PCB trace resistance) and is independent of switching frequency.

On the other hand, the SSL occurs at low switching frequencies, when the output impedance is dominated by the capacitor charge sharing loss, owing to the large instantaneous capacitor current at phase transitions. As can be seen in Fig. 2.5, when two capacitors  $C_1$  and  $C_2$  with different initial voltages are connected in parallel by closing switch  $S_1$ , the initial voltage mismatch between the two capacitors  $\Delta V_0$  can only be present across the small series resistance  $R_{esr}$  in the circuit, assuming the parasitic inductance is negligible. This will result in an exponentially decaying charging current with a high initial value of  $I_0 = \frac{\Delta V_0}{R_{esr}}$ ,

and  $R_{\text{esr}}$  will dissipate a power of

$$\begin{aligned}
 P_{\text{loss}} &= \frac{1}{T} \int_0^T R_{\text{esr}} (I_0 e^{-\frac{t}{\tau}})^2 dt \\
 &= \frac{1}{T} \int_0^T R_{\text{esr}} \left( \frac{\Delta V_0}{R_{\text{esr}}} e^{-\frac{t}{\tau}} \right)^2 dt \\
 &= \frac{\Delta V_0^2}{T R_{\text{esr}}} \int_0^T e^{-\frac{2t}{\tau}} dt
 \end{aligned} \tag{2.1}$$

where  $\tau$  is the RC time constant of the equivalent circuit. Assuming  $C_1 = C_2 = C$ , then  $\tau = \frac{R_{\text{esr}}C}{2}$ . Provided that the switching period  $T$  is sufficiently long compared to  $\tau$  (i.e. in SSL region of operation), (2.1) can be simplified to

$$P_{\text{loss}} = \frac{1}{4} C \Delta V_0^2 f_{\text{sw}} \tag{2.2}$$

where  $f_{\text{sw}} = \frac{1}{T}$  is the switching frequency of switch  $S_1$ . It can be seen that this power loss is independent of the magnitude of  $R_{\text{esr}}$ , indicating that reducing the switch on-resistance cannot improve the efficiency when the SC converter is operating in the SSL region.

Since the initial difference in capacitor voltages in one switching cycle is due to the charge transfer  $\Delta Q_0$  in the previous cycle, which is further proportional to the output current  $I_{\text{out}}$ , we can get

$$\Delta V_0 = \frac{\Delta Q_0}{C} = \frac{k_c I_{\text{out}}}{f_{\text{sw}} C} \tag{2.3}$$

where  $k_c$  is a topology-dependent constant. Now we find that the power loss in (2.2) is proportional to

$$P_{\text{loss}} \propto \frac{1}{f_{\text{sw}}}, \frac{1}{C}, I_{\text{out}}^2. \tag{2.4}$$

One straightforward way to reduce  $\Delta V_0$  and thereby the  $P_{\text{loss}}$  in SSL is to increase the switching frequency. However, it is often not favorable to do so, since the transistor switching losses, as well as the bottom plate capacitance losses in integrated SC converters, increase proportionally with respect to the switching frequency. Alternatively,  $\Delta V_0$  can be reduced by increasing the flying capacitance  $C$ , so that the SC converter can enter FSL at a lower switching frequency. But this method will reduce the energy utilization factor of the capacitor and lead to a larger converter size/volume. In summary, capacitor charge sharing loss undermines the energy density advantage of capacitors, resulting in an unavoidable trade-off between achievable efficiency and capacitor size. More discussion about the capacitor energy utilization factor is presented in Chapter 3.

In-between the FSL and the SSL, the output impedance can be approximated by the geometric mean of SSL impedance and FSL impedance [7], or obtained analytically [14], [15].



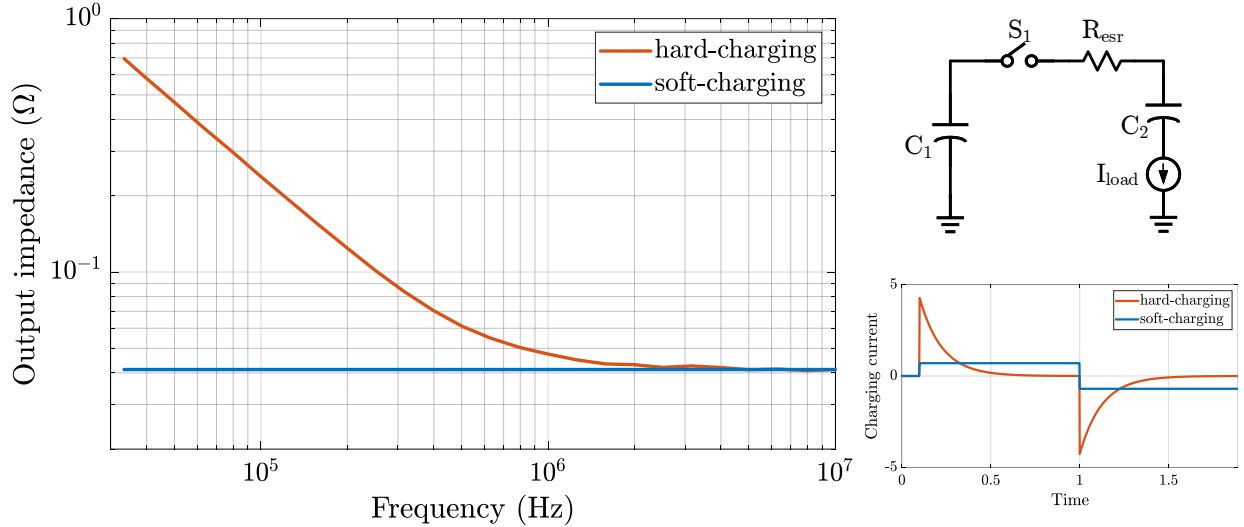


Figure 2.6: Soft-charging operation with ideal current load.

## 2.2 Soft-Charging Operation

The pioneering concept of soft-charging operation was first proposed in [16]. It is a technique that can greatly improve the efficiency and power density of SC converters, by eliminating the capacitor charge sharing loss. An idealized version of soft-charging operation is illustrated in Fig. 2.6. By inserting a controlled current load into the capacitor charging/discharging path, the majority of voltage mismatch between the flying capacitors and input/output voltage sources will be across the current load, instead of across the series resistance in the circuit as in the pure SC case. As shown in Fig. 2.6, given same amount of transferred charge per switching cycle, the constant soft-charging current has a much lower peak and rms values than the impulse current in the hard-charging case. As a result, the power loss is greatly reduced to  $P_{\text{loss}} = I_{\text{load}}^2 R_{\text{esr}}$ , and is no longer dependent on the switching frequency and the flying capacitance.

It means that with a controlled current load, the SC converter can approach its FSL performance limit at a much lower frequency. Consequently, the switching loss is reduced compared to a pure SC converter operating in FSL region. Moreover, the capacitors can have larger voltage ripples without sacrificing efficiency. This allows for the use of smaller capacitance with a significantly improved energy utilization factor.

In practice, the majority of loads are voltage-source loads or current-source loads with large decoupling capacitors. An inductive element whose terminal voltage can change instantaneously is needed to interface the SC stage and the voltage-source load. Typically, this can be satisfied by a buck converter [16]–[18] or an inductor [13], [19], [20]. Since a

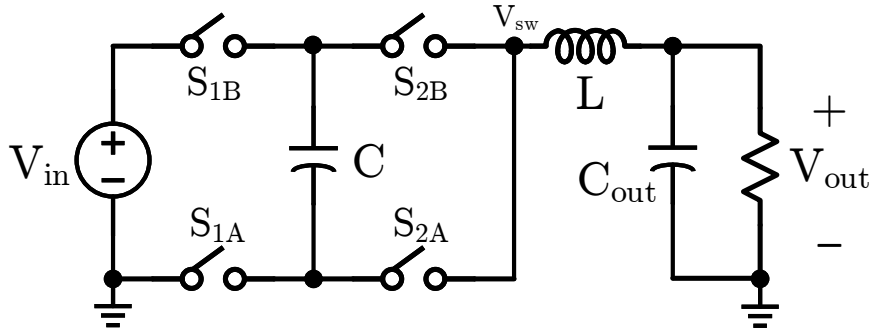


Figure 2.7: Schematic drawing of a three-level buck converter / 2-to-1 ReSC converter.

buck converter can precisely control its inductor current and thereby the input current, it can simultaneously soft-charge its front-end SC converter and regulate the output voltage. Alternatively, inductor(s) can be directly augmented to the SC converter to accommodate the voltage mismatch between the flying capacitors and input/output voltage sources during phase transitions. The SC converters with augmenting inductor(s) are called hybrid and resonant SC converters. As the name implies, the augmenting inductor(s) can facilitate soft-charging in different operation modes. In the next section, the two major operation modes for soft-charging are discussed. In Section 2.4, different inductor augmenting strategies along with their pros and cons are presented.

### 2.3 PWM Regulated Mode vs. Fixed-Ratio Mode

The schematic drawing of a basic 2-to-1 SC converter with an augmenting inductor at the output node is shown in Fig. 2.7. Depending on the design and operating parameters, it can be viewed as two different converters:

1. Three-level buck converter: a hybrid SC converter with regulation capability.
2. 2-to-1 ReSC converter: a resonant SC converter with fixed conversion ratio.

A three-level buck converter is a hybrid version of buck converter with enhanced performance. It can achieve output voltage regulation through PWM duty cycle control. Even though it uses four switches rather than two switches as in a buck converter, the total switch VA rating remains the same, as the switches are rated at  $\frac{V_{in}}{2}$  only. The high-side switches  $S_{1B}$  and  $S_{2B}$  have the same duty ratio and there is a  $180^\circ$  phase-shift between them. The low-side switches  $S_{1A}$  and  $S_{2A}$  operate complementarily to  $S_{1B}$  and  $S_{2B}$ , respectively. In addition to the two voltage levels ( $V_{in}$  and ground) in a buck converter, the flying capacitor creates a third voltage level at  $\frac{V_{in}}{2}$ , giving rise to the name of the “three-level buck converter”. Fig. 2.8

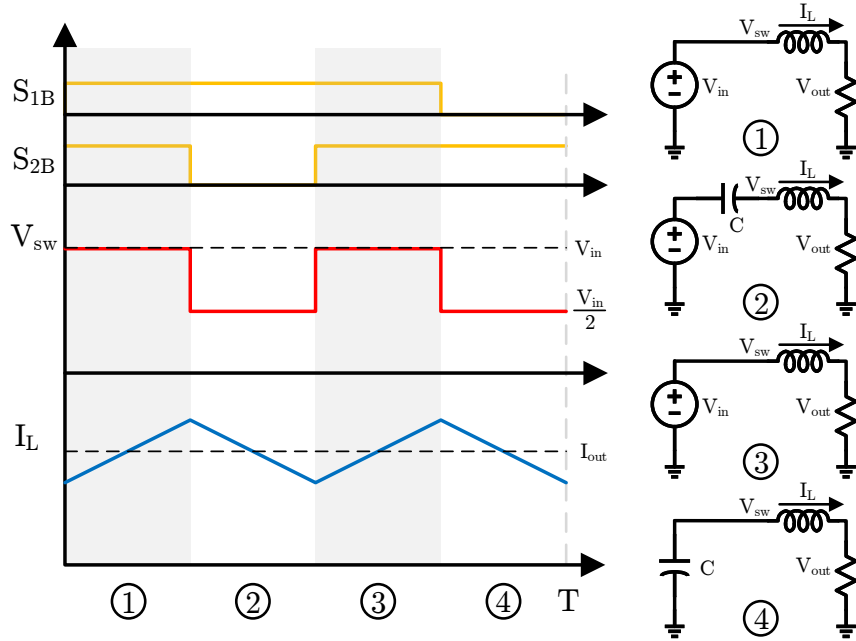


Figure 2.8: Key operating waveforms and circuit states of a three-level buck converter at duty ratio  $> 0.5$ .

illustrates the switch node voltage, inductor current, and the associated equivalent circuits for duty ratios greater than 0.5. It can be seen that the inductor sees reduced voltage (between  $V_{in}$  and  $\frac{V_{in}}{2}$ ), at doubled switching frequency. This can reduce the inductor volume by up to 4x as compared to a buck converter with the same switching frequency and power rating. In addition, the inductor is always present in the charging/discharging path of the flying capacitor, and thereby eliminates the capacitor charge sharing loss. Note that in this PWM regulated mode, the inductor sees a staircase voltage and its current is piecewise linear. The operating principle and the characteristics of a generalized N-level flying capacitor multilevel converter is given in Chapter 5.

A 2-to-1 resonant switched-capacitor (ReSC) converter can be viewed as a special case of the three-level buck converter, with the duty ratio fixed at 0.5. Its operating waveforms and equivalent circuits are shown in Fig. 2.9. Since the switch node voltage  $V_{sw}$  is always equal to the output voltage at  $\frac{1}{2}V_{in}$ , there is no voltage across the inductor except the flying capacitor ripple voltage. Therefore, a very tiny inductor (on the order of nH) can be selected. By tuning the switching frequency to the resonant frequency of the flying capacitor  $C$  and the output inductor  $L$  ( $f_{sw} = \frac{1}{2\pi\sqrt{LC}}$ ), the flying capacitor will be charged/discharged in a resonant fashion. For fixed flying capacitance and inductance, this condition corresponds to the minimum operating frequency that allows for full soft-charging [13]. Moreover, thanks to

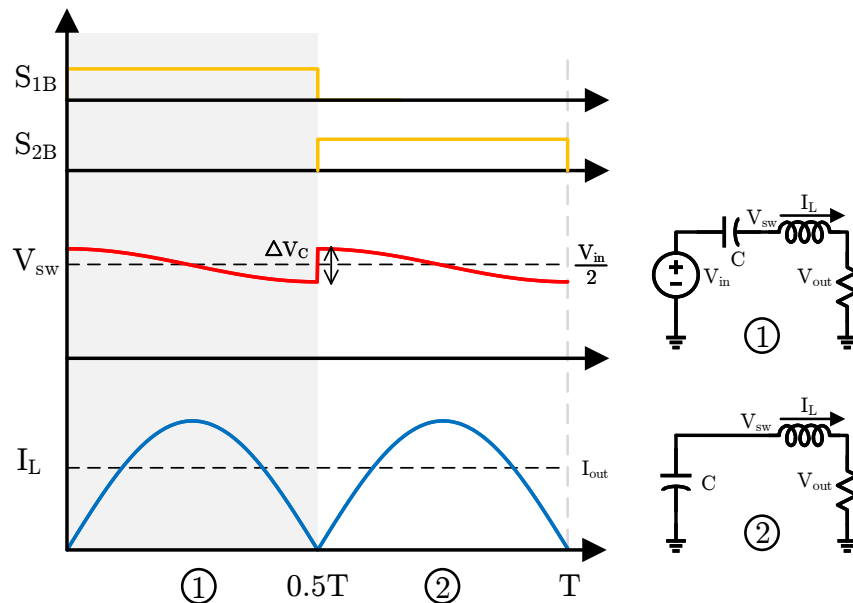


Figure 2.9: Key operating waveforms and circuit states of a 2-to-1 resonant SC converter.

the resonant operation, zero-current switching (ZCS) is naturally achieved and the overlap switching loss caused by the simultaneous existence of switch voltage and current during switching transitions is minimized. As will be discussed in Chapter 6, by tuning the LC tank to be slightly inductive, zero-voltage switching (ZVS) is achievable, eliminating the switch output capacitance loss. Owing to the soft-switching feature, as well as the very small size of the resonant inductor and the resultant low magnetic loss, a 2-to-1 ReSC converter can achieve even higher efficiency and power density than a three-level buck converter. However, this comes at the cost of losing regulation capability, since the small resonant inductor is incapable of handling the required voltage-seconds when the duty ratio deviates from 0.5. Therefore, fixed-ratio resonant SC converters are mainly used as high-efficiency, high-power-density DC transformers. Table 2.1 summarizes and compares the key characteristics of three-level buck converters and 2-to-1 ReSC converters.

The above example is based on a basic 2-to-1 SC converter. In order to determine if an arbitrary SC topology is able to take full advantage of the soft-charging operation with a single inductor at output, a generalized analysis framework is presented in [19]. For topologies that cannot achieve full soft-charging due to the violation of KVL during phase transitions at the internal voltage nodes, a split-phase control technique can be applied [21].

Table 2.1: Comparison of three-level buck converter and 2-to-1 ReSC converter

	Three-level Buck	2-to-1 Resonant SC
Soft-charging	Triangular current	Sinusoidal current
Duty ratio	Adjustable	50%
Regulation	Duty cycle control	2:1 fixed ratio
Required inductance	Low	Very low
Soft-switching	Quasi-Square-Wave	ZCS, ZVS
Efficiency	High	Very high
Power density	High	Very high
Substitute	Buck	DC Transformer

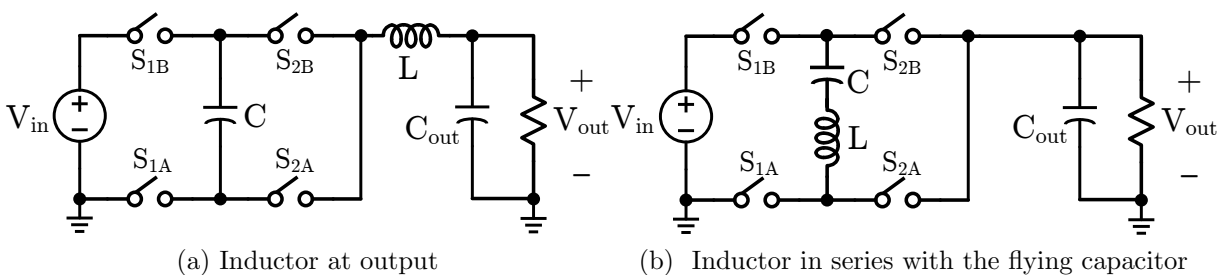


Figure 2.10: 2-to-1 SC converter with different augmenting inductor locations.

## 2.4 Inductor Placement Strategy

In general, there are two ways to augment SC converters with inductor(s). One is placing the inductor at the output node as in the examples shown in Section 2.3. The other is placing the inductor(s) in series with the flying capacitor(s). These two methods are illustrated in Fig. 2.10 with a 2-to-1 SC converter as the base topology.

Under the assumption of fixed-ratio operation with 50% duty ratio, the converters' output impedances are simulated and plotted in Fig. 2.11. The inductor currents at different operating frequencies are shown in Fig. 2.12. It can be seen that, while the two strategies have similar behaviors for switching frequencies lower than the resonant frequency  $f_{\text{crit}} = \frac{1}{2\pi\sqrt{LC}}$ , the output impedance of the “inductor in series with capacitor” configuration increases

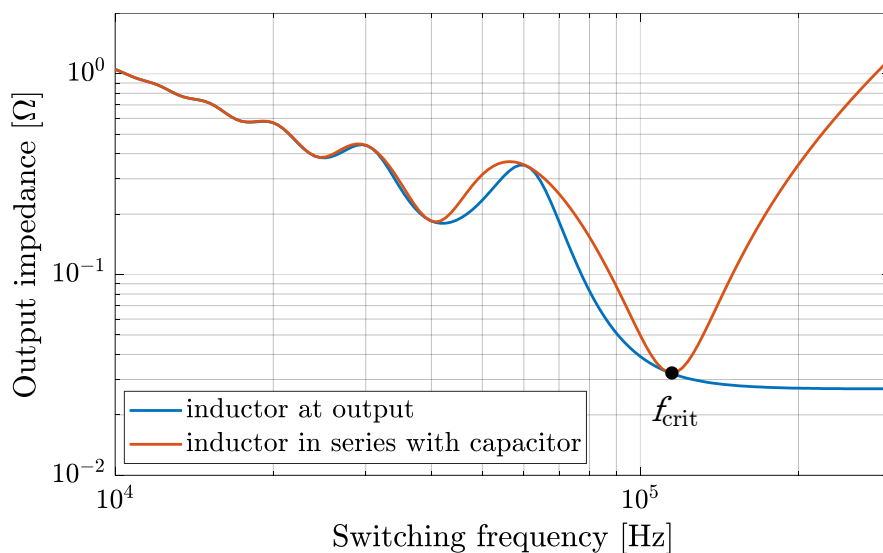


Figure 2.11: Output impedance with respect to inductor location.

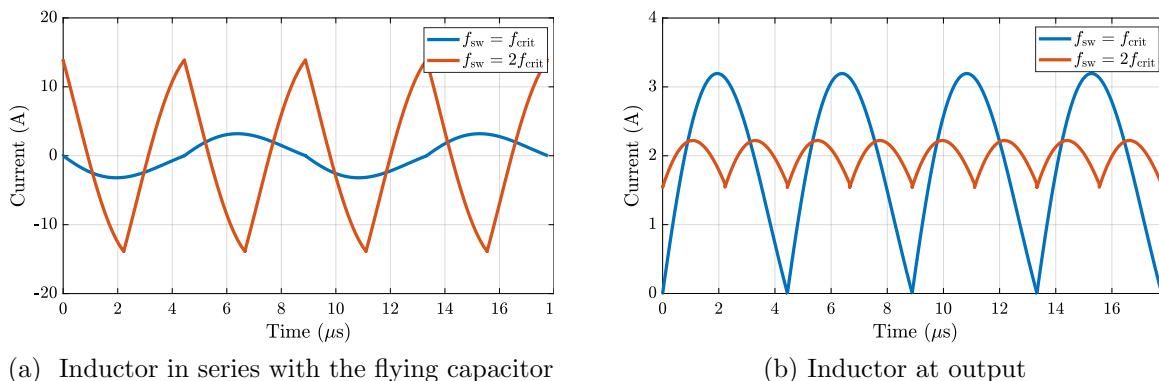


Figure 2.12: Inductor current at different locations and frequencies.

sharply when the frequency is higher than  $f_{\text{crit}}$ . This is due to the fact that the LC tank becomes inductive with both positive and negative current within one switching state, resulting in large circulating current and associated power loss. Therefore, the most viable way to operate such a converter is at the resonant frequency  $f_{\text{crit}}$ . This requires precise tuning of the inductance and capacitance with very tight tolerance. Class-I multilayer ceramic capacitors (MLCCs) are usually needed for their stable performance over temperature, dc-bias, and aging. However, they are usually less energy dense and more expensive than Class-II MLCCs. The resonant inductors should also go through careful factory measurement and calibration to ensure low variations from nominal values. Recently, a lock-in controller IC has been designed to optimize the performance of such resonant SC converters, by automatically

detecting the resonance point and adjusting the switching frequency intelligently [22].

In comparison, the “inductor at output” configuration enters the fast switching limit (FSL) region for  $f_{sw} > f_{crit}$ , with a fixed output impedance that is slightly smaller than that at the resonant frequency. This is because the inductor filtering effect leads to a smoother current waveform, which has a smaller RMS value than that of the sinusoidal current in resonant operation. As a result, it is viable to operate the “inductor at output” resonant SC converters at  $f_{sw} \geq f_{crit}$ . This allows for more relaxed component tolerance compared to the “inductor in series of capacitor” configuration, as no precise LC tank tuning is needed and high energy density Class-II MLCCs can be used, despite their dc-bias and temperature-varying characteristics.

However, the “inductor at output” configuration also has limitations. Firstly, it is only applicable to selective topologies [13], whereas the “inductor in series with capacitor” can be applied to all SC topologies. It should be noted that the switched-tank converter [23] can also be viewed as a type of “inductor in series with capacitor” converter. Even though it is composed of a Dickson converter with augmenting inductors added to every other flying capacitor, LC tanks are present in all current branches. The topology therefore shares the characteristics of the “inductor in series with capacitor” configuration.

Secondly, in the “inductor at output” configuration, the switches will see the flying capacitor ripple voltage on top of their nominal blocking voltage. This could result in limited allowable voltage ripple on flying capacitors in practical implementations, even though soft-charging theoretically permits unconstrained capacitor ripple without an efficiency penalty. In contrast, in the “inductor in series with capacitor” converters, the inductors always shield switches from the capacitor voltage ripples, and thus the theoretical switch voltage rating is always the nominal voltage. Consequently, the capacitors are allowed to have a large ripple without increasing the switch stress, thus compensating for the need of relatively low energy density Class-I MLCCs.

Thirdly, the duty ratio of certain “inductor at output” converters may deviate from 50% and lead to increased switch RMS current and power loss. As discussed in [24], [25], in order to maintain capacitor charge balance, when augmenting a single inductor to the output node of a N-to-1 series-parallel converter, the duty ratio of the series-phase and the parallel-phase need to be adjusted to  $\frac{1}{N}$  and  $\frac{N-1}{N}$ , respectively. In contrast, if distributed inductors are inserted in series with every flying capacitor, the duty ratio of all switches remain at 50%. This also applies to other topologies, such as the Fibonacci converter and the multi-resonant SC converters presented in Chapter 7. To illustrate the effect of duty ratio on RMS current and power loss, Fig. 2.13 compares the current of two switches that have the same switching period, the same amount of transferred charge, but different duty ratio. Assuming a constant capacitor current  $I_{pk}$ , the rms value can be calculated as:

$$I_{rms} = I_{pk}\sqrt{D}. \quad (2.5)$$

It can be seen that the switch with  $D = \frac{1}{8}$  has twice the rms current and therefore four times the loss in comparison to the one with  $D = \frac{1}{2}$ , even though they have the same average

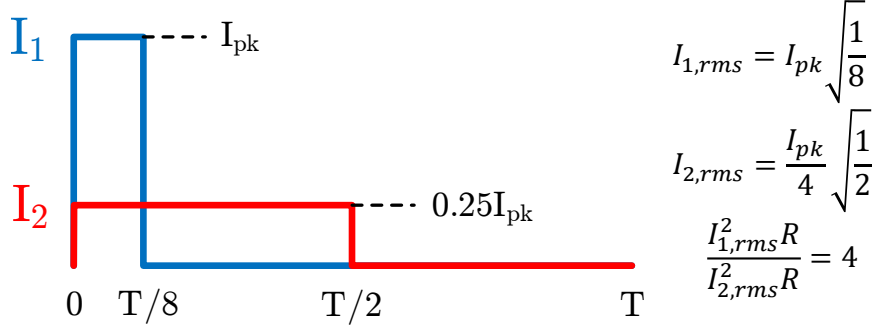


Figure 2.13: Effect of duty ratio on rms current and output impedance.

Table 2.2: Comparison of different inductor placement strategies

	Inductor at output	Inductor in series with capacitor
Operating frequency	$f_{sw} \geq f_{crit}$	$f_{sw} = f_{crit}$
Tolerance to component mismatch	Relatively good tolerance	Precise matching required
Duty ratio	Dependent on capacitor charge balance	50%
Output impedance	Increase when duty ratio deviates from 50%	Lowest possible
Applicability	Selective topologies	All topologies
Switch ratings	Switch sees capacitor voltage ripple	Capacitor voltage ripple shielded by inductor
Soft switching	Achievable	Achievable
Regulation capability	Regulation possible	Regulation possible

current. This may put the “inductor at output” resonant SC converters in a less favored position in comparison to the “inductor in series with flying capacitor” converters at high conversion ratios, when the switch area cannot be optimized accordingly. This is particularly a challenge for discrete implementations.

Lastly, regulation is achievable with both inductor augmenting strategies. For the “inductor at output” configuration, duty cycle control can be used as in the three-level buck converter. Phase-shift control or frequency control can also be used for the “inductor in series with capacitor” resonant SC converters [26]–[28], similar to dual-active-bridge converters and series-resonant converters. However, the regulation capability comes at a cost in terms of efficiency and power density, as the inductor size needs to be scaled up compared to the value required in the fixed-ratio resonant operation.



## Chapter 3

# Modeling and Comparison of Passive Component Volume

The added inductor(s) in hybrid and resonant switched-capacitor (SC) converters offer an additional degree of freedom in the design space, and it is of great interest to understand the trade-offs between capacitor and inductor size and volume allocation. In this chapter, we analyze the reactive power processed by the passive components and use it to calculate the total passive component volume. It is shown that the total passive component volume of resonant SC (ReSC) converters can be expressed as a function of flying capacitor voltage ripple, and the optimized capacitor voltage ripple that minimizes the total volume is dependent on topology specific parameters and the relative energy density ratio between the capacitor(s) and inductor(s). Moreover, we also demonstrate through theoretical analysis and experimentation that ReSC converters use significantly less passive component volume than conventional SC and buck converters for the same amount of power converted. Next, to compare different ReSC topologies, a normalized passive volume parameter is proposed for simple and fair comparison. This can be used along with a normalized switch stress parameter (based on switch VA ratings) to create a framework to showcase the relative performance of different topologies. This framework can be used to visualize and compare the passive and active component utilizations among different topologies. Additionally, the proposed reactive power analysis is extended to hybrid converters with regulation capability.

### 3.1 Background and Motivation

As discussed in Chapter 2, the augmenting inductor(s) can eliminate the capacitor charge sharing loss present in pure SC converters through soft-charging operation [16], [17], [19], thereby allowing larger capacitor voltage ripple and better capacitor energy utilization. However, depending on the relative energy density of the inductors and capacitors, it is unclear whether the capacitor volume reduction could offset the volume of the augmenting inductor and lead to a smaller overall volume than that of a pure SC converter. Moreover, as the

augmenting inductors offer an additional degree of freedom in the design space, it is crucial to evaluate and find the optimum inductor and capacitor allocation that minimizes the total passive component volume.

Besides optimizing a specific ReSC converter, it is also of great interest to compare the performance of different ReSC topologies. When developing analytical models for topology comparison, a dilemma often faced is the trade-off between complexity and accuracy. To get tractable expressions with moderately good accuracy, a common and reasonable assumption for ReSC converters made by [29], [30] is that the losses are mainly contributed by the semiconductor switches while the volume is solely determined by the passive components. Here, the losses of the passive components are assumed to be comparable among different topologies and could be cautiously omitted during comparison. This is because most existing high performance ReSC converters operate at a relatively low switching frequency (e.g., less than 500 kHz) and the resonant inductors typically have low inductance value (e.g., less than 200 nH) and see the capacitor ripple voltage only, so the ac-related losses of the inductors are relatively small. On the other hand, the DCR loss of the inductors is more dependent on the rating of the output current and should be comparable among topologies. Thus, under these assumptions, if a single overall performance figure-of-merit, – including both volume and efficiency, is not the desired metric, the passive component volume and the semiconductor loss comparisons can be decoupled.

In this Chapter, we strive to gain a better understanding of these questions from the perspective of the fundamental reactive energy/power processed by the passive components. In Section 3.2, we showcase that the total passive component volume of ReSC converters can be ultimately expressed and optimized as a function of flying capacitor voltage ripple. The minimized total volume is only dependent on topology specific parameters and the relative energy density between capacitor and inductor. Following this, a number of observations and design guidelines are derived in Section 3.3 to facilitate practical ReSC converter designs. Additionally, a hardware prototype is built to experimentally demonstrate that ReSC converters use significantly less passive volume than conventional SC and buck converters for the same amount of power converted, while maintaining the best efficiency performance. In Section 3.4, we generalize the proposed reactive power analysis to provide direct passive volume comparison among different ReSC topologies. Combining this with the classical switch total VA rating metric, which reflects potential efficiency, we provide a simple yet powerful framework to evaluate the relative performance (in terms of active and passive component utilization) of different ReSC topologies. Moreover, the theoretical lower-bound limits of passive and active components are derived to identify the framework boundaries such that any new emerging topologies can be analyzed and incorporated into the comparison space. In Section 3.5, with the examples of three-level buck converters and series-capacitor buck converters, the proposed reactive power analysis is extended to hybrid converters with regulation capability.

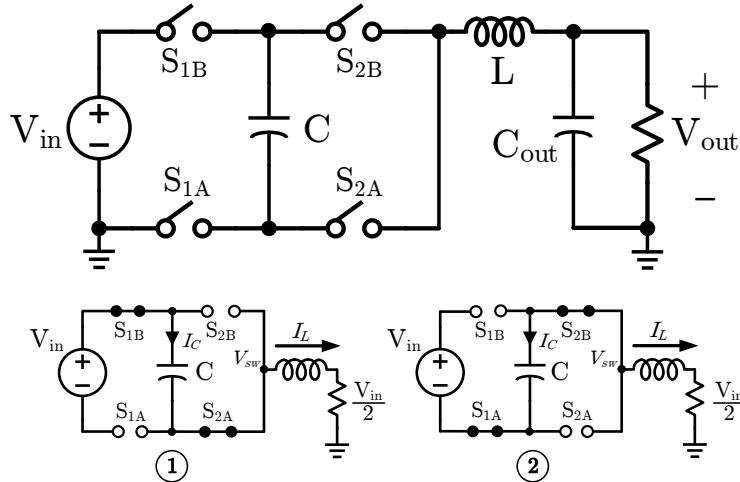


Figure 3.1: Schematic drawing of a 2-to-1 resonant switched-capacitor converter and its two operating states.

### 3.2 Analysis of Basic 2-to-1 Resonant Switched-Capacitor Converter

The volume of a passive component is directly related to the peak energy it can store, as well as its type and technology. In ReSC converters, the resonant inductors are able to transfer all stored energy as the sinusoidal inductor current reaches zero each switching cycle. In contrast, each flying capacitor can typically only deliver a portion of its stored energy which is determined by the magnitude of its voltage ripple on top of the dc average voltage. To calculate the total passive component volume of ReSC converters, we propose an energy-based method by fundamentally analyzing the reactive power processed by the passive components. Note that the term “reactive power” is also referred to as “indirect power” in [31]. Here, we use the basic 2-to-1 ReSC converter as an example to demonstrate the proposed method. The reactive power processed by the flying capacitor and the resonant inductor is first calculated. Then, this processed power is related to the required stored energy through an energy utilization factor. Finally, the passive component volume is derived by dividing the required stored energy by the energy density of the corresponding passive components. It will be shown that the total passive volume can be expressed and subsequently optimized as a function of the flying capacitor voltage ripple ratio.

The schematic drawing of a 2-to-1 ReSC converter and its two operating states are shown in Fig. 3.1. All switches have a fixed duty ratio of 50%, and there is a  $180^\circ$  phase shift between the “A” switches and the “B” switches. The switching frequency is the resonant frequency of the flying capacitor and the inductor ( $f_{sw} = \frac{\omega_r}{2\pi} = \frac{1}{2\pi\sqrt{LC}}$ ), as it is the minimum

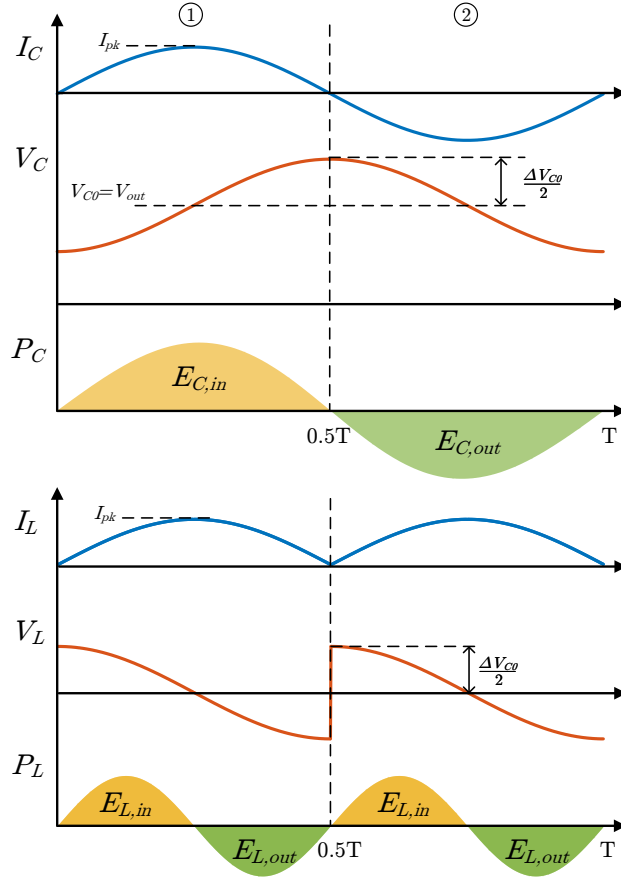


Figure 3.2: Current, voltage, and power waveforms of the flying capacitor and the resonant inductor in a 2-to-1 ReSC converter.

frequency with full soft-charging for hybrid SC converters [19]. As shown in Fig. 3.2, the flying capacitor has a sinusoidal current  $I_C = I_{pk} \sin(\omega_r t)$ , and the corresponding capacitor voltage has a dc component of  $V_{C0} = V_{out}$  and an ac component of  $-\frac{I_{pk}}{C\omega_r} \cos(\omega_r t)$ , with a peak-to-peak ripple voltage of  $\Delta V_{C0} = \frac{2I_{pk}}{C\omega_r}$ . In contrast, the inductor current is a rectified sine wave with the same amplitude as that of the capacitor current, and the voltage across the inductor has the same peak magnitude as the capacitor voltage ripple, but at twice the frequency. By multiplying the current and the voltage waveforms, the instantaneous power processed by the capacitor  $V_C(t)I_C(t)$  and the inductor  $V_L(t)I_L(t)$  can be derived as shown in Fig. 3.2, and the shaded areas represent the energy going into and out of the passive component in each cycle.

In periodic steady-state, the average power  $P_k$  processed by a reactive element  $k$  can be expressed in terms of the cyclically stored energy  $E_{in}$ , delivered energy  $E_{out}$  and the switching period  $T$ :  $P_k = \frac{1}{T} \cdot \frac{E_{in} + E_{out}}{2} = \frac{1}{T} E_{in}$ , for the assumption of lossless components. By factoring

out the operation dependent term  $T$ , this average reactive power term  $P_k$  can readily reflect the intrinsic property of the topology. The average power processed by the flying capacitor,  $P_{C0}$ , can be calculated as

$$\begin{aligned}
 P_{C0} &= \frac{E_{C,in}}{T} \\
 &= \frac{1}{T} \int_0^{\frac{T}{2}} I_c(t)V_c(t)dt \\
 &= \frac{1}{T} \int_0^{\frac{T}{2}} I_{pk}\sin(\omega_r t)(V_{out} - \frac{I_{pk}}{C\omega_r}\cos(\omega_r t))dt \\
 &= \frac{1}{2}V_{out}I_{out}
 \end{aligned} \tag{3.1}$$

where  $I_{out} = \frac{2}{\pi}I_{pk}$  is the average output current. Similarly, the average power of the resonant inductor is given by

$$\begin{aligned}
 P_{L0} &= \frac{E_{L,in}}{T} \\
 &= \frac{1}{T} \int_0^{\frac{T}{4}} I_L(t)V_L(t)dt \\
 &= \frac{1}{T} \int_0^{\frac{T}{4}} I_{pk}\sin(\omega_r t)\frac{I_{pk}}{C\omega_r}\cos(\omega_r t)dt \\
 &= \frac{I_{out}^2}{32Cf_{sw}}.
 \end{aligned} \tag{3.2}$$

Note that the integral is from 0 to  $\frac{T}{4}$  only. This is because the inductor sees doubled frequency and stores and delivers energy twice per switching cycle. Therefore, from an energy *storage* perspective, the calculation of the inductor processed power should consider one energy transfer cycle only (half of the switching cycle in this case), resulting in an integral from 0 to  $\frac{T}{4}$ . This deviates from the Wolaver definition on Page 63 of [32]. Wolaver focused on how much reactive energy needs to be *transferred* to the load per switching cycle, and therefore defined the reactive power processed by a reactive element  $k$  to be  $P_k = \frac{1}{2} \cdot \frac{1}{T} \int_0^T |V_k I_k| dt$ . This definition would lead to a result that is twice that of (3.2).

Eqn. (3.2) can be further expressed as a function of flying capacitor voltage ripple ratio. By substituting in the average-to-peak capacitor voltage ripple  $\frac{1}{2}\Delta V_{C0} = \frac{I_{pk}}{C\omega_r} = \frac{I_{out}}{4Cf_{sw}}$ , we get

$$P_{L0} = \frac{I_{out}\Delta V_{C0}}{16} = \frac{P_{out}}{16} \cdot \frac{\Delta V_{C0}}{V_{out}} = \frac{P_{out}}{16} \cdot \frac{\Delta V_{C0}}{V_{C0}} \tag{3.3}$$

where  $V_{C0} = V_{out}$  is the dc average voltage of the flying capacitor. Now that the reactive power processed by the flying capacitor and the resonant inductor have been derived, we can next calculate the energy that needs to be stored by these passive components. For the

flying capacitor, the processed energy  $E_{C0}$  (also equals to  $E_{C,\text{in}}$  and  $E_{C,\text{out}}$  in Fig. 3.2) can be expressed as the average power  $P_{C0}$  divided by the switching frequency. Alternatively, it equals the difference between the peak and minimum stored energy per switching cycle:

$$\begin{aligned} E_{C0} &= \frac{P_{C0}}{f_{\text{sw}}} \\ &= \frac{1}{2}C[(V_{C0} + \frac{1}{2}\Delta V_{C0})^2 - (V_{C0} - \frac{1}{2}\Delta V_{C0})^2] \\ &= CV_{C0}\Delta V_{C0}. \end{aligned} \quad (3.4)$$

Next, we define the energy utilization factor of the capacitor as the energy transferred by the capacitor per cycle divided by the peak energy stored by the capacitor:

$$\mu_C = \frac{E_{C0}}{E_{C,\text{store}}} = \frac{E_{C0}}{\frac{1}{2}C(V_{C0} + \frac{1}{2}\Delta V_{C0})^2} = \frac{2\frac{\Delta V_{C0}}{V_{C0}}}{(1 + \frac{1}{2}\frac{\Delta V_{C0}}{V_{C0}})^2}. \quad (3.5)$$

For a fixed amount of processed energy, a higher  $\mu_C$  indicates a lower stored energy and smaller capacitor size, and vice versa. The capacitor volume  $\text{Vol}_C$  can then be expressed with respect to the capacitor processed power as:

$$\text{Vol}_C = \frac{E_{C,\text{store}}}{\rho_{E,C}} = \frac{E_{C0}}{\rho_{E,C}\mu_C} = \frac{P_{C0}}{f_{\text{sw}}\rho_{E,C}\mu_C} \quad (3.6)$$

where  $\rho_{E,C}$  is the energy density of the capacitor; it is physically limited by the maximum electrical field of the dielectric material.

For the resonant inductor, the sinusoidal current reaches zero every half cycle. Thus, the inductor processed energy equals the stored energy (i.e. its energy utilization factor  $\mu_L = 1$ ) and

$$\text{Vol}_L = \frac{E_{L,\text{store}}}{\rho_{E,L}} = \frac{E_{L0}}{\rho_{E,L}} = \frac{P_{L0}}{f_{\text{sw}}\rho_{E,L}}, \quad (3.7)$$

where  $\rho_{E,L}$  is the energy density of the inductor; it is physically limited by the maximum flux density of the magnetic material.

Revisiting (3.1) and (3.3), it can be observed that the power processed by the capacitor is a fixed value. Moreover, it can be shown that this value is equal to the power processed by the flying capacitor in a pure 2-to-1 SC converter. Even though the augmenting inductor does not change the power/energy that is processed by the flying capacitor, it allows unconstrained capacitor voltage ripple  $\frac{\Delta V_{C0}}{V_{C0}}$  without efficiency penalty through resonant soft-charging operation, and therefore improves the energy utilization factor of the flying capacitor and results in a smaller capacitor volume. However, the capacitor volume reduction comes as a cost. As shown in (3.3), the power processed by the inductor is an increasing function of  $\frac{\Delta V_{C0}}{V_{C0}}$ , which leads to an increase in inductor volume (3.7) when the capacitor volume is reduced. The effects of  $\frac{\Delta V_{C0}}{V_{C0}}$  on capacitor volume and inductor volume are plotted in Fig. 3.3, assuming  $\rho_{E,C}/\rho_{E,L} = 100$ .

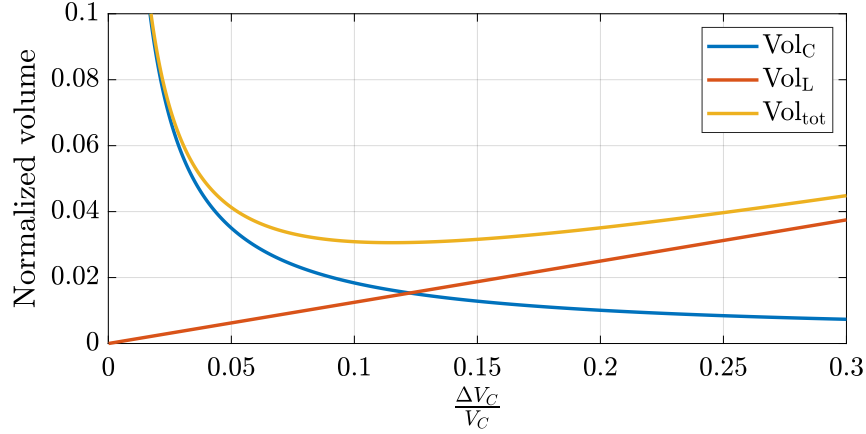


Figure 3.3: The effects of flying capacitor voltage ripple on capacitor volume, inductor volume and overall volume for a 2-to-1 ReSC converter (assuming  $\rho_{E,C}/\rho_{E,L} = 100$ ).

The trade-off between the capacitor volume and the inductor volume can be observed more clearly from:

$$\begin{aligned} \text{Vol}_{\text{tot}} &= \text{Vol}_C + \text{Vol}_L \\ &= \frac{P_{\text{out}}}{f_{\text{sw}}} \left( \frac{\frac{1}{4} \left( 1 + \frac{V_{C0}}{\Delta V_{C0}} + \frac{\Delta V_{C0}}{4V_{C0}} \right)}{\rho_{E,C}} + \frac{\frac{1}{16} \frac{\Delta V_{C0}}{V_{C0}}}{\rho_{E,L}} \right) \end{aligned} \quad (3.8)$$

where  $\text{Vol}_C$  is primarily a function of  $\frac{V_{C0}}{\Delta V_{C0}}$  whereas  $\text{Vol}_L$  is a function of  $\frac{\Delta V_{C0}}{V_{C0}}$ . For a given set of  $P_{\text{out}}$ ,  $f_{\text{sw}}$ ,  $\rho_{E,C}$  and  $\rho_{E,L}$ , (3.8) can be differentiated with respect to the capacitor ripple ratio  $\frac{\Delta V_{C0}}{V_{C0}}$  to find the value that minimizes the total volume:

$$\frac{d\text{Vol}_{\text{tot}}}{\frac{\Delta V_{C0}}{V_{C0}}} = 0 \implies \left( \frac{\Delta V_{C0}}{V_{C0}} \right)^* = \sqrt{\frac{4\rho_{E,L}}{\rho_{E,L} + \rho_{E,C}}} \approx 2\sqrt{\frac{\rho_{E,L}}{\rho_{E,C}}}. \quad (3.9)$$

It can be seen that  $\left( \frac{\Delta V_{C0}}{V_{C0}} \right)^*$  is inversely proportional to  $\sqrt{\frac{\rho_{E,C}}{\rho_{E,L}}}$ . When  $\frac{\rho_{E,C}}{\rho_{E,L}}$  increases,  $\left( \frac{\Delta V_{C0}}{V_{C0}} \right)^*$  decreases, corresponding to a passive component allocation with more capacitance and less inductance.

Substituting (3.9) into (3.8), the minimized volume of a 2-to-1 ReSC converter is then given by

$$\text{Vol}_{\text{tot},\text{min}} \approx \frac{P_{\text{out}}}{f_{\text{sw}}\rho_{E,L}} \left( \frac{\frac{\rho_{E,L}}{\rho_{E,C}} + \sqrt{\frac{\rho_{E,L}}{\rho_{E,C}}}}{4} \right). \quad (3.10)$$

Note that the above analysis assumes that the passive components are ideal and lossless. The capacitor ESR loss and inductor dc and ac losses are not considered for the volume

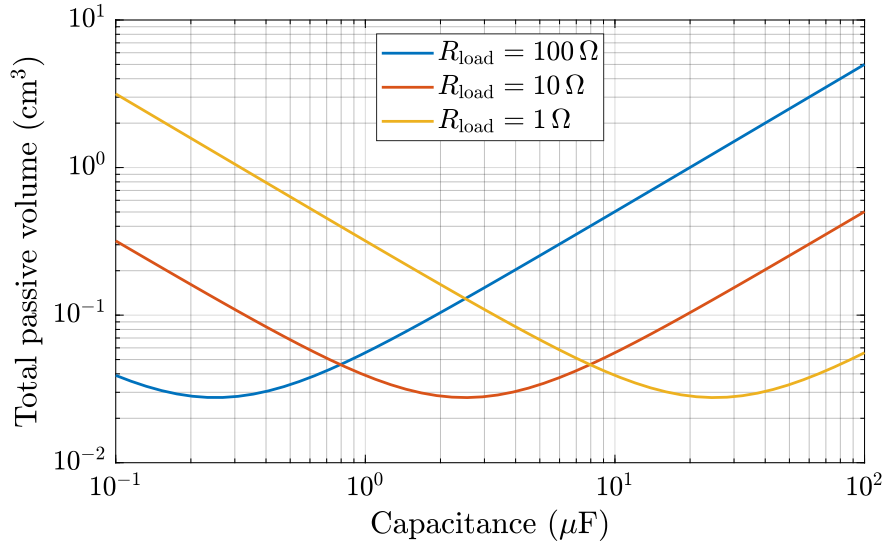


Figure 3.4: Given fixed output power and switching frequency, the 2-to-1 ReSC converter can always achieve the same minimum total passive component volume. But the optimum capacitance (and inductance) allocation depends on the magnitude of the load resistance. Parameters for the plot:  $P_{\text{out}} = 100 \text{ W}$ ,  $f_{\text{sw}} = 100 \text{ kHz}$ ,  $\rho_{E,C} = 0.1 \text{ J/cm}^3$ ,  $\rho_{E,C}/\rho_{E,L} = 100$ .

optimization. This is based on the fact that the capacitor ESR at the frequency range of interest can be much lower than the switch on-resistance in practical implementations, as usually multiple capacitors are placed in parallel. Similarly, the inductor DCR loss and core loss also only contribute a small portion to the overall loss, as the resonant operation leads to very small inductor volt-second and core size [33]. Therefore, the lossless assumption is applicable and enables simplification of the problem without greatly affecting the practicality of the results. In the next section, the above theoretical analysis will be used to derive guidelines for practical designs, followed by experimental verification.

### 3.3 Design Guidelines and Comparisons with Other Solutions

#### Design Guidelines

Given fixed output power and switching frequency, the total passive component volume of the 2-to-1 ReSC converter is plotted in Fig. 3.4 with respect to flying capacitance. It can be seen that, regardless of the magnitude of the load resistance  $R_{\text{load}}$ , the ReSC converter can always achieve the same minimized total passive component volume, which agrees with (3.10). The optimum flying capacitance that provides the lowest total passive volume is



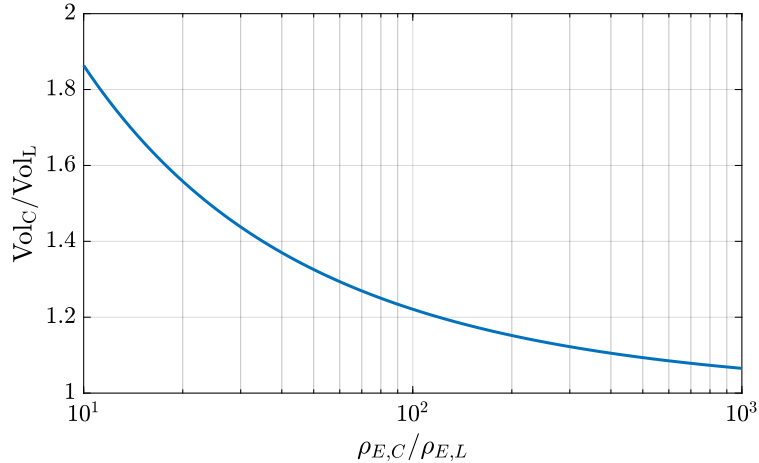


Figure 3.5: The optimum volume ratio between capacitor and inductor with respect to their energy density ratio.

inversely dependent on the load resistance. It indicates that, with fixed output power and switching frequency, higher capacitance (and lower inductance) should be used for applications with lower output voltage and higher output current. This is based on the fact that, given fixed nominal capacitance and inductance values, the capacitor volume depends on the voltage, while the inductor volume depends on the current. The capacitor and the inductor volume that give the minimized total volume can be calculated by substituting the optimized capacitor ripple ratio  $(\frac{\Delta V_{C0}}{V_{C0}})^*$  of (3.9) into (3.6) and (3.7), respectively. Fig. 3.5 plots the optimized volume ratio with respect to the energy density ratio between capacitor and inductor. Within a practical range of  $100 \leq \rho_{E,C}/\rho_{E,L} \leq 1000$ , the optimum volume ratio is slightly greater than 1, indicating that the flying capacitor and the resonant inductor should have similar volume. Note that even though this analysis is based on the assumption of lossless passive components, the result matches with the finding in [34], where the optimized passive component allocation is derived for minimized total power loss.

## Comparison with Buck Converter

Now that we have derived the minimized total passive component volume of a 2-to-1 ReSC converter, it is of great interest to compare the result with other types of converters, such as the magnetic-based converters. Since both the inductor in the buck converter and the transformer in the transformer-bridge converter have similar volt-second product requirements, the size of their respective magnetic components will be similar [35]. Here, we calculate the minimum required inductor size of a buck converter at 2-to-1 conversion ratio, with the same output power and switching frequency as that of the ReSC converter.

As derived in [32], the average power processed by the inductor is  $P_{L0} = \frac{1}{2}P_{\text{out}}$ , when the duty ratio  $D$  is 0.5. To maximize the inductor energy utilization factor  $\mu_L$ , the buck converter should operate in boundary conduction mode so that the inductor current goes to zero every switching cycle and its energy utilization factor is maximized ( $\mu_L = 1$ ). Then, the minimized volume of the inductor of a buck converter can be found to be

$$\text{Vol}_{L,\text{buck}} = \frac{\frac{1}{2}P_{\text{out}}}{f_{\text{sw}}\rho_{E,L}} \quad (3.11)$$

Compared to (3.8), it can be seen that the minimized total volume of the 2-to-1 ReSC converter is 1.2 times that of a 2-to-1 buck converter when  $\rho_{E,C} = \rho_{E,L}$ . In order for the ReSC converter to achieve a smaller volume than that of a buck converter, we need  $\rho_{E,C} \gg \rho_{E,L}$ . For instance, if  $\rho_{E,C} = 100\rho_{E,L}$ , the volume of the ReSC converter is 0.055 times that of the buck converter.

Note that this comparison is based on the assumption that all passive components in the ReSC converter and the buck converter are lossless. In practice, the buck inductor is more lossy than the LC tank of the ReSC converter as will be shown in the experimental verification section. Therefore, this ideal lossless comparison disadvantages the ReSC converter compared to the buck converter.

## Comparison with Pure SC Converter

Compared to a pure SC converter, the augmenting inductor of the ReSC converter can help eliminate the capacitor charge sharing loss and therefore allow higher capacitor voltage ripple without degrading the efficiency. However, depending on the relative energy density of inductor and capacitor, it is unclear whether the capacitor volume reduction can offset the volume of the augmenting inductor and lead to a smaller overall volume than that of a pure SC converter.

Moreover, as shown in Fig. 3.4, the capacitance and inductance allocation is dependent on the load resistance. An optimum allocation tends to use more capacitance and less inductance when the load resistance decreases and output current increases. For very low-voltage high-current applications such as the latest GPU power delivery at 1 V and 1000 A [36], the optimum inductance (of each single converter in a multi-phase configuration) might still be very small, giving rise to the question of whether pure SC converters is a better choice than ReSC converters.

Here, we compare the relative passive component volume of the 2-to-1 ReSC converter and the 2-to-1 pure SC converter. It can be easily shown that the power processed by the flying capacitor of a 2-to-1 pure SC converter is the same as that in the ReSC case:  $P_C = \frac{1}{2}P_{\text{out}}$ . However, its minimized total passive volume cannot be derived with the same method. This is because there is no inductor to constrain its flying capacitor voltage ripple ratio  $\frac{\Delta V_C}{V_C}$ , and thus its energy utilization factor  $\mu_C$  is unconstrained and can be as large as 1. Nevertheless, unlike the ReSC converter in which the capacitor voltage ripple and the power loss are decoupled because of soft-charging operation, the pure SC converter suffers

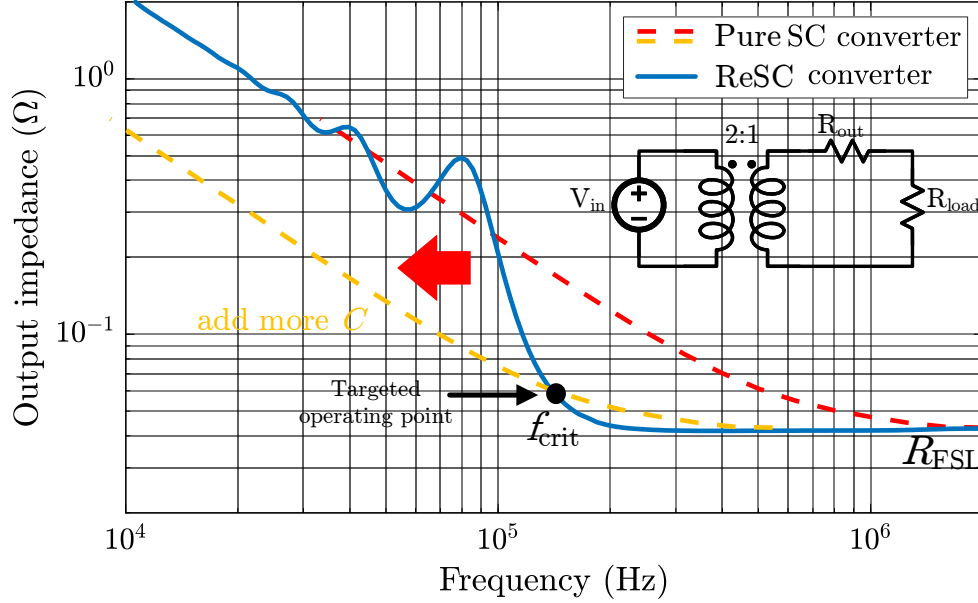


Figure 3.6: Output impedance of 2-to-1 Pure SC and ReSC converters vs. frequency.

from capacitor charge sharing loss, which is dependent on the capacitor voltage ripple ratio. Therefore, in order to have a fair volume comparison, the efficiency of the pure SC converter and the ReSC converter should be kept the same.

Switched-capacitor converters can be modeled by an ideal transformer [7]. The output impedance at the secondary side of the transformer is a good indication of the efficiency performance. In Fig. 3.6, the simulated output impedance of 2-to-1 pure SC converter and 2-to-1 ReSC converter are plotted in red and blue, respectively. They have the same switch on-resistance and flying capacitance. It can be seen that both converters approach the same lowest possible output impedance  $R_{\text{FSL}}$  at the fast switching limit (FSL) region, which is solely determined by the series resistance in the circuit (e.g., switch on-resistance, capacitor ESR) [7]. With an augmenting inductor, the ReSC converter can approach  $R_{\text{FSL}}$  at a much lower switching frequency. As derived in [14], when operating at the resonant frequency  $f_{\text{crit}} = \frac{1}{2\pi\sqrt{LC}}$ , the output impedance of the ReSC converter is

$$R_{\text{out,ReSC}} = \frac{\pi^2}{8} R_{\text{FSL}}. \quad (3.12)$$

In contrast, [14] also shows that the output impedance of 2-to-1 pure SC converter with respect to its switching frequency  $f_{\text{sw}}$  and flying capacitance  $C_p$  is

$$R_{\text{out,pureSC}} = \frac{\coth\left(\frac{1}{4R_{\text{FSL}}C_p f_{\text{sw}}}\right)}{4C_p f_{\text{sw}}}. \quad (3.13)$$

In order for the pure SC converter to have the same efficiency performance, the two converters should have the same output impedance at the same switching frequency. As illustrated in Fig. 3.6, this can be achieved by adding more capacitance to shift the impedance curve of the pure SC converter to the left. By equating (3.12) and (3.13), we get

$$C_p \approx \frac{1}{3.43 R_{\text{FSL}} f_{\text{sw}}}. \quad (3.14)$$

For the simplicity of the following derivation, the numerical constant in (3.14) is substituted with  $\zeta = 3.43$ :

$$C_p \approx \frac{1}{\zeta R_{\text{FSL}} f_{\text{sw}}}. \quad (3.15)$$

In order to keep the switching loss approximately the same for both converters,  $f_{\text{sw}}$  should be equal to the resonant frequency of the ReSC converter  $f_{\text{crit}}$ :

$$f_{\text{sw}} = f_{\text{crit}} = \frac{1}{2\pi\sqrt{LC}} \quad (3.16)$$

where  $L$  and  $C$  are the resonant inductance and flying capacitance of the 2-to-1 ReSC converter.

Now we calculate the volume of the 2-to-1 pure SC converter,  $\text{Vol}_{\text{pureSC}}$ , based on its peak stored energy and the energy density of the capacitor,  $\rho_{E,C}$ :

$$\text{Vol}_{\text{pureSC}} = \frac{\frac{1}{2} C_p (V_o + \frac{1}{2} \Delta V_o)^2}{\rho_{E,C}}. \quad (3.17)$$

Its peak-to-peak capacitor voltage ripple  $\Delta V_o$  can be expressed as

$$\Delta V_o = \frac{\Delta q_{\text{in}}}{C_p} = \frac{I_{\text{in}} T}{C_p} = \frac{\frac{P_{\text{out}}}{2V_o} T}{C_p} = \frac{P_{\text{out}}}{2f_{\text{sw}} V_o C_p}. \quad (3.18)$$

By substituting (3.15) and (3.18) into (3.17), we get

$$\text{Vol}_{\text{pureSC}} = \frac{(V_o + \frac{\zeta P_{\text{out}} R_{\text{FSL}}}{4V_o})^2}{2\zeta \rho_{E,C} f_{\text{sw}} R_{\text{FSL}}}. \quad (3.19)$$

Next, dividing (3.19) by (3.10) yields the relative volume ratio:

$$\frac{\text{Vol}_{\text{pureSC}}}{\text{Vol}_{\text{ReSC}}} = \frac{(4 + \frac{\zeta R_{\text{FSL}}}{R_{\text{load}}})^2}{8\zeta \frac{R_{\text{FSL}}}{R_{\text{load}}} (1 + \sqrt{\frac{\rho_{E,C}}{\rho_{E,L}}})} \quad (3.20)$$

where  $R_{\text{load}} = \frac{V_o^2}{P_{\text{out}}}$  is the output load resistance. It can be seen that the relative volume ratio is dependent on not only the energy density ratio of capacitor and inductor  $\sqrt{\frac{\rho_{E,C}}{\rho_{E,L}}}$ , but also

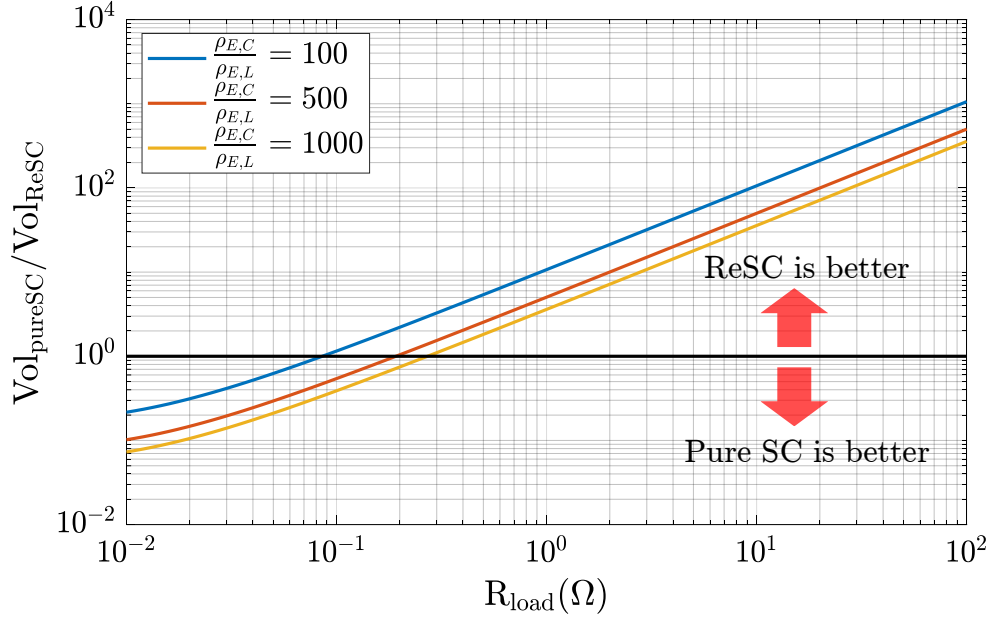


Figure 3.7: Relative passive component volume comparison between 2-to-1 pure SC converter and 2-to-1 ReSC converter (assuming converter series resistance  $R_{\text{FSL}} = 5 \text{ m}\Omega$ ).

the ratio of the converter's series resistance and the load resistance  $\frac{R_{\text{FSL}}}{R_{\text{load}}}$ . Assuming both converters have a total series resistance  $R_{\text{FSL}}$  of  $5 \text{ m}\Omega$ , we plot the relative volume ratio as a function of  $R_{\text{load}}$  as shown in Fig. 3.7. Taking the  $\frac{\rho_{E,C}}{\rho_{E,L}} = 100$  case as an example, with the same efficiency performance, the 2-to-1 ReSC converter can achieve smaller total passive component volume when  $R_{\text{load}}$  is greater than  $85 \text{ m}\Omega$ , otherwise the 2-to-1 pure SC converter is more favorable. If  $\frac{\rho_{E,C}}{\rho_{E,L}} = 1000$ , the boundary  $R_{\text{load}}$  increases to  $270 \text{ m}\Omega$ , making the pure SC approach attractive for a broader load range.

Alternatively, we can express the relative volume ratio with respect to converter efficiency. Based on the ideal transformer model [7], the efficiency of SC converters is given by

$$\eta = \frac{R_{\text{load}}}{R_{\text{out}} + R_{\text{load}}}. \quad (3.21)$$

As shown in (3.12),  $R_{\text{out}} = \frac{\pi^2}{8} R_{\text{FSL}}$  at the desired resonant operating point and therefore

$$\eta = \frac{R_{\text{load}}}{\frac{\pi^2}{8} R_{\text{FSL}} + R_{\text{load}}}. \quad (3.22)$$

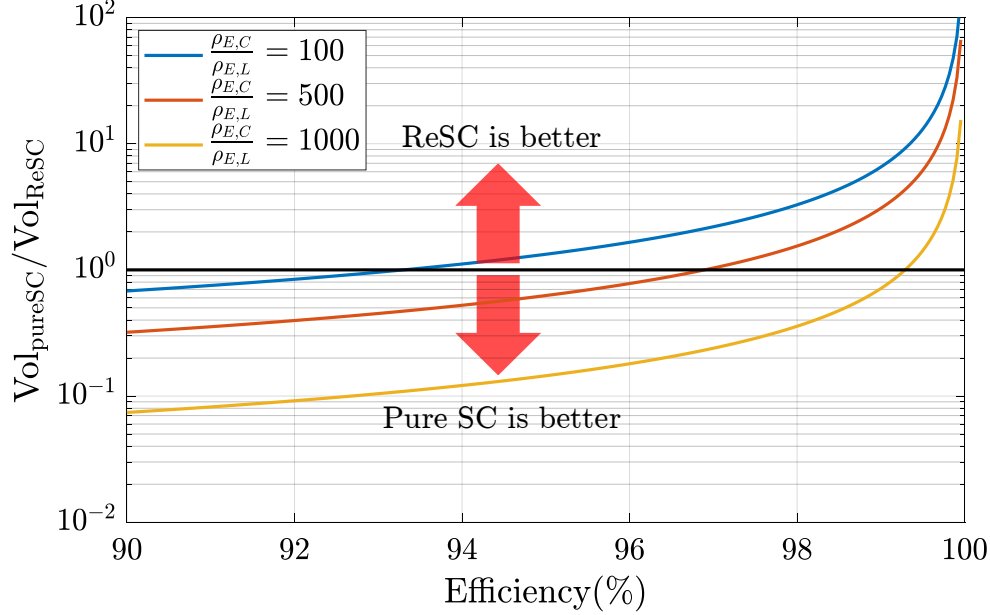


Figure 3.8: Relative passive component volume comparison between 2-to-1 pure SC converter and 2-to-1 ReSC converter with respect to converter efficiency.

Thus,  $\frac{R_{\text{FSL}}}{R_{\text{load}}}$  can be written as  $\frac{R_{\text{FSL}}}{R_{\text{load}}} = \frac{8}{\pi^2} \left( \frac{1}{\eta} - 1 \right)$  and (3.20) is equivalent to

$$\frac{\text{Vol}_{\text{pureSC}}}{\text{Vol}_{\text{ReSC}}} = \frac{\left( 4 + \frac{8\zeta}{\pi^2} \left( \frac{1}{\eta} - 1 \right) \right)^2}{\frac{64\zeta}{\pi^2} \left( \frac{1}{\eta} - 1 \right) \left( 1 + \sqrt{\frac{\rho_{E,C}}{\rho_{E,L}}} \right)}. \quad (3.23)$$

This way, we are able to directly observe the trade-off between efficiency and passive component volume of different approaches as plotted in Fig. 3.8. For a practical value of  $\frac{\rho_{E,C}}{\rho_{E,L}} = 100$ , the 2-to-1 ReSC converter can have smaller volume than the pure SC case when the designed efficiency is greater than 93.3%. However, for very low-voltage high-current applications, such efficiency number might be unreachable due to the limits of  $\frac{R_{\text{FSL}}}{R_{\text{load}}}$  and pure SC converters could be a better choice.

Note that this analysis assumes the ReSC converter and the pure SC converter have the same series resistance, including switch on-resistance and capacitor ESR. In practice, the capacitor ESR will be slightly higher for the ReSC converter as it uses less capacitors in parallel. In addition, the loss of the resonant inductor, which is mainly dominated by the DCR loss, is also not considered here. If a more precise comparison is desired, the inductor DCR should be incorporated into the total series resistance  $R_{\text{FSL}}$  for the ReSC converter. Then, instead of directly equating (3.12) and (3.13) to get (3.14), (3.12) should first be scaled

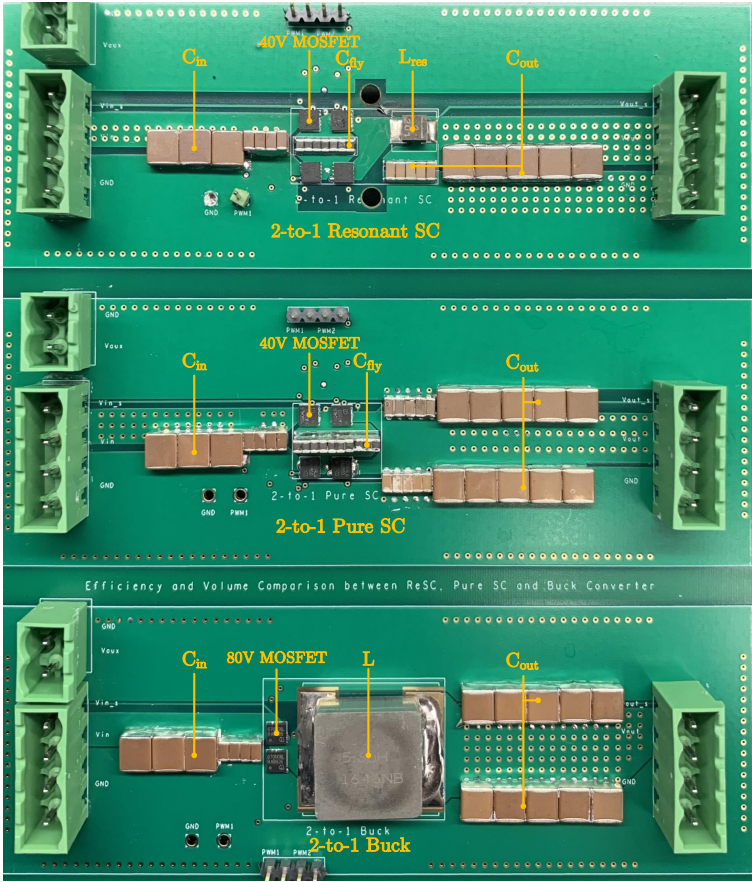


Figure 3.9: Photograph of the hardware prototype for passive component volume and efficiency comparisons.

to take inductor DCR into consideration. This will slightly shift the curves in Fig. 3.7 and 3.8 to the right side, but will not alter the major trend qualitatively.

### Experimental Verification

Three hardware prototypes are designed to verify the above passive volume analysis and comparisons. As can be seen from Fig. 3.9, there are three 2-to-1 converters on the board, including an ReSC converter, a pure SC converter and a buck converter. They share the same operating parameters as shown in Table 3.1. Since the efficiency analysis of SC converters in the last subsection mainly considers conduction loss, a relatively low switching frequency of 100 kHz and a high output current of 15 A are selected here to make sure the converters operate at heavy-load region and are conduction-loss dominated.

The major active and passive components of the converters are highlighted in Fig. 3.9, and

Table 3.1: Key converter operating parameters

Input voltage	48 V
Output voltage	24 V
Output current	15 A
Power rating	360 W
Switching frequency	100 kHz

their parameters are tabulated in Table 3.2. Sufficient filtering capacitance is used to ensure negligible input and output voltage ripples, so that their effects on efficiency performance is minimized. For the ReSC converter, given a desired resonant frequency of 100 kHz, the resonant inductor and capacitor are selected as follows. First, the inductor should be able to use all of its stored energy (i.e., its energy utilization factor is  $\mu_L = 1$ ). This requires that the peak inductor current should be close to its saturation point:  $I_{\text{sat}} \approx I_{\text{pk}} = \frac{\pi}{2} I_{\text{out}}$ . Under this constraint, an inductor with lower profile is desired. However, in order to not degrade the efficiency significantly, the inductor DCR should be comparable to or lower than the equivalent total switch on-resistance. Second, as illustrated in Fig. 3.5, a volume ratio  $\frac{\text{Vol}_C}{\text{Vol}_L}$  close to one is more likely to minimize the total passive component volume. This principle can be used to guide the  $L$  and  $C$  allocation. After evaluating the available commercial components, 200 nH Coilcraft XEL4030 inductor is selected for its good balance of volume and loss, and 35V 0805 X5R TDK ceramic capacitors are selected as the flying capacitors. Besides very high energy density, the selected capacitors also have small package size which allows for fine tuning the total flying capacitance. The selected  $LC$  tank has an energy density ratio of  $\frac{\rho_{E,C}}{\rho_{E,L}} = 233$ , a total volume of 76 mm<sup>3</sup> and a volume ratio of  $\frac{\text{Vol}_C}{\text{Vol}_L} = 0.6$ . Note that this  $\frac{\text{Vol}_C}{\text{Vol}_L}$  slightly deviates from the theoretical optimum due to the limited selection of inductor sizes.

The pure SC converter uses the same switches and flying capacitors as those of the ReSC converter. Given same power rating and switching frequency, its efficiency can be controlled by the amount of flying capacitance. In order to compare the required passive volume with the ReSC converter, an efficiency sweep is performed repeatedly with an increasing amount of flying capacitance, until the pure SC converter can achieve the same efficiency performance as that of the ReSC converter at 15 A output current. The measured efficiency performance is shown in Fig. 3.10. It is found that the pure SC converter needs 272 mm<sup>3</sup> of flying capacitors to match the efficiency of the ReSC converter. This results in a volume ratio  $\frac{\text{Vol}_{\text{pureSC}}}{\text{Vol}_{\text{ReSC}}}$  of 3.6, as compared to a calculated value of 4.4. The deviation is possibly from the additional loss of the resonant inductor, which is not considered in the model.

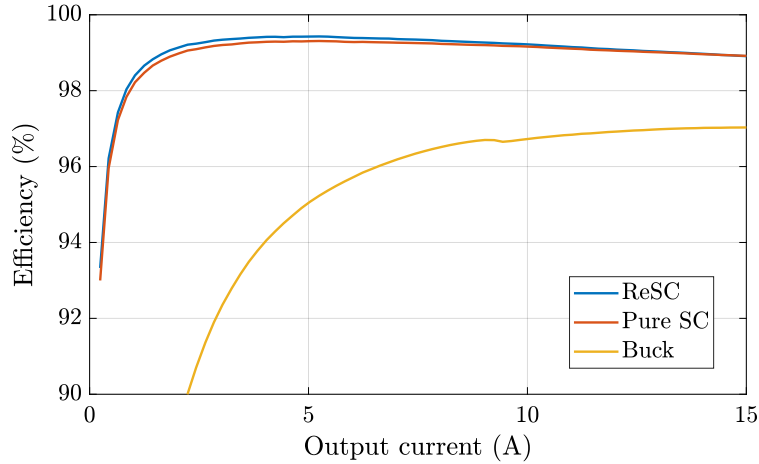
For the buck converter, it is very challenging to achieve 99% efficiency at this operating point. Therefore, the comparison of its passive volume is mainly focused on the minimal energy storage requirement, rather than comparable efficiency performance. By performing inductor volt-second analysis, it can be found that when converting 48 V to 24 V at 100 kHz,



Table 3.2: Main component listing of the hardware prototype

	Component	Part number	Parameters
ReSC	Switch	Infineon BSZ018N04LS6	40 V, 1.6 m $\Omega$
	Flying capacitor	TDK C2012X5R1V226M125AC	X5R, 35 V, 22 $\mu\text{F}^* \times 9$
	Resonant inductor	XEL4030-201ME	200 nH, 22 A $I_{\text{sat}}$
Pure SC	Switch	Infineon BSZ018N04LS6	40 V, 1.6 m $\Omega$
	Flying capacitor	TDK C2012X5R1V226M125AC	X5R, 35 V, 22 $\mu\text{F}^* \times 87$
Buck	Switch	Infineon BSZ070N08LS5	80 V, 5.9 m $\Omega$
	Inductor	Vishay IHLP6767GZER5R6M01	5.6 $\mu\text{H}$ , 40 A $I_{\text{sat}}$

\* The capacitance listed here is the nominal value before dc derating.


 Figure 3.10: Measured 48-to-24 V efficiency ( $f_{\text{sw}} = 100$  kHz).

a minimum 4  $\mu\text{H}$  inductance is needed to maintain boundary conduction mode at 15 A output current. Among off-the-shelf inductors, the Vishay IHLP6767 family is found to be a good candidate which can meet both the inductance and saturation current requirements. The selected inductor has 5.6  $\mu\text{H}$  and 40 A saturation current, and thus a total energy storage greater than the minimum requirement. It has a volume of 2059  $\text{mm}^3$  and an energy density ratio  $\frac{\rho_{E,C}}{\rho_{E,L}}$  of 94, compared to the resonant capacitor in the 2-to-1 ReSC converter. Note that the energy density of this buck inductor is different and higher than that of the resonant inductor in the ReSC converter. Based on (3.10) and (3.11), the theoretical volume ratio is found to be  $\frac{\text{Vol}_{\text{buck}}}{\text{Vol}_{\text{ReSC}}} = 11.5$ . On the other hand, the hardware-based actual volume ratio

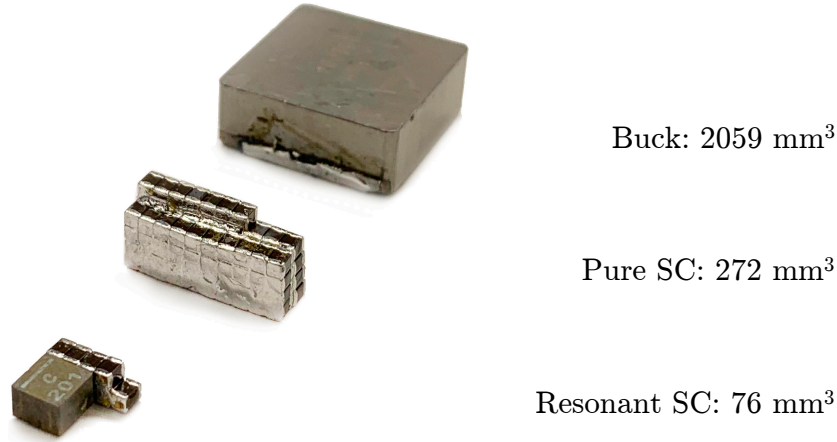


Figure 3.11: Required passive component volume to achieve the efficiency performance shown in Fig. 3.10.

Table 3.3: Comparison between calculation and experiment

	Calculation	Experiment
$\frac{\text{Vol}_{\text{pureSC}}}{\text{Vol}_{\text{ReSC}}}$	4.4	3.6
$\frac{\text{Vol}_{\text{buck}}}{\text{Vol}_{\text{ReSC}}}$	11.5	11*

\* After factoring out the excess energy.

is  $\frac{\text{Vol}_{\text{buck}}}{\text{Vol}_{\text{ReSC}}} = 27$ . This is because the selected inductor is over-sized with an energy storage capability greater than the required amount. After factoring out the excess stored energy of the inductor ( $\frac{4\mu\text{H}\cdot 30\text{A}^2}{5.6\mu\text{H}\cdot 40\text{A}^2}$ ), the true volume ratio  $\frac{\text{Vol}_{\text{buck}}}{\text{Vol}_{\text{ReSC}}}$  becomes 11, which closely matches with the calculated result.

Fig. 3.11 showcases the required passive component volume of different solutions, and Table 3.3 compares the experimental volume ratios with the calculated results. The ReSC converter can deliver its promised benefits and achieve the highest efficiency with significantly less passive component volume than conventional solutions.

### 3.4 Generalized Analysis

So far, we have shown that through reactive power/energy analysis, the total passive component volume of a 2-to-1 ReSC converter can be calculated and optimized based on only  $P_{\text{out}}$ ,

$f_{\text{sw}}$  (resonant frequency),  $\rho_{E,C}$ , and  $\rho_{E,L}$ , by adjusting the capacitor ripple ratio  $\frac{\Delta V_{C0}}{V_{C0}}$ . There is no need to assume or constrain the  $L$  and  $C$  values. Next, we generalize this method to any ReSC topologies with any number of flying capacitors and inductors.

## Equation Formulation

Since all topologies degenerate to the same basic structure at a conversion ratio of 2, we can use the result of the 2-to-1 ReSC converter as a baseline. Assuming the 2-to-1 ReSC converter has inductance  $L$ , flying capacitance  $C$ , switching frequency  $f_{\text{sw}} = \frac{1}{2\pi\sqrt{LC}}$ , output voltage  $V_{\text{out}}$  and output current  $I_{\text{out}}$ , its peak-to-peak capacitor voltage ripple can be derived as  $\Delta V_{C0} = \frac{I_{\text{out}}}{2Cf_{\text{sw}}}$ , and the power processed by the inductor is  $P_{L0} = \frac{I_{\text{out}}\Delta V_{C0}}{16}$ . When expanding to higher conversion ratios, the capacitance ratio among the flying capacitors should be first determined by the soft-charging requirement [19] and other practical considerations (e.g. same resonant frequency for different  $LC$  tanks). For most common topologies (e.g. series-parallel, Dickson, FCML), all added flying capacitors should have the same capacitance  $C$  as compared to the 2-to-1 case. For the Doubler topology [37], the capacitance ratio is  $C_1 = C$ ,  $C_2 = \frac{1}{4}C$ , ... ,  $C_n = \frac{1}{2^{2n-2}}C$ . If an ReSC converter has multiple resonant inductors, it is usually required to have the same resonant frequency for all resonant tanks. Therefore, for the topologies with equal capacitance  $C$ , all inductors should have the same value of  $L$ . For the Doubler topology, the inductance ratio is  $L_1 = L$ ,  $L_2 = 4L$ , ... ,  $L_n = 2^{2n-2}L$ . Additionally, both  $V_{\text{out}}$  and  $I_{\text{out}}$  remain the same as in the 2-to-1 case. Now, we can express the processed reactive power  $P_{C,i}$ , average dc voltage  $V_{C,i}$  and ac ripple voltage  $\Delta V_{C,i}$  of any given flying capacitor  $C_i$  in terms of  $P_{\text{out}}$ ,  $V_{\text{out}}$  and  $\Delta V_{C0}$  (the capacitor ripple voltage in the 2-to-1 case):

$$C_i \Rightarrow \begin{cases} P_{C,i} = k_i P_{\text{out}} \\ V_{C,i} = \alpha_i V_{\text{out}} \\ \Delta V_{C,i} = \beta_i \Delta V_{C0} \end{cases} \quad (3.24)$$

where  $k_i$ ,  $\alpha_i$  and  $\beta_i$  are topology dependent parameters. An example of how these parameters can be derived will be given in the next subsection. Once these parameters have been calculated, the ripple voltage ratio of  $C_i$  can be expressed as

$$\frac{\Delta V_{C,i}}{V_{C,i}} = \frac{\beta_i \Delta V_{C0}}{\alpha_i V_{\text{out}}} \quad (3.25)$$

and the energy utilization factor  $\mu_{C,i}$  can be generalized from (3.5) as

$$\mu_{C,i} = \frac{2 \frac{\Delta V_{C,i}}{V_{C,i}}}{\left(1 + \frac{1}{2} \frac{\Delta V_{C,i}}{V_{C,i}}\right)^2} = \frac{\frac{2\beta_i \Delta V_{C0}}{\alpha_i V_{\text{out}}}}{\left(1 + \frac{\beta_i \Delta V_{C0}}{2\alpha_i V_{\text{out}}}\right)^2}. \quad (3.26)$$

The required energy storage  $E_{C_i, \text{store}}$  of capacitor  $C_i$  at a switching frequency of  $f_{\text{sw}}$  can be derived as

$$\begin{aligned} E_{C_i, \text{store}} &= \frac{P_{C_i}}{f_{\text{sw}} \mu_{C_i}} = \frac{k_i P_{\text{out}}}{f_{\text{sw}} \mu_{C_i}} \\ &= \frac{P_{\text{out}}}{f_{\text{sw}}} \left( \frac{k_i}{2} + \frac{k_i \alpha_i}{2 \beta_i} \frac{V_{\text{out}}}{\Delta V_{C0}} + \frac{k_i \beta_i}{8 \alpha_i} \frac{\Delta V_{C0}}{V_{\text{out}}} \right). \end{aligned} \quad (3.27)$$

Next, the total required energy storage of the sum of the  $n$  flying capacitors is given by

$$\begin{aligned} E_{C, \text{tot}} &= \sum_{i=1}^n E_{C_i, \text{store}} \\ &= \frac{P_{\text{out}}}{f_{\text{sw}}} \left( K_{\text{tot}} + A_{\text{tot}} \frac{V_{\text{out}}}{\Delta V_{C0}} + B_{\text{tot}} \frac{\Delta V_{C0}}{V_{\text{out}}} \right) \end{aligned} \quad (3.28)$$

where  $K_{\text{tot}} = \frac{1}{2} \sum_{i=1}^n k_i$ ,  $A_{\text{tot}} = \frac{1}{2} \sum_{i=1}^n \frac{k_i \alpha_i}{\beta_i}$ , and  $B_{\text{tot}} = \frac{1}{8} \sum_{i=1}^n \frac{k_i \beta_i}{\alpha_i}$ . Similarly, the power processed by an inductor  $L_i$  can be expressed as a ratio with the  $P_{L0}$  in the basic 2-to-1 case:

$$P_{L_i} = \gamma_i P_{L0} \quad (3.29)$$

and the total required energy of the sum of the  $m$  inductors is

$$E_{L, \text{tot}} = \sum_{i=1}^m E_{L_i} = \frac{P_{L0}}{f_{\text{sw}}} \sum_{i=1}^m \gamma_i = \frac{P_{L0}}{f_{\text{sw}}} Y_{\text{tot}} \quad (3.30)$$

with  $Y_{\text{tot}} = \sum_{i=1}^m \gamma_i$ . Note that this analysis is general in nature, and can be applied to any ReSC converters with different inductor locations, including ‘‘inductor at output’’ and ‘‘inductor in series with flying capacitor’’ configurations [38].

Following the same procedure as that in (3.8), we can express the total passive volume as a function of  $\frac{\Delta V_{C0}}{V_{\text{out}}}$ :

$$\begin{aligned} \text{Vol}_{\text{tot}} &= \text{Vol}_C + \text{Vol}_L \\ &= \frac{P_{\text{out}}}{f_{\text{sw}}} \left( \frac{K_{\text{tot}} + A_{\text{tot}} \frac{V_{\text{out}}}{\Delta V_{C0}} + B_{\text{tot}} \frac{\Delta V_{C0}}{V_{\text{out}}}}{\rho_{E,C}} + \frac{\frac{1}{16} Y_{\text{tot}} \frac{\Delta V_{C0}}{V_{\text{out}}}}{\rho_{E,L}} \right). \end{aligned} \quad (3.31)$$

By differentiating  $\text{Vol}_{\text{tot}}$  with respect to  $\frac{\Delta V_{C0}}{V_{\text{out}}}$ , the optimized capacitor ripple ratio  $r^*$  and the minimized total passive volume  $\text{Vol}_{\text{tot}, \text{min}}$  can be derived:

$$r^* = \left( \frac{\Delta V_{C0}}{V_{\text{out}}} \right)^* = \sqrt{\frac{16 A_{\text{tot}} \rho_{E,L}}{16 B_{\text{tot}} \rho_{E,L} + Y_{\text{tot}} \rho_{E,C}}} \quad (3.32)$$

$$\text{Vol}_{\text{tot}, \text{min}} = \frac{P_{\text{out}}}{f_{\text{sw}} \rho_{E,L}} \left( \frac{\rho_{E,L}}{\rho_{E,C}} \left( K_{\text{tot}} + A_{\text{tot}} \frac{1}{r^*} + B_{\text{tot}} r^* \right) + \frac{Y_{\text{tot}} r^*}{16} \right). \quad (3.33)$$

When  $\rho_{E,C} \gg \rho_{E,L}$  and  $Y_{\text{tot}}\rho_{E,C} \gg 16B_{\text{tot}}\rho_{E,L}$ ,  $r^*$  can be further simplified to:

$$r^* = \sqrt{\frac{16A_{\text{tot}}\rho_{E,L}}{16B_{\text{tot}}\rho_{E,L} + Y_{\text{tot}}\rho_{E,C}}} \approx \sqrt{\frac{16A_{\text{tot}}\rho_{E,L}}{Y_{\text{tot}}\rho_{E,C}}} \quad (3.34)$$

yielding an approximated minimized total volume of

$$\text{Vol}_{\text{tot,min}} \approx \frac{P_{\text{out}}}{f_{\text{sw}}\rho_{E,L}} \left( K_{\text{tot}} \frac{\rho_{E,L}}{\rho_{E,C}} + \frac{1}{2} \sqrt{\frac{A_{\text{tot}}Y_{\text{tot}}\rho_{E,L}}{\rho_{E,C}}} \right). \quad (3.35)$$

In this expression, no detailed  $L$  and  $C$  values need to be assumed or constrained. The  $P_{\text{out}}$ ,  $f_{\text{sw}}$ ,  $\rho_{E,L}$  and  $\rho_{E,C}$  terms depend on the operating condition and the remaining terms are purely topology specific parameters. This equation can be used to quantitatively calculate the minimum achievable passive volume of any hybrid resonant SC converter at a given power level and switching frequency. Note that this analysis assumes that all flying capacitors have an energy density of  $\rho_{E,C}$  and all resonant inductors have an energy density of  $\rho_{E,L}$ . For the topologies that use multiple types of capacitors and inductors with different power densities [23], (3.31) can be modified to incorporate multiple  $\rho_{E,C_i}$  and  $\rho_{E,L_i}$ .

### Example of N-to-1 Resonant Series-Parallel Converter

Here, we use an N-to-1 resonant series-parallel converter as an example to demonstrate how the topology dependent parameters  $k_i$ ,  $\alpha_i$ ,  $\beta_i$  and  $\gamma_i$  in (3.24) and (3.29) can be derived.

Resonant series-parallel converters can be implemented with two types of augmenting inductors: distributed inductors and a single inductor at output. The circuit schematics and the associated current waveforms of these two types of implementations are shown in Fig. 3.12. In an N-to-1 series-parallel converter, there are  $N - 1$  flying capacitors with equal capacitance. All are connected in series in the series-phase  $\phi_s$  and paralleled in the parallel-phase  $\phi_p$ . Through KVL analysis, it can be found that all capacitors have an average dc voltage of  $V_{\text{out}}$ . According to (3.24),  $V_{C,i} = \alpha_i V_{\text{out}}$ , thus

$$\alpha_1 = \alpha_2 = \dots = \alpha_{N-1} = 1. \quad (3.36)$$

As derived in [32], the power processed by a capacitor  $C_i$  can be calculated as

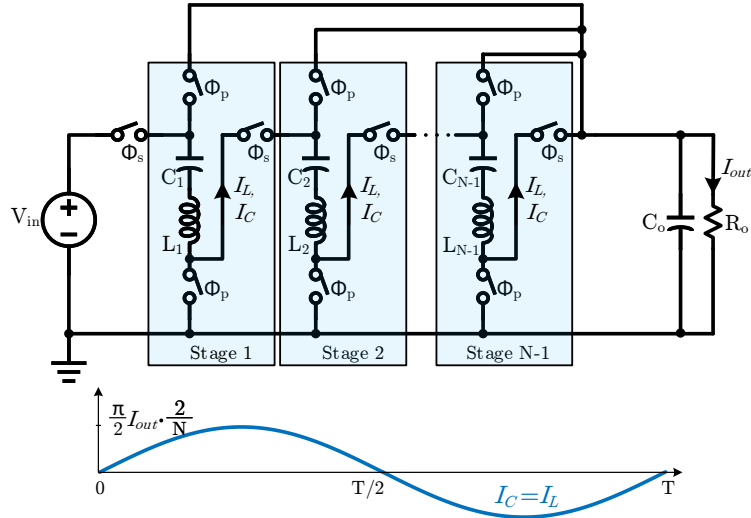
$$P_{C,i} = \frac{1}{2} \overline{|V_{C,i} I_{C,i}|} \quad (3.37)$$

where

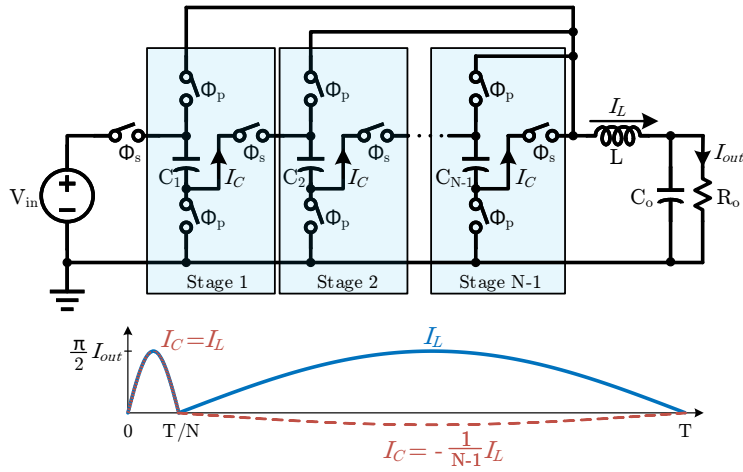
$$\overline{|V_{C,i} I_{C,i}|} \triangleq \frac{1}{T} \int_0^T |V_{C,i} I_{C,i}| dt. \quad (3.38)$$

For ReSC converters, (3.37) can be simplified to

$$P_{C,i} = \frac{1}{2} V_{C,i} I_{C,i} \quad (3.39)$$



(a) Distributed inductors



(b) Single inductor at output

Figure 3.12: N-to-1 resonant series-parallel converters with different inductor locations.

where  $V_{C,i}$  is the average dc voltage and  $I_{C,i}$  is the average charging (or discharging) current through  $C_i$ .

Through charge flow analysis [7], it can be found that  $I_{C,i} = \frac{2}{N} I_{out}$  in a N-to-1 series-parallel converter. Thus,  $P_{C,i} = k_i V_{out} I_{out} = \frac{V_{out} I_{out}}{N}$  and

$$k_1 = k_2 = \dots = k_{N-1} = \frac{1}{N}. \quad (3.40)$$

The voltage on capacitor  $C_i$  is  $V_{C,i} = \frac{I_{pk_{c,i}}}{C_i \omega_{r_{c,i}}} \cos(\omega_{r_{c,i}} t)$ . Thus, its peak-to-peak voltage ripple is

$$\Delta V_{C,i} = \frac{2I_{pk_{c,i}}}{C_i \omega_{r_{c,i}}} \quad (3.41)$$

where  $I_{pk_{c,i}}$  is the peak current flowing through  $C_i$  and  $\omega_{r_{c,i}}$  is the resonant frequency of the  $LC$  tank associated with  $C_i$ . For the distributed inductor configuration in Fig. 3.12a,  $C_i$  and  $\omega_{r_{c,i}}$  are the same as those in the basic 2-to-1 case, whereas its peak current  $I_{pk_{c,i}}$  is  $\frac{2}{N}$  times of the baseline value  $I_{pk}$ , yielding  $\Delta V_{C,i} = \frac{2}{N} \Delta V_{C0}$  and

$$\beta_{1,dis} = \beta_{2,dis} = \dots = \beta_{N-1,dis} = \frac{2}{N}. \quad (3.42)$$

For the single inductor at output configuration in Fig. 3.12b, the duty ratio of  $\phi_s$  changes to  $\frac{T}{N}$  to maintain capacitor charge balance. In  $\phi_s$ , all capacitors are connected in series ( $C_{eq} = \frac{1}{N-1}C$ ) and conduct the entire output current ( $I_{pk} = \frac{\pi}{2}I_{out}$ ). The voltage ripple of each capacitor is

$$\Delta V_{C,i} = \frac{1}{N-1} \cdot \frac{2I_{pk}}{C_{eq} \frac{1}{\sqrt{LC_{eq}}}} = \frac{1}{\sqrt{N-1}} \Delta V_{C0} \quad (3.43)$$

leading to a set of different  $\beta$  values compared to the distributed inductor case:

$$\beta_{1,single} = \beta_{2,single} = \dots = \beta_{N-1,single} = \frac{1}{\sqrt{N-1}}. \quad (3.44)$$

The power processed by inductor  $L_i$  can be calculated with the integral method in (3.2). Alternatively, if all inductors are assumed to have the same value  $L$ ,  $P_{L,i}$  can be related to  $P_{L0}$  by comparing the amplitude of its peak current  $I_{pk_{L,i}}$  and the effective switching period  $T_{eff}$ . For the distributed inductor case, the inductor current is related to the baseline current by  $I_{pk_{L,i}} = \frac{2}{N}I_{pk}$ , resulting in  $E_{L,i} = \frac{4}{N^2}E_{L0}$ . Since  $T_{eff} = T = 2\pi\sqrt{LC}$  is the same as the 2-to-1 case,  $P_{L,i} = \frac{E_{L,i}}{T_{eff}} = \frac{4}{N^2}P_{L0}$  and

$$\gamma_{1,dis} = \gamma_{2,dis} = \dots = \gamma_{N-1,dis} = \frac{4}{N^2}. \quad (3.45)$$

For the single inductor at output case, the inductor conducts the entire output current  $I_{pk_{L,i}} = I_{pk}$  and therefore  $E_{L,i} = E_{L0}$ . The effective switching period can be calculated as the average of the series resonant period and the parallel resonant period:

$$T_{eff} = \frac{T_{series} + T_{parallel}}{2} = \frac{2\pi(\sqrt{L\frac{C}{N-1}} + \sqrt{L(N-1)C})}{2} \quad (3.46)$$

resulting in  $P_{L,i} = \frac{2\sqrt{N-1}}{N}P_{L0}$  and

$$\gamma_{single} = \frac{2\sqrt{N-1}}{N}. \quad (3.47)$$

Table 3.4: Key parameters of N-to-1 series-parallel converter

	$k_i$	$\alpha_i$	$\beta_i$	$\gamma_i$
Distributed inductors	$\frac{1}{N}$	1	$\frac{2}{N}$	$\frac{4}{N^2}$
Single inductor	$\frac{1}{N}$	1	$\frac{1}{\sqrt{N-1}}$	$\frac{2\sqrt{N-1}}{N}$

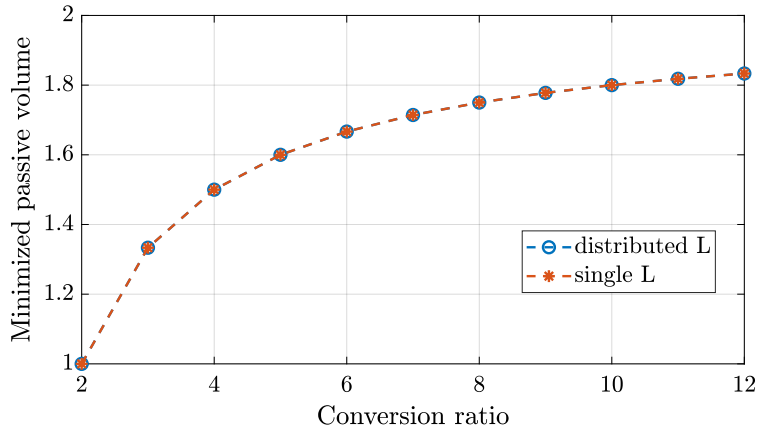


Figure 3.13: Minimized total passive volume of N-to-1 resonant series-parallel converters with different inductor locations (normalized to the 2-to-1 case).

The calculated topology dependent parameters are summarized in Table 3.4. It can be seen that the capacitor ripple term  $\beta_i$  and the inductor power term  $\gamma_i$  are different for the two types of inductor locations. Nevertheless, as shown in Fig. 3.13, they can achieve the same total minimized passive volume, as calculated from (3.33). This example demonstrates that the proposed method is applicable to generalized ReSC topologies with different inductor placement strategies.

### 3.5 Resonant SC Topology Comparison

Besides optimizing the total passive component volume, the proposed method can also be used to compare the relative volume of different ReSC topologies. It can be observed from (3.35) that the expression of the minimized total passive volume consists of two parts. The first part  $\frac{P_{out}}{f_{sw}\rho_{E,L}}$  depends on the operating conditions, and can be viewed as the volume of an inductor that stores all of the energy delivered to the load in each switching cycle. The remaining part contains topology dependent parameters and the energy density ratio of



capacitor and inductor. It represents the relative volume ratio to an inductor whose volume is  $\frac{P_{\text{out}}}{f_{\text{sw}}\rho_{E,L}}$  and can be considered as a “passive component utilization factor” of the topology. By normalizing with respect to the  $\frac{P_{\text{out}}}{f_{\text{sw}}\rho_{E,L}}$  portion of (3.35), a normalized passive component volume  $M_p$  is defined as

$$\begin{aligned}
 M_p &= \frac{\text{Vol}_{\text{tot,min}}}{\frac{P_{\text{out}}}{f_{\text{sw}}\rho_{E,L}}} \\
 &= \frac{\rho_{E,L}}{\rho_{E,C}} \left( K_{\text{tot}} + A_{\text{tot}} \frac{1}{r^*} + B_{\text{tot}} r^* \right) + Y_{\text{tot}} r^*.
 \end{aligned} \tag{3.48}$$

Note that this  $M_p$  is independent of  $f_{\text{sw}}$  and  $P_{\text{out}}$ , indicating that it can provide a direct volume comparison among different topologies at the same output power and switching frequency.

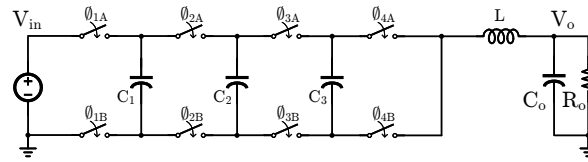
Here, we compare the normalized passive component volume  $M_p$  of various ReSC topologies that are adapted from common SC converters [23], [38]–[41]. The circuit schematic of the series-parallel topology is shown in Fig. 3.12 and the schematics of the other topologies under investigation are shown in Fig. 3.14. Their  $M_p$  values are calculated and plotted in Fig. 3.15, and a buck converter is included for reference. Even though empirical data shows that the ratio of  $\frac{\rho_{E,C}}{\rho_{E,L}}$  can be as high as 1000 [42], a relatively conservative ratio of  $\frac{\rho_{E,C}}{\rho_{E,L}} = 100$  is used here. The buck converter is assumed to operate at the boundary conduction mode such that its inductor energy utilization is maximized.

It can be seen from Fig. 3.15 that, thanks to the high energy density of capacitors, all ReSC converters outperform the buck converter by a wide margin, especially at relatively low conversion ratios. In particular, the series-parallel topology achieves the lowest passive component volume among all topologies. This result agrees with the finding in [35], [42], where the series-parallel converter is at the theoretical Wolaver limit [32] of passive components. Additionally, although requiring high voltage capacitors, the FCML topology achieves relatively good passive component utilization, owing to the frequency multiplication effect that reduces the energy storage requirement of the components.

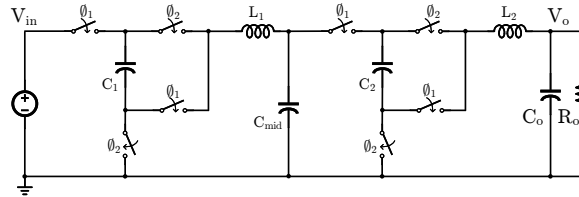
For the same switching frequency, a lower total switch stress indicates a potentially lower conduction loss, lower switching loss, and smaller switch size. Therefore, it can be used as a good indication of potential efficiency [30]. The switch stress is defined as

$$\text{Total switch stress} = \sum_{\text{switches}} V_{ds} I_{ds} \tag{3.49}$$

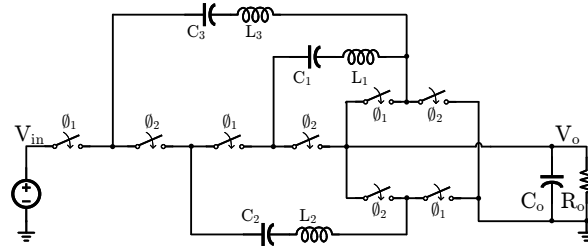
where  $V_{ds}$  is the peak blocking voltage seen by the switch and  $I_{ds}$  is the average current through the switch. As discussed in [24], the rms current value should be used for the best accuracy when the duty ratio is deviated from 50%. However, as most ReSC topologies of interest operate at 50% duty ratio and the rms/average ratio is fixed, the average current value is used here as a close approximation. Since one can express  $V_{ds}$  using the output voltage ( $\beta_v V_{\text{out}}$ ), and  $I_{ds}$  using the output current ( $\beta_i I_{\text{out}}$ ), the normalized switch stress  $M_s$



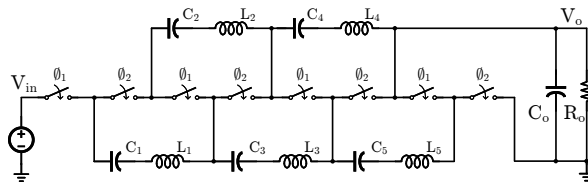
(a) FCML



(b) Doubler



(c) Dickson



(d) Ladder

Figure 3.14: 4-to-1 resonant switched-capacitor converter topologies.

can be defined as

$$M_s = \frac{\text{total switch stress}}{V_{\text{out}} I_{\text{out}}} = \sum_{\text{switches}} \beta_v \beta_i. \quad (3.50)$$

This can be viewed as the total switch power rating necessary to deliver a certain power to the output. More details regarding this metric can be found in [13]. Fig. 3.16 shows the calculated  $M_s$  of the topologies of interest, with the Dickson [21], [43] and Ladder topologies at the Wolaver limit [35]. It should be emphasized that the derived  $M_p$  and  $M_s$  reflect the intrinsic performance of passive and active component utilization and are independent of detailed operating conditions (e.g.,  $P_{\text{out}}$ ,  $f_{\text{sw}}$ ).

Fig. 3.17 compares the relative performance of various topologies at a ratio of 4-to-1. In general, the topologies that have high normalized switch stress tend to have lower

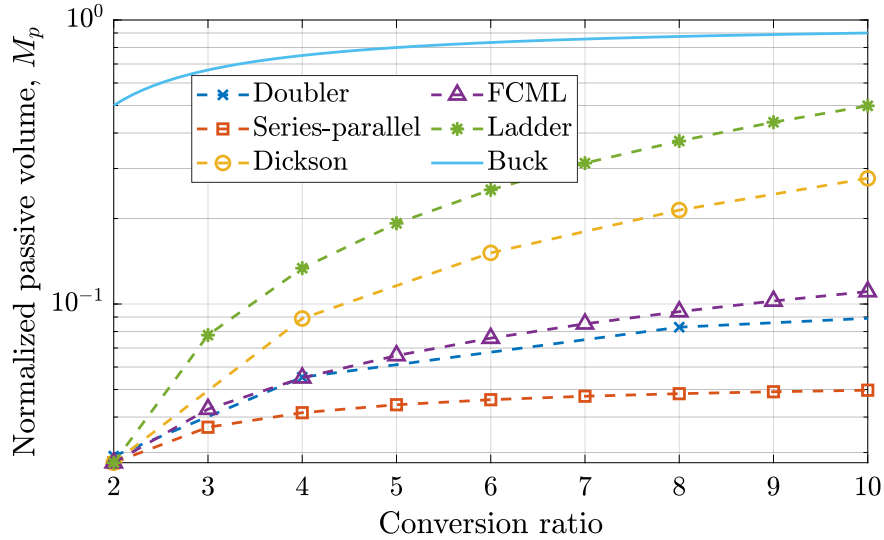


Figure 3.15: Normalized passive volume (assuming  $\rho_{E,C}/\rho_{E,L} = 100$ ). Lower is better.

normalized passive volume, and vice versa. With the series-parallel and Dickson topologies at the theoretical boundaries of passive and active component Wolaver limits, respectively, all other classical and emerging topologies will fit inside those bounds. Note that the switched-tank (STC) converter [23] has the same theoretical performance as the Dickson as they share the same fundamental structure. This plot allows designers to quickly visualize and compare the trade-offs of different solutions.

It should be noted that practical converter designs have more considerations and the actual performance of different topologies can be different than what is plotted here. For instance, the lowest voltage rating of widely available discrete power MOSFETs is at present about 25 V. Thus, for discrete applications with input voltage lower than 25 V, the topologies with low switch voltage rating and switch VA stress (e.g., Dickson) cannot fully utilize their potential. In this case, the topology efficiency comparison should be based on switch conductance  $G$  rather than  $GV^2$  (VA rating) [24]. Then, it is found that the series-parallel topology can achieve one of the lowest output impedances among all ReSC topologies, even though its normalized switch stress is the highest in Fig. 3.17. In addition, the implementation complexity should also be considered, such as the number of components, the design of gate drive circuit and the ease of PCB layout. This may put the doubler topology in an attractive position because of its simple and highly modular design. Note that the inter-stage decoupling capacitors in the doubler topology are not included in the passive volume calculation, as they can be eliminated by two-phase interleaving operation, which is detailed in Chapter 6.

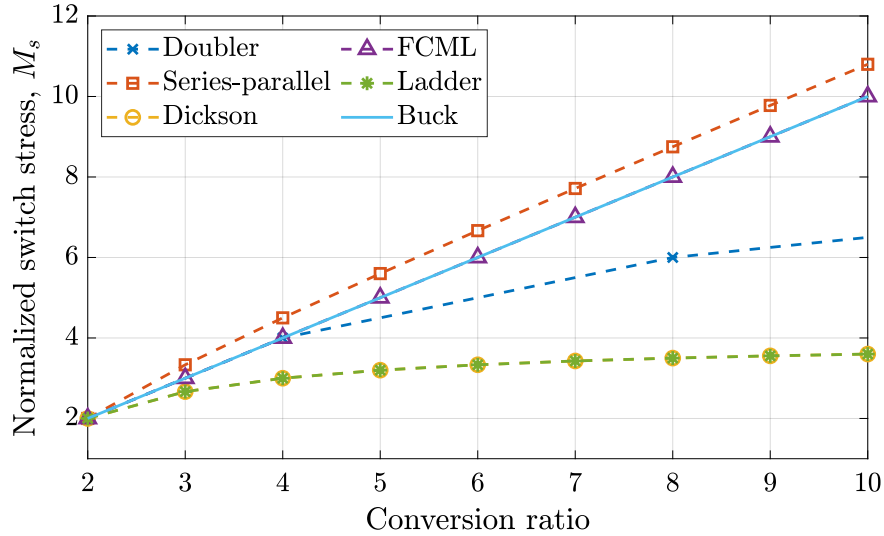


Figure 3.16: Normalized switch stress. Lower is better.

### 3.6 Comparison of Regulated Hybrid Converters

So far, all analysis has focused on fixed-ratio ReSC converters, in which the inductors see only the flying capacitor voltage ripples. Next, we briefly discuss how the reactive power calculation can be applied to analyze and compare hybrid SC converters with regulation capability. In such converters, the switched-capacitor stage is typically combined with a buck stage. The buck stage can achieve voltage regulation through pulse-width modulation (PWM), while serving as a current source for capacitor soft-charging operation. In this section, we analyze two basic hybrid converter topologies, the three-level buck converter and the series-capacitor buck converter. Their circuit schematics are shown in Fig. 3.18. In spite of having the same number of switches and flying capacitor, they have very different operating characteristics and advantages owing to different inductor placement strategy.

#### Calculating the Reactive Power of Three-Level Buck Converter

Here, we detail the reactive power calculation of a three-level buck converter. The same method can be applied to any other regulated hybrid SC topologies. Since the three-level buck converters have different circuit operating states for duty ratio  $D < 0.5$  and  $D > 0.5$ , the calculations are carried out for these two intervals separately.

(1)  $D < 0.5$

The four circuit operating states and the corresponding durations are shown in Fig. 3.19. Assuming the flying capacitor  $C_1$  is at its nominal voltage  $\frac{1}{2}V_{in}$  with no voltage ripple, then the switch node voltage  $V_{sw}$  will be at  $\frac{1}{2}V_{in}$  during state 1 and 3, and at ground during state

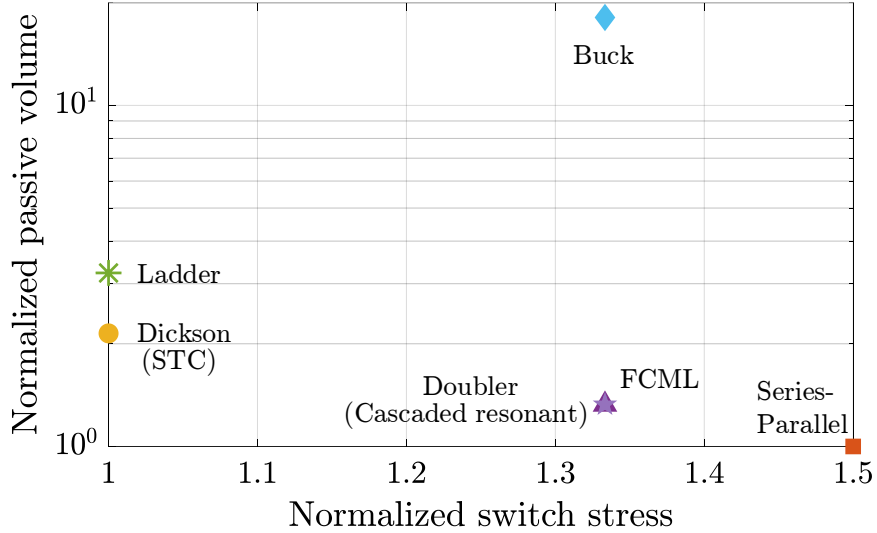
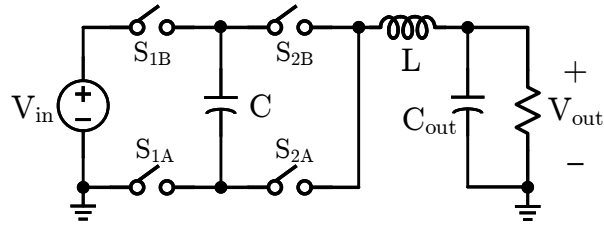


Figure 3.17: 4-to-1 ReSC topology comparison.

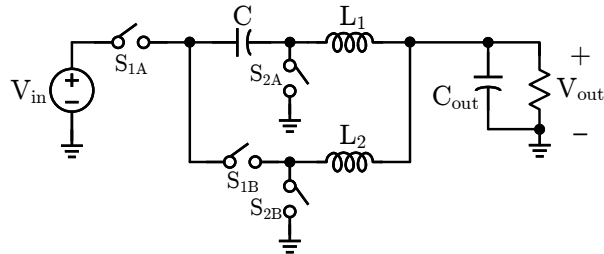
2 and 4. Since  $C_1$  is only charged in one state (state 1) and discharged in another (state 3), its processed power simply equals the charging power at state 1 (or the discharging power at state 3). Assuming the inductor current is constant, we find:

$$\begin{aligned}
 P_C &= P_{C, \text{state1}} \\
 &= \frac{\frac{1}{2} V_{in} I_{out} DT}{T} \\
 &= \frac{1}{2} \frac{V_{out}}{D} I_{out} D \\
 &= \frac{1}{2} P_{out}.
 \end{aligned} \tag{3.51}$$

It can be seen that the power processed by the flying capacitor is a constant value for  $D < 0.5$ . The power processed by the inductor can be calculated in a similar way. However, since it transfers energy twice per switching cycle, only one charging state should be considered for



(a) three-level buck converter



(b) Series-capacitor buck converter

Figure 3.18: Schematic drawings of two example regulated hybrid converters.

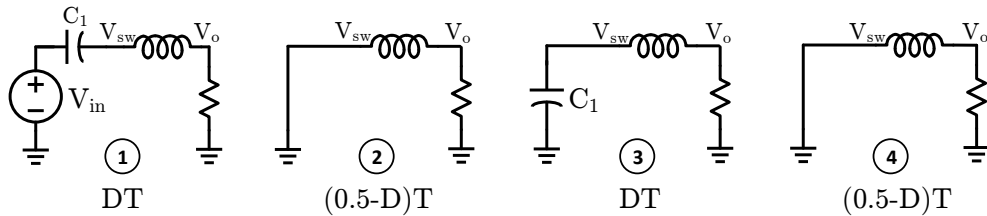


Figure 3.19: Circuit operating states of a three-level buck converter at  $D < 0.5$ .

power calculation:

$$\begin{aligned}
 P_L &= P_{L, \text{state1}} \\
 &= \left(\frac{1}{2}V_{\text{in}} - V_{\text{out}}\right)I_{\text{out}}D \\
 &= \left(\frac{1}{2} - D\right)\frac{V_{\text{out}}}{D}I_{\text{out}}D \\
 &= \left(\frac{1}{2} - D\right)P_{\text{out}}
 \end{aligned} \tag{3.52}$$

(2)  $D > 0.5$

The circuit operating states for  $D > 0.5$  is shown in Fig. 3.20, and the capacitor and inductor power can be calculated as follows:

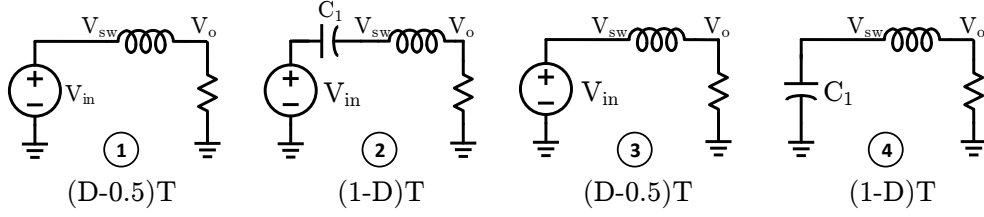


Figure 3.20: Circuit operating states of a three-level buck converter at  $D > 0.5$ .

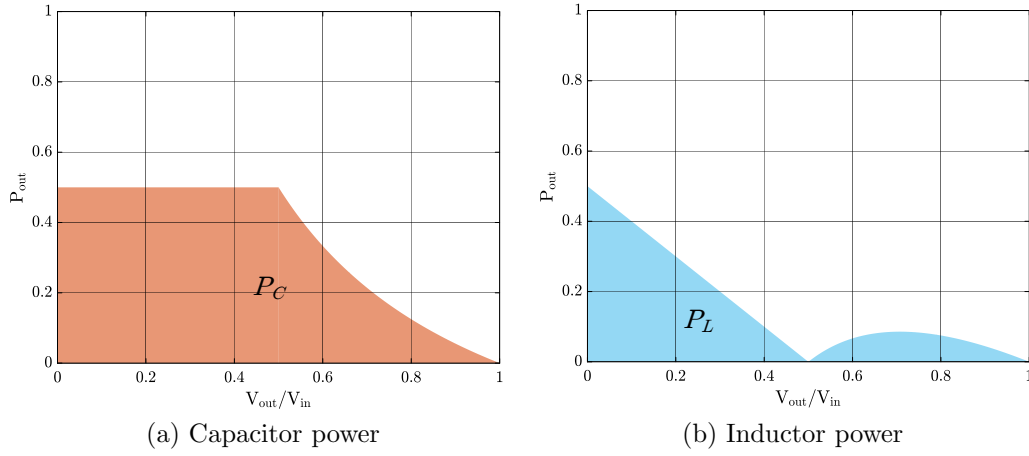
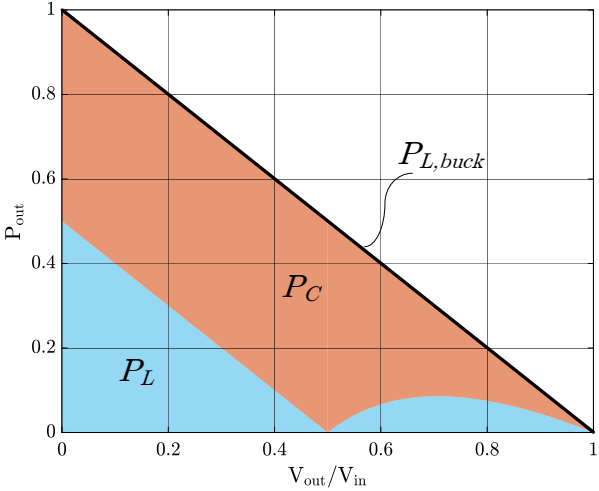


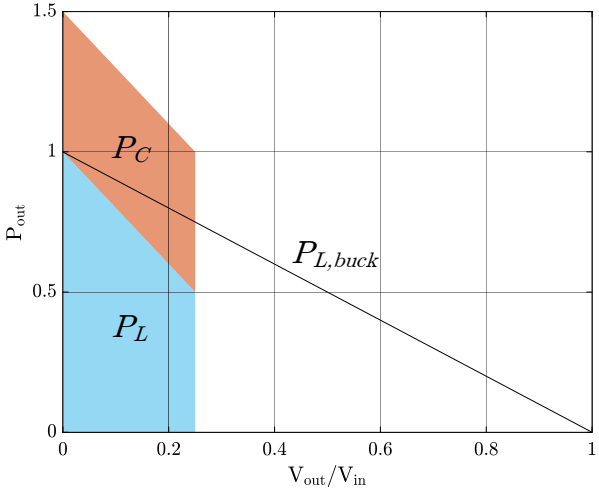
Figure 3.21: Reactive power processed by the passive components of a three-level buck converter.

$$\begin{aligned}
 P_C &= P_{C,\text{state2}} \\
 &= \frac{1}{2} V_{\text{in}} I_{\text{out}} (1 - D) \\
 &= \frac{1 - D}{2D} P_{\text{out}}
 \end{aligned} \tag{3.53}$$

$$\begin{aligned}
 P_L &= P_{L,\text{state1}} \\
 &= (V_{\text{in}} - V_{\text{out}}) I_{\text{out}} (D - 0.5) \\
 &= (1 - D) \frac{V_{\text{out}}}{D} I_{\text{out}} (D - 0.5) \\
 &= \left(-D + \frac{3}{2} - \frac{1}{2D}\right) P_{\text{out}}
 \end{aligned} \tag{3.54}$$



(a) Three-level buck converter



(b) Series-capacitor buck converter

Figure 3.22: Average power processed by the passive components in hybrid converters.

The above calculated  $P_C$  and  $P_L$  are plotted in Fig. 3.21, and the combined total reactive power is plotted in Fig. 3.22a.

### Comparison of Three-Level Buck and Series-Capacitor Buck

Fig. 3.22 plots the reactive power processed by the passive components of the three-level buck converter and the series-capacitor buck converter, as a function of conversion ratio  $\frac{V_{out}}{V_{in}}$ . This reactive power analysis can directly reflect the passive component utilization



of a hybrid converter. In [32], Wolaver derived that the reactive power  $P_{\text{ind}}$  that needs to be processed by a converter with a gain of  $G$  ( $G = \frac{V_{\text{in}}}{V_{\text{out}}}$  for a step-down converter) is governed by  $P_{\text{ind}} \geq \frac{G-1}{G}P_{\text{out}}$ . It can be seen from Fig. 3.22a that the total reactive power of the three-level buck converter is equal to that of a conventional buck converter, which is known to be at the Wolaver limit. Thanks to the reduced voltage stress and the frequency doubling effect, the inductor experiences less volt-second and processes significantly less power than a conventional buck converter. Even though the total processed power remains the same, a great portion is now processed by the high energy-density flying capacitor, resulting in reduced total passive component volume and less power loss on the inductor. When  $\frac{V_{\text{out}}}{V_{\text{in}}} = 0.5$ , there is no voltage across the inductor except for the flying capacitor voltage ripple. Thus, the 2-to-1 ReSC converter can be considered as a special operating mode of three-level buck converter with minimum required inductance, at the cost of no regulation capability.

The series-capacitor buck converter can be viewed as a 2-to-1 SC converter cascaded by a two-phase interleaved buck converter, whose maximum duty ratio is 0.5. This leads to a maximum conversion ratio of  $\frac{V_{\text{out}}}{V_{\text{in}}} = 0.25$ . Its detailed operating principle can be found in [44]. The reactive power processed by the series-capacitor buck converter is shown in Fig. 3.22b. Because of the nature of cascaded converters, its total processed reactive power is unavoidably higher than the Wolaver limit. However, the series-capacitor buck still has the potential to achieve less total passive component volume and higher power density than the conventional buck converter. It can be shown that the power processed by the flying capacitor is a fixed value of  $P_C = \frac{1}{2}P_{\text{out}}$ , whereas the inductor power is equal to that of a buck converter with half of the input voltage  $P_L = \frac{G-2}{G}P_{\text{out}}$ . When  $\frac{V_{\text{out}}}{V_{\text{in}}} = 0.25$ , the power processed by the inductor is 33% lower than that of a buck converter rated for the full input voltage. Even for a high conversion ratio of  $\frac{V_{\text{out}}}{V_{\text{in}}} = 0.1$ , an 11% inductor power reduction is achieved. Given the same switching frequency and inductance value, this can be translated to an 11% inductor current ripple reduction. This property is noteworthy since even meager reductions in inductor current ripple may result in significant savings in core loss. Additionally, the series-capacitor buck converter has attractive features such as reduced switching loss owing to lower voltage stress on switches, and automatic current balancing for interleaving operation.

To calculate and compare the total passive component volume of different topologies at a given conversion ratio, a current ripple ratio of the inductor and a voltage ripple ratio of the flying capacitor need to be assumed first. Then, the corresponding energy utilization factors are known and the passive component volume can be derived with the method presented in Section 3.2. Considered the very high energy density ratio between capacitor and inductor (e.g.,  $\frac{\rho_{E,C}}{\rho_{E,L}} > 100$ ), it is desirable to use the SC network to achieve a higher voltage conversion ratio, so that the voltage and power stress of the following buck stage can be reduced. This strategy has the potential to further reduce both the total passive component volume and the power loss on the inductor, given that the implementation complexity of the SC stage can be properly managed. A new hybrid SC topology with an 8-to-1 SC stage is proposed

in Chapter 8.

### 3.7 Chapter Summary

This chapter models the passive component volume of hybrid resonant switched-capacitor converters from the perspective of the reactive power processed by the passive components. It is shown that the total passive component volume can be expressed as a function of flying capacitor voltage ripple, and the optimum inductor and capacitor allocation that minimizes the total volume is dependent on their relative energy density and topology specific parameters. Detailed analysis and experimental results are also provided to showcase that a 2-to-1 ReSC converter can use significantly less passive volume than conventional SC and buck converters for the same power conversion, while maintaining the best efficiency performance. To compare the passive component utilization of different ReSC topologies, a normalized passive volume parameter is proposed for direct and fair comparison. Along with the normalized switch stress parameter (based on switch VA ratings), a framework to compare the relative performances of different ReSC topologies is created. Using the proposed method, the series-parallel topology exists at the theoretical lower limit of passive volume, whereas the Dickson and the Ladder topologies exist at the lower limit of switch stress. These boundaries can ultimately help evaluate the performance of other newly proposed topologies. Lastly, the proposed passive component modeling method is extended to hybrid converters with regulation capabilities.

## Chapter 4

# Capacitor Voltage Balancing of Flying Capacitor Multilevel Converters

Capacitor voltage natural balancing is an attractive feature of flying capacitor multilevel (FCML) converters. However, with the commonly used phase-shifted pulse-width modulation (PSPWM), the capacitor voltages still can deviate from nominal, and active balancing is often required. Although the natural balancing mechanism and its dynamics have been extensively studied in existing literature, the sources that are responsible for capacitor imbalance in engineering practice are still unclear. This chapter experimentally investigates the origins of the voltage imbalance in practical implementations of FCML converters and presents the corresponding circuit analysis as well as solutions that improve balancing. It is shown that the source impedance and the input capacitor can greatly deteriorate capacitor balancing. Moreover, we also demonstrate in theory and with experiments that an FCML converter with an even number of levels inherently has stronger immunity to such disturbance than one with an odd number of levels. It is also found that the gate signal propagation delay mismatch in half-bridge gate drivers can lead to capacitor imbalance, and this problem is addressed by an alternative gate drive power supply design. Last, the variations of on-resistance among different switches are found to have a relatively small impact on capacitor voltage balancing.

### 4.1 Background and Motivation

Recently, the FCML converter [45] has received increased attention owing to its potential for high-density high-efficiency power conversion. While originally developed for high-voltage high-power applications, recent advances in semiconductor devices (e.g., GaN and SiC) and multilayer ceramic capacitors (MLCCs) have also made the FCML topology attractive for applications with lower voltage and power ratings. Its promising performance has been demonstrated by recent works for a variety of applications, including dc/dc converters with high-conversion-ratio [33], [46], [47], single-phase ac/dc power-factor-correction (PFC) front-

end and energy buffer [48], [49], and dc/ac inverters for renewable integration and transportation electrification [50], [51].

A major implementation challenge of FCML converter is flying capacitor voltage balancing, which describes the scenario where the capacitor voltages deviate from their nominal values due to various disturbances, resulting in an increase of the drain-to-source voltage stress across the switches. To prevent switch failures from capacitor imbalance, typically over-rated switches have to be used for an extra safety margin with accompanying performance penalties.

To regulate the capacitor voltages within a desired set of bounds, active balancing techniques [47], [52]–[57] can be applied to selectively charge or discharge one or more flying capacitors by adjusting the duty ratio of the corresponding switches. Such techniques require the monitoring of capacitor states, which can be achieved by direct flying capacitor voltage sensing [53], switch node voltage sensing [54], and peak and valley inductor current detection [47], [55]. However, these methods can be difficult/costly to apply to FCML converters with a high number of levels, high switching frequency and small capacitor values, due to the high bandwidth sensing and control required and the added area overhead.

Alternatively, FCML converters can rely on the natural balancing property of the PSPWM scheme [50], [58]–[60]. The existence of the natural balancing mechanism and its dynamics has been widely studied in both frequency domain [60]–[62] and time domain [63]–[65]. The general consensus is that the current harmonics at multiples of switching frequency are responsible for self-balance. These harmonics are the result of capacitor voltage imbalance, and will act to counteract the imbalance by dissipating power through the series resistance of the circuit. As a result, the capacitor voltages converge to their nominal values. This self-balancing property can offset the adverse effect of the non-idealities and the disturbances in the circuits. Yet, its strength depends on a number of factors, including duty ratio, inductor and load resistor values, switching frequency and more. To improve the natural balancing strength, passive RLC balance booster [61] or alternative modulation schemes [65] can be used at the cost of additional power loss and implementation complexity.

Compared to the study of balancing theories and techniques, the sources of the disturbances that cause capacitor imbalance have not been extensively investigated in past works. It is of great interest to understand the physical origins of the non-idealities responsible for capacitor voltage imbalance so that they can be eliminated or reduced by design. This way, high-density and naturally-balanced FCML converters can be made, facilitating a wider adoption of such topology. In this chapter, a number of practical factors that introduce capacitor voltage imbalance are investigated experimentally, and the corresponding mitigation strategies are presented.

In Section 4.2, the operating principle of FCML converters is briefly reviewed. In Section 4.3, the effect of source impedance and input capacitance are studied and found to have a strong influence on capacitor balancing. Moreover, we demonstrate in theory and with experimental results that an FCML converter with an even number of levels has significantly stronger immunity to voltage-type disturbances (such as input voltage ripple) than one with an odd number of levels. In Section 4.4, we show that the slight difference in gate drive

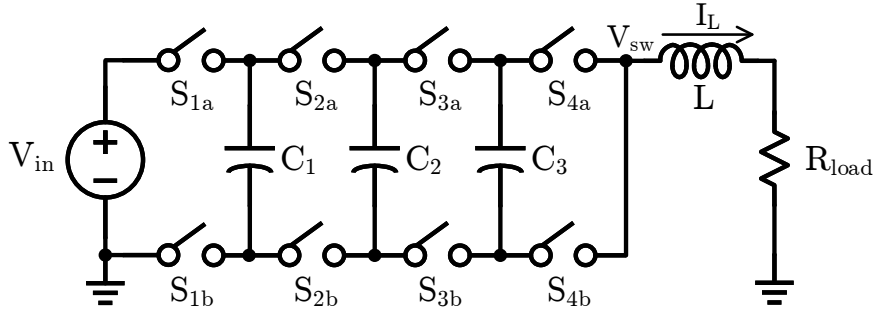


Figure 4.1: Schematic drawing of a five-level FCML buck converter.

supply voltage can cause mismatch of the gate signal propagation delays, and thus lead to capacitor imbalance. To minimize the delay mismatch, a modified cascaded bootstrap circuit is designed, which can supply equal voltages to all gate drivers and improve capacitor voltage balancing. In addition, we also experimentally show that the variation in switch on-resistance has a relatively small impact on the capacitor voltage balancing.

## 4.2 Operating Principle of FCML Converters

In an  $N$ -level FCML converter with an input voltage  $V_{in}$ , there are  $(N - 1)$  pairs of switches and  $(N - 2)$  flying capacitors with voltage ratings of  $\frac{V_{in}}{N-1}, \frac{2V_{in}}{N-1}, \dots, \frac{(N-2)V_{in}}{N-1}$ , respectively. With phase-shifted pulse-width modulation (PSPWM) [58], the  $(N - 1)$  pairs of switches turn on and off with a phase shift of  $\frac{360}{(N-1)}$  degrees, creating  $(N - 2)$  intermediate voltage levels. Therefore, the filter inductor has less voltage ripple ( $\frac{V_{in}}{N-1}$ ) at increased pulse frequency  $((N - 1)f_{sw})$ , resulting in significantly reduced size. Moreover, since the switch voltage stress is the difference between the voltages of adjacent capacitors, each switch has an ideal voltage rating of  $\frac{V_{in}}{N-1}$ .

The schematic drawing of an example five-level FCML buck converter is shown in Fig. 4.1. The top side “a” switches have a duty ratio of  $D$ , the complementary “b” switches at the bottom side have a duty ratio of  $(1 - D)$ , and the output voltage is given by  $V_{out} = DV_{in}$ . Figure 4.2 shows the gate signals of the “a” switches, the switch node voltage and the inductor current of the five-level converter operating at  $D = \frac{5}{8}$ . It can be seen that each switch has a phase lag of  $90^\circ$  from the previous one. This modulation technique creates 8 sub-circuits within one switching period as shown in Fig. 4.2. Assuming the flying capacitors have balanced voltages at their nominal values,  $V_{C1} = \frac{3V_{in}}{4}$ ,  $V_{C2} = \frac{V_{in}}{2}$  and  $V_{C3} = \frac{V_{in}}{4}$ , then the switch node alternates between  $\frac{V_{in}}{2}$  and  $\frac{3V_{in}}{4}$ , at four times of the switching frequency. This reflects a significant reduction in the applied volt-seconds across the inductor, compared to a two-level converter switching between ground and  $V_{in}$ .

In practical implementations, the flying capacitor voltages can often deviate from their nominal values due to various reasons. This can result in unbalanced switch node voltage,

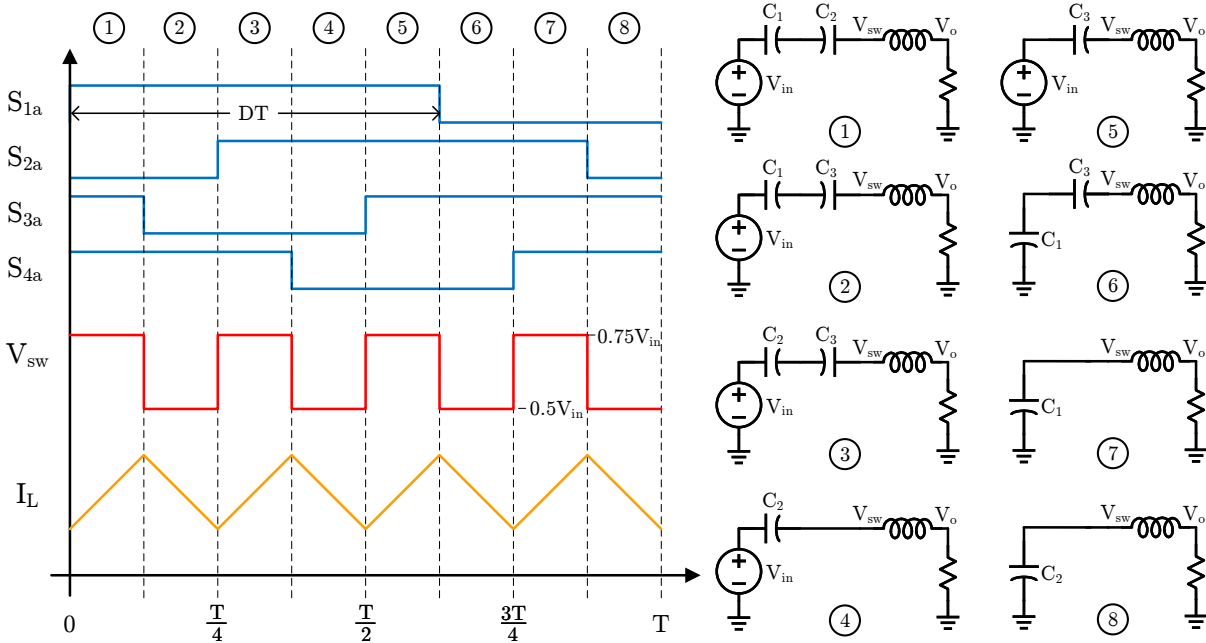


Figure 4.2: PWM, switch node voltage, and inductor current waveforms of a five-level FCML buck converter at  $\frac{1}{2} < D < \frac{3}{4}$ .

increased current ripple and associated loss on the inductor. More importantly, this can lead to an increased drain-to-source voltage stress across the switches. To isolate and study the various disturbances individually, an FCML converter testbed with flexible configuration capability (3/4/5-level, gate drive voltage, switch selection) is designed and built. Its schematic drawing is shown in Fig. 4.3 and an annotated hardware photograph is shown in Fig. 4.4. Since the focus is on steady-state capacitor voltage variations rather than balancing dynamics, dc/dc tests are performed. However, the results can also be informative to ac/dc and dc/ac cases as they can be viewed as dc/dc operations with slowly varying duty ratios

### 4.3 Imbalance Caused by Source Impedance

In prior capacitor balancing works, the input is treated as an ideal voltage source [60]–[62], [64], [65]. However, as shown in Fig. 4.3, there is usually a large and mainly inductive source impedance  $Z_{in}$  between the input voltage source  $V_{DC}$  and the actual converter input  $V_{in}$  in practical implementations. This results in a triangular-shape input voltage ripple whose magnitude ( $\Delta V_{in} = \frac{D(1-D)I_{out}}{C_{in}f_{sw}}$ ) is partly determined by the amount of low-ESR low-ESL input capacitors that are placed close to the converter input. It is found that this ripple can cause capacitor voltage imbalance, and its effect is significantly more drastic if the FCML

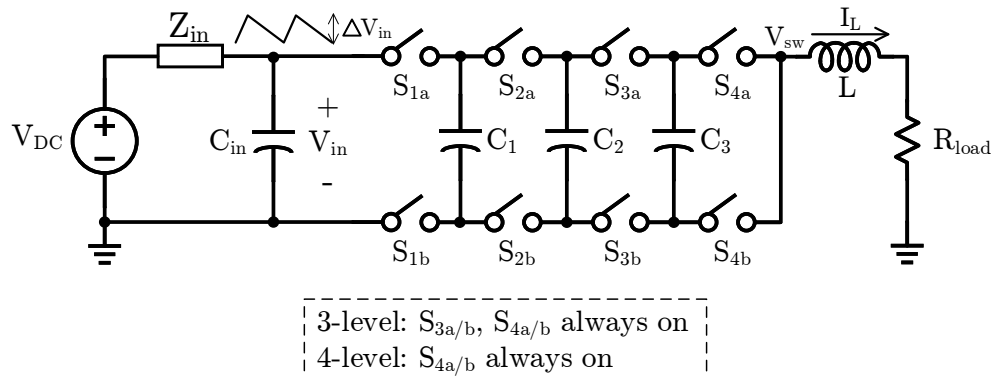


Figure 4.3: Schematic drawing of the configurable 3/4/5-level FCML buck converter prototype. There is a source impedance  $Z_{in}$  between the input voltage source  $V_{DC}$  and the actual converter input  $V_{in}$ . The magnitude of the input voltage ripple  $\Delta V_{in}$  is determined by the low-ESR low-ESL input capacitor.

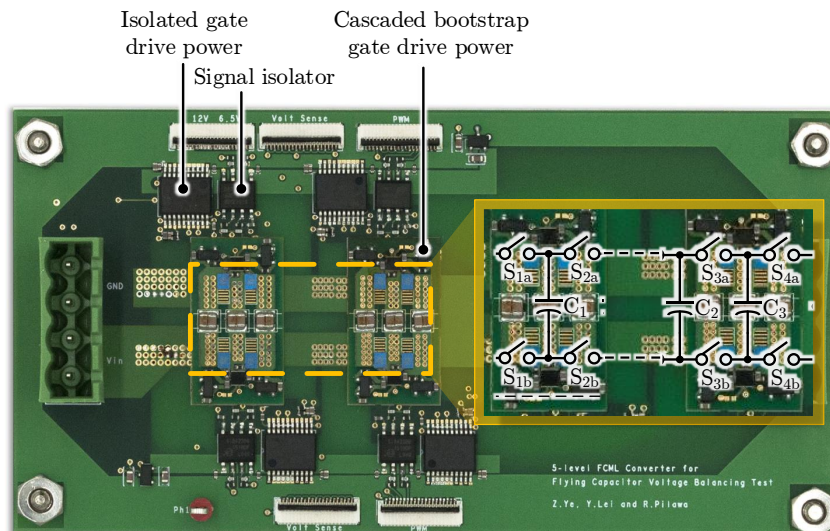


Figure 4.4: Photograph of the configurable 3/4/5-level FCML buck converter prototype.

converter has an odd number of levels.

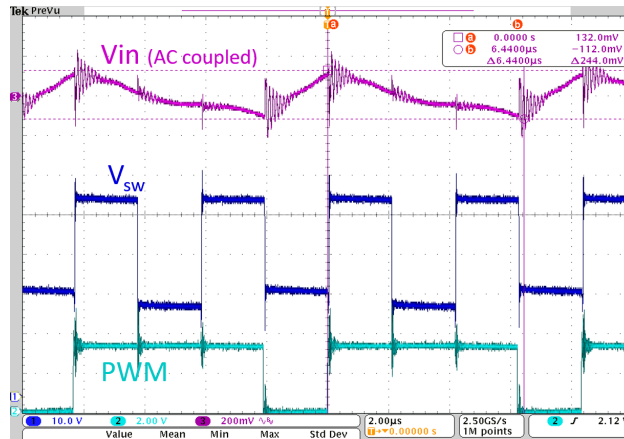


Figure 4.5: Measured input voltage ripple of a three-level FCML converter.

## The Three-Level Case

### Experiment

An FCML buck converter prototype with flexible configuration capability (3/4/5-level) is implemented as shown in Fig. 4.4. The flying capacitor voltage of the FCML prototype operating as a three-level converter (schematic shown in Fig. 4.3) is measured with different input capacitance. The prototype uses 100 V EPC2016C GaN switches, and is operated with 50 V input voltage, 120 kHz switching frequency, 10  $\mu\text{F}$  flying capacitor, 1  $\mu\text{H}$  filter inductor, and up to 4 A output current. There is a source impedance owing to the twisted wire pairs between the power supply and the input of the prototype.

The triangular-shape input voltage ripple can be observed in Fig. 4.5. Figure 4.6a shows the normalized flying capacitor voltage ( $V_{C1}/V_{in}$ ) with 13  $\mu\text{F}$  of input capacitance (X7R ceramic, after dc bias derating). It can be seen that the capacitor voltage quickly deviates from its nominal value ( $V_{C1}/V_{in} = 0.5$ ) when the duty ratio and output current increase. In comparison, as shown in Fig. 4.6b, the balancing improves dramatically when the input capacitance increases to 65  $\mu\text{F}$ . Note that the balancing performance can be further improved by eliminating the gate signal delay mismatch, which will be discussed in Section 4.4.

### Theoretical Analysis

Here, we perform a time-domain analysis to explain this phenomenon. The FCML converter of Fig. 4.3 is configured with  $S_{3a}$ ,  $S_{3b}$ ,  $S_{4a}$  and  $S_{4b}$  are all shorted, thereby generating a three-level converter. The circuit states of the three-level converter operating in CCM mode (inductor current does not go negative) at  $D > 0.5$  (where  $D$  is the duty ratio) and the corresponding waveforms are shown in Fig. 4.7. For ease of illustration, large flying capacitors are assumed here such that the capacitor voltage ripple is negligible. In the case where the input is an ideal voltage source ( $Z_{in} = 0$ ), the switch node waveform ( $V_{sw}$  in Fig. 4.7) will be



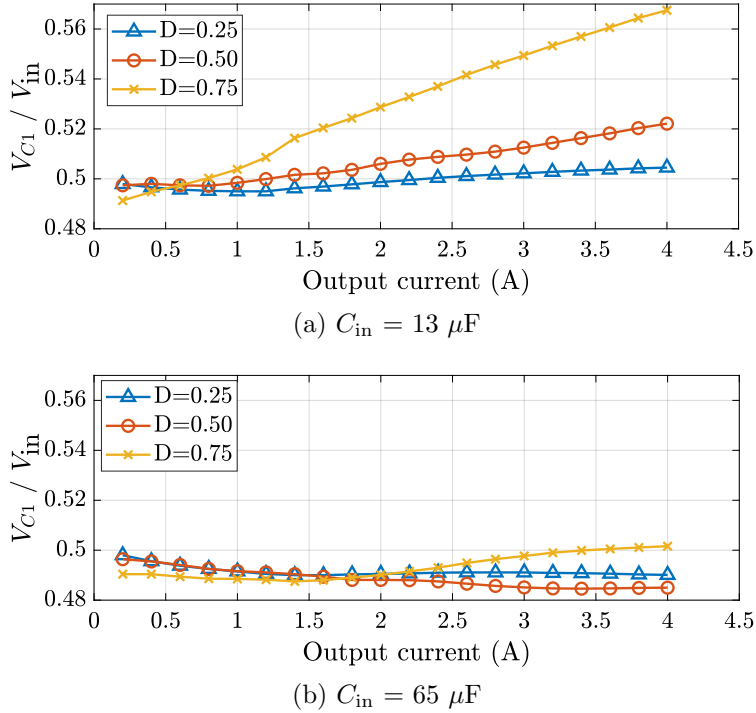


Figure 4.6: Measured flying capacitor voltage of a three-level FCML converter.

a rectangular pulse wave between  $V_{DC}$  and  $\frac{1}{2}V_{DC}$ . In practice, if we consider the triangular-shape input voltage ripple that would result from a non-negligible source impedance, the actual switch node voltage ( $V_{sw}$  labeled with large  $Z_{in}$  in Fig. 4.7) will be higher than  $V_{DC}$  in state 1, but lower than  $V_{DC}$  in state 3. As a result, the inductor sees different voltages in these two states, and the corresponding current slopes will be different. This leads to a higher capacitor charging current in state 2, assuming the converter has ideal initial conditions (e.g. balanced capacitor voltage). Consequently, the net charge into the capacitor over one complete switching cycle will be positive. This results in a flying capacitor voltage increase, which matches the experimental results. Note that this analysis does not apply to the  $D < 0.5$  case. In general, when an FCML converter operates at its bottom operating region ( $V_{sw}$  is between ground and  $\frac{V_{in}}{N-1}$  for a  $N$ -level converter), the input voltage source only connects to the rest of the circuit for one sub-period, and thus on average it has negligible effect to the switch node voltage and capacitor balancing. It can be seen from Fig. 4.6a that, even with insufficient  $C_{in}$  (therefore relatively large input voltage ripple), the three-level converter can still have a relatively good balancing for  $D = 0.25$ .

The above graphical interpretation can also be formulated for more general analysis. To capture the capacitor charge/discharge behaviors, all of the operating states within a switching cycle are analyzed in sequence. As can be inspected from Fig. 4.7, state 1 and 3

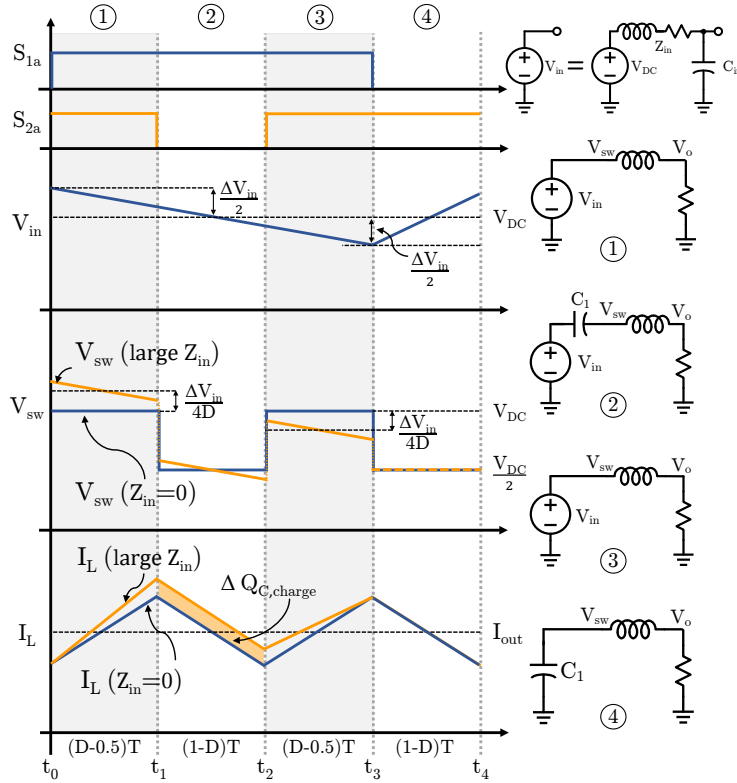


Figure 4.7: The flying capacitor voltage of a three-level FCML converter will increase in the presence of input voltage ripple.

have the same duration of  $d_1 = (D - 0.5)$ , whereas state 2 and 4 have  $d_2 = (1 - D)$ . Here we take  $\Delta V_{C_1}$  as the state variable, which is defined as the deviation of the flying capacitor voltage from its nominal value:

$$\begin{aligned} \Delta V_{C_1} &= V_{C_1} - V_{C_1, \text{nominal}} \\ &= V_{C_1} - \frac{V_{\text{in}}}{2}. \end{aligned} \quad (4.1)$$

Since  $\Delta V_{C_1}$  is determined by the net charge flowing through the capacitor, the standard inductor volt-second analysis can be performed to determine the current flow and thereby  $\Delta V_{C_1}$ . As can be seen in Fig. 4.7, the voltage across the inductor is the difference between  $V_{\text{sw}}$  and  $V_o = DV_{\text{in}}$ . When the triangular-shape input voltage ripple is considered (whose peak-to-peak amplitude is  $\Delta V_{\text{in}}$ ), the switch node voltage  $V_{\text{sw}}$  will also experience the same amount of ripple. Through geometric calculation, it can be shown that  $V_{\text{sw}}$  will be higher than the ideal case by  $\frac{\Delta V_{\text{in}}}{4D}$  (on average) in state 1, and lower by  $\frac{\Delta V_{\text{in}}}{4D}$  in state 3. Therefore

we can write the inductor voltage in each state as

$$\begin{cases} V_{L1} = (1 - D)V_{\text{in}} + \frac{\Delta V_{\text{in}}}{4D} \\ V_{L2} = (1 - D)V_{\text{in}} - V_{C1} \\ V_{L3} = (1 - D)V_{\text{in}} - \frac{\Delta V_{\text{in}}}{4D} \\ V_{L4} = V_{C1} - DV_{\text{in}} \end{cases} \quad (4.2)$$

Then the peak and valley inductor current in each switching interval can be calculated using volt-second balance on the inductor. This results in

$$\begin{cases} i(t_1) = i(t_0) + V_{L1}d_1T/L \\ i(t_2) = i(t_1) + V_{L2}d_2T/L \\ i(t_3) = i(t_2) + V_{L3}d_1T/L \\ i(t_4) = i(t_3) + V_{L4}d_2T/L \end{cases} \quad (4.3)$$

Since capacitor  $C_1$  is charged in state 2 and discharged in state 4, the average charging and discharging current can be found as

$$I_{C1,\text{charge}} = \frac{i(t_1) + i(t_2)}{2} \quad (4.4)$$

$$I_{C1,\text{discharge}} = \frac{i(t_3) + i(t_4)}{2} \quad (4.5)$$

And finally, by using

$$\Delta I_{C1} = I_{C1,\text{charge}} - I_{C1,\text{discharge}} \quad (4.6)$$

$$= C_1 \frac{d\Delta V_{C1}}{dt} = C_1 \Delta \dot{V}_{C1} \quad (4.7)$$

to combine all of the above equations together, we then get:

$$\Delta \dot{V}_{C1} = 0 \cdot \Delta V_{C1} + \frac{(2D - 1)T}{8DLC_1} \cdot \Delta V_{\text{in}}. \quad (4.8)$$

It indicates that for the case considered here ( $D > 0.5$ ), the voltage on  $C_1$  will keep increasing in the presence of input voltage ripple, if the three-level FCML converter is ideal and lossless. In practice, a natural-balancing mechanism will try to counteract this effect and limit the capacitor voltage deviation. The general consensus is that the current harmonics at multiples of switching frequency are responsible for self-balance. These harmonics are the result of capacitor voltage imbalance, and will act to counteract the imbalance by dissipating power through the parasitic resistance of the circuit [60]–[65]. To quantitatively predict the boundary of capacitor deviation, a methodology with combined continuous and discrete state-space analysis is presented in [66], which analyzes the equivalent LCR circuit of each sub-circuit within a switching period.

## The Four-Level and Five-Level Cases

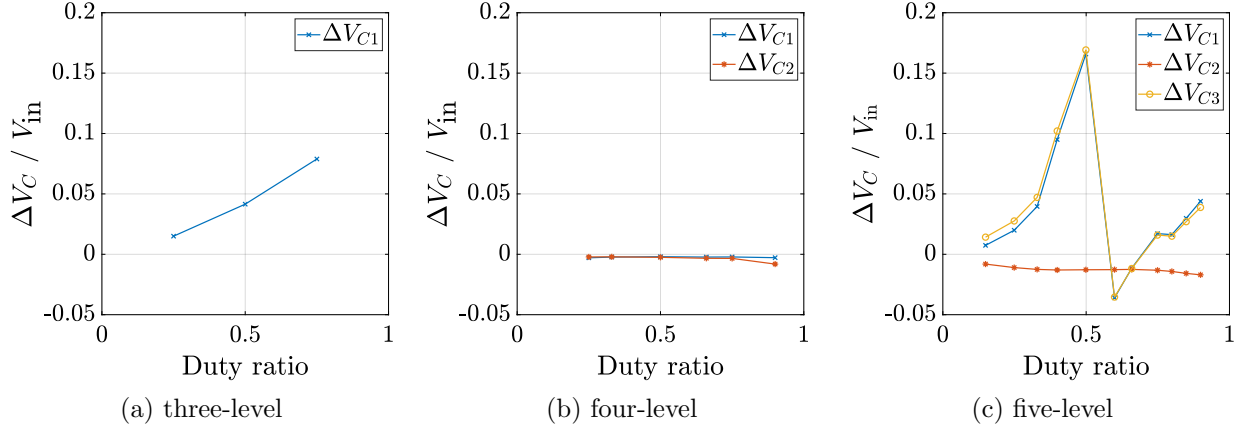


Figure 4.8: Measured flying capacitor voltage variations ( $C_{in} = 13 \mu\text{F}$ ,  $I_{out} = 4 \text{ A}$ ).

To further investigate the effect of source impedance on capacitor balancing, the FCML converter testbed is then configured to four-level mode and five-level mode, respectively. Fig. 4.8 compares the balancing performance ( $\Delta V_C = V_{C,actual} - V_{C,nominal}$ ) of the three possible configurations under the same operating conditions. It can be seen that at this small-input-capacitance high-load-current condition, the capacitor voltage deviation  $\Delta V_C$  of the three-level mode and the five-level mode can be as high as 8% and 18% of  $V_{in}$ , respectively. In comparison, the four-level mode shows near perfect capacitor balancing, with a maximum  $\Delta V_C$  of 0.8%  $V_{in}$ . To understand this unique behavior, we extend the preceding state-space method to four-level and five-level cases.

### State-Space Analysis

The system equations of the FCML converter under the influence of input voltage ripple are listed in (4.9) - (4.11) for three-level, four-level and five-level cases, respectively. The system parameters of (4.10) and (4.11) are tabulated in Table 4.1 and Table 4.2, where  $T$  is the switching period and  $C_i$  stands for the flying capacitor in its corresponding row. As discussed in the previous subsection, the very low duty ratio region (where  $V_{sw}$  switches between ground and  $\frac{V_{in}}{N-1}$ ) is not considered in this analysis, since the input voltage ripple has less effect on capacitor balancing at this region.

$$\underbrace{\Delta \dot{V}_{C1}}_{\dot{x}} = \underbrace{0}_A \cdot \underbrace{\Delta V_{C1}}_x + \underbrace{\frac{(2D-1)T}{8DLC_1}}_B \cdot \underbrace{\Delta V_{in}}_u \quad (4.9)$$

$$\underbrace{\begin{bmatrix} \Delta \dot{V}_{C1} \\ \Delta \dot{V}_{C2} \end{bmatrix}}_{\dot{x}} = \underbrace{\begin{bmatrix} 0 & a_1 \\ -a_2 & 0 \end{bmatrix}}_A \cdot \underbrace{\begin{bmatrix} \Delta V_{C1} \\ \Delta V_{C2} \end{bmatrix}}_x + \underbrace{\begin{bmatrix} b \\ 0 \end{bmatrix}}_B \cdot \underbrace{\Delta V_{in}}_u \quad (4.10)$$

$$\underbrace{\begin{bmatrix} \Delta \dot{V}_{C1} \\ \Delta \dot{V}_{C2} \\ \Delta \dot{V}_{C3} \end{bmatrix}}_{\dot{x}} = \underbrace{\begin{bmatrix} 0 & a_1 & 0 \\ -a_2 & 0 & a_2 \\ 0 & -a_3 & 0 \end{bmatrix}}_A \cdot \underbrace{\begin{bmatrix} \Delta V_{C1} \\ \Delta V_{C2} \\ \Delta V_{C3} \end{bmatrix}}_x + \underbrace{\begin{bmatrix} b_1 \\ b_2 \\ b_3 \end{bmatrix}}_B \cdot \underbrace{\Delta V_{in}}_u \quad (4.11)$$

Table 4.1: Four-level converter system parameters

Duty	(0.33, 0.66)	(0.66, 1)
$a_i$	$\frac{(-6D^2+6D-1)T}{2LC_i}$	$\frac{(1-D)T}{2LC_i}$
$b$	$\frac{(-3D^2+4D-1)T}{12DLC_1}$	$\frac{(9D-5)T}{36DLC_1}$

Table 4.2: Five-level converter system parameters

Duty	(0.25, 0.5)	(0.5, 0.75)	(0.75, 1)
$a_i$	$\frac{(-8D^2+8D-1)T}{4LC_i}$	$\frac{(-8D^2+8D-1)T}{4LC_i}$	$\frac{(1-D)T}{2LC_i}$
$b_1$	$\frac{(-16D^2+16D-3)T}{64DLC_1}$	$\frac{(-16D^2+24D-7)T}{64DLC_1}$	$\frac{(8D-5)T}{32DLC_1}$
$b_2$	$\frac{(16D^2-8D+1)T}{64LC_2}$	$\frac{(-48D^2+64D-19)T}{64DLC_2}$	$\frac{T}{32DLC_2}$
$b_3$	$\frac{(-16D^2+8D-1)T}{64LC_3}$	$\frac{(48D^2-64D+19)T}{64DLC_3}$	$\frac{-T}{32DLC_3}$

It can be observed from (4.9) - (4.11) that the FCML converter has a uniform system equation structure, which will be generalized to  $N$ -level in the next subsection. However, due to the unique characteristics of the  $A$  matrix, it is singular for three-level and five-level as their determinants are zero. It indicates that (4.9) and (4.11) have no steady-state solution unless the input  $u$  is zero. In other words, due to the input voltage ripple, the capacitor voltage will continue to diverge in this lossless system. The simulated step responses of the five-level case are shown in Fig. 4.9a to 4.9c. It predicts that, while the voltage on capacitor  $C_2$  stay close to its nominal value, the voltages on  $C_1$  and  $C_3$  will increase continuously when  $D \in (0.25, 0.5)$  and  $(0.75, 1)$ , and will decrease continuously when  $D \in (0.5, 0.75)$ . In practice, the system is not lossless, and the series resistance in the circuit will act to bring the capacitor voltages back

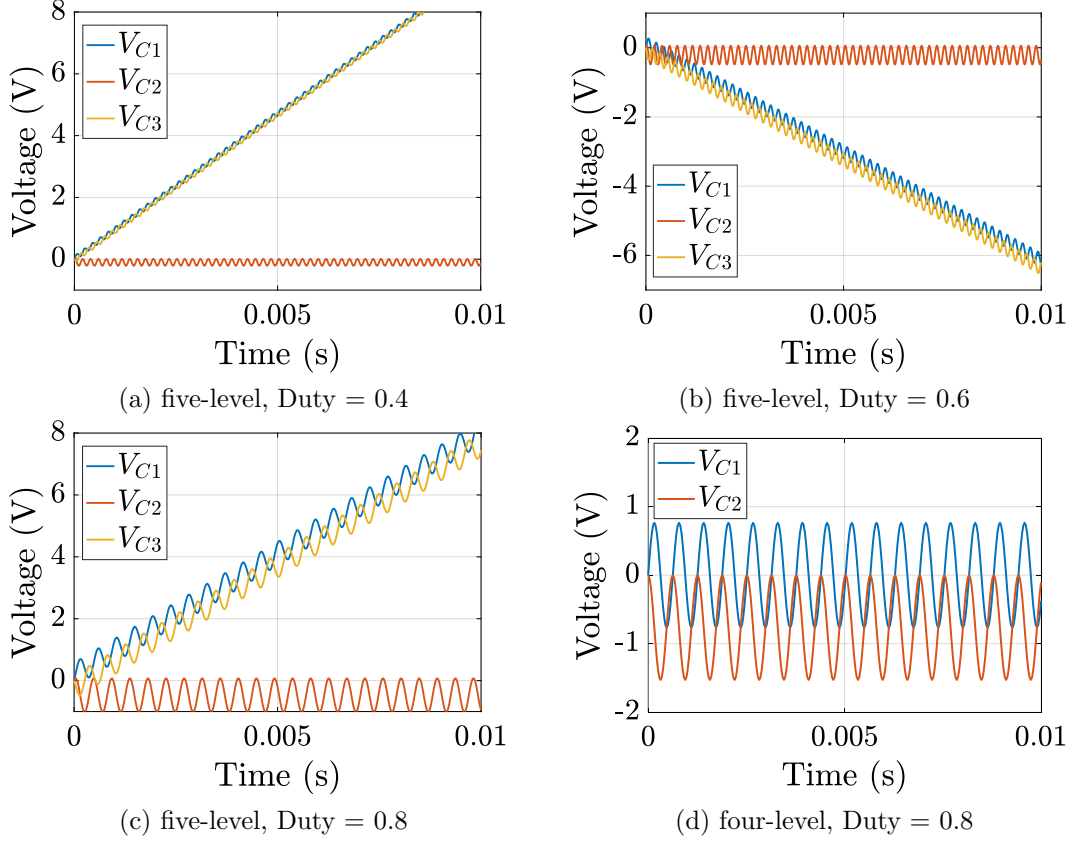


Figure 4.9: Simulated step response of the flying capacitor voltages using the proposed models ( $\Delta V_{in}$  is the input).

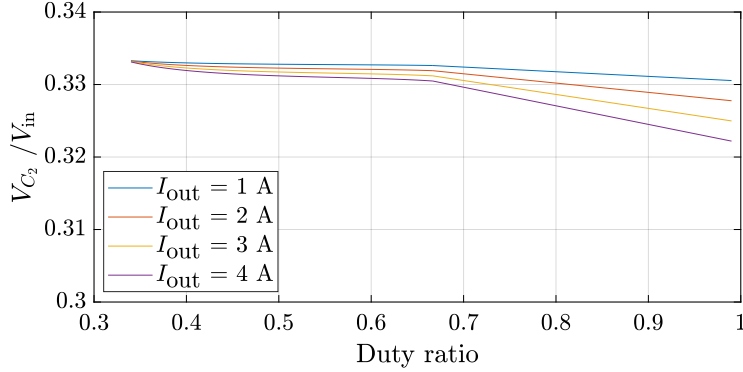
towards their nominal values, through the natural balancing property discussed in existing literature [60]–[65]. Nevertheless, the natural balancing strength depends on a number of factors, and it can often times be limited.

In contrast, a four-level FCML converter can have significantly stronger immunity to the input ripple disturbance. Although the form of (4.10) looks similar to that of (4.9) and (4.11), the determinant of its  $A$  matrix is nonzero. In this case, steady-state solutions exist for the four-level converter, and they are found as:

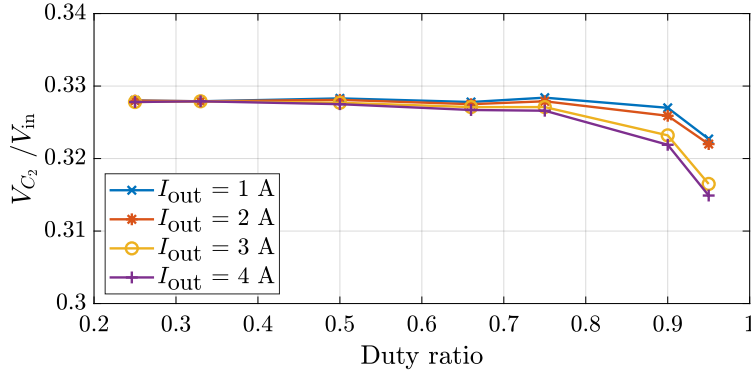
$$\Delta V_{C1} = 0 \quad (4.12)$$

$$\Delta V_{C2} = \begin{cases} \frac{-3D^2+4D-1}{6D(6D^2-6D+1)} \cdot \Delta V_{in} & D \in (0.33, 0.66) \\ \frac{5-9D}{18D(1-D)} \cdot \Delta V_{in} & D \in (0.66, 1) \end{cases} \quad (4.13)$$

This indicates that, under the influence of the input voltage ripple, the voltage on capacitor  $C_1$  will stay at its nominal value ( $0.66 V_{in}$ ) and the voltage on  $C_2$  (nominal value:  $0.33 V_{in}$ )



(a) Calculated



(b) Measured

Figure 4.10: Capacitor voltage variation of a four-level FCML converter under the influence of input voltage ripple.

will be disturbed by a fraction of  $\Delta V_{in}$ . This can also be observed from the step response of the system, which is plotted in Fig. 4.9d.

Given fixed input capacitance and switching frequency ( $C_{in} = 13 \mu\text{F}$ ,  $f_{sw} = 120 \text{ kHz}$  in this example), the input voltage ripple can be calculated with respect to the duty ratio and the output current, using  $\Delta V_{in} = \frac{D(1-D)I_{out}}{C_{in}f_{sw}}$ . Then the variation of  $V_{C_2}$ , due to  $\Delta V_{in}$ , can be derived using (4.13), as plotted in Fig. 4.10a. It can be seen that  $C_2$  remains near-perfect balancing when  $D \in (0.33, 0.66)$ , regardless of the magnitude of  $I_{out}$  and the corresponding  $\Delta V_{in}$ . For  $D \in (0.66, 1)$ , the capacitor voltage decreases linearly with a slope determined by  $I_{out}$  (also affected by  $C_{in}$  and  $f_{sw}$ ). Nevertheless, even with the small input capacitance in this example,  $V_{C_2}$  only drops by 1.4%  $V_{in}$  at heavy load and extreme duty ratio, reflecting satisfactory capacitor balancing.

In order to understand the reason for this different behavior, a graphical illustration is presented in Fig. 4.11. As in the three-level case, in the presence of input voltage ripple, the switch node voltage is disturbed and will therefore change the slope of the inductor current. However, the difference is that after the voltage of  $C_2$  deviates by an amount calculated

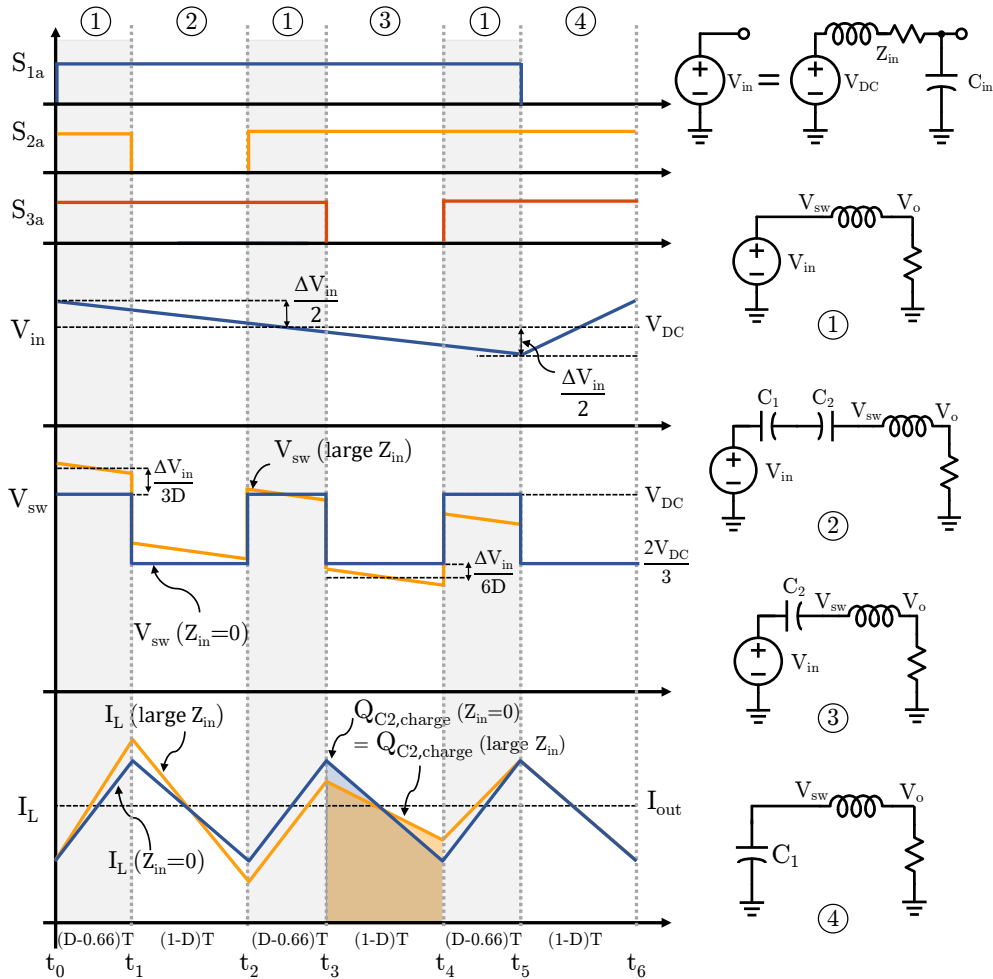


Figure 4.11: The flying capacitor voltages of a four-level FCML converter can stabilize themselves in the presence of input voltage ripple.

in (4.13), the inductor current will have the same average value as that of the ideal case ( $Z_{in} = 0$ ) in state 2 and 3, resulting in zero net charge on  $C_1$  and  $C_2$  per switching cycle. It indicates that the capacitor voltages are balanced to this point without further deviation. Even though this analysis assumes the FCML system is ideal and lossless, the capacitors here are able to stabilize themselves regardless, without the help of the natural balancing mechanism through parasitic resistance.

### Experimental Results

To verify the theory above, the prototype is first configured to a four-level FCML converter with  $13 \mu\text{F}$  input capacitance. Figure 4.10b shows the voltage of capacitor  $C_2$  with respect to duty ratio. As predicted,  $V_{C2}$  maintains its nominal value for the majority of the duty



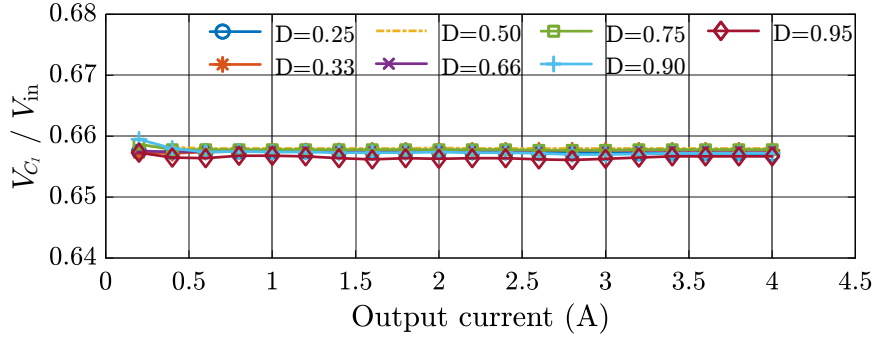
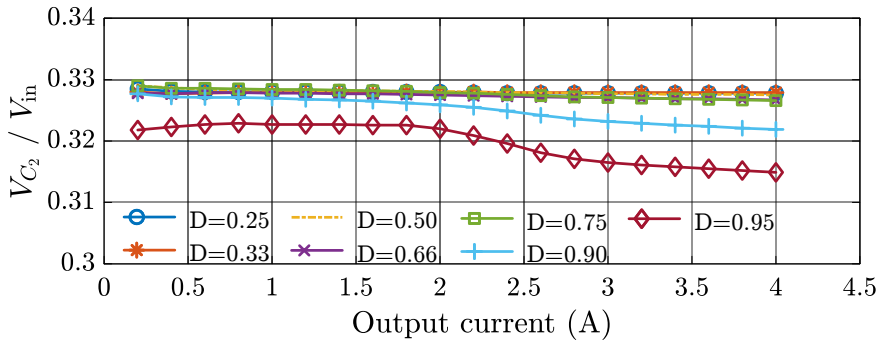

 (a) Flying capacitor  $C_1$ 

 (b) Flying capacitor  $C_2$ 

 Figure 4.12: Measured flying capacitor voltages of a four-level FCML converter ( $C_{in} = 13 \mu\text{F}$ ).

ratios, but starts to decrease at heavy load when  $D > 0.9$ , which is in good agreement with Fig. 4.10a. It can also be seen from Fig. 4.12 that while  $C_2$  experiences a small amount of voltage deviation at extreme cases,  $C_1$  can stay close to its nominal value over the full load range for all duty ratios. Considering the small input capacitance used in this test, we conclude that a four-level converter has outstanding self-balancing performance regardless of the input voltage disturbance.

Similar experimental validation was performed with the prototype configured as a five-level converter. At  $D = 0.4$ , the input voltage ripple causes  $V_{C_1}$  and  $V_{C_3}$  to drift up. Although the natural balancing property strives to bring the capacitor voltages back, its effectiveness is limited and large voltage deviation can be observed from the blue line in Fig. 4.13a. With larger input capacitance,  $\Delta V_{in}$  is reduced, leading to the reduced imbalance (red line) in Fig. 4.13a. The experimental result shown in Fig. 4.13b for  $D = 0.6$  also agrees with the prediction of the step response ( $V_{C_1}$  and  $V_{C_3}$  decrease due to  $\Delta V_{in}$ ,  $V_{C_2}$  remains at its nominal value).

The measured  $V_{C_1}$  across the entire duty ratio range is shown in Fig. 4.14. Even though greater input capacitance can help improve capacitor balancing, the system can still be very unbalanced when the duty ratio is close to 0.5. This is because PSPWM cannot guarantee

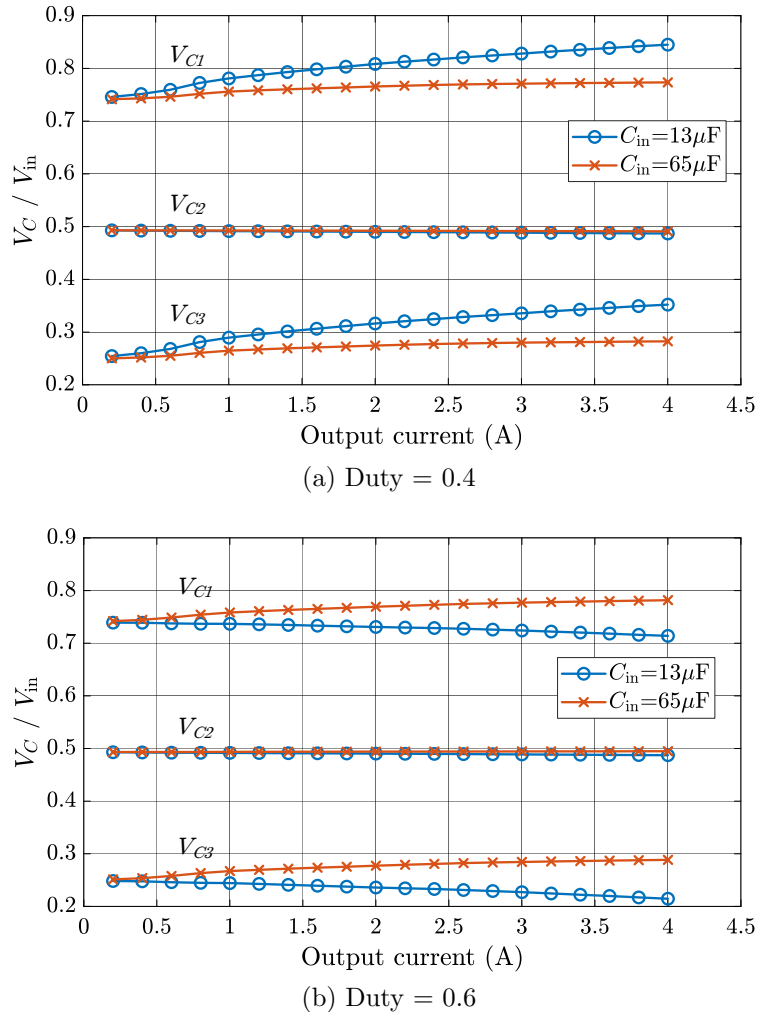


Figure 4.13: Measured flying capacitor voltages of a five-level FCML converter.

natural balancing for a five-level converter at this region, due to the inefficient use of redundant states [64], [65]. As shown in Fig. 4.15, there are six possible circuit configurations that can generate the  $\frac{1}{2}V_{in}$  voltage level, whereas the PSPWM only utilizes the first four states, in which  $C_1$  and  $C_3$  are always connected with opposite polarities. As a result, they only need to maintain a fixed voltage difference of  $\frac{1}{2}V_{in}$  but their absolute values are unconstrained. In [67], an alternative modulation technique which uses more redundant states (state 5 and 6 in Fig. 4.15) has been proposed to improve the balancing performance.

## The N-Level Case

Next, we generalize the state-space analysis in the last subsection to an FCML converter with any number of levels  $N$  (and with  $n = N - 2$  flying capacitors), and show that an

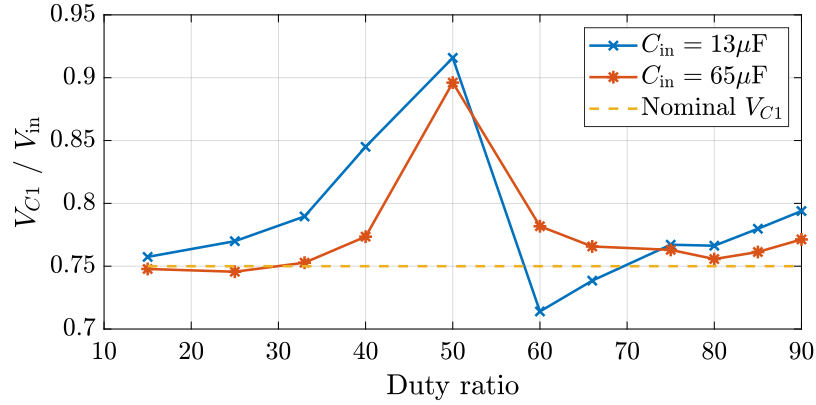


Figure 4.14: Measured  $C_1$  voltage of five-level FCML converter.

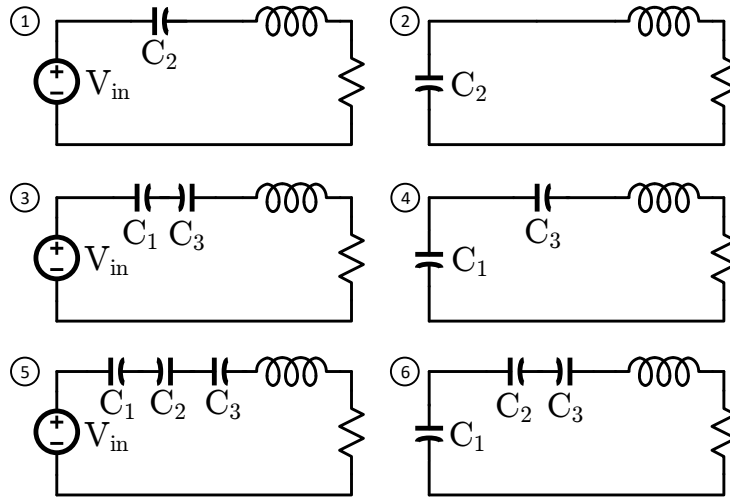


Figure 4.15: Six possible circuit configurations that can generate the  $\frac{1}{2}V_{in}$  voltage level in a five-level FCML converter. PSPWM utilizes the first four states.

even-level converter can have fundamentally better immunity to voltage-type disturbances (e.g., input voltage ripple) than one with an odd number of levels. As demonstrated through (1) to (8), by analyzing the equivalent circuit of each sub-interval within one switching cycle, the piece-wise linear system can be modeled in state-space form as

$$\dot{\mathbf{v}} = A\mathbf{v} + B\mathbf{u} \quad (4.14)$$

where  $\mathbf{v}$  is a column vector of the voltage variations of the flying capacitors from their nominal values

$$\mathbf{v} = [\Delta V_{C_1} \quad \Delta V_{C_2} \quad \cdots \quad \Delta V_{C_n}]^T. \quad (4.15)$$

The input  $u$  is a voltage-type disturbance, which can be either the input voltage ripple as analyzed in this work or any other type of voltage variation that is applied to the system. Regardless of the specific source of  $u$ , the  $A$  matrix reflects the intrinsic system characteristics and will remain the same as long as the timing of each sub-interval is accurate. To demonstrate the unique structure of the  $A$  matrix, we use

$$\Delta I_C = C \Delta \dot{V}_C \quad (4.16)$$

to rearrange (4.14). By moving the flying capacitance terms in the denominators of  $A$  (as can be observed from Table 4.1 and Table 4.2) to the left side of the equation,  $\dot{\mathbf{v}}$  becomes

$$\mathbf{i} = [C_1 \Delta \dot{V}_{C1} \quad C_2 \Delta \dot{V}_{C2} \quad \cdots \quad C_n \Delta \dot{V}_{Cn}]^T \quad (4.17)$$

and the state-space equation now becomes

$$\mathbf{i} = A' \mathbf{v} + B' u \quad (4.18)$$

with a system matrix  $A'$  of

$$A' = \begin{bmatrix} 0 & a_{1,2} & a_{1,3} & \cdots & a_{1,n-1} & a_{1,n} \\ a_{2,1} & 0 & a_{2,3} & \cdots & a_{2,n-1} & a_{2,n} \\ a_{3,1} & a_{3,2} & 0 & \cdots & a_{3,n-1} & a_{3,n} \\ \vdots & \vdots & \vdots & \ddots & \vdots & \vdots \\ a_{n-1,1} & a_{n-1,2} & a_{n-1,3} & \cdots & 0 & a_{n-1,n} \\ a_{n,1} & a_{n,2} & a_{n,3} & \cdots & a_{n,n-1} & 0 \end{bmatrix}. \quad (4.19)$$

This  $A'$  can be further simplified to the form of

$$A' = \begin{matrix} & & j & & i & & \\ & & \vdots & & \vdots & & \\ & & \vdots & & \vdots & & \\ j & \cdots & 0 & \cdots & a_{j,i} & \cdots & \\ & & \vdots & \ddots & \vdots & & \\ i & \cdots & a_{i,j} & \cdots & 0 & \cdots & \\ & & \vdots & & \vdots & \ddots & \end{matrix}. \quad (4.20)$$

The interpretation of the above system matrix  $A'$  is as follows: owing to the nature of PSPWM, there can be only one or two flying capacitors connected in series in the power loop at any time. During the time when two capacitors are connected in series, they share the same current with one being charged and the other being discharged. Therefore, for any two arbitrary flying capacitors  $C_i$  and  $C_j$  that are connected, we have

$$a_{i,j} = -a_{j,i}. \quad (4.21)$$

Since the focus is on the structure of the  $A'$  matrix, the detailed expression of  $a_{i,j}$  is omitted here, but can be derived with the periodic steady-state volt-second analysis presented in Section 4.3 for each duty ratio range.

Furthermore, considering all of the states that  $C_i$  is connected in the circuit, it can be found that the voltage variation of  $C_i$  will not induce any net current on itself. Therefore, all of the diagonal terms in the square matrix are zero:

$$a_{i,i} = 0. \quad (4.22)$$

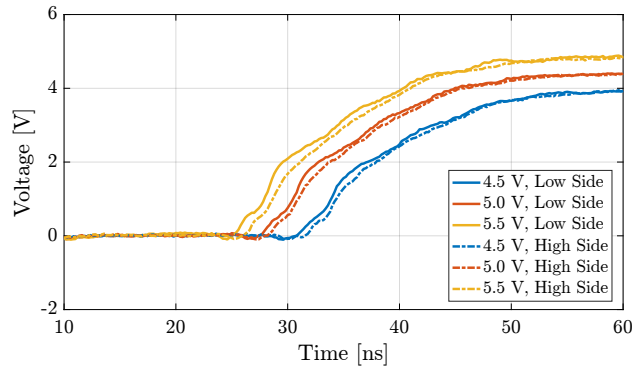
The above unique properties of FCML converter with PSPWM lead to the special structure of the  $A'$  in (4.20), which is a square matrix whose transpose equals its negative ( $A'^T = -A'$ ). This is known as a skew-symmetric matrix, and a key property is that the determinant vanishes to zero if its rank  $n$  is odd. Thus, without considering the series resistance and the corresponding natural balancing mechanism, portions of the flying capacitors in an odd-level converter will continue to diverge if a disturbance is present, whereas an even-level converter can reach a steady-state value. This finding agrees with the 3/4/5-level analysis, and proves that an FCML converter with an even number of levels has fundamentally better immunity to disturbances than one with an odd number of levels. Note that at nominal duty ratios where  $D = \frac{m}{n}$  ( $m = 1, \dots, n-1$ ), an even-level converter can also exhibit imbalance when  $m$  and  $n$  are not co-prime [68]. The good balancing performance of even-level converters have been demonstrated by recent six-level ac/dc work [69] and ten-level dc/ac work [70]. In addition, [70] also presents a control technique that can maintain good capacitor balancing during startup.

## 4.4 Imbalance Caused by Gate Driver Delay and Uneven Switch Resistance

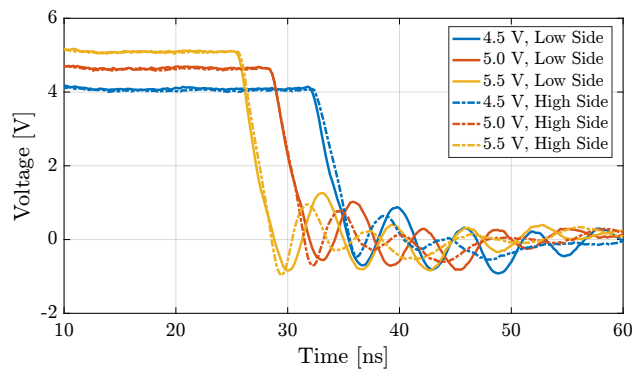
### Gate Driver Delay Mismatch

In practical implementations of FCML converters, to reduce the complexity and footprint of the gate drive circuit, every two adjacent switches can be grouped into a pair and be driven by a half-bridge gate driver. The low-side switch of each half-bridge can be powered by an isolated power supply [71], and the high-side switch can be powered by the bootstrap method. Because of the forward drop of the bootstrap diode, the supply voltage of the high-side switch can be lower than that of the low-side by approximately 0.5 – 0.6 V. It is found that this slight supply voltage difference between the low-side and high-side drivers can result in a mismatch of the gate signal propagation delay (from the input to the output of the gate driver). As a result, both the phase shift and the duty ratio of the control signals will be distorted, even with precise PWM generation.

The rising and falling edge propagation delays of TI LM5113 GaN half-bridge driver [72] are measured with different supply voltages, and the results are shown in Fig. 4.16. It is



(a) Rising edge delay after gate resistor



(b) Falling edge delay

Figure 4.16: Measured LM5113 gate driver propagation delay (from gate driver input to output).

found that in real scenarios where the low-side segment has a 5 V supply and the high-side segment has a 4.5 V supply, there is approximately an additional 7 ns turn-on delay and an additional 4 ns turn-off delay for the high-side driver.

To illustrate the effect of these additional delays, a time-domain analysis is performed. The circuit schematic is shown in Fig. 4.17 and the analytic waveforms are shown in Fig. 4.18. Compared to switch  $S_{2a}$  (driven by the low-side driver), both the turn-on and turn-off time of  $S_{1a}$  (driven by the high-side driver) will be delayed (by  $t_{r,\text{delay}}$  and  $t_{f,\text{delay}}$  in Fig. 4.18), resulting in a phase shift distortion. Since  $t_{r,\text{delay}} > t_{f,\text{delay}}$ , the duty ratio is also distorted, and both the capacitor charging time and the charging current will be less than their counterparts in the discharging state, leading to a capacitor voltage decrease. This effect can pose challenges to high-density designs that aim for high switching frequency and simple gate drive solutions. Note that the additional delay of the low-side switch  $S_{2b}$  over  $S_{1b}$  is not considered. This is due to the fact that the inductor current will naturally flow through the corresponding body diodes during deadtime and that the delay will not change the current path.

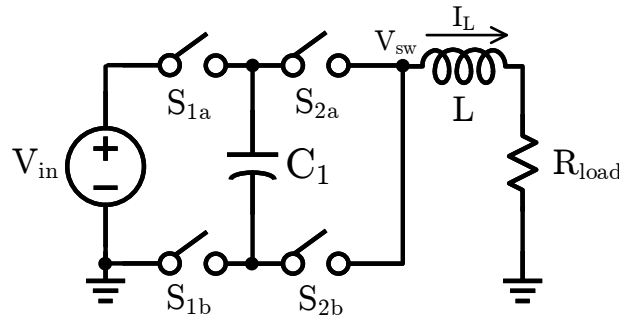


Figure 4.17: Schematic drawing of a three-level FCML buck converter.

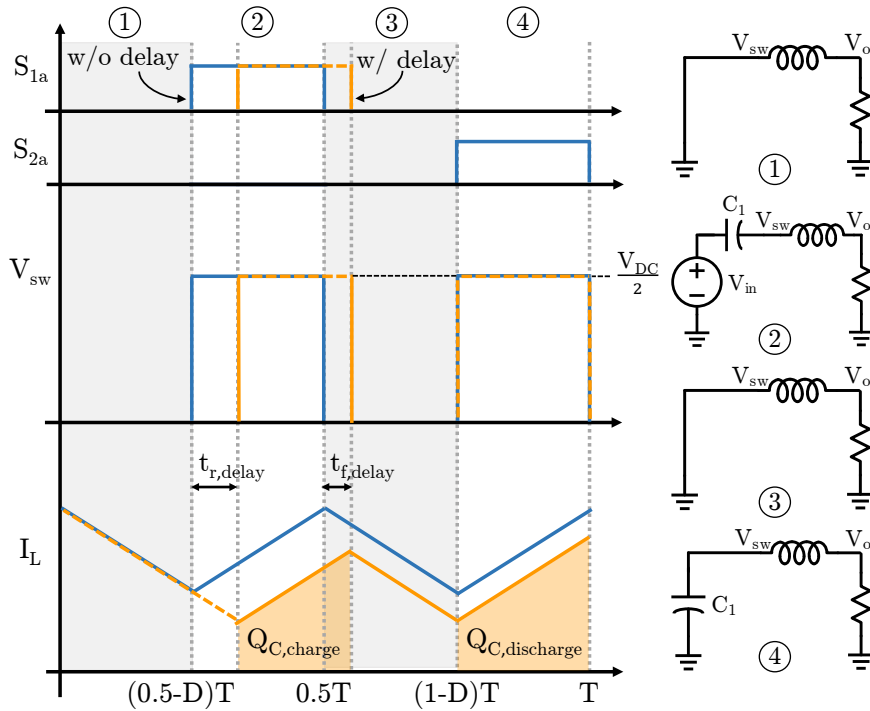


Figure 4.18: The effects of gate signal delay mismatch on capacitor balancing for a three-level FCML converter.

The previous experimental results shown in Fig. 4.6 are obtained with this kind of gate drive configuration. In order to eliminate the delay mismatch, a modified cascaded bootstrap circuit (as shown in Fig. 4.19) is designed to supply equal gate drive voltages to all of the gate drivers. The proposed circuit is discussed in more detail in Chapter 5, and is more efficient, compact and cost-effective than the isolated dc/dc solution. Another solution that can provide near equal gate drive voltages is the synchronous bootstrap method [73]. It

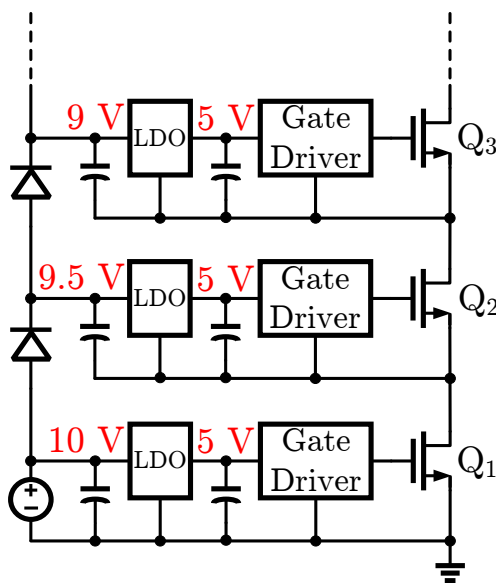


Figure 4.19: Schematic drawing of a cascaded bootstrap circuit.

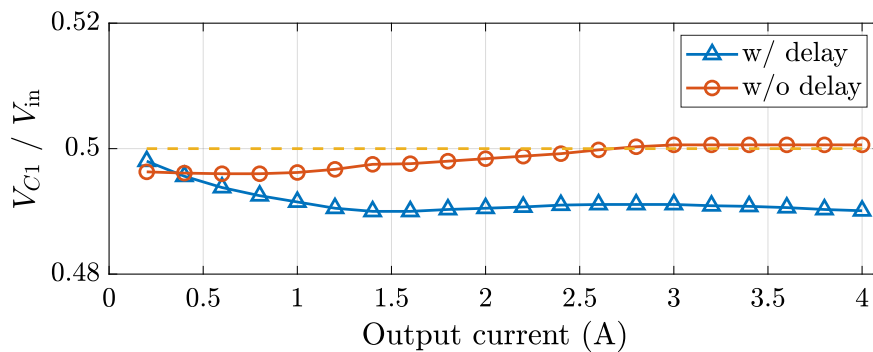


Figure 4.20: Measured effect of gate delay mismatch on capacitor voltage (three-level,  $C_{in} = 65 \mu\text{F}$ ,  $D = 0.25$ ).

replaces the bootstrapping diode with an actively controlled switch, so that the voltage drop can be greatly reduced.

To validate the benefits of such a design, the three-level prototype is reconfigured to be powered by this method. It can be seen from Fig. 4.20 that, compared to the original gate drive method which causes the flying capacitor voltage to be lower than the nominal value, the proposed gate drive method can eliminate the delay mismatch and help achieve near perfect capacitor balancing. The complete results with various duty ratios are shown in Fig. 4.21a. In contrast to Fig. 4.6b, the capacitor voltage increases to its nominal value



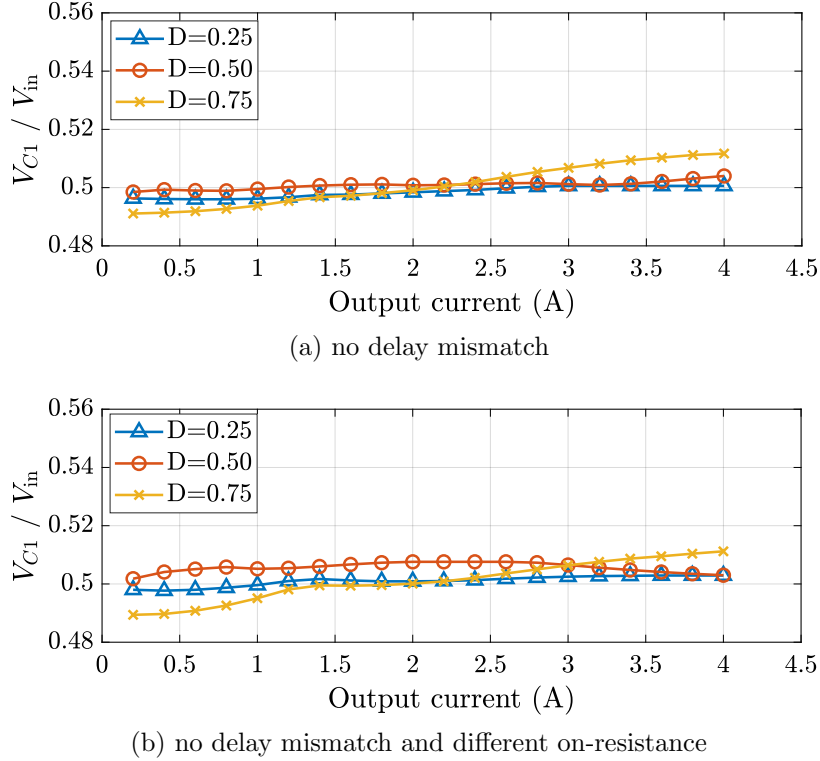


Figure 4.21: Measured flying capacitor voltage of a three-level FCML converter ( $C_{in} = 65 \mu\text{F}$ ).

for  $D = 0.25$  and  $D = 0.5$ . In addition, the prototype also demonstrates improved capacitor balancing for  $D = 0.75$ , a situation where the input voltage ripple strongly disturbs the capacitor balancing. However, in this case the flying capacitor voltage is lower than its nominal value when the load current is low, which is inconsistent with the analysis shown in Fig. 4.7. The reason behind this discrepancy is that the input voltage ripple has a different waveform at light-load, due to the negative inductor current in forced CCM mode.

The analytic waveforms showing  $V_{sw}$  and  $I_L$  at light-load condition are depicted in Fig. 4.22. Assuming that the output current is zero and the three-level FCML converter operates in forced CCM mode, the inductor only carries the ripple current. In this case, the input voltage ripple is no longer a triangular shape. Instead, it is quadratic with a smaller amplitude (compared to the triangular input voltage ripple during normal operation), which is similar to the output voltage ripple of a buck converter. Because of this quadratic voltage ripple, the switch node voltage is slightly higher than normal in state 1 and 3, but lower in state 2. Thus, the slope of the inductor current is steeper at the first three states, leading to a current flowing through  $C_1$  in state 4 that is higher than normal. As shown in Fig. 4.22, the inductor current reverses polarity later than expected in state 4, which results in net

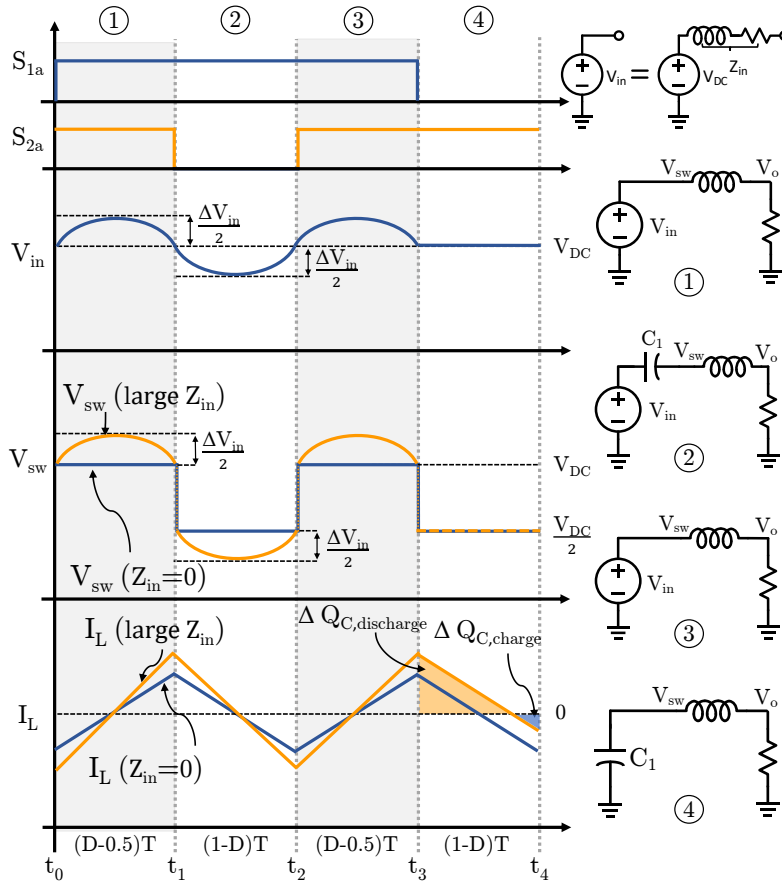


Figure 4.22: The effect of input ripple on capacitor balancing at light-load condition of a three-level converter with  $D > 0.5$ .

charge flowing out of the capacitor. In comparison to the analysis in Fig. 4.7, this demonstrates that depending on the amplitude of the load current, the input voltage ripple can cause the flying capacitor voltage to deviate towards opposite directions, which agrees with the measured three-level case at  $D = 0.75$  in Fig. 4.21a.

### Uneven Switch Resistance

The supply voltage difference produced by the original gate drive circuit can not only introduce gate signal delay mismatch, but also result in slightly higher on-resistance at the high-side switch (compared to the low-side). To investigate the effect of on-resistance variations on capacitor balancing, we modify the prototype by keeping the high-side switches the same as before ( $16 \text{ m}\Omega R_{ds,on}$ ), but changing the low-side ones to EPC2001C GaN switches with  $7 \text{ m}\Omega R_{ds,on}$  (as shown in Fig. 4.23). The gate signal delay mismatch is eliminated by the proposed cascaded bootstrap circuit, and the turn-on time are tuned to be the same for

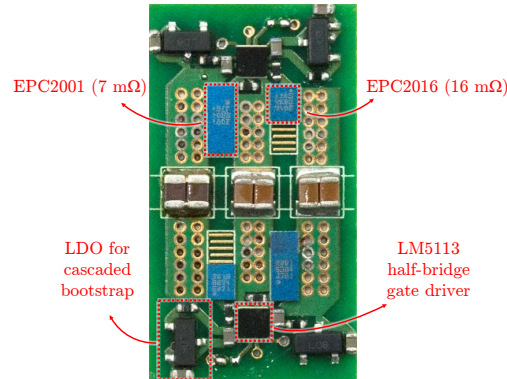


Figure 4.23: Switching cell design.

all switches with different gate resistance (the turn-off time can still be slightly different). As shown in Fig. 4.21b, the influence of uneven resistance on balancing is small compared to the other two factors discussed. The capacitor voltage remains almost the same as before for  $D = 0.25$  and  $D = 0.75$ , and drifts slightly for  $D = 0.5$ , which is a special duty ratio where the inductor does not see any voltage ripple.

## 4.5 Chapter Summary

This chapter investigates the origins of the non-idealities that can cause flying capacitor voltage imbalance in practical implementations of FCML converters. A number of effects are characterized in detail experimentally, along with theoretical circuit analysis that explains their existence. It is first found that the source impedance and the associated input capacitance can have a drastic impact on capacitor balancing, especially for odd-level converters. A state-space analysis is then performed to show that the determinant of the system matrix is zero when the FCML converter has an odd number of levels, and results in no steady-state solutions for the system when a disturbance is present. In comparison, an even-level converter has a non-zero determinant and thus an inherently better immunity to voltage-type disturbances including the input voltage ripple. It is also discovered that the slight supply voltage difference in half-bridge gate drivers can cause a mismatch of gate signal propagation delays, which leads to a distortion of phase-shift and duty ratio, and ultimately gives rise to capacitor imbalance. An alternative gate drive power supply circuit is designed to address this problem. Even with large (e.g.,  $> 2x$ ) variations of on-state resistance among various switches, the impact on capacitor voltage balancing is small.

## Chapter 5

# Circuit Techniques for Powering Floating Gate Drivers

A major challenge in the implementation of flying capacitor multilevel (FCML) converters and hybrid switched-capacitor (SC) converters is providing gate drive power to the large number of floating switches. A common solution uses isolated dc/dc converters, which are bulky, expensive, and energy inefficient. To design more compact and efficient gate drive power supply circuits, five methods are presented and compared in this chapter: bootstrap at deadtime, cascaded bootstrap with low-dropout (LDO) regulator, double charge pump, gate-driven charge pump, and synchronous bootstrap. By leveraging the inherent properties of multilevel converters, these methods can overcome the limitation of conventional bootstrap method (diode forward voltage drop) and make it possible to transfer ground-referenced power to all of the floating switches for any FCML or hybrid SC converters. Compared with the typical isolated dc/dc solution, these methods have simple structure and operating principle and can be implemented with a small number of diodes, capacitors, and LDOs. Experimental results show that an example power supply circuit can cut the size of the power stage of a state of the art seven-level FCML converter by half at 1/6 of the cost.

### 5.1 Background and Motivation

As discussed in Chapter 4, FCML converters have demonstrated excellent performance for a variety of applications [45], [50], [51], [74]–[78]. From a broader perspective, the FCML topology can be viewed as a type of hybrid switched-capacitor (SC) converter topology, which mainly uses high energy density capacitors in the power conversion process and thereby reduces the filter inductor size. It has been shown that hybrid SC converters have the potential

---

Part of this chapter was presented in the author’s master thesis [94]. This chapter includes new circuit techniques (cascaded bootstrap with LDOs and synchronous bootstrap potential), more analysis and comparison of different methods, potential IC implementations, as well as the applicability to more hybrid SC converter topologies.

to outperform conventional two-level converters by a wide margin [29]. Besides ac conversions, these hybrid SC converters have also shown promise in low voltage dc/dc applications, including data center power delivery, CMOS point-of-load converters, automotives, etc. [23], [37], [79], [80].

In order to use the flying capacitors to generate the required multilevel voltages in FCML and hybrid SC converters, a large number of switches are needed, and most of them are not ground-referenced (i.e., are “floating switches”). To drive these floating switches, both the gate signals and the gate drive power need to be level-shifted from the control potential (typically ground), imposing challenges in practical implementations. In addition to digital isolators, the level-shifting of gate control signals can be alternatively achieved with isolated gate drivers (GDs) or high-side GDs with built-in level-shifters, resulting in no additional circuit components than the GD. In comparison, providing power to the floating GD is more challenging. The state of the art uses on-chip isolated dc/dc converters with integrated transformers [71]. Although this is an easy-to-use integrated solution, the large space occupied by the chip and the associated components (compared to the power switches and the GDs) and the poor energy efficiency (as low as 20%) can significantly reduce the theoretical efficiency and power density advantages of FCML and hybrid SC topologies, when the power level of the application is relatively low. Furthermore, the high bill-of-materials cost also prevents the widespread adoption of such converters.

Since the FCML and the hybrid SC are non-isolated topologies, it is not strictly required to employ galvanically isolated power supplies for the GDs. Alternative methods to provide power to high-side drivers have thus been explored in past works. Through charge pumping circuitry, it is possible to generate higher voltages from a single, ground-reference voltage source. One such example is the self-boost charge pump circuit in [81], which can transfer power to any floating reference. However, it becomes difficult to scale to a large number of floating switches owing to high circuit complexity. Another technique utilizes the switching characteristics of the main converter to transfer energy from the power stage to the floating GDs. The pulsed linear regulator proposed in [82] can also provide floating power by taking advantage of the high  $dv/dt$  transient during switching transition. A concern of this method is the reliability and applicability under all operating conditions, as the variation of parasitics can have a direct effect on its operation. Instead of exploring methods to power a generic floating switch, the scope of this chapter is limited to FCML converters and hybrid SC converters. Even though these topologies have a large number of floating switches, they are topologically connected to either other switches or flying capacitors (which can be viewed as voltage sources). Thus, as shown in this chapter, it is possible to utilize these unique characteristics to simplify the design of floating power supplies for these types of converters. The resulting solution should not only achieve the same functionality as that of an isolated dc/dc converter, but also needs to be simple, compact, efficient, and inexpensive. IC compatible circuit elements are preferred as the final goal is to monolithically integrate the GD and its power supply.

The bootstrap technique [83], [84] is the simplest and the most widely used method to drive the high-side switch of a half-bridge. It can be viewed as a 1-to-1 charge pump (or SC

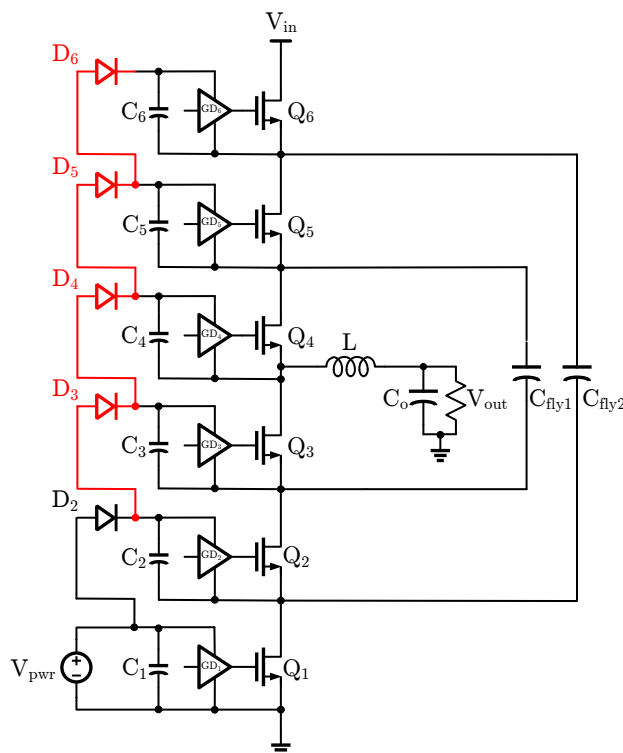


Figure 5.1: Schematic drawing of a cascaded bootstrap circuit on a four-level FCML buck converter.

converter) that consists of one diode and one switch. The bootstrap capacitor gets charged when the low-side switch is turned on, and then, it is automatically level-shifted to power the high-side switch with the diode blocking the drain-to-source voltage of the low-side switch. This method only requires one bootstrap diode that is integratable with the gate driver, and no control is needed. Since the multilevel topology has a string of series-connected switches, the concept of bootstrap can be extended to charge any floating switch from its neighboring low-side switch [8], [85]–[87]. A schematic drawing of an example four-level FCML converter powered by the cascaded bootstrap method is shown in Fig. 5.1. However, one practical limitation of this circuit is the effect of bootstrap diode forward voltage drop, which limits the achievable gate drive voltage at nodes in later stages of the cascade. This is a particularly important consideration when employing GaN transistors, as the allowed gate drive voltage is relatively narrow, leaving little room for deviations both above and below the limit (e.g., 4.5–6 V [88]).

In this chapter, we propose and investigate five methods to improve the original bootstrap technique. All proposed circuits have a simple structure and operating principle, and can be combined wisely to power any FCML converters and hybrid SC converters in a compact and efficient manner. In Section 5.2, we first start by analyzing the overcharge effect of bootstrap during deadtime, which is a special case for GaN transistors that can be used to

compensate the forward drop of the bootstrap diode. The implementation constraints and design considerations are discussed in detail in the context of FCML converters. In Section 5.3, an improved cascaded bootstrap circuit with LDOs is designed, which can provide equal gate drive voltage for all switches. To study the effect of varying duty cycle (in dc/ac and ac/dc operations) on the charging behavior of the bootstrap circuit, an in-depth numerical analysis is performed to help size the bootstrap capacitance, and various FCML prototypes are built to verify its performance. While being a simple and robust solution, the cascaded bootstrap with LDOs requires a relatively high voltage ground-referenced power supply (e.g., 16 V for a seven-level FCML) which may not be easily accessible for certain applications. Thus, in Section 5.4, we present another technique named double charge pump, which is a 1-to-2 voltage doubler constructed with two diodes and the two internal switches of the GD. It can generate a sufficiently high voltage at each stage such that a low-voltage ground-referenced power supply (e.g., 6 V) can be used for the cascaded operation without issues. Another limitation of the cascaded bootstrap method is the inherent cascaded efficiency penalty. Owing to the forward voltage drop of the bootstrap diodes, the efficiency of the overall bootstrap circuit goes down as the number of stages increases. In Section 5.5, we propose another charge pump circuit named gate-driven charge pump, which uses a low-side driver to transfer power to a corresponding high-side driver. This method decouples the chain relationship of the cascaded bootstrap, and can be applied to power a large number of high-side switches in FCML converters efficiently. In Section 5.6, we also explore the synchronous bootstrap technique proposed in [89], which replaces the bootstrap diode with self-controlled eGaN FET. Owing to the low on-resistance of eGaN FETs, the forward voltage drops in the cascaded bootstrap circuit is significantly reduced and the overall efficiency can be improved.

Combining the original cascaded bootstrap with the double charge pump and the gate-driven charge pump, a complete gate drive power supply circuit is built for a seven-level FCML converter in Section 5.7. Compared with the state of the art seven-level design [50] for the Google Little Box Challenge, the proposed circuit can cut the size of the power stage by half, with 15% gate drive loss reduction and more than 80% cost reduction. Moreover, these methods are also applicable to other hybrid SC converters, such as the Dickson converter and the series-parallel converter. Furthermore, the cascaded bootstrap circuit with LDOs has been tested on a number of prototypes, including the seven-level boost PFC front-end in [77], the six-level buck PFC front-end in [90], as well as the six-level dc/ac in [91]. With great robustness and usability, this method has proved itself to be an excellent replacement for the isolated dc/dc ic chips. A GD chip with built-in cascaded bootstrap LDO and gate-driven charge is also proposed and defined, with the potential to achieve more power dense FCML designs.

Providing reliable power to the GDs directly relates to the safe operation of power converters. Compared with isolated dc/dc gate drive power supplies, the proposed bootstrap and charge pump circuits rely on the operation of the main power circuit. Therefore, designers should understand the safe operating area as well as the limitations of the methods, and then select the most suitable one(s) based on the characteristics of the converter topol-

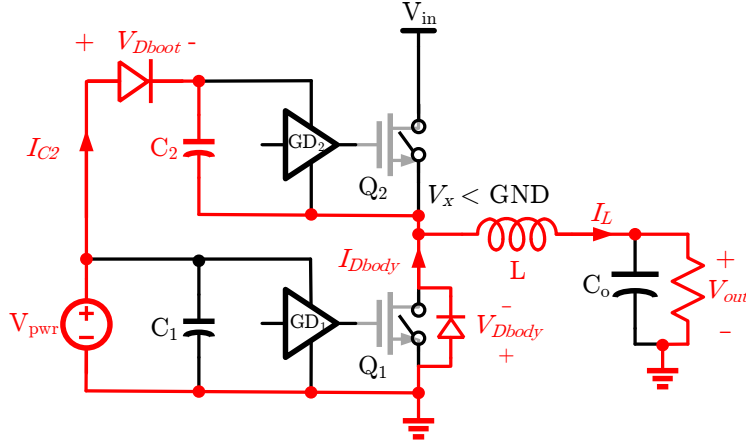


Figure 5.2: Inductor current flow in a two-level buck converter during deadtime.

ogy. It is crucial to make sure that all gate drive voltages are within the desired range (no over-voltage or under-voltage), at the designed switching frequency and duty cycle, and are stable under all conditions including start-up, light-load, and heavy-load. In Section 5.8, the five methods are compared with more discussions on design tradeoffs so that they can be appropriately applied to other topologies.

## 5.2 Bootstrap at Deadtime

### Operating Principle

The overcharge effect of bootstrapping during deadtime is illustrated in Fig. 5.2 with a two-level buck converter as an example. Assuming that the inductor current remains positive at the deadtime when both switches are off, the body diode of the low-side switch will conduct to keep the inductor current flowing. As a result, the switch node voltage  $V_x$  will be lower than the ground potential by one body diode's forward voltage drop, and the bootstrap capacitor  $C_2$  can be charged with the charging current  $I_{C2}$  flowing into the inductor, yielding the Kirchhoff's current law (KCL) constraint of (5.1) and the Kirchhoff's voltage law (KVL) constraint of (5.2)

$$I_L = I_{C2} + I_{Dbody} \quad (5.1)$$

$$V_{C2} = V_{pwr} - V_{Dboot} + V_{Dbody} \quad (5.2)$$

where  $V_{Dboot}$  represents the forward voltage drop of the bootstrap diode and  $V_{Dbody}$  represents the effective voltage drop across the transistor when the body diode is on. Although a GaN transistor does not have a conventional body diode, its reverse bias operation has a similar function, which leads to an equivalent  $V_{Dbody}$  as high as 2 V (with a strong dependence on switch current [92]). Therefore, the voltage drop across the bootstrap diode  $V_{Dboot}$  can be



canceled by this factor, and the voltage on the bootstrap capacitor can be overcharged to exceed the ground-referenced gate drive power supply. Note that this is usually considered as an undesirable behavior in the literature [93], as the extra voltage on  $C_2$  (thereby extra high  $V_{gs}$ ) may result in damage of the GaN transistor. However, with proper implementation, this mechanism may help get equal or higher voltage on bootstrap capacitors through repeated bootstrap operation, and make the gate drive circuit shown in Fig.5.1 achievable.

## Design Considerations

In practice, the aforementioned overcharge mechanism does not apply to all floating switches in a FCML converter, and the magnitude of the overcharge also depends on the converter's operating condition. Here, we analyze the factors that affect its performance and discuss the conditions that need to be satisfied before applying this special mechanism for the cascaded bootstrap operation.

### Magnitude and Direction of Inductor Current

The key idea of this method is to exploit the inductor current that flows through the body diode (or equivalent body diode caused by reverse conduction of GaN switches) during deadtime and use the associated forward voltage drop to cancel the voltage drop of the bootstrap diode. However, at start-up and light-load when the average inductor current is low, only the small inductor ripple current will flow through the body diode. This will not only result in smaller voltage drop across the body diode, but also limit the bootstrap charging current, which is constrained by (5.1). That said, the overcharge effect at deadtime is minimal when the inductor current is low, and the voltage on the bootstrap capacitor will approach that of the typical bootstrap operation ( $V_{C2} = V_{pwr} - V_{Dboot}$ ). Owing to this unavoidable forward voltage drop at each stage during start-up, it is crucial to make sure that the bootstrap capacitor voltage at later stages of the cascade will not trigger the undervoltage protection of the GD, and is sufficient to turn on the switch. After the load current increases, the bootstrap capacitors will have higher voltage due to the overcharge effect.

The direction of the inductor current also matters. For the buck converter shown in Fig. 5.2, the current always flows from the inductor into the load (assuming the inductor current ripple is small compared to the average current), indicating that only the low-side switch will experience reverse current flowing through its body diode. The same rule also applies to FCML buck converters, in which the body diodes of the high-side switches will never turn on. This indicates that these switches cannot benefit from the overcharge effect (e.g.,  $Q_5$  and  $Q_6$  in Fig. 5.1. Note that  $Q_4$  is an exception as it is charged by the low-side  $Q_3$ ). The situation of a FCML boost converter is the opposite. Since the current always flows out of the inductor and then flows into the load through the high-side switches, only the body diodes of these switches will conduct during deadtime. Therefore, the bootstrap overcharging during deadtime only applies to power the high-side switches in a step-up implementation.

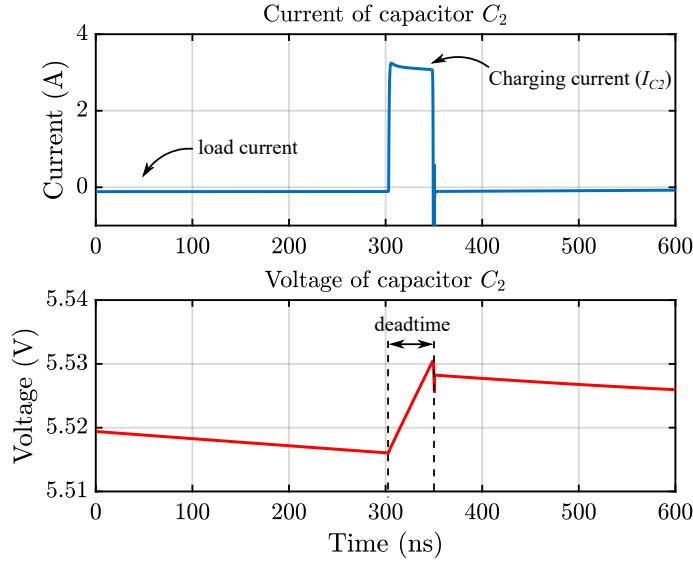


Figure 5.3: Simulated cascaded bootstrap circuit during deadtime ( $V_{\text{pwr}} = 5 \text{ V}$ ,  $V_{D_{\text{body}}} = 2 \text{ V}$ ,  $V_{D_{\text{boot}}} = 0.6 \text{ V}$ ).

### Gate Drive Power

While (5.2) gives the theoretical maximum voltage of bootstrap capacitor  $C_2$ , its actual operating voltage will be lower due to the insufficient charging time (the deadtime) and the large current flowing through the bootstrap diode (corresponding to the load current that needs to be delivered to the gate drive circuit). The FCML converter with cascaded bootstrap shown in Fig. 5.1 is simulated in LTspice with a detailed model of the EPC2016C GaN transistor [88]. The voltage and current of  $C_2$  are shown in Fig. 5.3. It can be seen that, during the deadtime, the capacitor is charged by a near constant current, which implies that the capacitor charge transfer is incomplete. Assuming a small capacitor voltage ripple, the average voltage of a bootstrap capacitor  $V_{C,i}$  is given by

$$V_{C,i} = V_{C,i-1} + V_{D_{\text{body}}} - V_{D_{\text{boot}}} - I_{C,i}R_{D_{\text{boot}}} \quad (5.3)$$

where  $R_{D_{\text{boot}}}$  is the equivalent resistance of the bootstrap diode and  $I_{C,i}$  is the charging current for capacitor  $C_i$  during the deadtime. Thus, the actual voltage drop across the bootstrap diode is  $(V_{D_{\text{boot}}} + I_{C,i}R_{D_{\text{boot}}})$ , which is greater than the minimum diode turn-on voltage  $V_{D_{\text{boot}}}$ . As shown in the bottom plot of Fig. 5.3, the average voltage of  $C_2$  is approximately 5.5 V, instead of 6.4 V as given by (5.2).

In a cascaded bootstrap configuration, a gate drive stage is powered by the bootstrap capacitor of the previous stage. For example,  $C_6$  provides power for  $\text{GD}_6$ , while  $C_5$  provides power for both  $\text{GD}_5$  and  $C_6$  (and thus indirectly  $\text{GD}_6$ ). Therefore, the charging current of

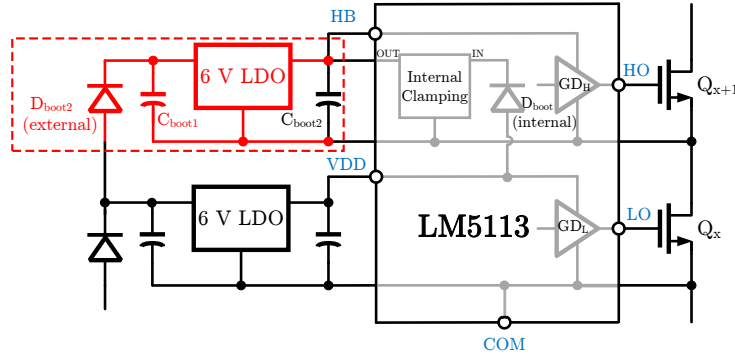


Figure 5.4: Additional circuitry to observe the overcharge effect of bootstrap operation at deadtime.

the  $i$ th bootstrap capacitor is given by

$$I_{C,i} = \frac{\sum_{x=i}^n Q_{\text{gate},x}}{t_{\text{dead}}} \quad (5.4)$$

where  $n$  is the total number of switches,  $Q_{\text{gate},x}$  is the charge delivered to the  $\text{GD}_x$  in one switching period, and  $t_{\text{dead}}$  is the length of deadtime. Combining (5.3) and (5.4), we can see that due to a larger load charge and the resultant larger charging current, the bootstrap capacitor closer to ground (corresponding to a smaller  $i$ ) will experience less overcharge effect.

### Length of Deadtime

As shown in Fig. 5.3, bootstrapping happens during the deadtime. Since the required gate drive charge is fixed per switching cycle, a longer deadtime can help reduce the charging current ( $\Delta Q = I\Delta t$ ), which further leads to higher average capacitor voltage according to (5.3). Nevertheless, as the current flowing through the body diode contributes to power loss, a smaller deadtime is preferred from the conversion efficiency perspective. If the cascaded bootstrap method is chosen, careful calculations and measurements should be performed to make sure the converter has sufficient gate drive voltages while maintaining a high overall conversion efficiency.

### Hardware Verification

A hardware prototype of the four-level FCML converter in Fig. 5.1 is implemented to validate the theory described above. The bottom four switches ( $Q_1 - Q_4$ ) are powered by the cascaded bootstrap method. Due to the direction of the current flow, the overcharge effect at deadtime does not apply to the top two switches ( $Q_5$  and  $Q_6$ ). Thus, they are powered by the gate-driven charge pump method (described in detail in Section 5.5) to ensure sufficient gate drive

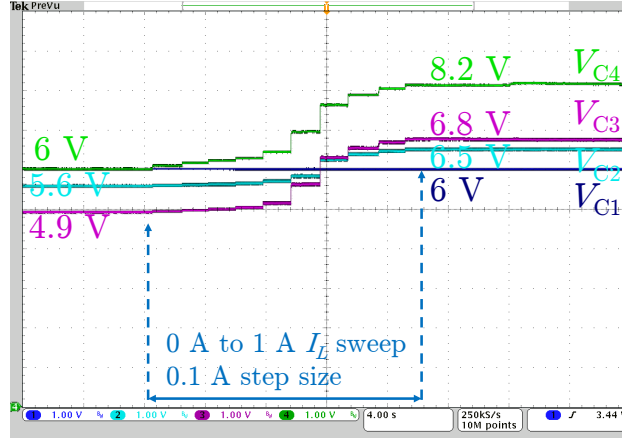


Figure 5.5: Voltage on cascaded bootstrap capacitors.

voltage magnitude. In order to reduce the number of components, TI LM5113 half-bridge GDs [72] are used so that only three drivers are needed to drive the six switches. Owing to the internal clamping of the built-in bootstrap diode in the LM5113, it is not possible to fully observe the body diode voltage gains through the cascaded bootstrap operation. For observational purpose, a redundant external diode is introduced to bypass the internal clamping function and an LDO is added to limit the  $V_{gs}$  of the GaN transistor, as illustrated in Fig. 5.4.

The voltage waveforms (corresponding to capacitors  $C_1$  to  $C_4$  in Fig. 5.1) with load current sweep is shown in Fig. 5.5. The switching frequency is 120 kHz. Capacitor  $C_1$  is connected to the ground power supply, and its voltage is fixed at 6 V. At zero load current, the voltages on  $C_2$  and  $C_3$  are each reduced by approximately one diode drop from the previous voltage, indicating that the overcharge effect at deadtime is not sufficient to compensate for the voltage drop of the bootstrap diodes. In this situation, it is important to make sure that the lowest voltage in the cascade ( $V_{C3} = 4.9$  V) can still fully enhance the GaN transistor [88], so that the effect of switch on-resistance mismatch on converter operation is minimal. Compared with  $C_3$ ,  $C_4$  is overcharged to 6 V at zero load current condition (only inductor ripple current exists). As explained in (5.4), the capacitor at the end of the cascaded bootstrap chain processes the least amount of gate drive power. Therefore, it has the lowest capacitor charging current and the most noticeable overcharge effect. After the load current increases,  $V_{C2}$  to  $V_{C4}$  all start to increase. When  $I_L$  is approximately 0.7 A, all bootstrap capacitor voltages exceed 6 V ( $V_{pwr}$ ). After  $I_L$  is increased to 1 A, the voltage on each bootstrap capacitor becomes higher than its low-side neighbor because of the overcharge effect. It can be observed from Table 5.1 that the length of deadtime has a strong influence on the gate voltage. A shorter deadtime design will require a higher load current to overcharge the bootstrap capacitors to exceed the voltage of the ground power supply.



As shown in Fig. 5.6, the ground-referenced power supply has a voltage  $V_{\text{pwr}}$  that is higher than the required gate drive voltage  $V_{\text{gdrv}}$ , such that there remains sufficient voltage at each stage of the cascade after the diode forward voltage drops. To protect the switch and the GD, an LDO is used at each stage to step down the bootstrapped voltage to the desired value. With sufficient voltage on the ground power supply, this simple and modular method can provide equal gate drive voltage for all floating switches.

## Design Guidelines

This method relies on the excess voltage on the power supply to make the bootstrap operation cascadable. However, this high voltage has to be stepped down to the required gate drive voltage in a resistive manner (by bootstrap diodes or LDO), resulting in an overall cascaded bootstrap efficiency of

$$\eta_{\text{total}} = \frac{V_{\text{gdrv}}}{V_{\text{pwr}}}. \quad (5.5)$$

This implies that the efficiency is reduced as the number of floating switches increases, because  $V_{\text{pwr}}$  needs to be increased to compensate for additional diode forward voltage drops. To optimize the efficiency,  $V_{\text{pwr}}$  should be tuned to ensure that the LDO of the top switch (the switch at the end of the cascade) sees a voltage that is only slightly higher than the required gate drive voltage ( $V_{c,n} \simeq V_{\text{gdrv}} + V_{\text{ldo,dropout}}$ ), as any excess voltage on the LDO is unnecessary loss. In order to understand the factors that affect the operation of the cascaded bootstrap circuit and determine a suitable  $V_{\text{pwr}}$ , we analyze the power flowing through the cascaded bootstrap circuit and discuss the important design considerations of such circuit.

As illustrated in Fig. 5.6, the gate drive power of stage  $n$  is provided by the bootstrap capacitor  $C_n$ . When switch  $Q_1$  is on,  $C_n$  is charged by its low-side neighbor  $C_{n-1}$  through bootstrap diode  $D_{n-1}$ . Assuming the average current flowing through  $D_{n-1}$  is  $I_{d,n-1}$ , then the average gate drive power transferred from stage  $n-1$  to stage  $n$  (from  $C_{n-1}$  to  $C_n$ ) is

$$P_{\text{in},n} = V_{c,n-1} I_{d,n-1}. \quad (5.6)$$

Since the average diode current  $I_{d,n-1}$  can be expressed in terms of the charge transferred per switching cycle  $I_{d,n-1} = Q_{d,n-1} f_{\text{sw}}$ , (5.6) can be alternatively written as

$$P_{\text{in},n} = V_{c,n-1} Q_{d,n-1} f_{\text{sw}}. \quad (5.7)$$

For bootstrap circuit operating at a relatively high switching frequency ( $> 100$  kHz), the on-state bootstrap charging current  $I_{\text{on},n-1}$  becomes a near constant value [94]. Thus,  $Q_{d,n-1}$  can be approximated to be

$$Q_{d,n-1} \simeq I_{\text{on},n-1} \frac{d}{f_{\text{sw}}} \quad (5.8)$$

where  $d$  is the duty ratio when the main switch is on and the bootstrap operation is active. Therefore, we can further express  $P_{\text{in},n}$  as

$$P_{\text{in},n} \simeq V_{c,n-1} I_{\text{on},n-1} \frac{d}{f_{\text{sw}}} f_{\text{sw}} = V_{c,n-1} I_{\text{on},n-1} d. \quad (5.9)$$

Next, by modeling the bootstrap diode as a voltage source  $V_f$  in series with an on-resistance  $R_{\text{on}}$ , the charging current can be derived to be

$$I_{\text{on},n-1} = \frac{V_{c,n-1} - V_{c,n} - V_f}{R_{\text{on}}}. \quad (5.10)$$

If we define  $(V_{c,n-1} - V_{c,n} - V_f)$  as  $\Delta V_{c,n-1}$ , then  $P_{\text{in},n}$  can be expressed as

$$P_{\text{in},n} \simeq \frac{V_{c,n-1} \Delta V_{c,n-1} d}{R_{\text{on}}}. \quad (5.11)$$

Excluding the loss on the bootstrap diode  $D_{n-1}$ , the actual power delivered to  $C_n$  at stage  $n$  is

$$P_{\text{in},n'} \simeq \frac{V_{c,n} \Delta V_{c,n-1} d}{R_{\text{on}}}. \quad (5.12)$$

This power is then consumed by the following LDO and gate drive circuit. The gate drive power includes the quiescent power and the switching power that goes into the switch:

$$P_{\text{gd}} = V_{\text{gdrv}} I_q + f_{\text{sw}} C_{\text{iss}} V_{\text{gdrv}}^2 \quad (5.13)$$

where  $V_{\text{gdrv}}$  is the gate drive voltage,  $I_q$  is the GD quiescent current and  $C_{\text{iss}}$  is the input capacitance of the switch. After including the power loss on the LDO, the total power consumed by stage  $n$  becomes

$$P_{\text{out},n} \simeq \underbrace{\frac{V_{c,n}}{V_{\text{gdrv}}}}_{1/\eta_{\text{LDO}}} \times \underbrace{V_{\text{gdrv}} (I_q + f_{\text{sw}} C_{\text{iss}} V_{\text{gdrv}})}_{\text{GD power}} \quad (5.14)$$

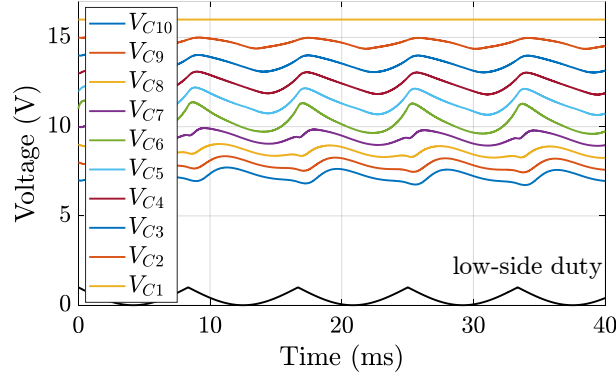
$$= V_{c,n} (I_q + f_{\text{sw}} C_{\text{iss}} V_{\text{gdrv}}). \quad (5.15)$$

Since the net power into  $C_n$  is zero in steady state, we get

$$P_{\text{in},n'} = P_{\text{out},n}. \quad (5.16)$$

With this equality, we are able to derive the ground power supply voltage of an  $N$ -level FCML dc/dc converter. For instance, with desired  $V_{\text{gdrv}}$ ,  $V_{c,n}$ ,  $d$  and  $f_{\text{sw}}$ ,  $V_{c,n-1}$  can be calculated through (5.16). Then,  $V_{c,n-2}$  can be derived with the updated  $P_{\text{out}}$  value, which is the sum of  $P_{\text{in},n}$  and  $P_{\text{out},n-1}$ . With  $N - 1$  iterations, the minimum  $V_{c,1}$  (corresponding to the highest possible overall gate drive efficiency) to supply equal gate drive voltage for all floating switches can be determined.

By comparing (5.12) and (5.15), it can be observed that the power consumed by the GD  $P_{\text{out},n}$  is a function of  $f_{\text{sw}}$ , but the input power supplied by the cascaded bootstrap circuit  $P_{\text{in},n'}$  is not. This is because all bootstrapped power comes from the ground power supply, and it is a function of duty ratio (or effective switch on-time) rather than switching frequency. This fundamental limitation may pose challenge to operation with very low duty ratio, which



(a) DC/AC operation, modulation index = 1

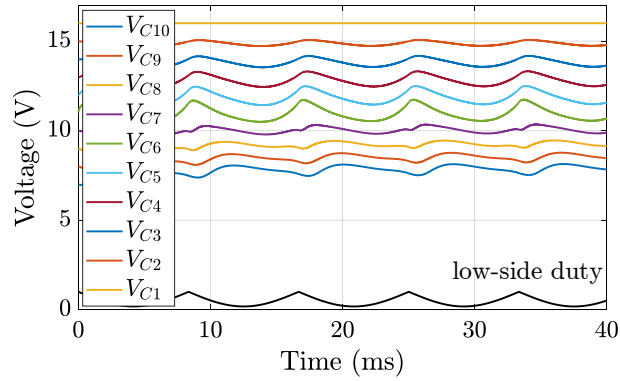

 (b) AC/DC operation,  $V_{\text{rms}} = 220 \text{ V}$ ,  $V_{\text{rec}} = 380 \text{ V}$ 

Figure 5.7: Simulated cascaded bootstrap voltages of a six-level FCML converter under different operating conditions ( $f_{\text{ac}} = 60 \text{ Hz}$ ,  $f_{\text{sw}} = 120 \text{ kHz}$ ,  $V_{\text{pwr}} = 16 \text{ V}$ ,  $C_{\text{boot}} = 20 \mu\text{F}$ , switch: GS61004B[95], GD: Si827x[96], diode:  $V_f = 0.6 \text{ V}$ ,  $R_{\text{on}} = 5 \Omega$ ).

may occur in dc/ac and ac/dc cases. For such cases, a higher ground power supply voltage than that of a dc/dc case with the same averaged duty ratio is required for extra headroom, so that the top switch at the end of the cascade can maintain normal operation in the worst case.

The simulated gate drive voltages of a six-level FCML converter operating in dc/ac and ac/dc modes are shown in Fig. 5.7. It can be seen that the bootstrap capacitors experience a voltage swing over the line cycle, owing to the change of available bootstrap charging time. More bootstrap capacitance can be used for better filtering and less voltage swing, but it can be limited by cost and space in practical implementations. Compared with the ac/dc case, the duty ratio of the low-side switches in the dc/ac case has lower average value and lower absolute value ( $d$  reaches 0). According to (5.11), given fixed ground power supply voltage, it will result in larger capacitor voltage drops and lead to lower voltage on the capacitor at each stage. Care must be taken to make sure that the minimum voltage at the last stage is sufficient to fully enhance the switch (6 V for the GaN switch in this example).



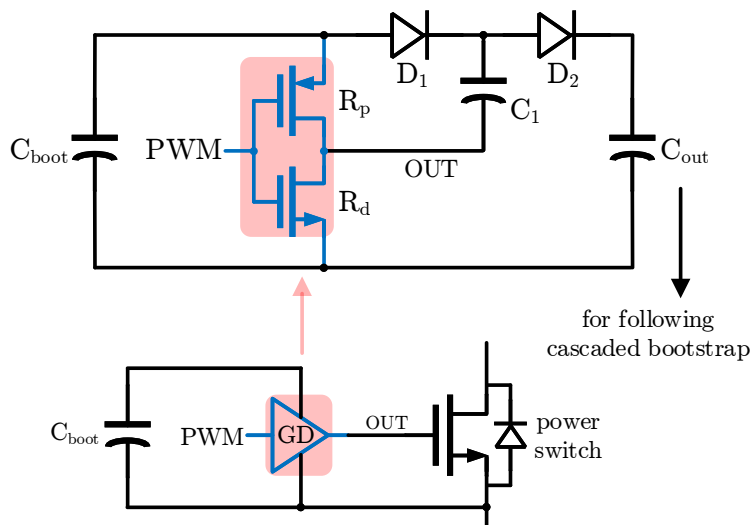


Figure 5.8: Schematic drawing of a double charge pump circuit.

The functionality and robustness of this method have been successfully verified on various ac/dc and dc/ac FCML converter prototypes [77], [90], [91]. In such implementations, the ground reference of the LDOs is not fixed. Instead, they experience the same magnitude of voltage swing (with high  $dv/dt$ ) as the main switches during switching transitions. Therefore, it is critical to minimize the parasitics in the layout, such that the LDOs can remain stable under all conditions. Additionally, owing to the low gate charge and the associated fast switching speed of GaN switches, suitable gate resistances should be employed to ensure the proper operation of the bootstrap circuit.

## 5.4 Double Charge Pump

As discussed above, the cascaded bootstrap circuit with LDOs is a simple and robust solution. However, it requires a high voltage power supply, which may not be easily accessible for certain applications. Here, we present another charge pump circuit to boost up the bootstrapped voltage, so that a low-voltage power supply can be used for the cascaded operation without the concerns of the diode forward voltage drops.

As shown in Fig. 5.8, a 1-to-2 voltage doubler (also called double charge pump) is constructed by utilizing the two existing internal switches of the GD. Only two diodes and two capacitors are needed, and no additional control signals are required. Since the diodes only need to block the input voltage ( $V_{C_{boot}} < 10$  V), low-voltage, low-profile Schottky diodes can be used. The double charge pump has two operating states. In the first state, the PWM signal is low and the pull-down switch  $R_d$  is active, so that  $C_1$  is charged by  $C_{boot}$  through diode  $D_1$ . In the second state, the PWM signal is high and the pull-up switch  $R_p$  is active. Therefore,  $D_1$  is reverse biased, and  $C_{out}$  is charged by the series combination of  $C_1$  and

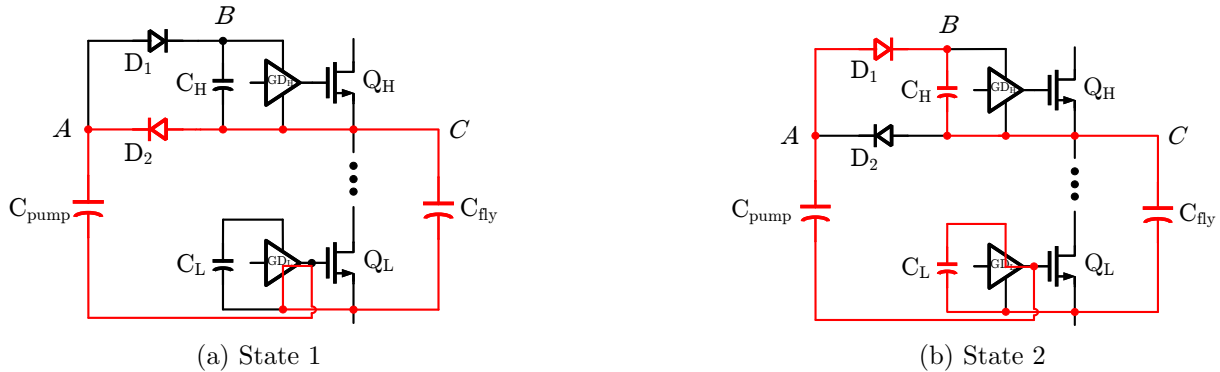


Figure 5.9: Schematic drawing of a gate-driven charge pump circuit.

$C_{boot}$  through  $D_2$ . The output voltage of this double charge pump will be approximately twice the gate drive voltage  $V_{C_{boot}}$  minus the forward drops of  $D_1$  and  $D_2$ . For instance, assuming the desired gate drive voltage is 6 V, and the drop of each diode is as high as 1 V (due to incomplete charge transfer and high charging current), the double charge pump can still provide 10 V output, which is sufficient to power the next 4–5 switches in an FCML converter through the cascaded bootstrap operation.

One concern of this method is the efficiency, since eventually the doubled voltage must be regulated to the desired gate drive voltage in a resistive manner, either through the voltage drops of the diodes or through the LDO in front of the GD. If  $n$  double charge pumps are used to power a given stage in the cascaded bootstrap, its efficiency will be  $\eta \simeq (\frac{1}{2})^n$ . Thus, double charge pumps should be utilized cautiously, as unnecessary use may degrade the efficiency of the power supply circuit. An implementation example is given in Section 5.7.

## 5.5 Gate-Driven Charge Pump

The three methods discussed above strive to overcome the effect of diode forward voltage drops in a cascaded bootstrap circuit. However, there remains another main limitation, which is the cascaded efficiency penalty. Because of the forward voltage drop of the bootstrap diodes, the efficiency of the overall bootstrap circuit goes down as the number of stages increases. Here, we propose another charge pump circuit named gate-driven charge pump. Instead of transferring power between neighboring switches through a bootstrap diode, the proposed circuit can transfer power from a low-side driver to a corresponding high-side driver, as long as the two drivers have a flying capacitor connected in between. This method can not only be applied to power a large number of high-side switches in an FCML converter efficiently, but also be used in various hybrid switched-capacitor topologies, as many of them share the same fundamental structure (two switches and a flying capacitor in between).

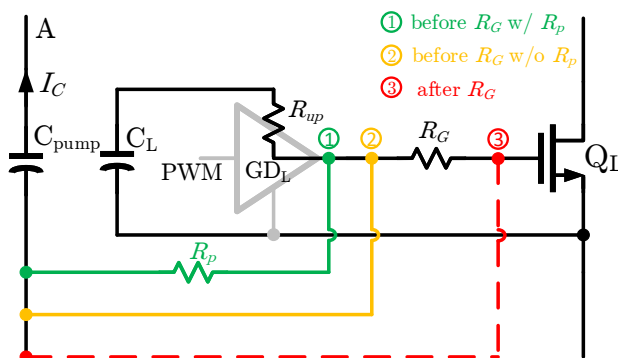


Figure 5.10: Different ways to connect gate-driven charge pump.

## Operating Principle

The schematic drawing of a gate-driven charge pump is illustrated in Fig. 5.9. In order to transfer charge from  $C_L$  to  $C_H$ , one capacitor  $C_{\text{pump}}$  and two low-voltage rating diodes  $D_1$  and  $D_2$  are needed. The positive terminal of  $C_{\text{pump}}$  is connected with  $C_{\text{fly}}$  through diode  $D_2$ . The negative terminal of  $C_{\text{pump}}$  is connected to the gate of switch  $Q_L$ . When  $Q_L$  is off, its gate is pulled low to its source. As a result, the voltage of  $C_{\text{pump}}$  will be charged to the voltage of  $C_{\text{fly}}$  minus the forward drop of  $D_2$ . In the other state, when  $Q_L$  is turned on by pulling its gate high,  $C_{\text{pump}}$  is connected to  $C_L$  through the pull-up transistor inside gate driver  $\text{GD}_L$ . Assuming  $C_L$  has a voltage of 6 V, the voltage at the positive side of  $C_{\text{pump}}$  (Node A) will also be 6 V higher than its value in State 1. Thus,  $D_2$  will be reverse biased, and  $D_1$  will conduct. Capacitor  $C_H$  can, therefore, be charged through the loop highlighted in red in State 2 of Fig. 5.9. The final voltage of  $C_H$  will be

$$V_{C_H} = V_{C_L} - V_{D_1} - V_{D_2}. \quad (5.17)$$

Since  $D_1$  and  $D_2$  only need to block the voltage of capacitor  $C_H$ , small Schottky diodes with low forward drop can be used. Experimental result shows that the forward drop of a 10 V Schottky diode can be as low as 0.2 V, and therefore only 0.4 V of voltage drop will occur during the gate-driven charge pump operation, reflecting good efficiency performance. In addition, the capacitor being charged, like  $C_H$  in this example, does not need to charge another capacitor. It means that the voltage drop will not continue to increase with respect to the number of levels, as in the cascaded bootstrap case. Furthermore, this proposed circuit does not require any pre-charge circuit for start-up. With small-signal analysis, it can be shown that  $\text{GD}_L$  operates as an ac voltage source, such that a few milliamperes current can flow through  $C_{\text{pump}}$  to charge  $C_H$  even if the voltage on  $C_{\text{fly}}$  is zero.

## Effect on the Main Switch

Because both the gate-driven charge pump and the double charge pump utilize the gate terminal of a power switch to transfer energy, care must be taken to ensure that the normal

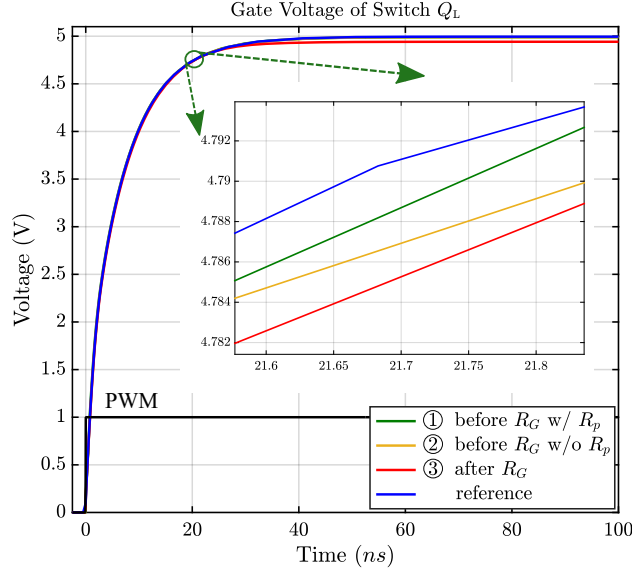


Figure 5.11: Turn-on behavior of EPC 2016C GaN switch with gate-driven charge pump connected (simulation parameters:  $R_{up} = 1 \Omega$ ,  $R_G = R_p = 10 \Omega$ ,  $C_L = C_H = C_{pump} = 1 \mu F$ ,  $V_{C_L} = 5 V$ ).

operation of the corresponding power switch will not be affected. Here, we analyze the turn-on behavior of a power switch which has a gate-driven charge pump connected. The analysis of a double charge pump can be performed in a similar manner.

Typically, a small-valued gate resistor is connected between the GD and the gate terminal of the power switch. As shown in Fig. 5.10, there are three possible ways to connect the gate-driven charge pump. The negative terminal of  $C_{pump}$  can be connected to either the GD side of the gate resistor  $R_G$  or the power switch side of the gate resistor. When connected to the GD side, an additional current limiting resistor  $R_p$  can be added to limit the peak current flowing through  $C_{pump}$ .

To study the turn-on behavior of the GaN switch with the three kinds of gate connections depicted in Fig. 5.10, an LTspice simulation with a detailed model of the EPC2016C GaN switch [88] is performed. The simulated gate-to-source voltages of  $Q_L$  is shown in Fig. 5.11. The blue line is a reference curve representing the normal switching behavior of  $Q_L$  without any gate-driven charge pump connected. It can be seen that the gate-driven charge pump has negligible effect on the switching operation of the power switch, regardless of the type of gate connection. This is mainly because the gate-driven charge pump only needs to transfer a small amount of charge (the gate charge of  $Q_H$ ) in each switching period and the corresponding charging process can be completed quickly. If the gate-driven charge pump needs to transfer more charge (e.g., for a digital isolator or another power switch), the resultant charging current will increase. It is recommended to connect the gate-driven charge pump to the GD side of the gate resistor (before  $R_G$ ). This way, the gate capacitance of  $Q_L$  and  $C_H$  has different charging paths (only share the pull-up resistor  $R_{up}$  inside the

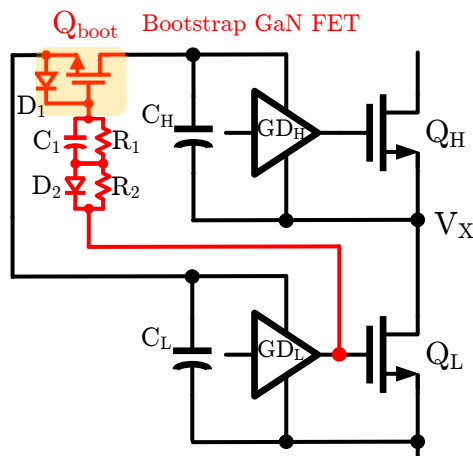


Figure 5.12: Schematic drawing of a synchronous bootstrap circuit.

GD), so that the charging operation of the gate-driven charge pump has minimal effect on the turn-on behavior of the power switch.

Alternatively, instead of using the GD of switch  $Q_L$  to transfer charge, an additional GD / CMOS inverter circuit which has the same ground reference can be added for charge pumping purpose. Although at the expense of one extra component, the gate-driven charge pump can operate without any limitations (e.g., no constraint on duty cycles, no effect on the operation of the main switch). It may also operate at a frequency higher than the switching frequency of the main switches, which could potentially reduce the size of the charge pump capacitor.

## 5.6 Cascaded Synchronous Bootstrap

Another method that can simultaneously overcome the diode drop issue and improve the efficiency is to replace the bootstrap diode with an actively-controlled transistor with lower on-resistance. The synchronous bootstrap technique proposed in [89] provides a simple way to control the GaN-based bootstrap switch. This is achieved by utilizing the gate terminal of the main switch to make the bootstrap eGaN FET switch synchronously, essentially operating as a bootstrap diode with very low voltage drop (limited only by the on-resistance of the bootstrap switch).

The schematic drawing of the synchronous bootstrap circuit is shown in Fig. 5.12. The bootstrap eGaN FET  $Q_{boot}$  [97] is an N-channel device, and has a built-in diode from source to gate. Notice that it has extremely small input capacitance (7 pF) so that no additional GD is needed. In order to make  $Q_{boot}$  switch synchronously with the low-side switch  $Q_L$ , a level-shifting circuit is built on top of the gate of  $Q_L$ . When the gate is pulled low, capacitor  $C_1$  can be charged to approximately the voltage of  $C_L$ . When the gate is pulled high,  $C_1$  will

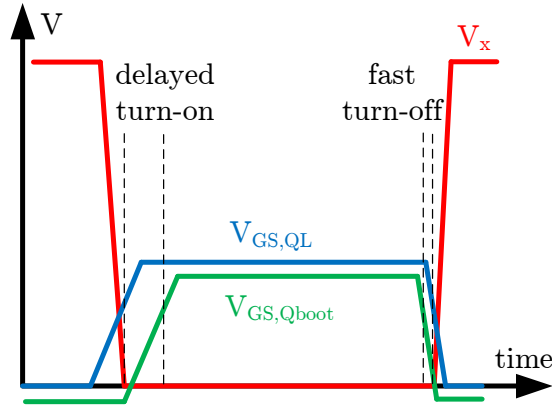


Figure 5.13: Key switching waveform of the synchronous bootstrap circuit.

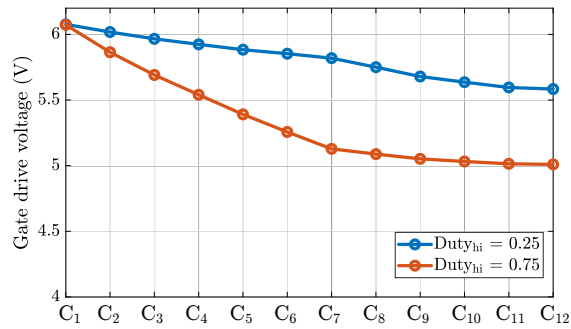


Figure 5.14: Measured cascaded synchronous bootstrap voltages on a seven-level FCML buck converter at no-load condition (switch: EPC2001C,  $f_{sw} = 140$  kHz).

pump the gate voltage of the bootstrap eGaN FET to be higher than its source terminal, so that  $Q_{boot}$  is turned on and  $C_H$  can be charged as in a traditional bootstrap.

Unlike a diode, the bootstrap eGaN FET can conduct bidirectionally. Care must be taken to make sure that  $Q_{boot}$  switches at the right time and current will never flow from  $C_H$  to  $C_L$ . Otherwise,  $Q_L$  may be damaged due to the overcharge of  $C_L$ . As shown in Fig. 5.13,  $Q_{boot}$  should not be switched on until  $Q_L$  is enhanced and its drain-to-source voltage  $V_x$  is discharged to zero. A current limiting resistor  $R_2$  is therefore used to slow down the turn-on speed of the bootstrap eGaN FET. During the turn-off transition, the bootstrap eGaN FET needs to be pulled down quickly by the diode  $D_2$ , before the switch node voltage  $V_x$  starts to ramp up. The resistance of  $R_1$  is selected to be much larger than that of  $R_2$ . This is so that the voltage divider they create can help charge  $C_1$  to  $(V_{CL} - V_{D1})$ , whose voltage is not decreased by the forward drop of  $D_2$ .

Assuming the voltage drop across  $Q_{boot}$  is small, the voltage of  $C_H$  can be charged up to approximately the voltage of  $C_L$ , with little voltage loss. This indicates that the synchronous bootstrap technique can be used to improve the cascaded bootstrap circuit in Fig. 5.1 with

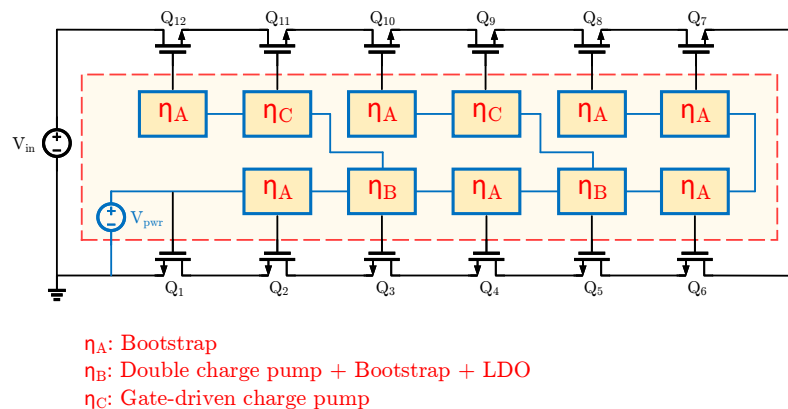


Figure 5.15: Proposed gate drive power supply methods for a seven-level FCML converter.

less cascaded voltage drops and higher gate drive efficiency. This proposed technique is tested on a seven-level FCML dc/dc converter prototype, and the measured bootstrap voltages are plotted in Fig. 5.14 ( $C_1$  corresponds to the bottom switch that connects to the ground,  $C_{12}$  corresponds to the top switch that connects to the input). With 6 V on the ground-referenced power supply, all of the 12 switches have a gate drive voltage greater than 5 V, which is within the accepted operating range. However, as predicted in (5.12), the bootstrapped voltages heavily depend on the duty ratio, and a higher duty ratio on the high-side switches will result in lower voltages due to less bootstrap charging time through the low-side switches. This may impose challenges for ac/dc or dc/ac operations, in which the duty ratio varies in a large interval. In addition, a higher switching frequency will also result in lower bootstrapped voltages, and it is difficult to improve besides further reducing the on-resistance of the bootstrap eGaN FETs. In comparison, at the expense of lower efficiency, these challenges can be easily addressed by the cascaded bootstrap method with LDOs discussed previously, as the input voltage can be increased to supply more power and the LDOs can filter out the voltage variations due to the ac operation. The 1000 unit price of the bootstrap eGaN FET [97] is around \$0.5, as compared to \$0.1 for a Schottky diode with the same voltage rating. For a seven-level FCML design, the cascaded synchronous bootstrap circuit may contribute \$5 extra cost. However, depending on the applications, this extra cost might be acceptable.

## 5.7 Implementation Examples

### FCML Converters

Fig. 5.15 is a simplified schematic showing the power supply method for each switch of a seven-level FCML converter. A complete schematic with detailed power circuit implementations can be found in [98]. To save the number of components, half-bridge GDs are used and every two adjacent switches (e.g.  $Q_1$  and  $Q_2$ ) are driven by one driver. The high-side

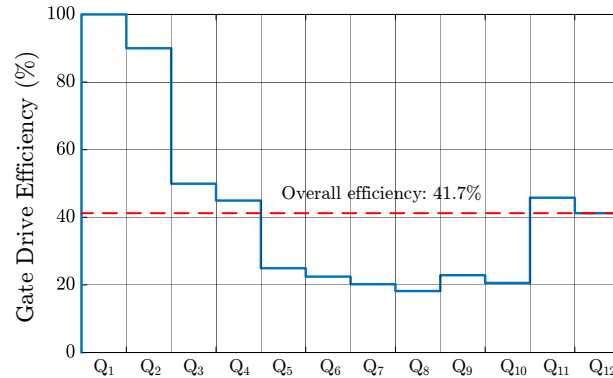


Figure 5.16: Calculated efficiency of the proposed gate drive power supply circuit.

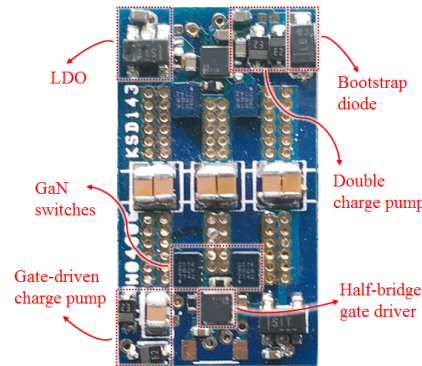


Figure 5.17: Power module (switching cell) design with proposed gate drive power supply circuit.

switch of each half-bridge ( $Q_i$ ,  $i$  is even) is powered by the intrinsic bootstrap diode and no additional circuit is needed. To overcome the accumulated diode drops, the double charge pump method is used twice (at  $Q_3$  and  $Q_5$ ) to boost up the gate drive voltage back to the desired value. Since  $Q_7$  is at the end of the cascade, the overcharge effect at deadtime can help increase the voltage and so double charge pump is not used. The high-side switches ( $Q_9$  and  $Q_{11}$ ) are powered by gate-driven charge pumps. Compared with bootstrap-based methods, this method does not suffer from the cascaded voltage drops and has higher efficiency. The efficiency analysis of the proposed gate drive power supply circuit is covered in [98] and the calculated result for every single switch in the seven-level implementation is shown in Fig. 5.16. As expected, the gate drive power supply efficiency decreases for the switches that are further away from the ground, as double charge pump and cascaded bootstrap methods are needed repeatedly to transfer the power. However, the efficiency increases for the top four switches. This is due to the use of the gate-driven charge pump, which is more efficient



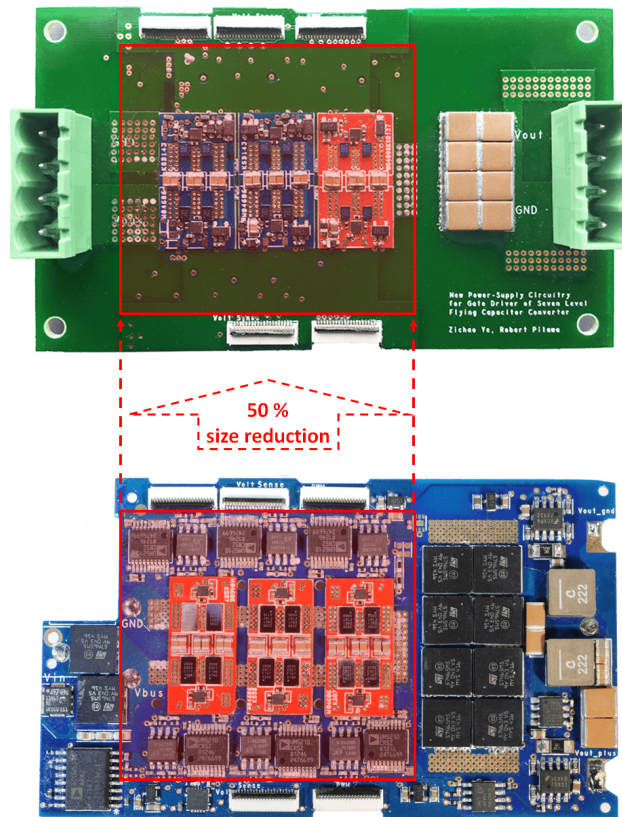


Figure 5.18: Comparison of the hardware prototype with [99].

than the other two methods.

To demonstrate the functionality of the proposed gate drive power circuit, a seven-level FCML converter prototype is built and its implementation details can be found in [98]. The size of prototype's power module (switching cell) is the same as that in [99], which is a state of the art Google Little Box Challenge finalist's design with a power density of  $216 \text{ W/in}^3$ . However, the difference is that the six isolated dc/dc power supplies used in [99] are replaced by the proposed power supply circuit, which is successfully integrated around the GaN switches and GDs as shown in Fig. 5.17. Note that for GaN-based implementations, it is particularly important to minimize the parasitic inductance in the gate drive loop and the main power commutation loop [50], [100], [101]. This modular switching cell design can not only reduce the parasitic loop inductance of FCML converters, but also reduce the fabrication and debugging complexity significantly. The digital isolators are put to the back side of the board (right beneath the switching cells) with no extra space. As a result, approximately 50% converter area reduction is achieved, with the capability to output the same amount of power with equal or better efficiency. Fig. 5.18 compares the photographs of the two prototypes and showcases the size reduction achieved.

Table 5.2: Measured gate drive power supply voltages of the seven-level FCML converter (at  $250 V_{DC}$  to  $100 V_{DC}$ )

C	No $V_{in}$	$I_L = 1A$	$I_L = 2A$	$I_L = 3.5A$	$I_L = 5A$
$C_1$	5.98 V	5.98 V	5.98 V	5.98 V	5.98 V
$C_2$	5.12 V	5.22 V	5.21 V	5.23 V	5.27 V
$C_3$	6.01 V	6.03 V	6.03 V	6.05 V	6.06 V
$C_4$	5.26 V	5.30 V	5.29 V	5.32 V	5.32 V
$C_5$	6.01 V	6.04 V	6.06 V	6.10 V	6.12 V
$C_6$	5.27 V	5.31 V	5.33 V	5.37 V	5.40 V
$C_7$	4.89 V	5.43 V	5.75 V	5.90 V	6.07 V
$C_8$	4.63 V	5.14 V	5.45 V	5.60 V	5.73 V
$C_9$	5.51 V	5.40 V	5.47 V	5.70 V	5.97 V
$C_{10}$	5.24 V	5.12 V	5.15 V	5.40 V	5.65 V
$C_{11}$	5.45 V	5.29 V	5.40 V	5.67 V	5.79 V
$C_{12}$	5.19 V	5.02 V	5.13 V	5.39 V	5.48 V

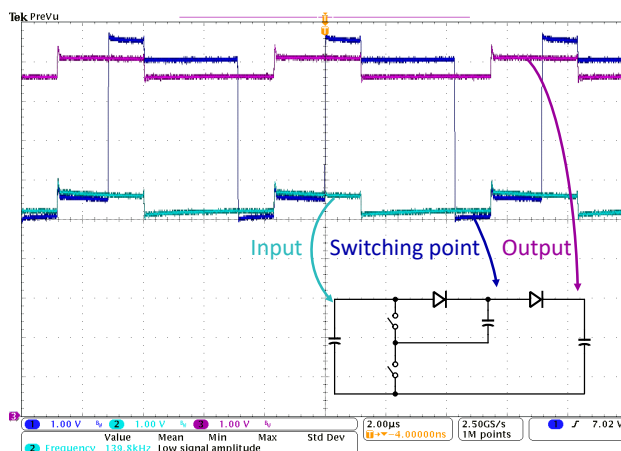


Figure 5.19: Measured double charge pump operation.

The measured gate drive voltage of each switch of the prototype is listed in Table 5.2 under various operating conditions. It can be seen that, the minimum gate drive voltage is greater than 4.5 V at start-up, which is sufficient to fully enhance the switch. When load current increases, the voltage difference between switches quickly reduces, leading to negligible on-resistance difference. The operations of the double charge pump and the gate-driven charge pump are captured and shown in Fig. 5.19 and Fig. 5.20. Table 5.3 compares the performance of the proposed gate drive power circuit with the isolated dc/dc converters used in [99]. The proposed solution takes much less space and has higher efficiency. Additionally, based on the

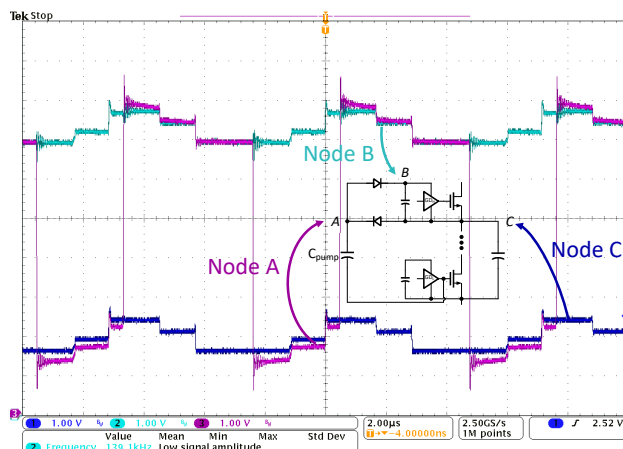


Figure 5.20: Measured gate-driven charge pump operation.

Table 5.3: Comparison with the state of the art solution

	Isolated DC/DC Converter	Proposed Circuit
Parts count	6 ICs, 36 caps and 12 res	11 diodes, 11 caps 5 LDOs and 2 res
Size	$> 6 \times 112 \text{ mm}^2$	$\sim 130 \text{ mm}^2$
Efficiency	$< 27\%$	$\sim 41.7\%$
Cost	$\sim \$19.00$	$\sim \$3.35$

1000-unit price, it is found that the cost of the proposed solution is only 1/6 of the isolated dc/dc solution.

## Hybrid SC Converters

The proposed methods are also applicable to the emerging hybrid and resonant switched-capacitor converters, as many of them share the same fundamental structures as FCML converters. An example gate drive power supply circuit for a 4-to-1 Dickson converter is shown in Fig. 5.21. Switch  $Q_5$  can be powered by  $Q_3$  with the cascaded bootstrap, and the diode forward drop is not a concern because of the overcharge effect at deadtime. Since  $Q_7$  and  $Q_4$  have a flying capacitor  $C_{\text{fly}}$  connected in between, a gate-driven charge pump can be used to power  $Q_7$ . If more switches and flying capacitors are added to the string for a higher conversion ratio, this method can be used repeatedly without issues.

A 4-to-1 series-parallel converter with its gate drive circuit is shown in Fig. 5.22. The three pairs of series and parallel switches ( $Q_{s1}/Q_{p1}$ ,  $Q_{s2}/Q_{p2}$ ,  $Q_{s3}/Q_{p3}$ ) can be easily driven by

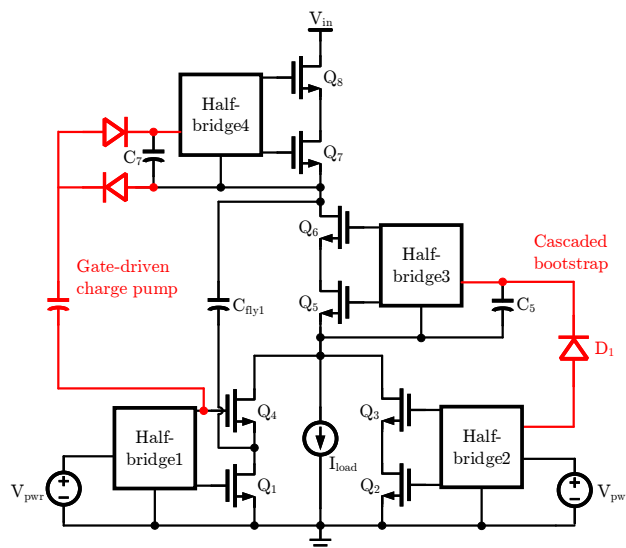


Figure 5.21: An example gate drive circuit for a 4-to-1 Dickson converter.

ground-referenced half-bridge drivers. Following  $Q_{s1}$ , there are four switches ( $Q_{p4}$ – $Q_{p6}$ ,  $Q_{s4}$ ) that need to be powered by the cascaded bootstrap. Considering the large diode drop due to the high transferred power through the bootstrap diode, a double charge pump is used to guarantee sufficient voltage for all following switches. Note that the discussion above focuses on providing floating gate drive power only. For signal level-shifting, a high-side driver can be used instead of a half-bridge driver, at the expense of more ICs. In either case, these power supply methods remain valid.

## Gate Driver IC Definition

The proposed cascaded bootstrap with LDO and the gate-driven charge pump could potentially be integrated with the GD itself. Fig. 5.23 shows the block diagram of a single isolated GD chip with a built-in LDO and two low-voltage diodes. A separate inverter buffer that has the same ground reference as the main GD is also added for dedicated gate-driven charge pump operation. As shown in Fig. 5.24, a four-level FCML converter can be driven by this standalone GD chip and a couple of decoupling capacitors and bootstrap diodes, without the need of any additional ICs. The bottom four GDs are powered through a cascaded bootstrap. Thanks to the built-in LDO, all GDs can have the same gate drive voltage. While the cascaded bootstrap can provide power to the top two GDs as well, gate-driven charge pumps can provide better gate drive power efficiency. With the built-in diodes and inverter buffer, GD\_6 can be powered by GD\_2, with one charge pump capacitor  $C_{pump1}$  only. Similarly, GD\_5 can be powered GD\_3.

Furthermore, this proposed GD chip can also be used for other hybrid SC converters.

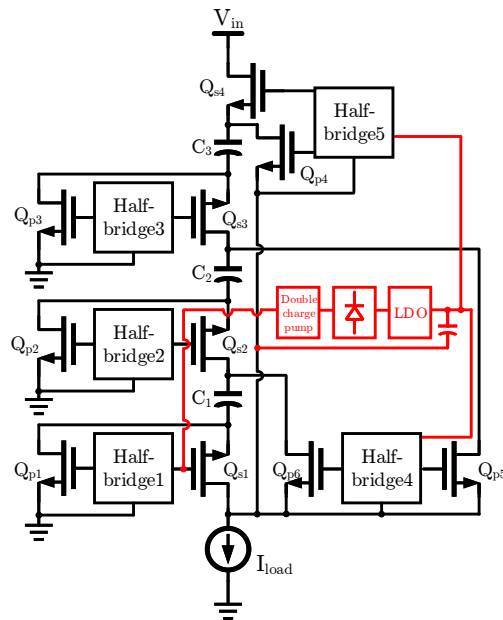


Figure 5.22: An example gate drive circuit for a 4-to-1 series-parallel converter.

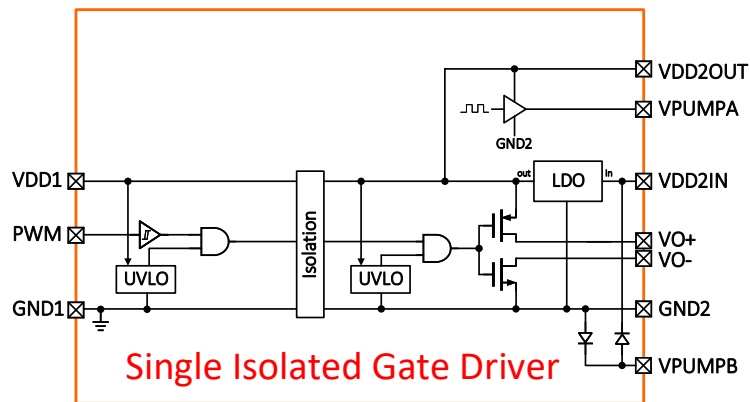


Figure 5.23: Block diagram of a proposed gate driver IC with built-in LDO and self-oscillatory inverter for cascaded bootstrap and gate-driven charge pump operations.

Through increased integration, the gate drive complexity and cost are reduced, and the power density and the reliability are improved, taking these emerging topologies a step closer to broader industry adoption.

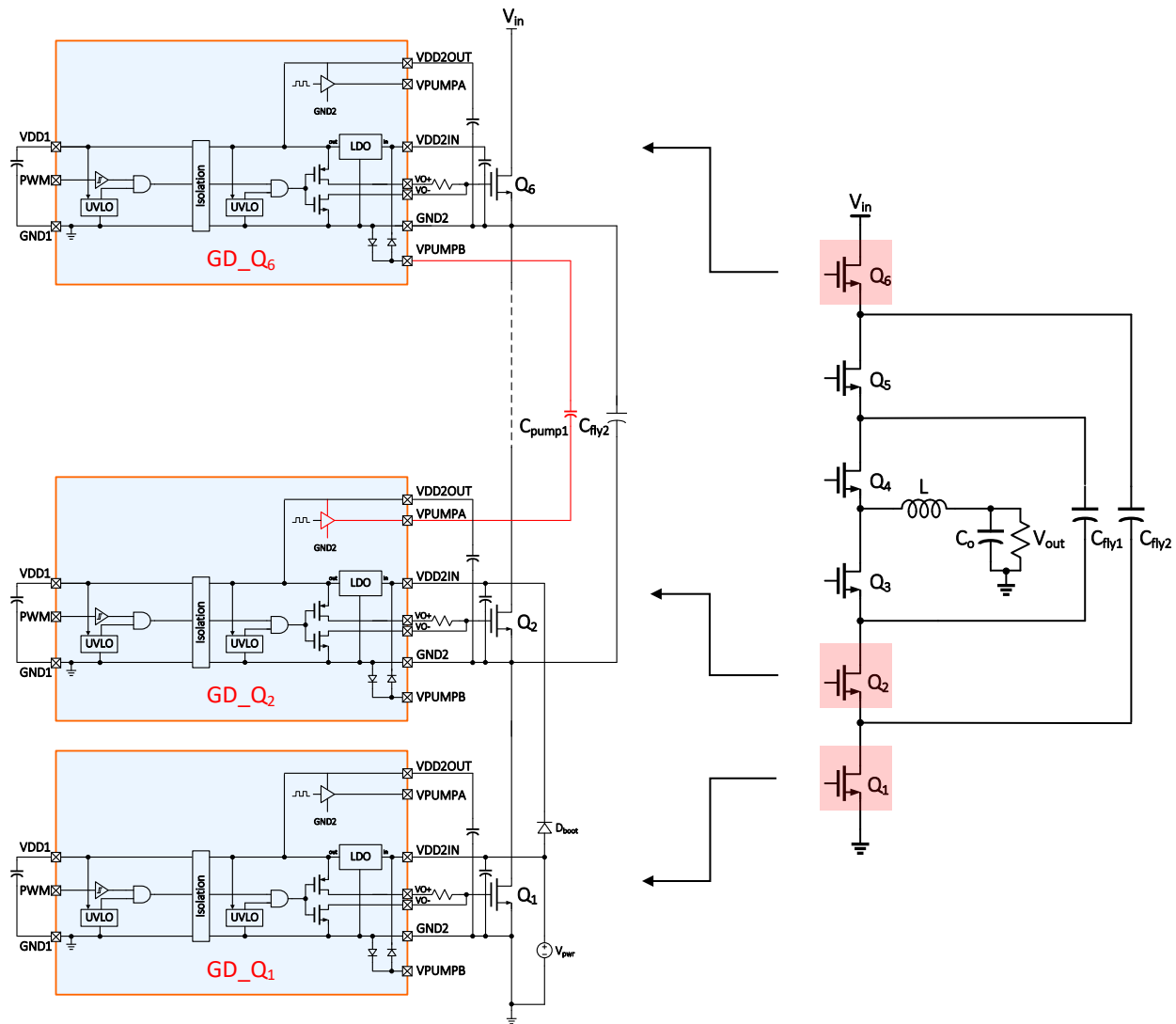


Figure 5.24: Powering a four-level FCML converter with the proposed gate driver IC.

## 5.8 Design Considerations

The proposed methods can potentially be applied to topologies beyond FCML and hybrid SC converters. To highlight their characteristics, the five methods are compared and summarized in Table 5.4. The first four focus on overcoming the forward voltage drops in the cascaded bootstrap operation, and the last method replaces bootstrap with a charge-pump based operation. The overcharge effect at deadtime can help compensate the forward drop of the bootstrap diode without the need for any additional circuits. However, it only applies to GaN switches and its effect depends on a number of factors. Usually, it can be safely used

Table 5.4: Key characteristics of the five proposed methods

Method	Basic structure	Constraints	Component counts	Efficiency	Notes
Bootstrap at deadtime	series connected switches	high	low	high	For GaN only. Operation depends on various factors, use with caution.
Cascaded bootstrap with LDOs	series connected switches	very low	low	depends on number of cascade	Low complexity, high applicability. Can power a large string of switches. Need high-voltage power supply.
Double charge pump	series connected switches	low	medium	low	Can boost the bootstrap voltage in the cascade at the cost of a relatively low efficiency.
Synchronous bootstrap	series connected switches	medium	medium	very high	Greatly reduced voltage drop compared to diode, but can still be a concern at extreme duty ratio and other cases.
Gate-driven charge pump	two switches with a flying capacitor in between	low	low	high	A preferred method to power the high-side switches of FCML converters and many hybrid SC converters.

to the last 1–2 switches in the cascade if their worst case voltages at no-load condition are already sufficient to enhance the switches. The overcharge effect at higher load can be used to further reduce the on-resistance. In comparison, the cascaded bootstrap method with LDOs has minimal constraints. If a high-voltage power supply is available, it can be used as a standalone method to drive any FCML converters and ladder-type SC converters, which have a large number of series-connected switches. Another method to get a sufficiently high bootstrap voltage is the double charge pump, which can be deployed anywhere in the converter. However, its efficiency ( $\sim 50\%$ ) is relatively low compared to that of other methods and so should be used with caution. Thanks to the low on-resistance bootstrap eGaN FET, the synchronous bootstrap method can achieve very high efficiency. Nevertheless, the forward voltage drops can still be a problem when the duty ratio is extreme and there are many switches in the string. Instead of powering a large string, if two switches have a flying capacitor in between, a gate-driven charge pump can be a good option. This simple and low-cost charge pump can power the high-side switches of FCML converters and Dickson converters with an efficiency higher than the bootstrap-based methods.

## 5.9 Chapter Summary

This chapter presents five bootstrap and charge pump based methods for powering the floating GDs of FCML converters and hybrid SC converters with detailed analytical discussions and experimental verifications. Depending on the converter topology, one or more of the proposed methods can be selected to build a customized power supply circuit and transfer ground-referenced power to the large number of floating GDs in an effective and efficient manner. All these methods have simple structures and can be implemented with a few basic circuit components, such as diodes, capacitors, and LDOs. Various FCML converter prototypes are successfully built and tested to verify the functionality of the proposed methods.

Experimental results indicate that the customized power supply circuit is more efficient and compact than the widely used isolated dc/dc power supply chips, with significantly reduced cost. The pros and cons of the methods are also discussed and tabulated so that they can be properly applied to more topologies with floating switches.



## Chapter 6

# Cascaded Resonant Switched-Capacitor Converter

Resonant switched-capacitor (ReSC) converters have efficient utilization of both active and passive components, and hold the potential to achieve higher efficiency and higher power density than conventional SC and magnetic-based converters. This chapter presents a new ReSC converter topology, comprising two cascaded 2-to-1 ReSC converters, to address high-conversion-ratio applications. The proposed cascaded resonant converter has a simple structure and operating principle, and can achieve one of the best overall performance among popular ReSC topologies. A 36-60 V input, 4:1 fixed-ratio bus converter prototype for data center application is designed and constructed. We present detailed design guidelines and discussions addressing practical challenges, such as component variations and interstage decoupling requirements. With 48 V input and operating at the typical zero-current switching (ZCS) mode of ReSC converters, the prototype achieves a peak efficiency of 98.85% (including gate drive loss) and a power density of 2500 W/in<sup>3</sup>, both of which are significantly higher than the-state-of-the-art. Furthermore, we propose a zero-voltage switching (ZVS) method to improve light-load efficiency. Through this control method, which greatly reduces the output capacitance loss, the prototype can maintain an efficiency above 97% starting from 3% of the rated load, with a peak of 99.0%.

### 6.1 Background and Motivation

In previous chapters, the fundamental limits and design techniques of hybrid and resonant SC converters are discussed. In this and the next two chapters, we focus on developing high-performance topologies and presenting cutting-edge hardware implementations. While the developed topologies are generic in nature, data center power delivery is selected as the core application we strive to work on, as it has become one of the most impactful fields which urgently needs innovative power electronics solutions. In modern data centers, there are various architectures to convert the 48 V bus voltage down to 1–2 V for digital

circuits. For the classic two-stage approach, ReSC converters can be used as intermediate bus converters to provide high-efficiency fixed-ratio conversion. This chapter discusses a high-performance 48-to-12 V solution based on a new ReSC topology, and Chapter 7 extends the ReSC discussion to higher conversion ratios. For the emerging single-stage approach, regulated hybrid SC converters with a merged buck stage can be used, and this approach is detailed in Chapter 8.

In this chapter, we focus on 4-to-1 fixed-ratio ReSC converters. As the name implies, ReSC converters operate at the resonant frequency of the flying capacitor and the augmenting inductor. This frequency is known as the minimum frequency (for inductor at output configuration) that allows full soft-charging operation. Since inductor volume is primarily dependent on the current rating, ReSC converters with minimum added inductance can be specifically suitable for low-voltage high-current applications like the commonly used 48-to-12 V conversion in data centers [23], [39], [102], where extreme efficiency and power density are critical, and voltage regulation is not required. As discussed in Section 3.3, with a given efficiency target, the capacitor and inductor values can be selected to achieve a minimal passive component volume, which can be significantly smaller than that of a conventional SC or a magnetic-based converter. Moreover, thanks to the resonant operation, zero-current switching (ZCS) is naturally achieved, and the switching loss caused by the simultaneous existence of switch voltage and current during switching transitions is minimized.

To further explore the potential of ReSC converters, we propose an interleaving-based method to cascade 2-to-1 ReSC converters for higher conversion ratios, in an efficient and compact manner. The proposed converter, named the cascaded resonant converter, inherits the simple structure and operating principle of its fundamental 2-to-1 element, and has the potential to outperform Dickson-based and FCML-based ReSC converters. In addition to the soft-charging and ZCS capabilities, we also demonstrate that zero-voltage switching (ZVS) operation is achievable, which can help eliminate the transistor output capacitance loss and further increase the efficiency.

A 36-60 V input, 4:1 fixed-ratio (unregulated), non-isolated bus converter prototype is designed and implemented based on the proposed topology. Depending on the deadtime and phase shift, the converter can operate in either ZCS or ZVS mode. Experimental results indicate that the ZVS operation can yield a higher light-load performance (efficiency remains above 97% starting from 3% of the rated load) and a higher peak efficiency (ZVS: 99.0%, ZCS: 98.85%, gate drive loss included). The prototype has a total box volume of 0.28 in<sup>3</sup> (4.586 cm<sup>3</sup>), and has been tested with up to 60 A output current (900 W at 15 V output), leading to an ultra-high power density of 3100 W/in<sup>3</sup> (190 kW/L).

The remainder of this chapter is organized as follows. Section 6.2 gives a brief overview of the data center power delivery architecture. Section 6.3 discusses the basic (ZCS) operation of the proposed cascaded resonant converter, presents an interleaving technique to reduce the interstage decoupling requirement, and compares this topology with other ReSC converters. Section 6.4 provides hardware design guidelines and experimental results. Section 6.5 presents a ZVS control technique to further improve the performance of the converter, followed by a loss analysis and a comparison with the-state-of-the-arts. Furthermore, Section

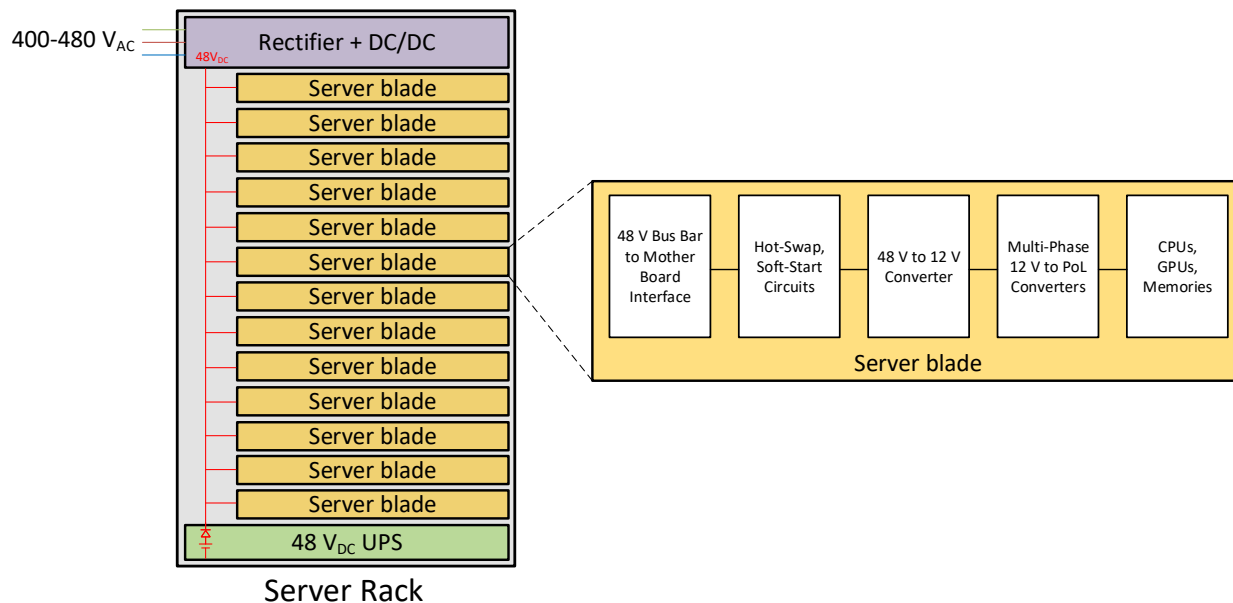


Figure 6.1: An example data center power delivery system from line to point-of-loads.

6.6 discusses the benefits of cascading and interleaving ReSC converters and generalizes the concept to other topologies.

## 6.2 Overview of Data Center Power Delivery Architecture

### 48 V Architecture

In [103], it is reported that in 2014, data centers used more than 1.8% of all electricity in the U.S. With emerging applications like data analytics, machine learning, artificial intelligence, and other high-performance computing use cases, the power consumption of data centers maintains a very fast growth rate. Therefore, improving the energy efficiency of data centers can have significant positive impacts, both economically and environmentally. In addition to efficiency, the increasing load current and power requirements on motherboards also pose great challenges for power integrity, thermal performance and reliability, and power density and scalability.

Because of the high bus bar and cabling loss and other limitations in the conventional 12 V distribution system, the industry has begun the transition to a 48 V distribution system. Compared to the 12 V architecture, the new 48 V architecture can reduce the distribution loss in the bus bars and interface components by up to 16x. Less copper planes and VIAs are needed due to the lower current flow at 48 V. Moreover, the 48 V bus also enables the

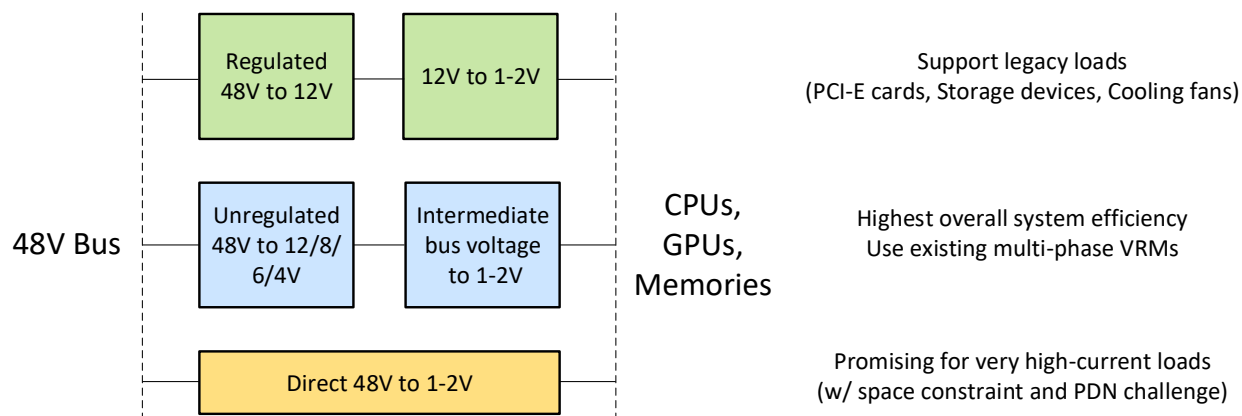


Figure 6.2: Comparison of different approaches to convert 48 V down to 1–2 V.

usage of in-rack back-up batteries during power outage, with better dynamic response and reliability. Since 48 V (48 V nominal, with a range of 36–60 V) is a safe voltage level for human contact during maintenance or accidental contact, galvanic isolation is not required (though the isolation function is typically still provided by the front-end converters) [104], and innovative non-isolated topologies with very high-performance can be adopted for step-down conversions from 48 V.

An example data center power delivery system with a 48 V dc bus is illustrated in Fig. 6.1. The three-phase line voltage is first stepped down to 48 V<sub>dc</sub> through an in-rack rectifier. To convert the 48 V down to 1–2 V for digital loads, a two-stage intermediate bus architecture (IBA) can be used [105]. In contrast to other architectures, the majority of the power conversion in IBA is performed on the motherboard, from 48 V backplane to 12 V bus using a bus converter, and then down to 1 V using multi-phase buck converters [105], [106].

## 48 V to Point-of-Load Conversion

A major challenge in such systems is the conversion from the 48 V bus to the extreme low voltage and high current operating levels of CPUs and GPUs. Various approaches have been proposed to address such a high step-down conversion ratio, and the three major ones are illustrated in Fig. 6.2.

The first and the most straightforward approach is using regulated 48-to-12 V bus converters, followed by multi-phase 12 V to point-of-load (PoL) voltage regulation modules (VRMs). The regulated 48-to-12 V converters enable the quick adaptation of 12 V based work loads to the 48 V system, including legacy 12 V motherboards and other commodities such as PCI-E cards, hard drives and cooling fans. Compared to the 12 V loads, the majority of the power is stepped down again to 1–2 V for CPUs, GPUs, and other power-hungry digital circuits. Since the voltage regulation is typically provided by downstream converters,

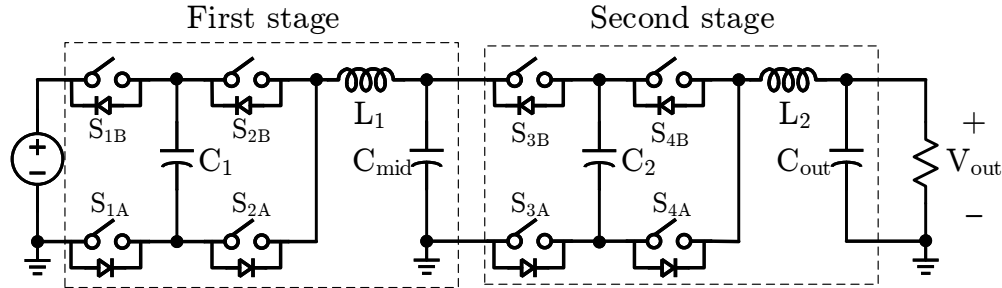


Figure 6.3: Schematic drawing of a cascaded resonant converter.

either in the 12V VRMs, or even on-chip using a fully integrated voltage regulation (FIVR) converter [107], the 12 V intermediate bus voltage does not need to be tightly regulated.

With the relaxed regulation requirement, innovative fixed-ratio topologies can be used to dramatically improve the performance of 48-to-12 V conversion. In this chapter, we propose a 4-to-1 cascaded resonant SC converter, which can have significantly higher efficiency and power density than other commonly used solutions.

Compared to a 12 V bus voltage, recent research [104], [108] suggests that a lower intermediate bus voltage (e.g., 6 V) may provide higher overall efficiency, once both the intermediate bus converters and the second-stage VRMs are considered. Moreover, with the reduced voltage stress at the second stage, the VRMs can have smaller inductors and therefore be placed closer to the input power pins of the load. This can reduce the power loss and improve the dynamic response associated with the power distribution network (PDN), which is particularly important for the application-specific integrated circuits (ASICs) with very high current demand. In Chapter 7, we propose new multi-resonant SC topologies with high conversion ratios for this improved two-stage approach.

In addition to two-stage approaches, a single-stage, direct 48 V to PoL approach has also been explored [109]–[113]. With well-defined specification of the targeted loads, a dedicated single-stage design may provide better overall efficiency, power density, and reduced system cost. The power stamp alliance (PSA) has worked on defining a standard product footprint and functions that provide a standard modular board-mounted 48V-to-PoL solution [111]. In Chapter 8, we present a hybrid SC based solution which has achieved promising performance according to the PSA specifications.

## 6.3 Cascaded Resonant Converter

### Operating Principle

The schematic drawing of the cascaded resonant converter is shown in Fig. 6.3, which can be seen as a cascade of two 2-to-1 SC structures with an inductor at each output. Although the operating principle is completely different, this topology can be viewed as two cascaded three-

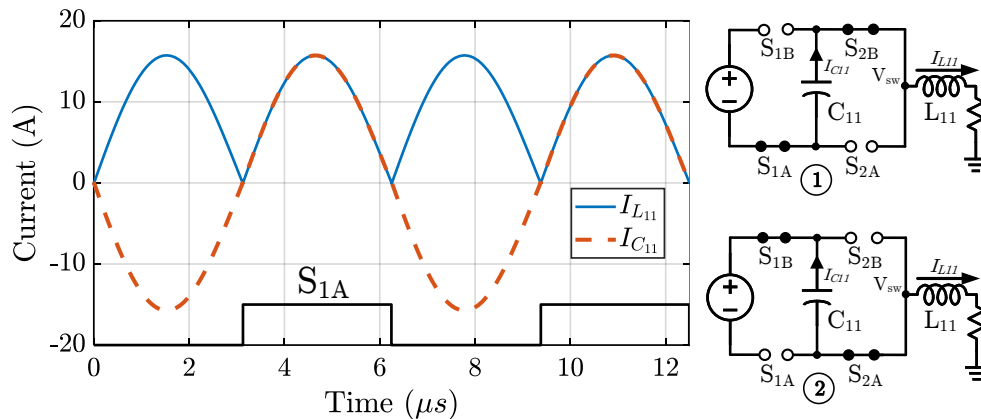


Figure 6.4: Simulated inductor/capacitor current at first stage.

level buck converters. Alternatively, the topology can also be viewed as an augmented 4-to-1 doubler SC converter [7], with two inductors inserted to achieve soft-charging operation. To achieve ultra efficient and compact fixed ratio (no regulation capability) resonant operation, all switches have a fixed duty ratio of 50%, and every two adjacent switches have a phase shift of  $180^\circ$ . The nominal switching frequency is the resonant frequency of the flying capacitor and the inductor ( $f_{sw} = \frac{1}{2\pi\sqrt{L_1C_1}} = \frac{1}{2\pi\sqrt{L_2C_2}}$ ), as it is the minimum frequency with low conduction loss for soft-charging hybrid SC converters [19]. As shown in Fig. 6.4, the flying capacitors are resonantly charged in one state and discharged in the other state, resulting in no charge-redistribution loss. Additionally, since the inductor current takes the shape of a rectified sine wave, the current reaches zero at moments of phase transitions and ZCS is achieved when switching at this frequency.

However, converters operated in this way require the point of coupling between the cascaded converters to present a stiff voltage, thus enforcing  $C_{mid} \gg C_1 \& C_2$ , so that  $C_{mid}$  does not take part in the resonant operation. Consequently, the volume of  $C_{mid}$  could dominate the size of the capacitors. As shown in Fig. 6.5, to avoid such penalty, we propose to introduce a second cascaded resonant converter, connected in parallel with the first converter at the input, middle and output point, and operated  $180^\circ$  out of phase. It can be seen from Fig. 6.6 that, with this interleaving operation, the combined input current of the second stage also becomes a rectified sine wave, which closely matches the inductor current of the first stage. Thus, an equal amount of charge is delivered and removed from  $C_{mid}$  at all times, ensuring a stiff midpoint voltage without requiring a large capacitor. The proposed control technique and interleaved topology thus enable a significant reduction of  $C_{mid}$  while still ensuring correct resonant operation. If multi-phase interleaving is used for higher load current, one should make sure that the number of phases is an even number such that every pair of phases can be  $180^\circ$  out of phase to cancel out  $C_{mid}$ . Moreover, since the first stage and the second stage have the same operating principle, the total input source current also becomes a continuous rectified sinusoidal current owing to the two-phase interleaving opera-

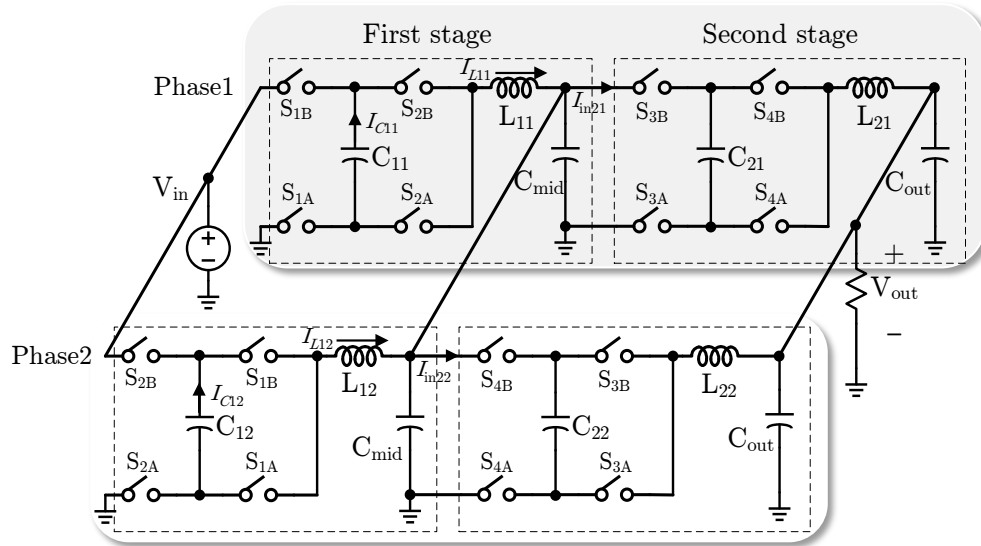


Figure 6.5: Schematic drawing of a two-phase interleaved cascaded resonant converter.

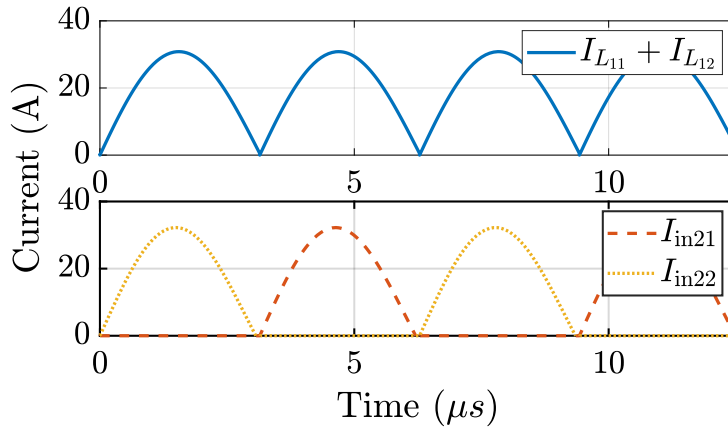


Figure 6.6: Minimize  $C_{mid}$  with interleaved design.

tion. This non-pulsating input current can greatly reduce the input decoupling requirement and simplify the EMI filter design.

### Topology Comparison

To illustrate the theoretical performance of the cascaded resonant converter, we replot Fig. 3.17 in Fig. 6.7. Generally speaking, switch stress reflects power loss and passive component volume reflects power density. For the same switching frequency, a lower total switch stress indicates a potentially lower conduction loss, lower switching loss, and smaller size. Thus, a converter with lower switch stress can operate at a higher switching frequency for

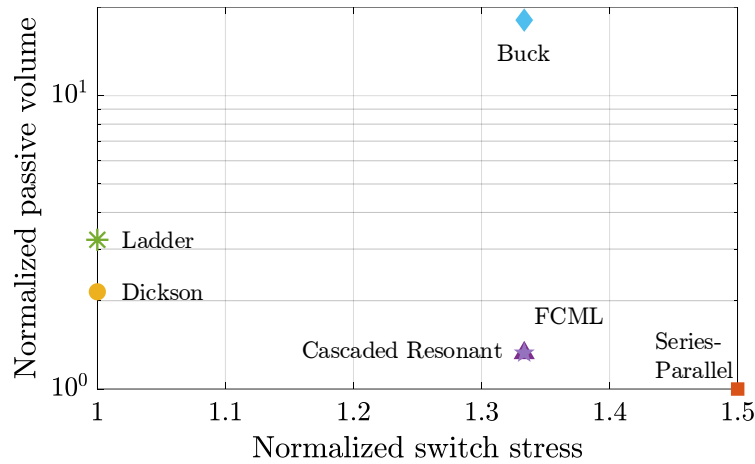


Figure 6.7: Comparison of various ReSC converters at a conversion ratio of 4-to-1.

the same amount of loss, which results in reduction of passive component volume. Therefore, comparing both metrics can be indicative of the overall performance potential of the converter.

Fig. 6.7 shows the calculated metrics of various topologies for delivering the same amount of power, at a conversion ratio of 4-to-1. The metrics are normalized with respect to the topology that has the lowest rating (i.e., the best performance). It is shown that all ReSC converters out-perform the buck converter by a wide margin, assuming the energy density of capacitors is 100 times higher than that of inductors. Among the ReSC converters, the split-phase Dickson converter with a single inductor at the output [21] has the best switch utilization, but has relatively large passive volume. On the other hand, the series-parallel converter with a single inductor at the output [41] has the best passive component utilization, but has high switch stress. In comparison, the proposed cascaded resonant converter has a good balance of active and passive component utilization, indicating the potential to achieve high efficiency and high power density simultaneously.

It should be noted that practical converter designs have more considerations regarding the circuit complexity and the actual performance of different topologies can be different than what is plotted here. For instance, as ReSC converters have a large number of floating switches, the switch quantity and the complexity of gate drive circuit is also an important design knob that affects the overall performance. In addition, the soft-switching ability and the characteristic of the input source current can affect EMI, and the number of passive components and the associated parasitic resistance can contribute additional conduction loss. After a comprehensive analysis of the theoretical performance, the available components on the market and the ease of gate drive circuit design/layout, the cascaded resonant topology is found to be the optimum ReSC solution for data center intermediate bus converters.



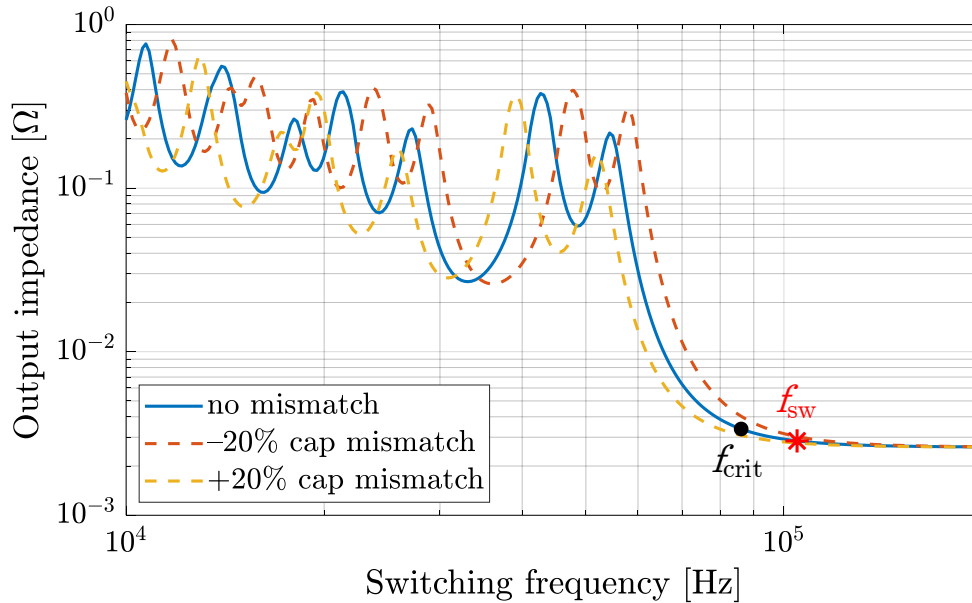


Figure 6.8: Output impedance plot for cascaded resonant converter.

## 6.4 Design Guidelines and Experimental Results

### Component Tolerance

In practical implementations, both the flying capacitor and the resonant inductor can deviate from their nominal values due to various reasons [114], and make it difficult to guarantee perfect resonant operation. To study the effects of component variations on the cascaded resonant converter, its output impedance with respect to the tolerance of the flying capacitor (nominal capacitance and 20% mismatch) is simulated in LTspice with a frequency sweep from 10 kHz to 200 kHz, and the result is plotted in Fig. 6.8. As expected, at the resonant frequency  $f_{\text{crit}}$ , the output impedance increases if the actual flying capacitors are smaller than their nominal values. On the other hand, when operating in the FSL region, the output impedance is insensitive to the capacitor variance. Therefore, for better component tolerance, it is worthwhile to trade off the ZCS operation at  $f_{\text{crit}}$ , and to operate the cascaded resonant converter at a slightly higher switching frequency. Moreover, for the high-current IBA application, the slight reduction of output impedance (and therefore conduction loss) in the FSL region may cancel out the increase in switching loss, and lead to a higher overall efficiency.

Thanks to this mitigation method, the cascaded resonant converter can have relatively good component tolerance. Thus, high-energy-density (which is comparable to electrolytic) low-dissipation-factor (typically less than 5%) Class-II ceramic capacitor can be used, despite of its dc-bias and temperature varying characteristics. By contrast, for those ReSC converters with the “inductor in series with capacitor” configuration, it is often necessary to use high

precision Class-I ceramic capacitors for perfect resonant operation, at the expense of higher cost and lower energy density.

## Loss Calculation

To better understand the loss distribution of the cascaded resonant converter, here we provide the calculation of the main sources of the losses. As will be shown in the experimental results, the conduction loss dominates in this kind of low-voltage high-current application. The total conduction loss can be calculated with  $P_{\text{cond}} = P_{\text{cond},1} + P_{\text{cond},2}$ , where  $P_{\text{cond},1}$  is the conduction loss of the first stage and  $P_{\text{cond},2}$  is the conduction loss of the second stage. At stage  $i$  ( $i \in \{1, 2\}$ ),  $P_{\text{cond},i} = \sum_{j=1}^2 I_{\text{rms},i}^2 R_i$ , where  $j$  is the number of phases and  $R_i$  is the sum of the series resistance in the current path, including switch on-resistance, capacitor ESR, inductor DCR and PCB trace resistance. The rms current can be alternatively expressed in terms of the average output current and the rms-to-average ratio:  $I_{\text{rms},i} = K_i I_{\text{out},i}$ . For perfect resonant operation where the inductor current is a rectified sine wave,  $K_i = 1.11$ . For higher switching frequency,  $K_i$  starts to decrease and approach 1. Its exact value can be determined from circuit simulation. Similarly, the converter switching loss needs to be calculated for every stage and every phase individually:  $P_{\text{sw}} = \sum_{i=1}^2 P_{\text{sw},i}$ , and  $P_{\text{sw},i} = \sum_{j=1}^2 (P_{\text{coss},i} + P_{\text{overlap},i})$ . The switch output capacitance loss  $P_{\text{coss},i}$  is given by  $P_{\text{coss},i} = n \cdot \frac{1}{2} f_{\text{sw}} C_{\text{oss},i} V_{\text{ds},i}^2$ , where  $n$  is the number of switches (4 in this case),  $C_{\text{oss},i}$  is the switch output capacitance and  $V_{\text{ds},i}$  is the voltage across the switch before it turns on. Note that this portion of the loss can be eliminated by the ZVS control technique that is introduced in the next section. The switch overlap loss can be approximately given by  $P_{\text{overlap},i} = n \cdot \frac{1}{2} V_{\text{off}} I_{\text{on}} (t_{\text{turn-on}} + t_{\text{turn-off}})$ , where  $V_{\text{off}}$  is the off-state voltage,  $I_{\text{on}}$  is the on-state current, and  $t_{\text{turn-on}}$  and  $t_{\text{turn-off}}$  are the duration for which the voltage and current overlap when the switch turns on and turns off, respectively. When operating at the resonant frequency, the converter is in ZCS mode and this overlap loss is nonexistent. However, as discussed above, the converter is recommended to operate slightly faster for lower conduction loss and better tolerance to component variations. This way, the converter has non-zero turn-off current and associated turn-off overlap loss, whereas the turn-on current is still close to zero with negligible turn-on loss.

## Hardware Design

The added inductor offers an additional degree of freedom in the design space. The values of capacitors and inductors should be designed to reach a desired resonant frequency, while minimizing the total passive component volume. The lower bound of the capacitance needed is set by the allowed capacitor voltage ripple and temperature rise. Although the hybrid resonant operation allows larger RMS current through capacitors than regular SC converters without efficiency penalty, the associated capacitor voltage ripple ( $\Delta V_{C_{\text{fly}}} = \frac{I_{\text{out}}}{2f_{\text{sw}}C_{\text{fly}}}$ ) will be present across the switches and must be considered when selecting switches. In addition, the temperature rise of a capacitor is also a function of RMS current, and should ideally be kept low (e.g., 10 °C) for reliability purposes. In terms of inductor selection, the saturation

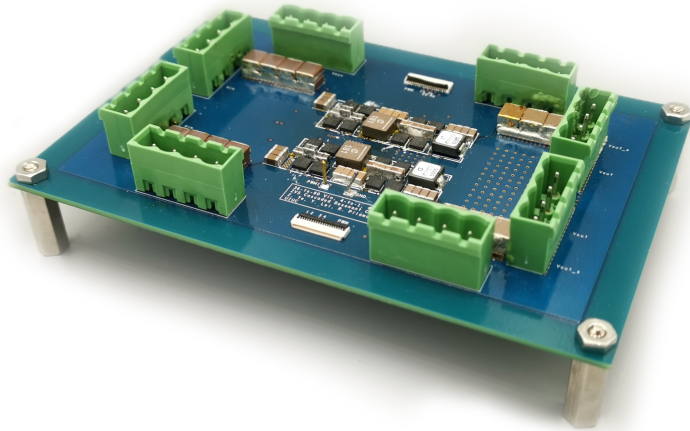


Figure 6.9: Photograph of the hardware prototype (two-phase interleaved).

Table 6.1: Main component listing of the cascaded resonant converter

Component	Part number	Parameters
1 <sup>st</sup> stage MOSFET	Infineon BSZ025N04LS	40 V, 2.5 m $\Omega$
1 <sup>st</sup> stage flying capacitor ( $C_1$ )	TDK C2012X5R1V226M125AC	35 V, 22 $\mu\text{F}^* \times 12$
1 <sup>st</sup> stage inductor ( $L_1$ )	Coilcraft XAL6030-181MEL	180 nH, 39 A $I_{\text{sat}}$
1 <sup>st</sup> stage output capacitor ( $C_{\text{mid}}$ )	TDK C3216X5R1H106K160AB	50 V, 10 $\mu\text{F}^* \times 19$
2 <sup>nd</sup> stage MOSFET	Infineon BSZ013NE2LS5I	25 V, 1.3 m $\Omega$
2 <sup>nd</sup> stage flying capacitor ( $C_2$ )	TDK CGA4J1X5R1C106K125AC	16 V, 10 $\mu\text{F}^* \times 16$
2 <sup>nd</sup> stage inductor ( $L_2$ )	Coilcraft SLC7530S-500ML	50 nH, 50 A $I_{\text{sat}}$
2 <sup>nd</sup> stage output capacitor ( $C_{\text{out}}$ )	TDK C3216X5R1E476M160AC	25 V, 47 $\mu\text{F}^* \times 8$
Gate driver	Texas Instruments LM5113	100 V half-bridge
Bootstrap diode	Infineon BAT6402VH6327XTSA1	40 V Schottky

\* The capacitance listed here is the nominal value before dc derating.

current ( $I_{\text{sat}}$ ) will likely become the most constraining factor, because of the high peak current ( $\frac{\pi}{2} I_{\text{out}}$ ) in resonant operation. Given constrained inductor height and volume, it is recommended to use the highest inductance that can satisfy the  $I_{\text{sat}}$  requirement. Besides optimizing the passive component volume, the ESR of the capacitors and the DCR of the inductors are also important design metrics that can significantly affect the efficiency.

Owing to the unique structure of the cascaded resonant topology, each switch only needs to block half of the input voltage (30 V for the 1<sup>st</sup> stage and 15 V for the 2<sup>nd</sup> stage) plus the

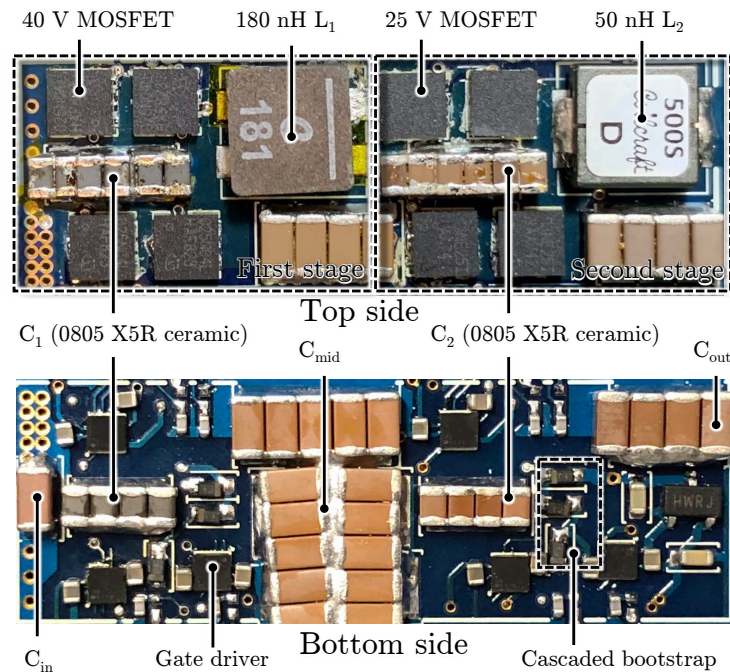
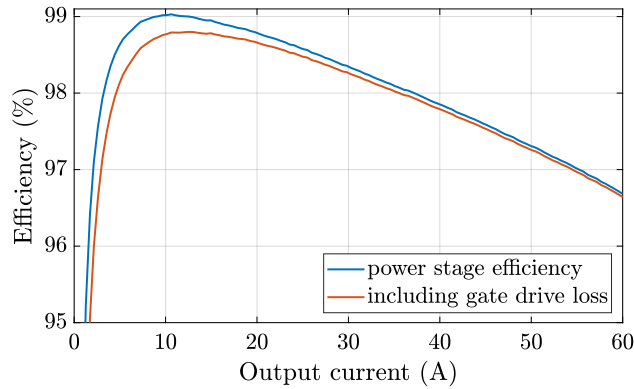
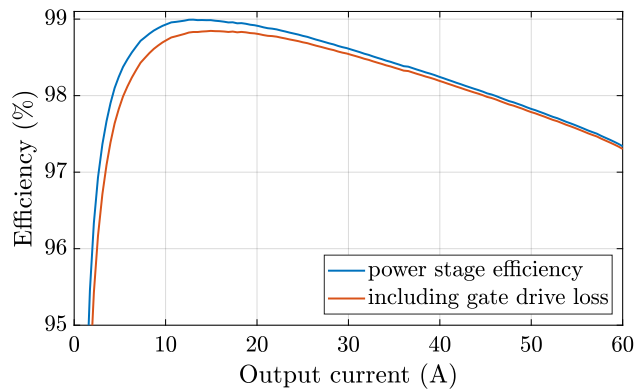


Figure 6.10: Annotated photograph of the converter (one phase).  
 Dimensions:  $1.38 \times 0.46 \times 0.22$  inch ( $3.5 \times 1.17 \times 0.56$  cm).

capacitor voltage ripple, allowing the use of low voltage MOSFETs (40 V and 25 V). Note that at this voltage rating, eGaN FETs generally do not outperform silicon MOSFET significantly (with slightly lower input/output capacitance and similar on-resistance/footprint), but have a much higher cost [115], [116]. Since the designed resonant frequency is relatively low ( $\sim 100$  kHz), the switching loss is not a dominating factor and MOSFETs are a better choice from a cost perspective.

In order to decrease the size and the power consumption of the gate drive circuit, high side gate drivers (with internal level-shifters) are used to drive the floating switches, and the cascaded bootstrap method presented in Chapter 5 is applied to provide the required floating gate drive power. Since this topology relies on its natural balancing property [117] to maintain the flying capacitor voltage at its desired value, the timing of the control signals (duty ratio, phase shift and gate drive propagation delay) should be carefully matched for all switches [118]. The photograph of the two-phase interleaved hardware prototype (with connectors and additional filter capacitors) is shown in Fig. 6.9. The PCB is a standard, low-cost 4-layer board with 2 oz copper. Fig. 6.10 provides a closer look of the converter (one phase) with key components highlighted. The metrics of the LC tanks as well as the other main components can be found from Table 6.1. Based on the largest quantity sell price on Digikey, the total cost of the main components is  $\sim \$70$ , excluding the cost of the PCB and the micro-controller. In particular, the gate drivers and the capacitors each contributes about 40% to the total cost.

Figure 6.11: Measured 36 V to 9 V efficiency ( $f_{sw} = 91$  kHz).Figure 6.12: Measured 48 V to 12 V efficiency ( $f_{sw} = 100$  kHz).

## ZCS Experimental Results

The two-phase interleaved prototype has been tested with up to 60 A output current with a Yokogawa WT3000E precision power meter. The converter can output 900 W power in 60-to-15 V conversion, with a very high power density of 3100 W/in<sup>3</sup> or 190 kW/L. The total volume is the sum of the two phases and the volume of each phase is measured by the smallest rectangular box that can contain the converter (the  $x$  and  $y$  dimensions are shown in Fig. 6.10 and the  $z$  dimension is the sum of the thickness of the PCB and the tallest components on the top and bottom sides of the board). For 48-to-12 V conversion, the power density is 2500 W/in<sup>3</sup> or 152 kW/L. Higher power density can be expected with further component optimization, as the current commercial off-the-shelf inductors (maximum height of 0.118 inch) are much taller than the other components (maximum height of 0.071 inch).

The efficiency performance at various input voltages are measured and plotted in Fig 6.11

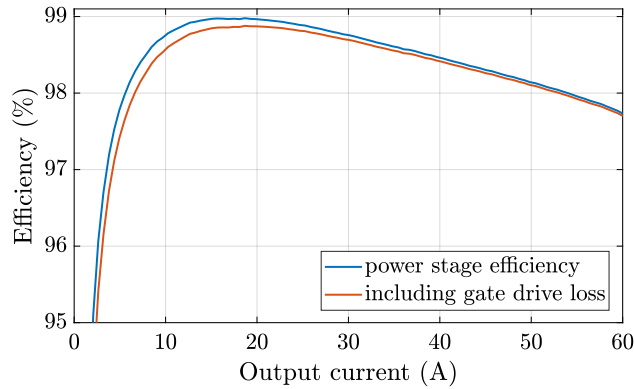


Figure 6.13: Measured 60 V to 15 V efficiency ( $f_{sw} = 111$  kHz).

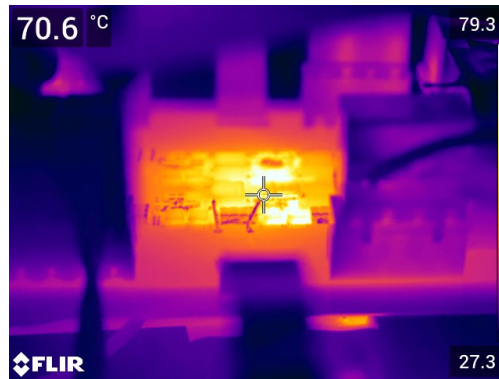


Figure 6.14: Thermal performance with fan cooling only ( $V_{in} = 48$  V,  $I_{out} = 60$  A).

to Fig 6.13. By slightly tuning the switching frequency, the prototype can achieve 99.0% peak power stage efficiency across the entire input range. For the commonly used 48-to-12 V conversion, the overall efficiency (including gate drive loss) has a peak of 98.85%, and maintains 97.23% at full power. This excellent efficiency performance can significantly reduce the complexity of thermal management design. As shown in Fig. 6.14, the converter can operate at a reasonable temperature at full power with fan cooling only. In addition, the high efficiency also reduces the impact of load regulation. Although the converter is in fixed-ratio mode (open loop), its output voltage only droops 350 mV (3% of  $V_{out}$ ) at full load. Thanks to the sufficient  $C_{mid}$  onboard, the two phases can also operate independently (no interleaving) with comparable efficiency performance, providing extra redundancy and robustness. Furthermore, phase-shedding can be implemented to improve light-load efficiency.

As shown in Fig. 6.15, the two-phase interleaved inductor currents have good current sharing, and the converter is operating at a frequency slightly higher than the resonant frequency with imperfect ZCS. Moreover, the currents at the second stage take a shape similar to that in the first stage (shown in Fig. 6.16), which can significantly reduce the

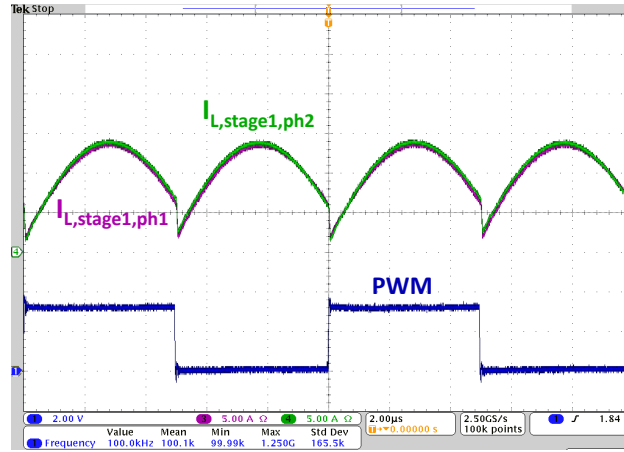


Figure 6.15: The interleaved inductor currents at the first stage.

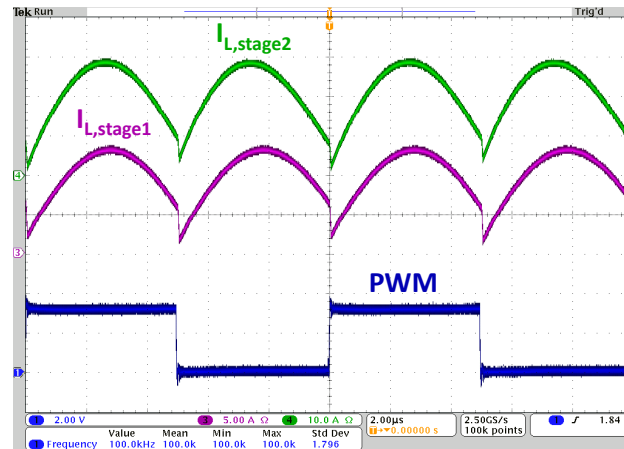


Figure 6.16: The inductor currents of the two stages (one phase).

decoupling requirement of  $C_{\text{mid}}$ . The prototype is also able to handle large load transients. In Fig. 6.17, a load step from 10 A to 30 A is introduced. The observed output voltage does not show significant undershoot, and stabilizes within a few switching cycles.

## 6.5 Zero Voltage Switching Technique

### Theoretical Analysis

Compared to ZCS, ZVS can further reduce the switching loss contributed by the transistor output capacitance ( $P_{\text{Coss}} \simeq \frac{1}{2} f_{\text{sw}} C_{\text{oss}} V_{\text{ds}}^2$ ), and greatly improve the light-load efficiency. Interestingly, the ZVS realization of ReSC converters demands that the switching frequency is higher than the resonant frequency [119], [120], which coincides with the strategy to improve component tolerance discussed in the last section. Here, we propose a technique to operate



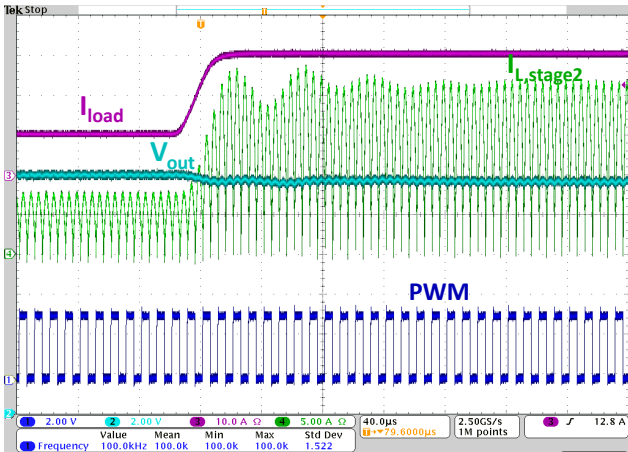


Figure 6.17: Transient response of 10 A to 30 A load step.

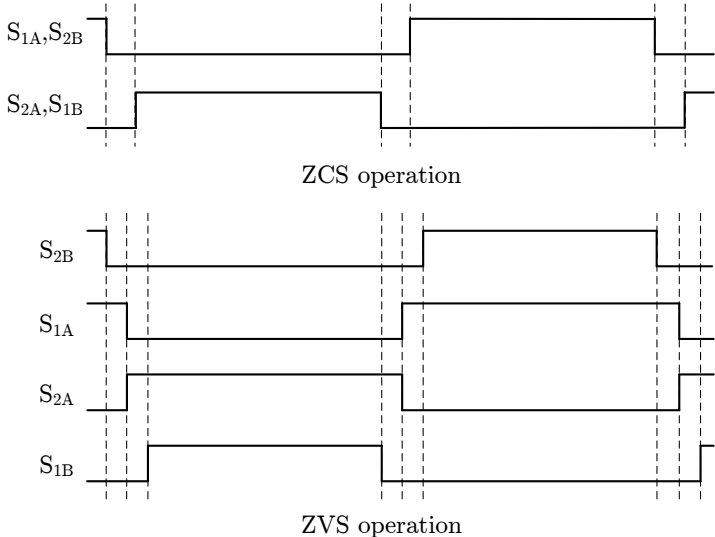


Figure 6.18: Control signals for different modes of operation.

the cascaded resonant converter in ZVS mode, and the required modifications of the control signals are shown in Fig. 6.18.

To turn on a switch with ZVS, one sufficient condition is that the body diode is conducting before the switch turns on. This condition demands that the current flowing through the switch is negative (from source to drain) during the switch turn-on period. In order for the cascaded resonant converter to fulfill the ZVS requirement, the bottom switches ( $S_{1A} - S_{4A}$  in Fig. 6.3) need to turn on when the inductor current is positive, and the top switches ( $S_{1B} - S_{4B}$ ) need to turn on when the inductor current is negative.

The waveforms of the inductor current and switch node voltage in ZVS mode are depicted in Fig. 6.19, and a zoomed-in view of the switching transition is shown in Fig. 6.20. Since



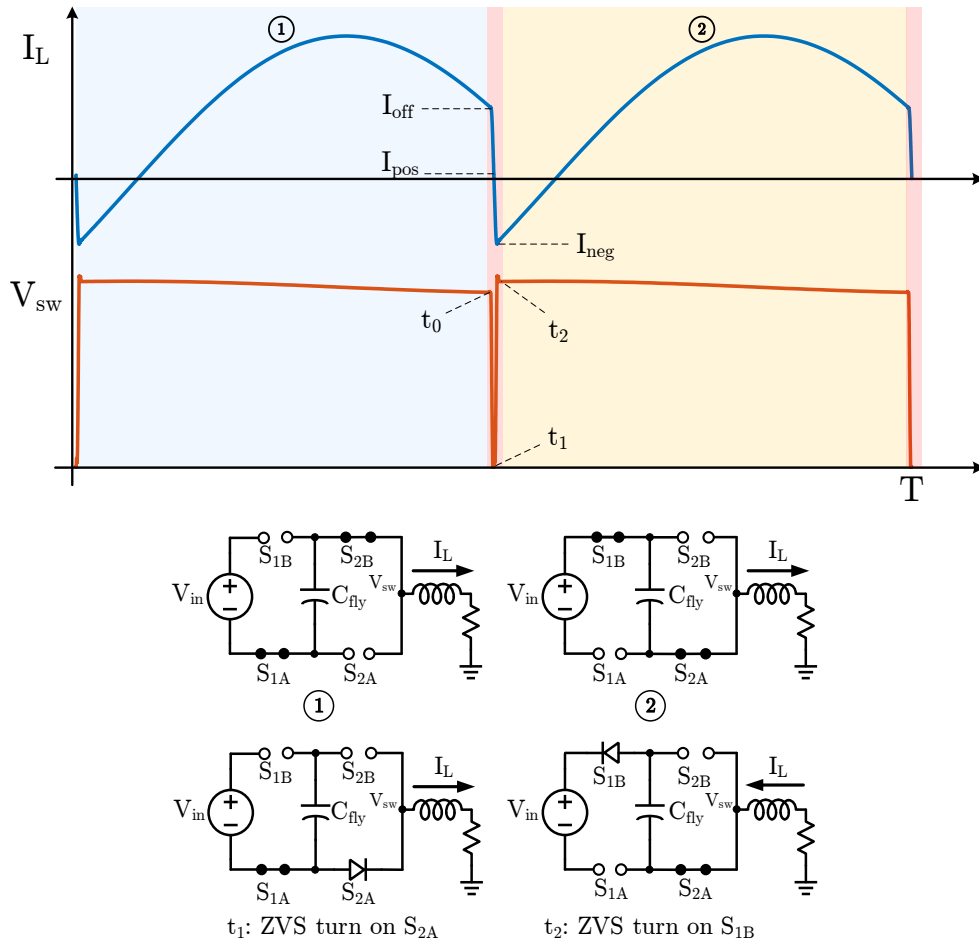


Figure 6.19: Zero voltage switching operation on cascaded resonant converter.

the switching frequency is higher than the resonant frequency, the inductor current remains positive ( $I_L = I_{\text{off}}$ ) at the end of state 1. After switch  $S_{2B}$  is turned off at  $t = t_0$  (which will introduce V-I overlap turn-off loss), the positive inductor current begins to discharge the  $C_{\text{oss}}$  of  $S_{2A}$  and to charge the  $C_{\text{oss}}$  of  $S_{2B}$  simultaneously. Assuming the drain-to-source voltage  $V_{\text{DS}}$  of  $S_{2A}$  decreases to 0 ( $V_{\text{sw}}$  also decreases to 0) while the inductor current is still greater than zero, the body diode of  $S_{2A}$  will begin to conduct. Thus, at  $t = t_1$ ,  $S_{2A}$  can be softly turned on with a slightly positive inductor current ( $I_L = I_{\text{pos}} \simeq 0$ ), and  $S_{1A}$  can be turned off at the same time with near-zero turn-off loss. Notice that if  $S_{2A}$  is not turned on in time and the inductor current reverses polarity, the  $C_{\text{oss}}$  of  $S_{2A}$  will be charged back up again and the ZVS condition is missed.

Since the switch node voltage  $V_{\text{sw}}$  is zero after  $S_{2A}$  is turned on at  $t = t_1$ , the inductor current will become negative, and resonantly charge the  $C_{\text{oss}}$  of  $S_{1A}$  (and discharge the  $C_{\text{oss}}$  of  $S_{1B}$ ). Given sufficient time, the  $V_{\text{DS}}$  of  $S_{1B}$  decreases to 0 (and  $V_{\text{sw}}$  goes back to  $\frac{V_{\text{in}}}{2}$ ) while the negative inductor current remains a near constant value flowing through  $S_{1B}$ 's body diode.

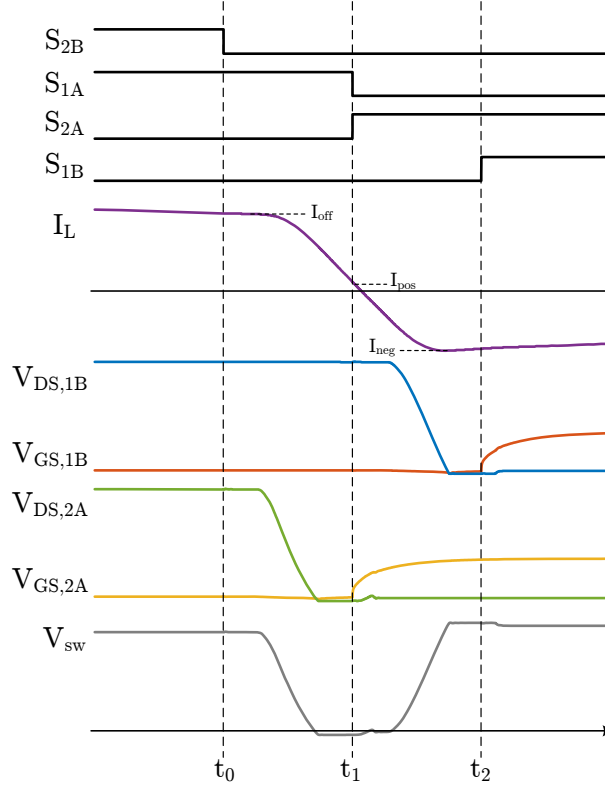


Figure 6.20: Detailed view at the ZVS switching moment.

Finally,  $S_{1B}$  is turned on with ZVS at  $t = t_2$  and the converter enters the next main operating state (state 2), after which  $S_{1A}$  and  $S_{2B}$  achieve ZVS turn-on.

To achieve the aforementioned ZVS operation, there are a few requirements on the design and control of the converter. First, the inductor needs to have sufficient energy to charge and discharge the transistor output capacitances (or equivalently the switch node capacitance):

$$LI_{\text{off}}^2 > C_{\text{oss,tot}} V_{\text{out}}^2 \quad (6.1)$$

$$LI_{\text{neg}}^2 > C_{\text{oss,tot}} V_{\text{out}}^2 \quad (6.2)$$

where  $C_{\text{oss,tot}} = 2C_{\text{oss}}$  is the sum of the output capacitances of a pair of low-side and high-side switches. Since  $C_{\text{oss}}$  is a nonlinear function of  $V_{\text{DS}}$ , the charge equivalent value should be used as discussed in [121]:

$$C_{\text{oss,Qeq}}(V_{\text{DS}}) = \frac{Q_{\text{oss}}(V_{\text{DS}})}{V_{\text{DS}}} = \frac{\int_0^{V_{\text{DS}}} C_{\text{oss}}(v) dv}{V_{\text{DS}}}. \quad (6.3)$$

It can be observed from (6.1) that, given fixed output capacitance energy, a higher inductance is desired as it can reduce the required turn-off current  $I_{\text{off}}$  and thereby turn-off switching

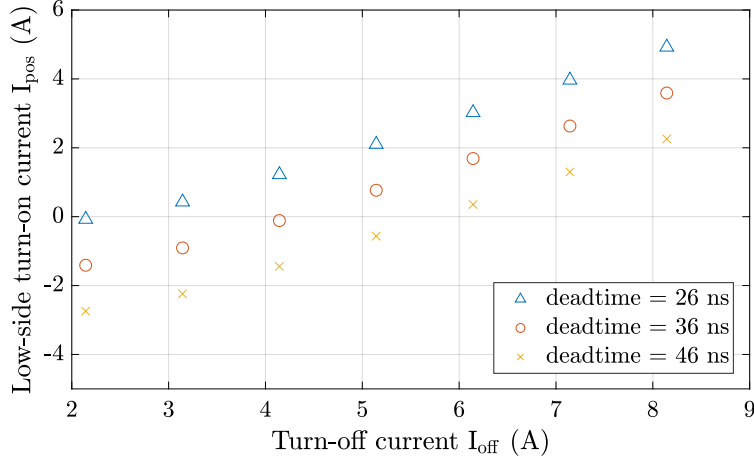


Figure 6.21: Effect of deadtime on the turn-on of low-side switch ( $L = 180$  nH,  $C_{oss,tot} = 1.5$  nF).

loss. The minimum  $I_{off}$  and  $I_{neg}$  can be derived from (6.1) and (6.2):

$$I_{off,min} = I_{neg} = \sqrt{\frac{C_{oss,tot} V_{out}^2}{L}}. \quad (6.4)$$

Assuming the low-side switch (e.g.,  $S_{2A}$  in Fig. 6.20) turns on at exactly  $I_{pos} = 0$ , then the minimum deadtime  $t_{dead,min} = t_2 - t_1$  to reach  $I_{neg}$  can be easily found to be one quarter of the resonant period:

$$t_{dead,min} = \frac{\pi}{2} \sqrt{LC_{oss,tot}}, \quad (6.5)$$

which sets the lower bound of the deadtime to turn on a high-side switch with ZVS. Fig. 6.21 illustrates the effects of a longer deadtime on the switching operation, using the circuit parameters of the first stage of the designed prototype. It can be seen that, with longer deadtime (e.g.,  $t_0 - t_1$  in Fig. 6.20), the turn-on current of the low-side switch,  $I_{pos}$ , may become negative when the turn-off current  $I_{off}$  is relatively low, indicating the absence of ZVS at light load. Thus, to achieve optimum light-load efficiency with ZVS, the deadtime should be set close to (6.5), as deviations below and above this value will both lead to imperfect ZVS and higher switching loss. Similarly, the switching frequency should be selected properly such that the turn-off current  $I_{off}$  is close to the value defined in (6.4) at light load.

The switching behavior of the switches with a deadtime of (6.5) is shown in Fig. 6.22. At light to medium load where  $I_{off}$  is relatively low ( $\sim 2$  A to  $\sim 4$  A), both the low-side and high-side switches can achieve ZVS turn on. At heavy load, the deadtime is insufficient for  $I_{neg}$  to go sufficiently negative so that the high-side switches will have  $C_{oss}$  loss. However, the converter is conduction loss dominated at heavy load. Therefore, it is unnecessary to pursue full range ZVS operation with dynamic deadtime, as the increase of conduction loss due to the increased RMS current resulting from the negative current requirement for ZVS, will be larger than the reduction of switching loss, and hurt the overall efficiency.

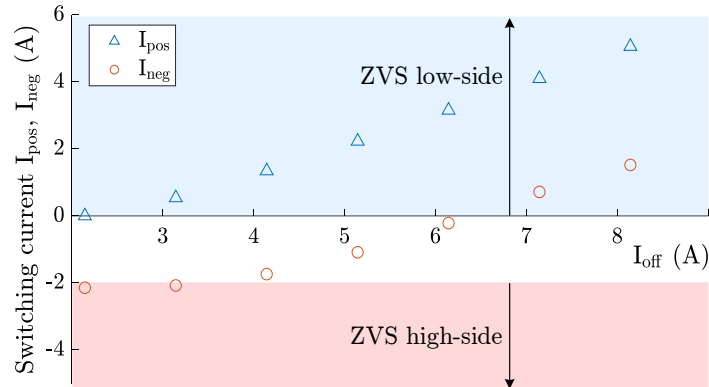


Figure 6.22: Achieving complete ZVS at light load with the optimum deadtime.

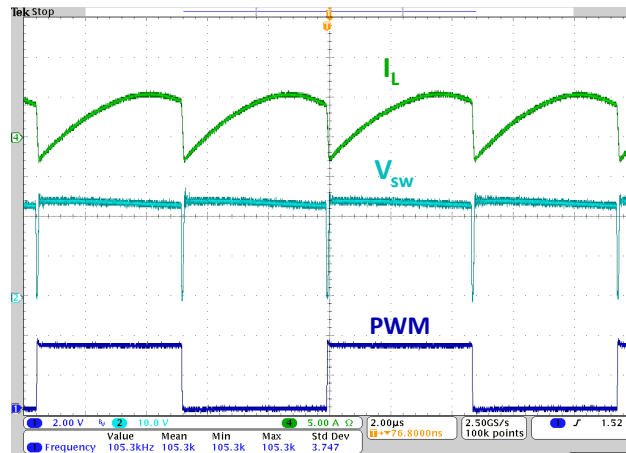


Figure 6.23:  $I_L$  and  $V_{sw}$  under ZVS.

## ZVS Experimental Results

The prototype is tested with the proposed ZVS technique, and the captured waveform of the inductor current and the switching node voltage is shown in Fig. 6.23, which closely matches the analytic plot in Fig. 6.19. As can be seen in Fig. 6.24, switch  $S_{1A}$  achieves ZVS turn-on when the inductor current is positive, followed by  $S_{2B}$  (shown in Fig. 6.25), when the inductor current reverses direction and completely discharges its output capacitance. By observing the switching operation of each switch ( $S_{1A,B}$  to  $S_{4A,B}$ ), it is possible to fine-tune the deadtimes of the two stages separately to optimize the overall efficiency.

The comparison of efficiency performance under different operation modes are plotted in Fig 6.26. It can be seen that the power stage efficiency under ZVS operation (3% load: 98.0%, peak: 99.2%, full load: 97.25%) is higher than that of the ZCS operation (3% load: 95.6%, peak: 99.0%, full load: 97.35%) at light to medium load, thanks to the elimination/reduction of the transistor output capacitance loss. At heavy load, when the conduction loss begins to

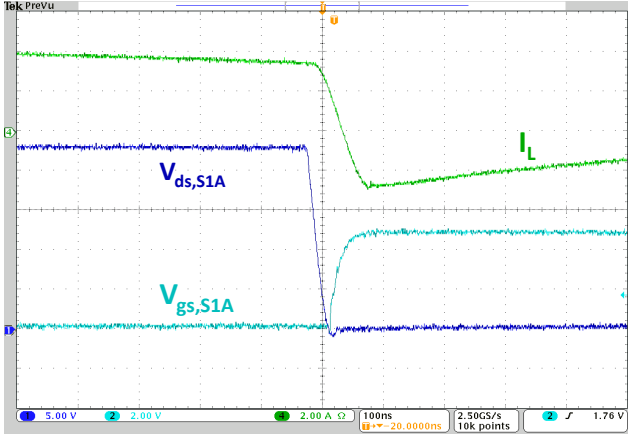


Figure 6.24: ZVS turn-on of  $S_{1A}$ .

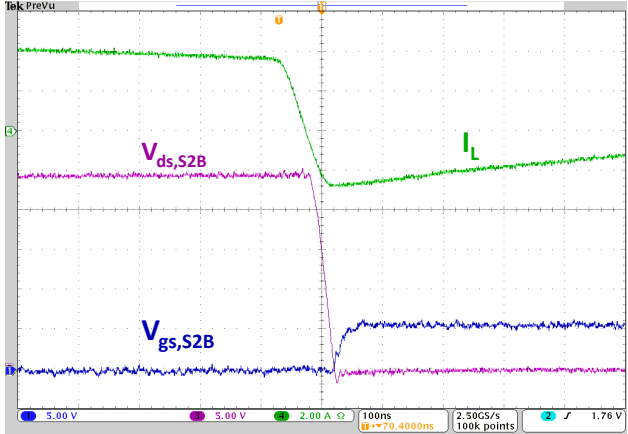


Figure 6.25: ZVS turn-on of  $S_{2B}$ .

dominate, the efficiency of the ZVS operation falls behind slightly, due to a higher total RMS current. The overall ZVS efficiency (including gate drive loss) at various input voltages is shown in Fig. 6.27. For the 48-to-12 V conversion, the overall efficiency has a peak of 99.0%, and maintains 97.2% at full power. It should be pointed out that the selected low-voltage Infineon OptiMOS switches have ultra low input and output capacitances that are comparable to the eGaN FETs in the same class. A more obvious efficiency improvement through the adoption of the ZVS technique can be expected when higher voltage MOSFETs (with higher parasitic capacitances) are used for other applications.

To better understand the operation and the potential improvements of the cascaded resonant converter, a loss analysis is performed and shown in Fig. 6.28. Not surprisingly, the conduction loss due to switch on-resistance, flying capacitor ESR and inductor resistance represents a large portion of the overall loss. In addition, the PCB copper loss (2 oz copper used in this design) is also significant, reflecting the importance of proper layout design,

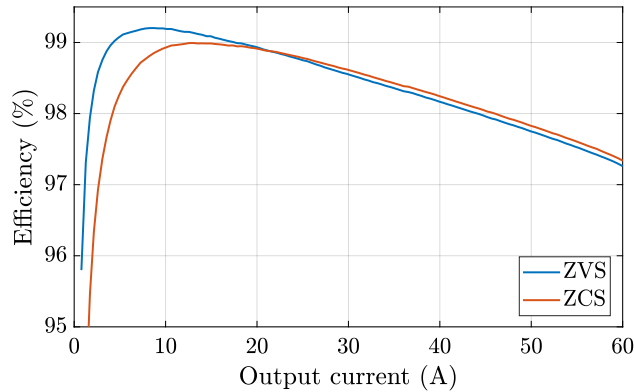


Figure 6.26: Comparison of measured 48-to-12 V power stage efficiency.

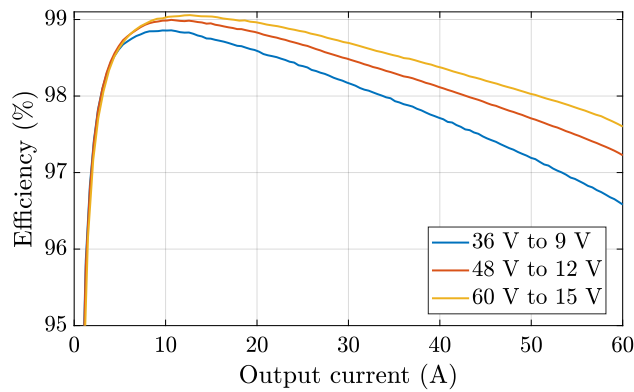


Figure 6.27: ZVS efficiency including gate drive loss.

especially when the current is high and the components are densely populated for high power density design. If cost permits, thicker copper (e.g. 5 oz) and more inner layers with better current carrying capability can be used to further improve the efficiency. At the peak efficiency point where conduction losses do not yet dominate, implementing ZVS to eliminate switch  $C_{oss}$  loss can help improve the overall efficiency. The remaining switching loss at this point is the V-I overlap loss of the high-side switches ( $S_{1B}$  to  $S_{4B}$ ) at turn-off time. When the load current increases, the inductor current will not go negative (unless the deadtime is increased), resulting in additional  $C_{oss}$  loss for the high-side switches. However, as can be seen from the pie chart at the full power point, even with the slight increase, the switching loss has minimal effect on the overall performance. Another noticeable source of loss at light load range is the gate drive loss, even though the applied cascaded bootstrap method has been shown to be one of the most efficient and compact ways to supply floating gate drive power [98]. Since this high gating loss is mainly due to the large number of switches associated with the converter, reducing the operation of the switches at light load with phase-shedding or burst mode control can help improve the efficiency. Manufacturer loss models were used to calculate inductor core loss and ac winding loss. Owing to the

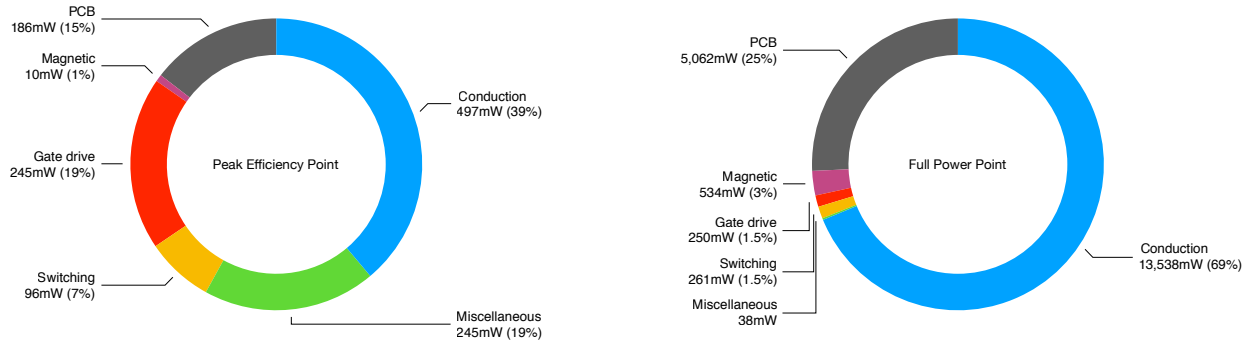


Figure 6.28: Loss breakdown of the prototype in ZVS mode.

relatively low switching frequency, the magnetic loss in the cascaded resonant converter is not a significant source of loss. The remainder of the losses, which are not accounted for in other loss models, are categorized as miscellaneous loss. More detailed magnetics loss models may increase the estimated magnetics losses. Additionally, recent work [3] has highlighted the increased capacitor losses when used in large dc bias and ac current amplitude as done here.

Finally, we perform a detailed survey and comparison to the-state-of-the-art converters in this space, including both industry and academic work [1], [23], [122]–[125]. Fig. 6.29 highlights both the isolation and regulation capabilities of the-state-of-the-art solutions, showcasing their effects on achievable performance and allowing designers to make trade-offs regarding the suitability of each design for various applications. Under the space of non-isolated and unregulated converters, this work is compared with other representative solutions that have similar voltage and power ratings. The results are tabulated in Table 6.2. Thanks to the high energy density of capacitors and the efficient utilization of the switches and passive components, the cascaded resonant converter can have performance superior to that of conventional SC and magnetic-based converters. Compared with the Google switched tank converter, this work uses a different ReSC topology with Class-II ceramic capacitors and inductor-at-output configuration. Despite the lack of auxiliary circuits (e.g., start-up, protection) and rigorous reliability tests that commercial products require, we demonstrate that the cascaded resonant converter is a promising ReSC topology with the potential to achieve high efficiency and high power density simultaneously.

## 6.6 Cascading and Interleaving Strategies

An alternative 12-switch design of the cascaded resonant converter is shown in Fig. 6.30. Since the output current of a 2-to-1 ReSC converter is a continuous rectified sine wave, two-phase interleaving is not required for the first stage. If the high-voltage switches in the first stage ( $S_{1A,1B}$ ,  $S_{2A,2B}$ ) have sufficiently low on-resistance to process the full rated power

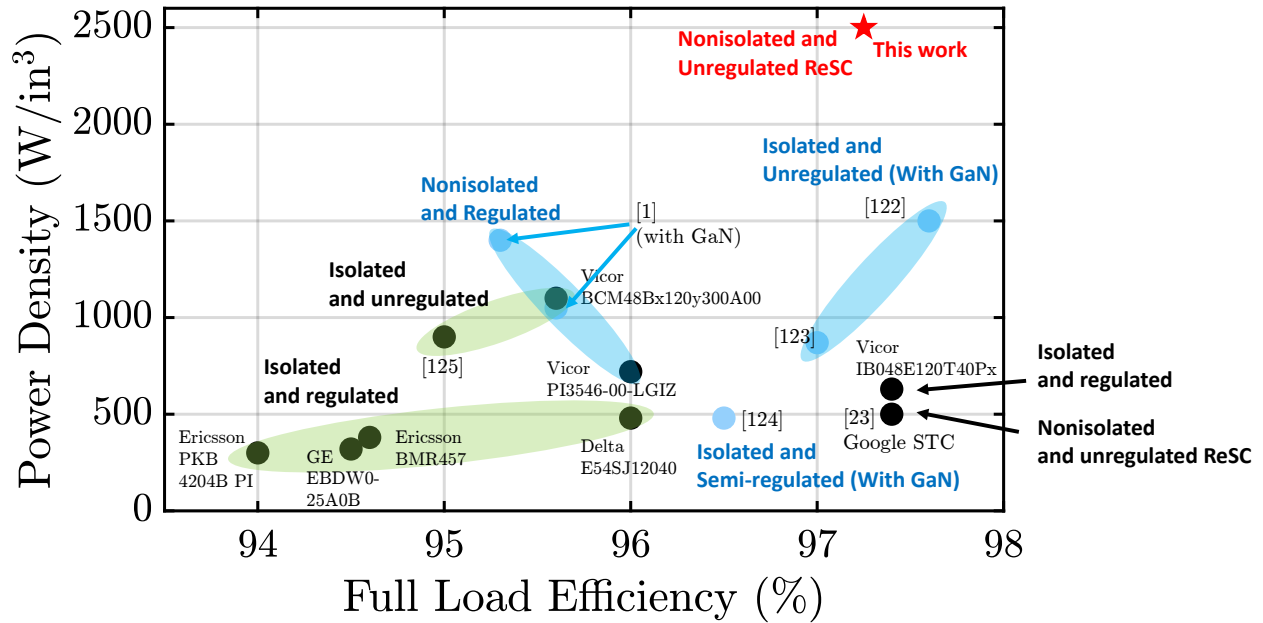


Figure 6.29: Comparison of full-load efficiency and power density of state-of-the-art commercial products and previously published research.

Table 6.2: Comparison of this work and existing non-isolated intermediate bus converters

Reference	Topology	Output current (A)	Power Density (W/inch <sup>3</sup> )	Efficiency	Notes
This work	cascaded resonant	60	2500	full load: 97.23% peak: 99.0%	based on 48:12V conversion, gating loss included
LTC7820 [8]	cascaded pure 2-to-1 SC	40	up to 1500	full load: $\leq 97.0\%$ peak: $\leq 98.6\%$	highly integrated 48:12 V design, detailed data unavailable (use conservative estimate)
EPC9130 [1]	5-phase interleaved buck	60	> 1000	full load: 95.8% peak: 96.2%	48:12V, GaN switches, <b>regulated</b>
Google switched tank converter [23]	modified Dickson	50	500 (power stage only: switches and passives)	full load: 97.41% peak: 98.61%	54 V input, 4:1 fixed ratio, components are not densely populated

with good efficiency performance, a cascaded design with non-interleaving first-stage can be considered to save component count and board area. A second revision of the cascaded resonant converter using this 12-switch design and the latest OptiMOS transistors is reported in [126]. With the same specifications (36–60 V input, 4-to-1 fixed-ratio, 60 A output current), the improved design achieves over 4000 W/in<sup>3</sup> power density and 98.0% full-load efficiency, while maintaining the same 99.0% peak efficiency. These results set a new record for the 48-to-12 V data center application, showcasing the superior performance of the cascaded resonant topology.



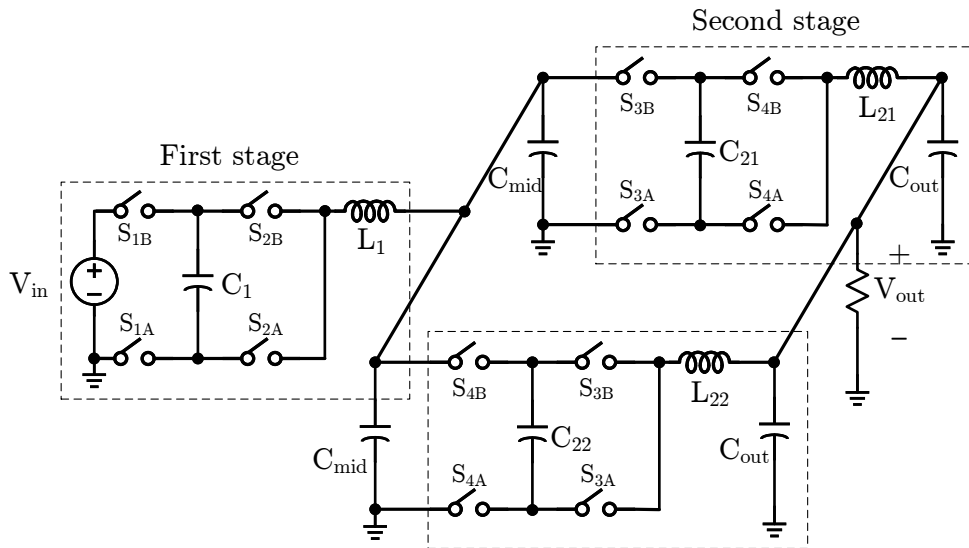


Figure 6.30: An alternative 12-switch design of the cascaded resonant converter with single first-stage.

Besides the basic 2-to-1 ReSC converters, the cascaded resonant concept can be extended to other more complex ReSC topologies for higher conversion ratios. Compared to building a high-ratio single-stage ReSC converter, cascading converters with simpler structures may greatly reduce the component count, control complexity, and system failure rate owing to less series-connected switches in the system. This is because the voltage conversion of SC converters is based on capacitor voltage “addition” or “subtraction”. In contrast, through cascading operation, capacitor voltage “multiplication” or “division” can be achieved.

Another challenge associated with the high conversion ratio is the simultaneous existence of high input voltage and high output current. For a single-stage ReSC converter, the achievable output power is usually limited by the output current, whereas the high-voltage devices at the input side are often times underutilized. By dividing the system into multiple cascaded stages, the high-voltage input stage and the high-current output stage can be designed and optimized separately. Specifically, by first stepping down the high input voltage with a simple but efficient 2-to-1 ReSC converter, the voltage stress of the rest of the system is greatly reduced. Then, multiple downstream ReSC converters can be paralleled to provide the requisite high output current. Since these converters see low input voltage, the topologies which favor low-voltage-rating devices can be used for optimal performance.

For instance, as shown in Fig. 6.31, two-phase interleaved switched-tank converters (STC) can be cascaded with a front-end 2-to-1 ReSC converter. The STC (or the Dickson converter) is known for its low switch voltage rating and good switch utilization (i.e., low VA rating). However, it requires high voltage capacitors and therefore suffers from relatively low achievable power density compared to other ReSC topologies. With halved input voltage, the

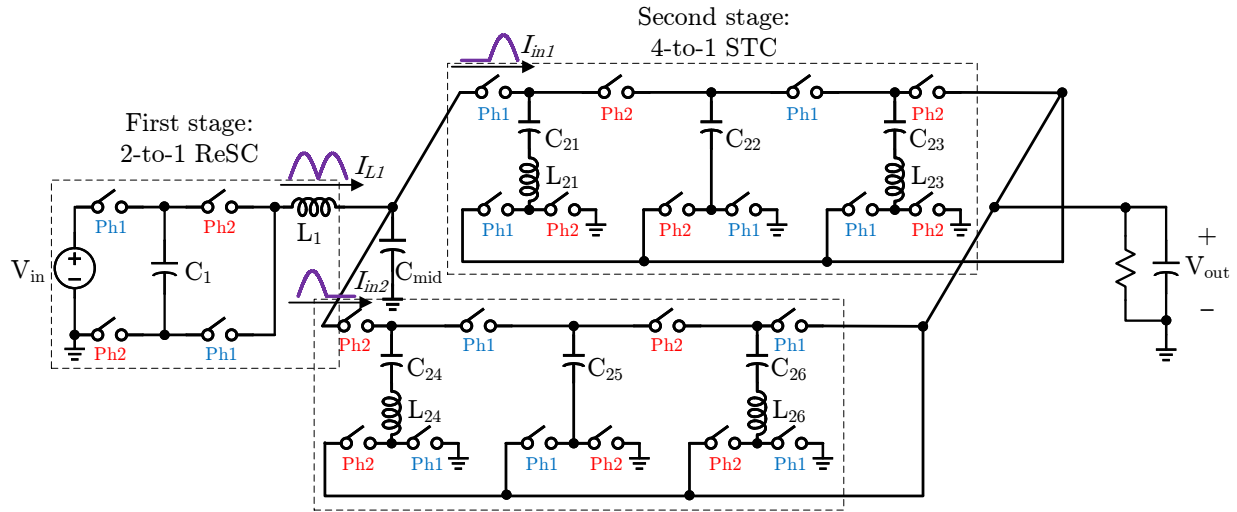


Figure 6.31: Cascading 2-to-1 ReSC with two-phase interleaved switched-tank converters (STC).

high-efficiency advantage of the STC topology can be fully utilized, and the disadvantage in passive component utilization is mediated. Moreover, as in the original cascaded resonant converter, the combined input current of the two-phase interleaved STC converter becomes a continuous rectified sine wave, which matches the output current of the 2-to-1 ReSC converter. As a result, the interstage decoupling requirement of  $C_{mid}$  can be greatly reduced.

The interleaving strategy can also be applied to other ReSC topologies with duty ratios other than 50%. Owing to the augmenting inductor at the output, the duty ratio of the series-phase and the parallel-phase of the 4-to-1 series-parallel converters become  $\frac{1}{4}$  and  $\frac{3}{4}$ , respectively. As shown in Fig. 6.32, four series-parallel converters can be paralleled and interleaved with  $90^\circ$  phase shift to make their combined input current a continuous rectified sine wave. By operating the 2-to-1 ReSC stage at twice the frequency of the series-parallel stage, the currents of the two stages are matched and  $C_{mid}$  can be reduced.

In addition to cascaded operation, a multi-operating-phase concept can be used to achieve high conversion ratio with ReSC converters, while maintaining a relatively low component count. In the next chapter, we present a family of multi-resonant SC converters with conversion ratios greater than 4-to-1.

## 6.7 Chapter Summary

This chapter presents a new ReSC converter topology and its control method. By cascading 2-to-1 ReSC converters and implementing an interleaved control method, high-performance

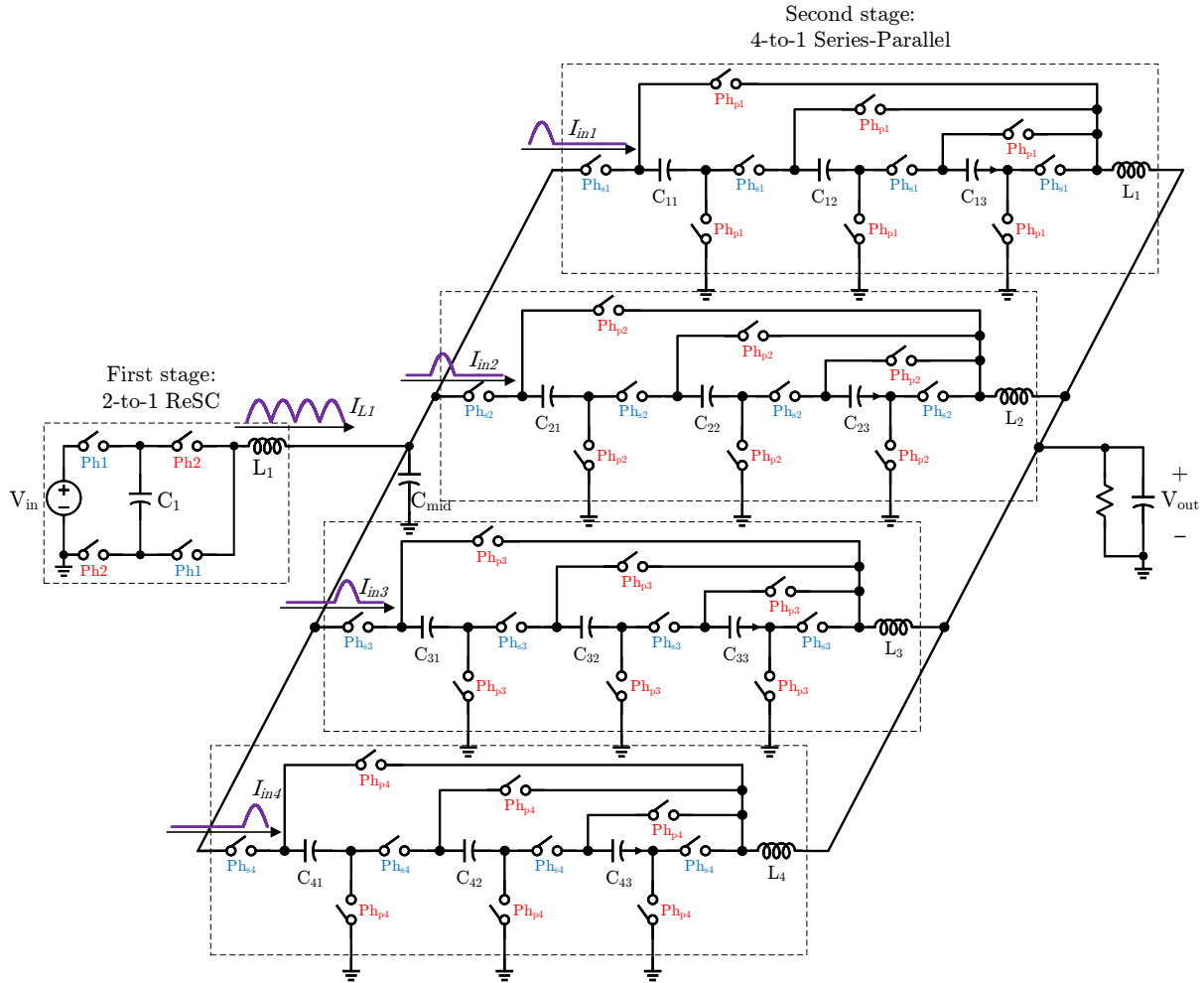


Figure 6.32: Cascading 2-to-1 ReSC with four-phase interleaved series-parallel converters.

high-conversion-ratio power conversion can be achieved with the original simple structure and operating principle. We demonstrate in theory and with a hardware prototype that, the proposed cascaded resonant converter has high utilization of both active and passive components, and is an excellent candidate for 48-to-12 V data center application. It is shown that the large interstage decoupling requirement in practical implementations can be alleviated with a two-phase interleaving method, and the effects of component variations can be mitigated by operating at a frequency slightly higher than the resonance. A ZVS control method is also developed to improve light-load efficiency, and the method can also be applied to other ReSC topologies. The prototype achieves 99.0% peak efficiency and up to 3100 W/in<sup>3</sup> power density. Finally, the concept of cascading and interleaving converters is extended to other more complex ReSC topologies for higher conversion ratios.

## Chapter 7

# Multi-Resonant Switched-Capacitor Converter

Compared with conventional SC converters with two operating phases, SC converters with multiple operating phases can achieve the same conversion ratio with fewer capacitors and switches. This feature makes multi-phase SC converters an attractive candidate for applications with high conversion ratios. This chapter presents a family of multi-phase ReSC converters with high conversion ratios. They are called multi-resonant SC converters, which can be synthesized from the basic doubler and the series-parallel topologies. Both theoretical analysis and experimental results from a practical implementation are provided to demonstrate the benefits of the multi-resonant approach. The hardware prototype can operate in both 6-to-1 mode and 8-to-1 mode, with one of the best in-class performances.

### 7.1 Background and Motivation

This chapter is a continuation of Chapter 6. We strive to build high-performance ReSC converters with high conversion ratios. One potential application is the two-stage power delivery architecture from 48 V to the point-of-load voltages for data centers. In contrast to 48-to-12 V bus converters for the legacy 12 V bus, recent research [104] suggests that a lower intermediate bus voltage (e.g., 4–6 V) may provide higher overall efficiency, once both the intermediate bus converter and the second-stage buck converters are considered. Therefore, there is increased interest in highly efficient fixed-ratio conversion with an 8-to-1 to 12-to-1 ratio. For such a high conversion ratio, a transformer is usually needed. Reference [127] demonstrates a GaN-based 48-to-6 V fixed-ratio LLC converter with 98% peak efficiency and 1100 W/in<sup>3</sup> power density, which uses a highly optimized 8-to-1 matrix transformer. In contrast, the majority of existing ReSC works focus on 4-to-1 or 6-to-1 ratios, and high performance ReSC works with higher conversion ratios have not been widely demonstrated. This is because the number of components (switches and capacitors) increases proportionally with respect to the conversion ratio, and the increased circuit implementation complexity

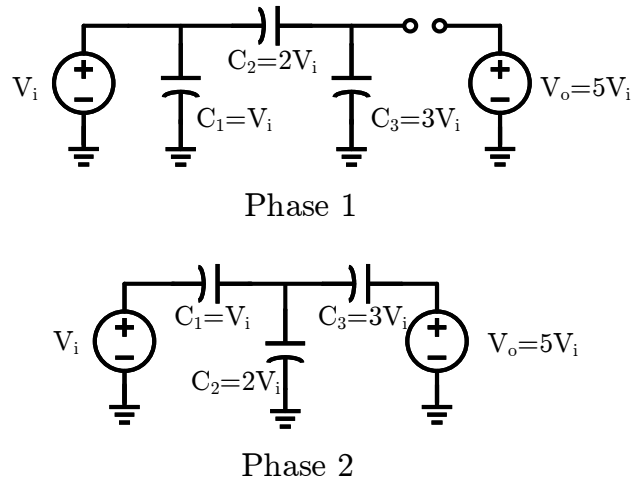


Figure 7.1: The maximum voltage gain in two-phase SC converters follows the Fibonacci sequence.

can potentially reduce the theoretical performance benefits. To address this challenge, the multi-operating-phase concept is proposed and explored in this chapter.

In Section 7.2, the theoretical performance limit of SC converters is briefly reviewed. Compared with typical SC converters which have two operating phases, multi-phase SC converters can achieve the same conversion ratio with significantly fewer switches and flying capacitors [128]. This is extremely beneficial in practical implementations when high conversion ratios are needed. In Section 7.3, we demonstrate how to generate and synthesize multi-phase SC topologies from conventional two-phase SC topologies, and compare their similarities and differences. In Section 7.4, an 8-to-1 multi-resonant-doubler converter is presented, with detailed theoretical analysis, experimental results, and performance comparison. This converter features the least-possible number of switches and capacitors among all SC converters at this conversion ratio. Even though the multi-resonant-doubler does not have a significant advantage in switch utilization compared to other two-phase SC converters, it has superior passive component utilization, as well as additional benefits in practical circuit design. A 48-to-6 V, 40 A, fixed-ratio converter prototype is designed and implemented. The prototype achieves 98.6% peak efficiency (98.0% including gate drive loss) and 1675 W/in<sup>3</sup> power density. In Section 7.5, the multi-resonant-doubler is modified to a 6-to-1 cascaded series-parallel converter, which also achieves the best overall performance in its class. Finally, in Section 7.7, the multi-operating-phase concept is generalized to a family of multi-resonant SC converters, with conversion ratios spanning from 8-to-1 to 12-to-1.

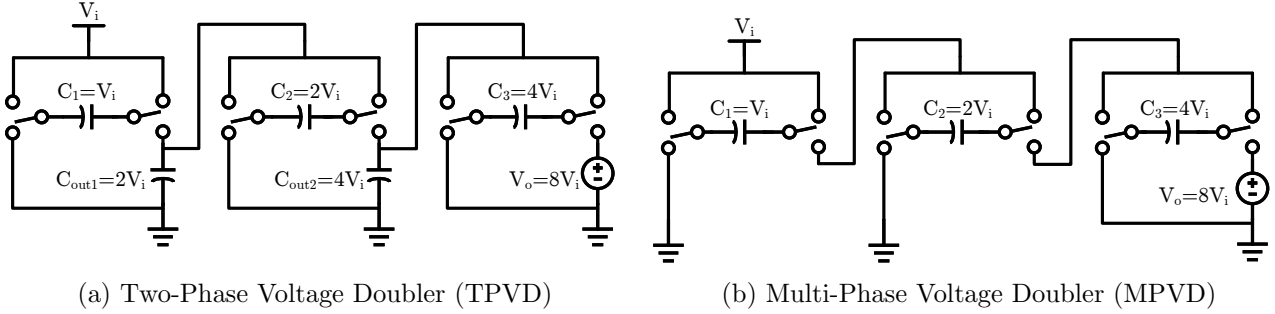


Figure 7.2: Exponential growth of voltage gain with voltage doublers.

## 7.2 Theoretical Performance Limit of SC converters

### Two-Phase SC Converters

According to [128], [129], for two-phase SC converters, the realizable conversion ratio with  $k$  capacitors ( $k-1$  flying capacitors and one output capacitor) is bounded by the  $k$ th Fibonacci number  $F_k$ :

$$M[k] = \frac{V_{out}}{V_{in}} = \frac{1 \leq P[k] \leq F_k}{1 \leq Q[k] \leq F_k} \quad (7.1)$$

where  $F_1 = 1, F_2 = 2, F_3 = 3, \dots, F_n = F_{n-1} + F_{n-2}$ . Similarly, the bound on the number of switches required in any SC circuit is found to be  $3k - 2$ . Intuitively, the voltage gain is achieved by capacitor voltage addition (or subtraction) in two-phase SC converters. By adding (or subtracting) the voltage of every two neighboring flying capacitors by turns, the capacitor voltages and the output voltage increases (or decreases) in a Fibonacci fashion, achieving the maximum achievable voltage gain. The two operating phases of a Fibonacci step-up converter with three flying capacitors  $C_1, C_2$ , and  $C_3$  are shown in Fig. 7.1. In Phase 1,  $C_1$  is charged to the input voltage  $V_i$  and  $C_3$  is charged by the series combination of  $C_1$  and  $C_2$  to  $3V_i$ . In Phase 2,  $C_2$  is charged by the series combination of  $C_1$  and input voltage to  $2V_i$ , whereas the output voltage is charged by  $C_2$  and  $C_3$  to  $5V_i$ . A property of the Fibonacci sequence is that the ratio of every two successive Fibonacci numbers approaches the golden ratio (1.618). It indicates that the fastest possible voltage growth rate (with respect to the number of flying capacitors) of a two-phase SC converter is 1.618.

### Multi-Phase SC Converters

As discussed in [130], given the same number of capacitors and switches, if multiple operating phases can be introduced, the maximum realizable gain with  $k$  capacitors ( $k-1$  flying capacitors and one output capacitor) becomes

$$M[k]_{max} = 2^{k-1} \quad (7.2)$$

Table 7.1: Maximum attainable conversion ratios

$p$ phases	Number of capacitors $k$				
	1	2	3	4	5
2 (Fibonacci)	1	2	3	5	8
3 (Tribonacci)	1	2	4	7	13
4 (Tetranacci)	1	2	4	8	15
5 (Pentanacci)	1	2	4	8	16

which is greater than the Fibonacci bound. From a circuit perspective, this can be implemented by a chain of 2-to-1 voltage doublers, which effectively achieves capacitor voltage multiplication (or division).

As shown in Fig. 7.2a, a voltage doubler with three flying capacitors  $C_1$ ,  $C_2$ , and  $C_3$  can achieve a gain of 8. However, with two-phase operation, the voltage doubler requires two intermediate decoupling capacitors  $C_{out1}$  and  $C_{out2}$ , resulting in a total required capacitor number that is higher than that predicted in (7.2). One method to eliminate the intermediate decoupling capacitors is to operate two two-phase doublers in parallel with interleaving control, which is discussed in Chapter 6. Alternatively, more operating phases can be added such that some flying capacitors are disconnected from the circuit for some phases, thereby relaxing the intermediate decoupling requirement. The multi-phase voltage doubler (MPVD) in Fig. 7.2b can achieve the theoretical maximum gain of (7.2) with 4 capacitors (3 flying capacitors and one output capacitor). Note that even though the gain becomes  $2^{k-1}$  for multi-phase operation, the minimum number of switches required remains  $3k - 2$ . It indicates that it is possible to further reduce the switch number of the MPVD in Fig. 7.2, from 12 switches to the theoretical minimum of 10 switches while keeping the voltage gain at 8. The formal expression and proof of the gain of multi-phase SC converters is provided in [131], [132]. With  $p$  operating phases, the maximum realizable gain is

$$M_{max}^{(p)}[k] = F_k^p \quad (7.3)$$

where  $F_k^p$  is the  $p$ -th order generalized Fibonacci number. The  $p$ -th hyper-Fibonacci numbers are defined by the recursion:

$$F_k^p = \begin{cases} 2^{k-1} & k = 1, \dots, p \\ F_{k-1} + \dots + F_{k-p} & k > p \end{cases} \quad (7.4)$$

It means that when the number of phases  $p$  is greater than or equal to the number of capacitors  $k$ , the highest possible conversion ratio  $2^{k-1}$  can be achieved. When  $p < k$ , the attainable gain is the  $p$ -th order Fibonacci summation. If  $p = 2$ , the equation degenerates

to the regular Fibonacci sequence. An example is provided in Table 7.1. With 4 capacitors (3 flying capacitors and one output capacitor), two-phase operation can provide a maximum gain of 5. If 3 phases are used, the gain equals the sum of the previous three Fibonacci numbers (Gain = 1 + 2 + 4 = 7). With 4 or more phases, the gain saturates at 8 (=  $2^{(4-1)}$ ).

### 7.3 Generation and Synthesis of Multi-Phase Topologies

In this section, we present an example of how to derive multi-phase SC converters from their two-phase counterparts while maintaining the same fundamental structure, through gating signal modification and/or minor circuit changes. The first circuit schematic shown in Fig. 7.3 is a classic 4-to-1 series-parallel topology, featuring 10 switches and 3 flying capacitors. Because an inductor is augmented at the output node for soft-charging operation, the duty ratios of the series-phase and the parallel-phase need to be adjusted accordingly, and they are  $\frac{T}{4}$  and  $\frac{3T}{4}$ , respectively.

Next, as shown in the second part of Fig. 7.3, by moving the source terminal of the top-most horizontal switch to the positive side of the second flying capacitor, a 6-to-1 cascaded series-parallel converter is derived. Note that this is a completely new topology that has not been explored in existing works, and its detailed operating principle is presented in Section 7.5. Compared to the 4-to-1 series-parallel converter, it has the same number of components, and only the rating of one switch and one flying capacitor are increased from  $V_o$  to  $3V_o$ . In order to achieve a higher conversion ratio, an extra operating phase is introduced, such that the converter can merge the operation of two cascaded converters together: the first four switches and the first flying capacitor forms a 2-to-1 SC stage, followed by a 3-to-1 series-parallel stage formed by the rest of the components. Note that the 2-to-1 step-down operation only takes place at the first  $\frac{1}{3}$  of the switching period.

Similarly, if the source terminal of the second top-most horizontal switch is relocated to that shown in the third part of Fig. 7.3, another classic topology, the Fibonacci converter, is derived. Given fixed capacitor and switch number, the conversion ratio of the Fibonacci topology is at the theoretical limit of two-phase SC converters.

Moreover, by introducing two extra operating phases, an 8-to-1 conversion ratio can be achieved with exactly the same structure. It can be viewed as another type of multi-phase voltage doubler, which features the minimum number of switches for this conversion ratio (less than the MPVD shown in Fig. 7.2b). The multi-phase operation of this structure was first proposed in [133]. Since the flying capacitors carry binary voltages ( $(\frac{1}{8}, \frac{2}{8}, \frac{4}{8}V_{in})$ ), it is known as a binary converter. Furthermore, [134], [135] have demonstrated that all fractions of the input voltage ( $(\frac{1}{8}, \frac{2}{8}, \frac{3}{8}, \dots, \frac{7}{8}V_{in})$ ) can be derived by adjusting the gating signals, and thus named it the extended binary converter (EXB). In Section 7.4, we expand upon this by exploring the performance of a new implementation of this structure, with an augmenting inductor for ultra-efficient 8-to-1 fixed-ratio conversion. This converter is called the



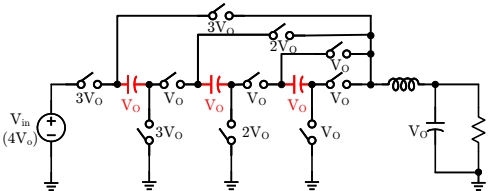
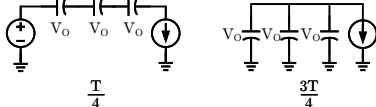
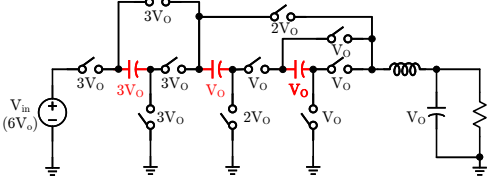
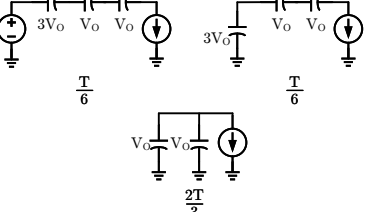
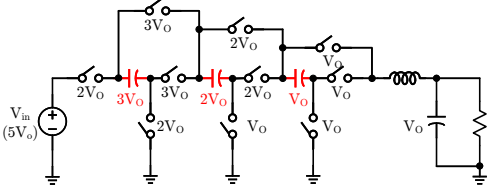
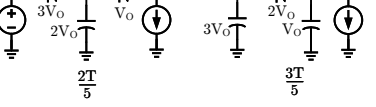
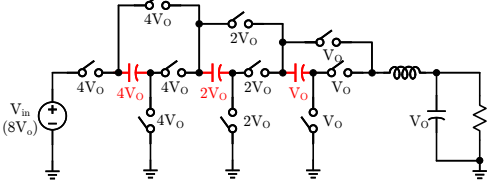
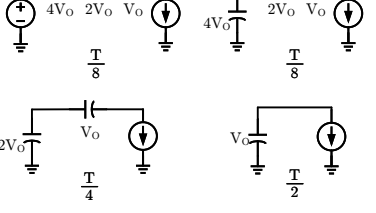
Circuit Schematic	Operating States	Switch VA Rating
 <p style="text-align: center;">4:1 Series-Parallel (two-phase)</p>		$VA_{avg} = 4.5 V_o I_o$ $VA_{rms} = 6.5 V_o I_o$
 <p style="text-align: center;">6:1 Cascaded Series-Parallel (three-phase)</p>		$VA_{avg} = 4.67 V_o I_o$ $VA_{rms} = 9 V_o I_o$ <p>In comparison, 6:1 Series-Parallel has:</p> $VA_{avg} = 6.67 V_o I_o$ $VA_{rms} = 9.6 V_o I_o$
 <p style="text-align: center;">5:1 Fibonacci (two-phase)</p>		$VA_{avg} = 4.8 V_o I_o$ $VA_{rms} = 6.9 V_o I_o$
 <p style="text-align: center;">8:1 Multi-Resonant-Doubler (four-phase)</p>		$VA_{avg} = 4.75 V_o I_o$ $VA_{rms} = 11.7 V_o I_o$ <p>In comparison, 8:1 Series-Parallel has:</p> $VA_{avg} = 8.75 V_o I_o$ $VA_{rms} = 12.43 V_o I_o$

Figure 7.3: Achieving different conversion ratios with the same fundamental structure.

multi-resonant-doubler (MRD), as the augmenting inductor resonates with different flying capacitor combinations in different phases and therefore forms multiple resonances within a switching period.

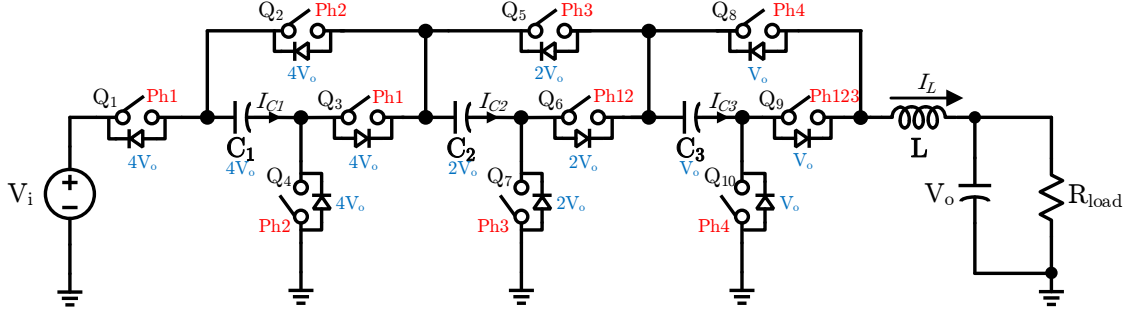


Figure 7.4: Schematic drawing of the 8-to-1 multi-resonant-doubler converter with device ratings and control signals labeled.

## 7.4 8-to-1 Multi-Resonant-Doubler Converter

### Operating Principle

The schematic drawing of the 8-to-1 multi-resonant-doubler (MRD) converter with four operating phases is shown in Fig. 7.4. Its basic SC structure can be viewed as one practical implementation of a multi-phase voltage doubler that achieves the theoretical maximum gain with the least number of components (3 flying capacitors and 10 switches for a gain of 8). Because of the voltage doubler structure, the flying capacitors carry binary voltages ( $C_1 = 4V_o$ ,  $C_2 = 2V_o$ ,  $C_3 = V_o$ ) and the switches see the same voltage as that of the corresponding capacitors ( $Q_{1-4} = 4V_o$ ,  $Q_{5-7} = 2V_o$ ,  $Q_{8-10} = V_o$ ). The key control signals, inductor and capacitor current waveforms, and the equivalent circuit of the four operating phases are shown in Fig. 7.5. It can be seen that all flying capacitors are charged and discharged in a resonant fashion, resulting in soft-charging and ZCS. The detailed operation of the four phases are as follows:

- Phase 1: The “Ph1”, “Ph12” and “Ph123” switches in Fig. 7.4 are ON.  $C_1$ ,  $C_2$ ,  $C_3$  and  $L$  are connected in series. All flying capacitors are resonantly charged by the input. The duration of phase 1 is  $\frac{1}{8}$  of the switching cycle. The equivalent resonant frequency of this phase is  $f_{r,ph1} = \frac{1}{2\pi\sqrt{LC_{eq1}}}$ , where  $\frac{1}{C_{eq1}} = \frac{1}{C_1} + \frac{1}{C_2} + \frac{1}{C_3}$ .
- Phase 2: The “Ph2”, “Ph12” and “Ph123” switches are ON. In this phase, all flying capacitors are still connected in series, but  $C_1$  is being discharged. The length of the phase and the equivalent resonant frequency remain the same as those of Phase 1.
- Phase 3: The “Ph3” and “Ph123” switches are ON. In this phase,  $C_1$  is disconnected and  $C_3$  is only charged by  $C_2$ . In order to maintain capacitor charge balance, the duration of this phase is doubled to  $\frac{1}{4}$  of the switching cycle. The equivalent resonant frequency of this phase is now  $f_{r,ph3} = \frac{1}{2\pi\sqrt{LC_{eq3}}}$ , where  $\frac{1}{C_{eq3}} = \frac{1}{C_2} + \frac{1}{C_3}$ .

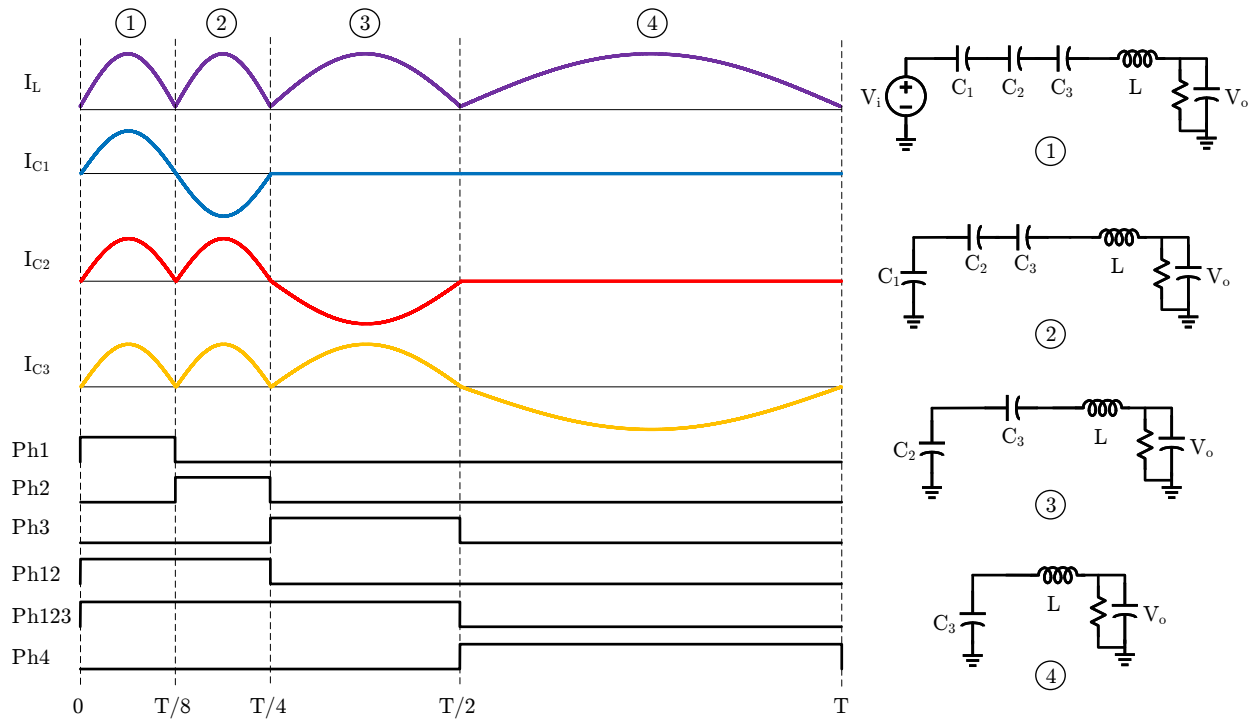


Figure 7.5: Inductor and capacitor current waveforms, control signals, and equivalent circuits of the 8-to-1 multi-resonant-doubler converter.

- Phase 4: Only the “Ph4” switches are ON. In this phase, both  $C_1$  and  $C_2$  are disconnected and  $C_3$  is resonantly discharged to the load. The equivalent resonant frequency of this phase is  $f_{r,ph4} = \frac{1}{2\pi\sqrt{LC_3}}$ . Since the duration of this phase is  $\frac{1}{2}$  of the switching cycle, the overall switching frequency with four phases combined would be the same as  $f_{r,ph4}$  ( $f_{sw} = f_{r,ph4} = \frac{1}{2\pi\sqrt{LC_3}}$ ), which is only determined by  $L$  and  $C_3$ .

By equating the relative length of different phases and the corresponding resonant frequency, the required ratio of the flying capacitors can be found to be  $C_1 = \frac{1}{12}C_3$  and  $C_2 = \frac{1}{3}C_3$ . These reduced capacitance requirements are due to the fact that the resonant charging currents of  $C_1$  and  $C_2$  are at higher frequencies than  $C_3$ . It indicates that even though  $C_1$  and  $C_2$  must be rated for higher voltages than  $C_3$ , their physical volume could still be very similar due to their reduced capacitance. Moreover, these capacitor ratios relate to two operation constraints. First, these exact ratios are needed to achieve ZCS for all switches. Second, these ratios determine the minimal capacitor values that are needed to achieve soft-charging operation. In practical implementations, it is very challenging to maintain an exact capacitor ratio. Nevertheless, the soft-charging operation is guaranteed as long as the actual capacitors exceed their minimum required values. In practice, the imperfect ZCS operation

Table 7.2: Comparison of component number of 8-to-1 SC converters

Topology	Switch Number	Capacitor Number	Notes
Multi-Resonant-Doubler	10 ( $4V_o \times 4$ , $2V_o \times 3$ , $V_o \times 3$ )	3 ( $4V_o$ , $2V_o$ , $V_o$ )	one inductor, four-phase operation
Cascaded Resonant	12 ( $4V_o \times 4$ , $2V_o \times 4$ , $V_o \times 4$ )	3 ( $4V_o$ , $2V_o$ , $V_o$ )	three inductors, two $C_{mid}$
Fibonacci	13 ( $5V_o \times 2$ , $3V_o \times 4$ , $2V_o \times 3$ , $2V_o \times 4$ )	4 ( $5V_o$ , $3V_o$ , $2V_o$ , $V_o$ )	at the limit of two-phase SC
Series-Parallel	22 ( $7V_o \times 3$ , $6 \cdot 2V_o \times 2$ , $V_o \times 9$ )	7 ( $V_o \times 7$ )	one inductor at output is possible
Dickson (Switched-Tank)	22 ( $2V_o \times 6$ , $V_o \times 16$ )	7 ( $7V_o$ , $6V_o$ , ..., $V_o$ )	four inductors for STC [23]

Table 7.3: Comparison of passive and active component utilization of 8-to-1 SC converters

Topology	Passive Volume	$VA_{rms}$ Rating	$R_{out}$ (assuming same R for all switches)
Multi-Resonant-Doubler	1.7	11.7	2.75 (10 switches), 2 (13 switches), 1.25 (22 switches)
Cascaded Resonant	1.7	8.5	2.625 (12 switches), 1.625 (16 switches), 1.125 (24 switches)
Fibonacci	2.2	8.9	2.165 (13 switches), 1.4775 (16 switches)
Series-Parallel	1	12.4	1.25 (22 switches)
Dickson (Switched-Tank)	4.4	5	0.8 (22 switches)

due to capacitor ratio mismatch is found to have a relatively minor effect on the performance of the converter.

## Performance Comparison

Next, we use the MRD as an example to compare the performance of multi-phase SC converters with typical two-phase SC converters. For discrete implementations (especially for low-voltage applications), both the switch number (and the associated gate drive circuitry) and the passive component number can greatly affect the solution size. Table 7.2 compares the required number of components of the MRD and other 8-to-1 SC converters. It can be seen that the MRD uses fewer components than all other topologies, including the cascaded resonant converter (a type of two-phase voltage doubler) and the Fibonacci converter, which is at the theoretical lower limit of two-phase SC converters. Moreover, as shown in Table 7.3, when considering the total passive component volume from the fundamental energy transfer perspective as discussed in Chapter 3, the doubler-based topologies are found to have excellent passive component utilization among all topologies. Because of these reasons, the MRD has the potential to achieve higher power density than its two-phase counterparts.

Nevertheless, the switch number reduction is not free and can result in higher switch VA rating and output impedance (which negatively impacts efficiency). Assuming all switches have the same on-resistance  $R$ , which is often the case for applications lower than 25 V due to limited discrete power MOSFET selection [24], the output impedance of the MRD is  $2.75R$  with the minimum number of switches (10 switches), which is higher than the other topologies. If conduction loss is a major concern, more switches can be paralleled in the key current path. The output impedance can be reduced to  $2R$  for 13 switches, or  $1.25R$  for 22 switches, resulting in comparable output impedance to other topologies with a similar

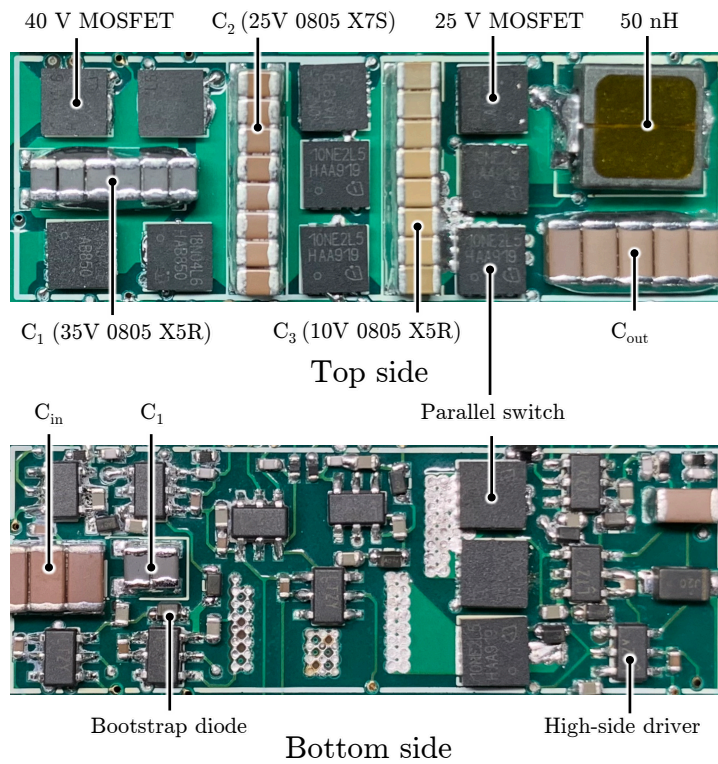


Figure 7.6: Photograph of the converter prototype. Dimensions:  $1.38 \times 0.46 \times 0.22$  inch ( $3.5 \times 1.17 \times 0.55$  cm).

number of total switches. Fundamentally, there is no win-win situation that can achieve low component count and low output impedance simultaneously. The Dickson and series-parallel converters can have low output impedance because they use a large number of switches to split the current into multiple parallel paths. In comparison, the MRD uses less switches but has only one current path and thereby higher output impedance.

However, in practical implementations, MRD's low required switch count can make it more adaptable to different applications compared to two-phase topologies with an inherently large number of switches and gate drivers. Depending on the design specifications, more switches can be paralleled to reduce the output impedance, without requiring additional gate drive circuits. In addition, the low component count can greatly simplify the PCB layout and increase power density. Since PCB loss contributes a large portion to the overall loss for low-voltage high-current applications, a clean and simple PCB layout is important for a high-performance design.

## Hardware Implementation and Experimental Results

An annotated photograph of the hardware prototype is shown in Fig. 7.6, with key components highlighted. Table 7.4 provides the main operating parameters of the converter and

Table 7.4: Key prototype parameters of the MRD converter

	Nominal	Range
Input voltage	48 V	40 – 60 V
Output voltage	6 V	5 – 7.5 V
Output current	40 A	40 A
Power rating	240 W	200 – 300 W
Switching frequency	70 kHz	70 – 78 kHz

Table 7.5: Main component listing of the MRD converter

Component	Part number	Parameters
Switch $Q_1$ - $Q_4$	Infineon BSZ018N04LS6	40 V, 1.8 m $\Omega$
Switch $Q_5$ - $Q_{10}$	Infineon BSZ010NE2LS5	25 V, 1 m $\Omega$
Flying capacitor $C_1$	TDK C2012X5R1V226M125AC	X5R, 35 V, 22 $\mu\text{F}^* \times 14$
Flying capacitor $C_2$	TDK C2012X7S1E106K125AC	X7S, 25 V, 10 $\mu\text{F}^* \times 16$
Flying capacitor $C_3$	Murata GRM21BR61A476ME15L	X5R, 10 V, 47 $\mu\text{F}^* \times 16$
Resonant inductor L	Coilcraft SLC7530S-500ML	50 nH, 50 A $I_{\text{sat}}$
Gate driver	Analog Devices LTC4440	80 V, high-side
Bootstrap diode	Infineon BAT6402VH6327XTSA1	40 V, Schottky

\* The capacitance listed here is the nominal value before dc derating.

Table 7.5 lists the specifications of the main components. Thanks to the reduced-voltage stress of the doubler topology, low voltage silicon MOSFETs can be used (40 V for  $Q_{1-4}$  and 25 V for  $Q_{5-10}$ ). In order to reduce the output impedance,  $Q_{8-10}$  are each implemented with two paralleled switches, one on each side of the board. The cascaded bootstrap method discussed in Chapter 5 is used to power the floating gate drivers. The PCB has 4 layers and is fabricated with 4 oz copper on the outer layers (where the critical conduction path is) and 3 oz copper on the inner layers.

The minimum switching frequency is determined by the inductor and the capacitor  $C_3$ , where  $f_{\text{sw,min}} = \frac{1}{2\pi\sqrt{LC_3}}$ . However, as discussed in Chapter 6, to counteract the effects of component non-idealities and further reduce the conduction loss, the converter can operate at a frequency that is slightly higher than resonance, at the expense of imperfect ZCS operation and slightly increased switching loss. For this prototype,  $f_{\text{sw,min}} = 52$  kHz and the actual switching frequency is 70 kHz when operating at 48-to-6 V. Measured waveforms of inductor current and switch node voltage are shown in Fig. 7.7. The converter is also able

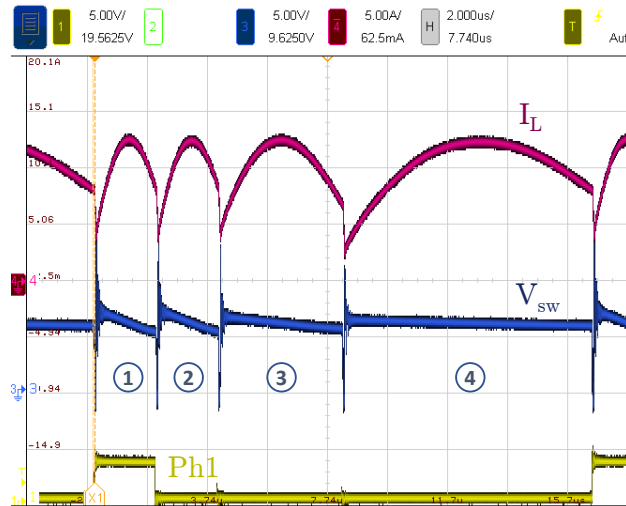


Figure 7.7: Waveform of inductor current and switch node voltage.

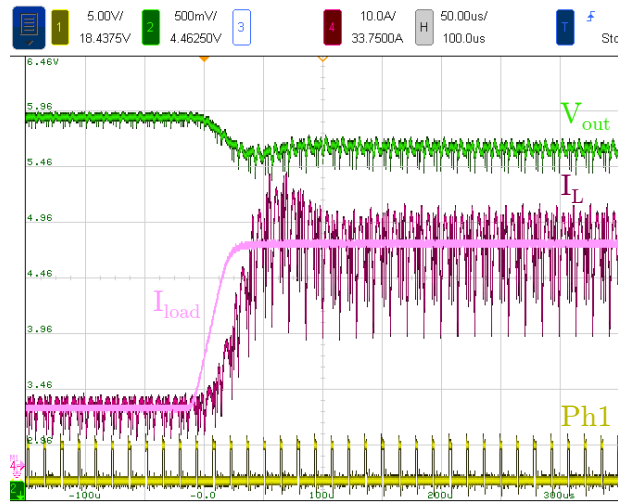
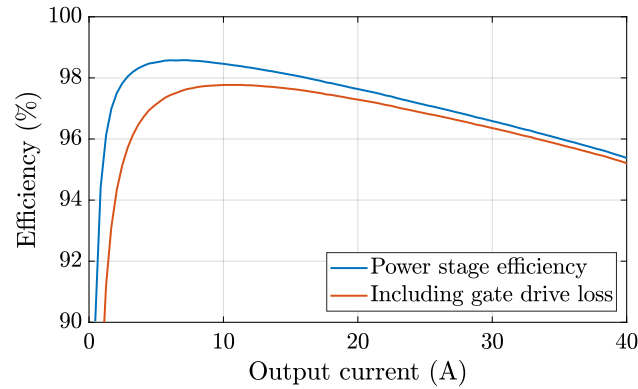
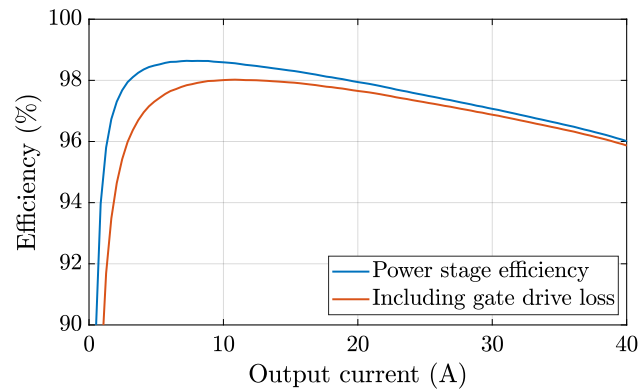


Figure 7.8: Load-step from 10 A to 40 A at 48 to 6 V.

to handle large load transients. In Fig. 7.8, the output voltage does not show significant undershoot after a 10 A to 40 A load step and stabilizes within a few switching cycles.

The converter has been tested up to 40 A output current. Based on the volume of the smallest rectangular box that can contain the converter, the power density is  $1675 \text{ W/in}^3$  (102 kW/L) for 48-to-6 V conversion and  $2100 \text{ W/in}^3$  (128 kW/L) for 60-to-7.5 V conversion. The efficiency is measured with a Yokogawa WT3000E precision power meter, and the results are plotted in Fig. 7.9 to Fig. 7.11 for various input voltages. For the nominal 48-to-6 V conversion, the peak efficiency is 98.6% (98.0% including gate drive loss). The full load

Figure 7.9: Measured 40 V to 5 V efficiency ( $f_{sw} = 70$  kHz).Figure 7.10: Measured 48 V to 6 V efficiency ( $f_{sw} = 70$  kHz).

efficiency at 40 A is 96.0% (95.9% including gate drive loss). The high efficiency performance can greatly reduce the thermal management requirement. As shown in Fig. 7.12, the converter maintains a maximum temperature of around  $60^{\circ}\text{C}$  at full power with fan cooling only. Additionally, the high efficiency also reduces the impact of load regulation. Even though the converter operates in fixed-ratio mode (open loop), the output voltage only droops 250 mV (4.2% of  $V_{out}$ ) at full load as depicted in Fig. 7.13.

Table 7.6 compares this work with some of the best existing works. Compared with the best in-class LLC converter [127], this work has very similar efficiency performance, but can achieve 50% more power density at a much lower power rating. This makes it easy to be placed very close to the actual load to minimize the power distribution loss, while maintaining the flexibility to scale up for higher power needs. Since there are no other 8-to-1 SC works for this application yet, we also compare the results with the 4-to-1 switched-tank converter [23]. Although the efficiency is slightly lower, the MRD can achieve doubled conversion ratio with much higher power density.



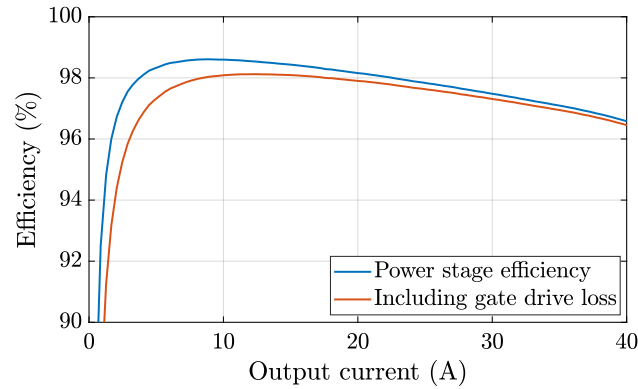


Figure 7.11: Measured 60 V to 7.5 V efficiency ( $f_{sw} = 78$  kHz).

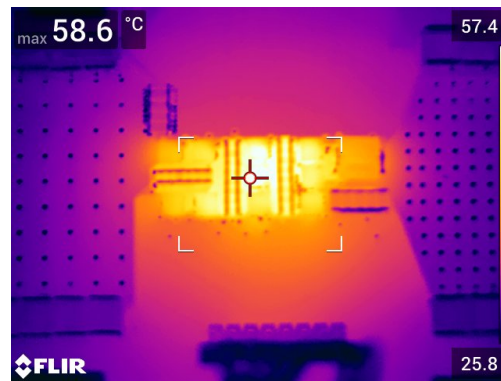


Figure 7.12: Thermal performance with fan cooling only ( $V_{in} = 48$  V,  $I_{out} = 40$  A).

## Parallel Operation for Higher Output Power

Owing to the nature of multi-phase operation, part of the converter only operates for a portion of the switching period. As shown in Fig. 7.14, capacitor  $C_1$  (rated at  $4V_o$ ) only operates in the first quarter period and  $C_2$  (rated at  $2V_o$ ) operates in the first half period. This unique characteristic can potentially be utilized to save component counts and space in interleaved parallel operation for higher output power. Since the first doubler stage ( $8V_o$  to  $4V_o$ ) only operates for one quarter of the period, it can be used to drive four paralleled phases (with  $90^\circ$  phase shift each), only at the cost of increased switching frequency (thereby switching loss) of the first stage, and four additional switches for the four parallel phases in the second stage. Similarly, each doubler at the second stage ( $4V_o$  to  $2V_o$ ) can drive two following stages ( $2V_o$  to  $V_o$ ). This arrangement can help fully utilize the availability of all circuit components, and save space and cost compared to traditional interleaving designs with straightforward converter paralleling. A simple version of this concept is demonstrated in [137].

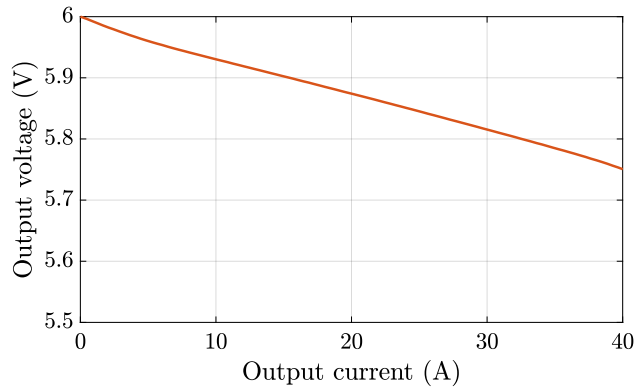
Figure 7.13: Load regulation ( $V_{in} = 48$  V,  $V_{out} = 6$  V).

Table 7.6: Comparison of this work and existing high-step-down bus converters

Reference	Topology	Voltage ratio	Output current	Power Density (W/inch <sup>3</sup> )	System Efficiency	Notes
This work	Resonant Multi-phase Doubler	48-to-6 V	40 A	1675	full load: 95.9% peak: 98.0%	fixed-ratio, silicon MOSFET
EPC AppNote014 [127]	LLC	48-to-6 V	150 A	1100	full load: 96.9% peak: 98.0%	fixed-ratio, Gen-5 GaN FET
EPC9205 [136]	Buck	48-to-6 V	14 A	$\leq 900$	full load: 91.8% peak: 93.9%	Gen-5 GaN FET
Google Switched-Tank [23]	Resonant Dickson	54-to-13.5 V	50 A	500	full load: 97.41% peak: 98.61%	54 V input, 4:1 fixed-ratio, components are not densely populated

## 7.5 6-to-1 Cascaded Series-Parallel Converter

### Operating Principle

With the same fundamental structure and the same number of components, the MRD converter can be converted to a 6-to-1 multi-resonant SC converter, by moving the source terminal of  $Q_5$  from the positive side of  $C_3$  to the switch node. Its circuit schematic is shown in Fig. 7.15. Through three-phase operation, the converter can behave as a 2-to-1 converter cascaded with a 3-to-1 series-parallel converter, herein named cascaded series-parallel converter. Thanks to the multi-phase operation, this topology uses fewer switches and capacitors than other two-phase 6-to-1 SC converters. Even though its conversion ratio is not as high as that of the MRD converter, its series-parallel stage can split the output current into two paths, thus reducing the conduction loss and improving the conversion efficiency.

The key control signals, inductor and capacitor current waveforms, and the equivalent circuit of the three operating phases are shown in Fig. 7.16. It can be seen that, the converter achieves a 2-to-1 step-down during the first  $\frac{1}{3}$  of the switching period through a series-mode

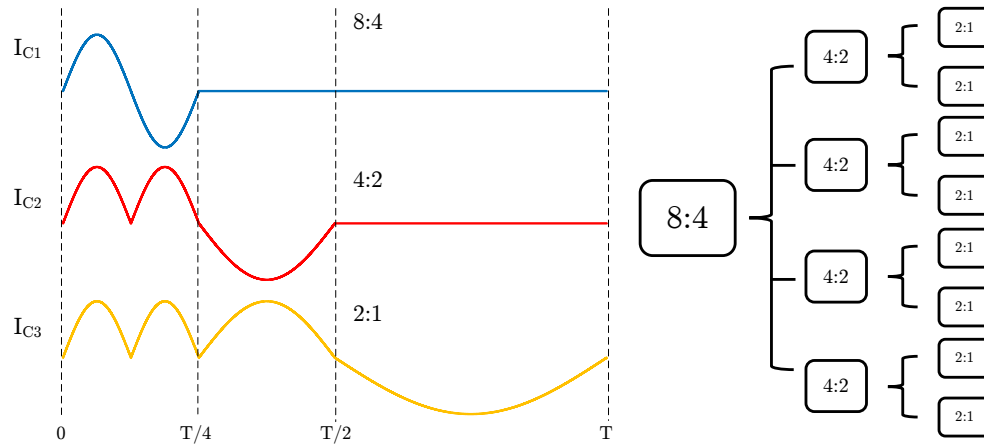


Figure 7.14: Parallel operation of MRD converters to optimize the utilization of the flying capacitors and the associated switches.

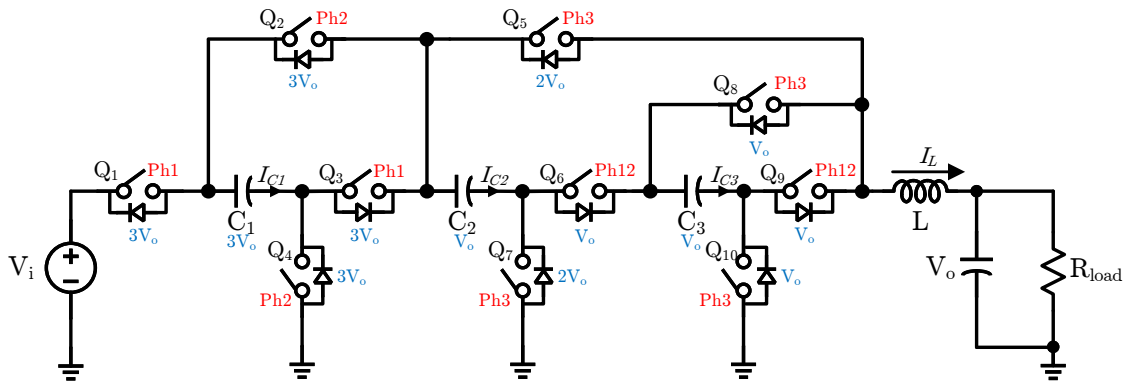


Figure 7.15: Schematic drawing of the 6-to-1 cascaded series-parallel converter with device ratings and control signals labeled.

operation, followed by a 3-to-1 parallel-mode operation during the last  $\frac{2}{3}$  of the switching period. The detailed operation of the three phases are as follows:

- Phase 1: The “Ph1” and “Ph12” switches in Fig. 7.15 are ON.  $C_1$ ,  $C_2$ ,  $C_3$  and  $L$  are connected in series. All flying capacitors are resonantly charged by the input. The duration of Phase 1 is  $\frac{1}{6}$  of the switching cycle. The equivalent resonant frequency of this phase is  $f_{r,ph1} = \frac{1}{2\pi\sqrt{LC_{eq1}}}$ , where  $\frac{1}{C_{eq1}} = \frac{1}{C_1} + \frac{1}{C_2} + \frac{1}{C_3}$ .
- Phase 2: The “Ph2” and “Ph12” switches are ON. In this phase, all flying capacitors are still connected in series, but  $C_1$  is being discharged. The length of the phase and

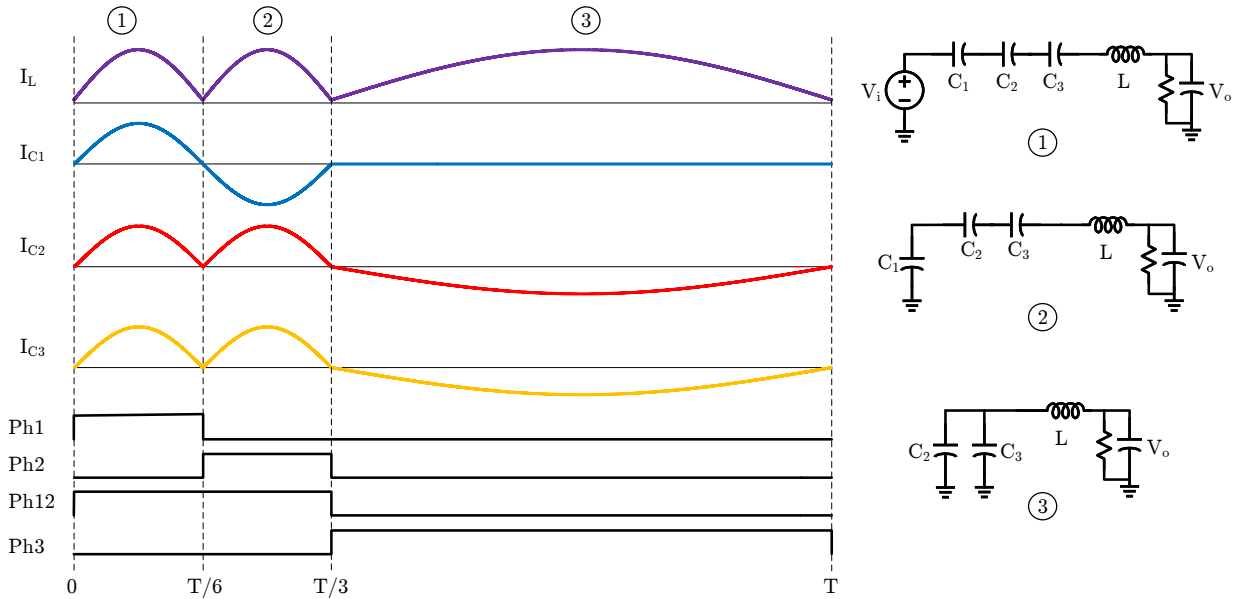


Figure 7.16: Inductor and capacitor current waveforms, control signals, and equivalent circuits of the 6-to-1 cascaded series-parallel converter.

the equivalent resonant frequency remain the same as in Phase 1.

- Phase 3: Only the “Ph3” switches are ON. In this phase,  $C_1$  is disconnected,  $C_2$  and  $C_3$  are in parallel, and are resonantly discharged to the load. The equivalent resonant frequency of this phase is  $f_{r,ph3} = \frac{1}{2\pi\sqrt{L(C_2+C_3)}}$ .

The parallel operation in Phase 3 demands that  $C_2 = C_3 = C$ , while capacitor charge balance analysis of  $C_1$  indicates that the minimum  $C_1$  that is required to achieve soft-charging operation is  $C_{1,\min} = \frac{1}{6}C$ .

Using the methodology outlined in Section 3.5, Fig. 7.17 compares the theoretical passive and active component utilization of various ReSC converters at a conversion ratio of 6-to-1. A buck converter is also included for reference. It can be seen that, the proposed cascaded series-parallel converter can achieve similar theoretical performance to the series-parallel converter even with a greatly reduced number of components. This is of note as the passive volume of the series-parallel topology is known to be at the theoretical lower limit [25]. Compared to the switched-tank converter (STC), the cascaded series-parallel converter can potentially achieve higher power density, even though the switch stress is higher. Moreover, as discussed in [138], the efficiency performance of the series-parallel based converters is underestimated by the switch VA analysis, when the switches cannot be sized optimally due to limited selections in discrete designs. This is often the case for ReSC-based 48 V

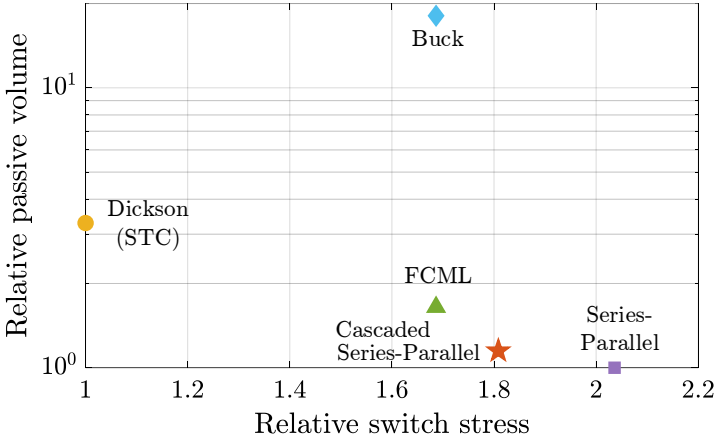


Figure 7.17: Theoretical performance comparison of various ReSC converters and buck converter at 6-to-1 conversion ratio.

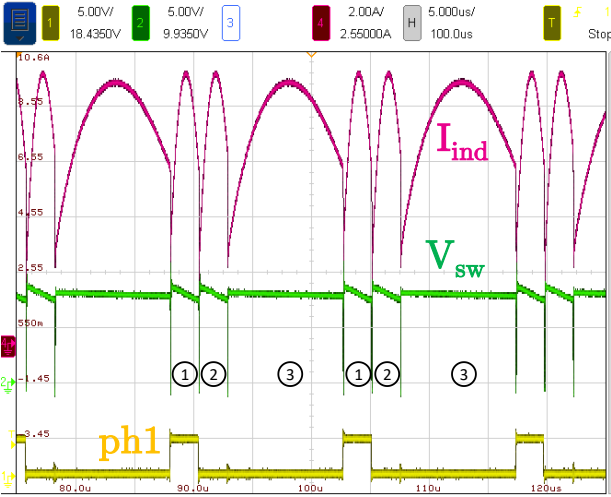


Figure 7.18: Inductor current and switch node voltage of the cascaded series-parallel converter.

bus converters for data centers, since discrete power MOSFETs below 25 V are not readily available and different topologies may end up using the same devices. As a result, the series-parallel based topologies with good passive component utilization are more favored, as their disadvantageous switch utilization is relatively mild considering the actual switches available.

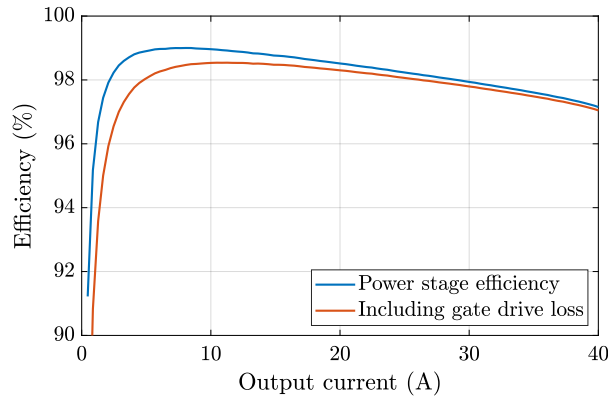


Figure 7.19: Measured 48 V to 8 V efficiency of the cascaded series-parallel converter ( $f_{sw} = 68$  kHz).

## Experimental Results

The prototype in Fig. 7.6 is modified to operate as a 6-to-1 cascaded series-parallel converter. All components remain the same, except that  $C_2$  and  $C_3$  are changed to have the same capacitance (16x Murata GRM21BR61A476ME15L). The measured waveforms of inductor current and switch node voltage are shown in Fig. 7.18. The converter has been tested up to 40 A at 48-to-8 V, with a power density of 2230 W/in<sup>3</sup>. The measured efficiency result is shown in Fig.7.19, with 99.0% peak efficiency (98.5% including gate drive loss) and 97.1% (97.0% including gate drive loss) full-load efficiency. More results can be found in [139].

These efficiency and power density numbers have approached those of the cascaded resonant converter with a 4-to-1 ratio in Chapter 6, demonstrating the great potential of this cascaded series-parallel topology. Note that the tested hardware is designed for the MRD converter with the source terminal of  $Q_5$  connected to the drain terminal of  $Q_8$ . Consequently,  $Q_8$  in fact carries all of the output current rather than half as shown in Fig. 7.15. With hardware specifically optimized for this topology, higher efficiency performance can be expected.

## 7.6 Alternative Topology Variations

The presented MRD and cascaded series-parallel multi-resonant converters are modular, and can be extended to higher conversion ratios. The basic building block is shown in Fig. 7.20. It consists of three switches and one capacitor. Depending on the desired conversion ratio and the number of operating phases, the right side of  $Q_1$  can be connected either to the neighboring block to form a doubler stage, or to the output inductor to form a series-parallel stage.

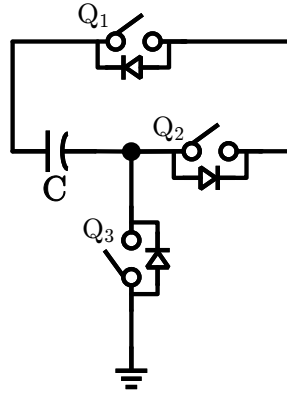


Figure 7.20: Fundamental building block of the multi-phase resonant SC converter.

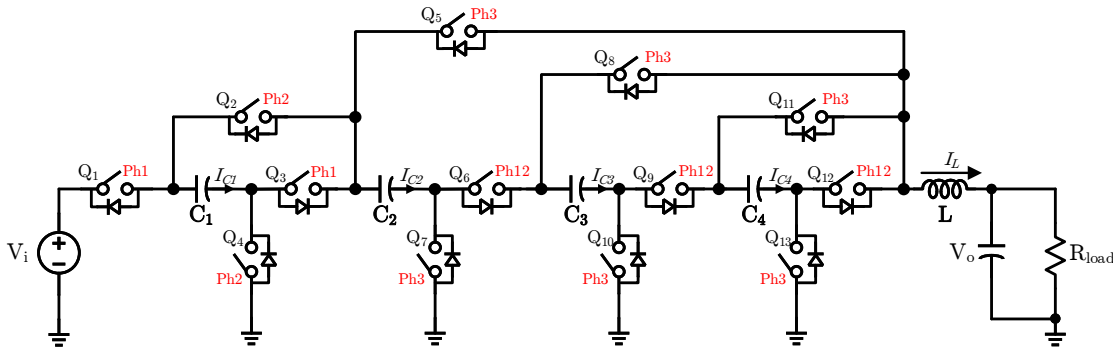


Figure 7.21: Schematic drawing of an 8-to-1 cascaded series-parallel converter (three-phase).

A few examples are demonstrated here. The circuit schematics and operating waveforms of three-phase, 8-to-1 and 10-to-1 cascaded series-parallel converters are shown in Fig. 7.21 to Fig. 7.24. They can be viewed as direct extensions of the 6-to-1 version in Fig. 7.15, which both have a 2-to-1 front-end stage followed by a series-parallel stage. Assuming there are  $N$  flying capacitors in total, then the series-parallel stage has  $N - 1$  capacitors and a corresponding conversion ratio of  $[(N - 1) + 1] = N$ . Therefore, the total conversion ratio is  $2N$  for a three-phase cascaded series-parallel converter with  $N$  flying capacitors. The total number of switches is  $3N + 1$ .

A 12-to-1 multi-resonant SC converter is shown in Fig. 7.25. To reduce the number of components, four-phase operation is used, with two cascaded doubler stages followed by a 3-to-1 series-parallel stage. Its key operating waveforms are shown in Fig. 7.26. This converter can be viewed as a modification of the MRD converter in Fig. 7.4, with one additional building block at the last stage to split the output current while achieving 3-to-1 conversion

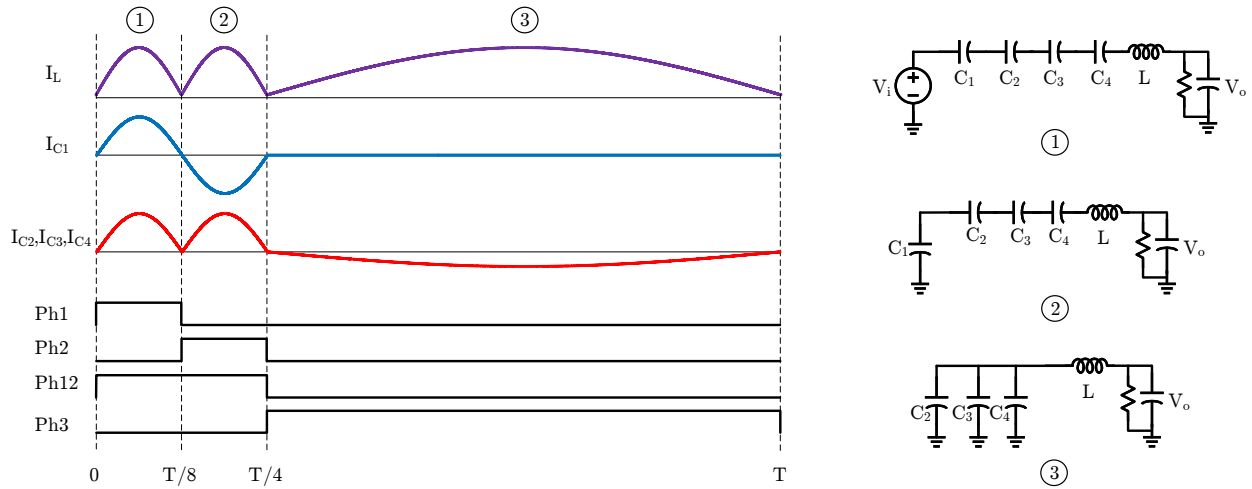


Figure 7.22: Inductor and capacitor current waveforms, control signals, and equivalent circuits of the 8-to-1 cascaded series-parallel converter.

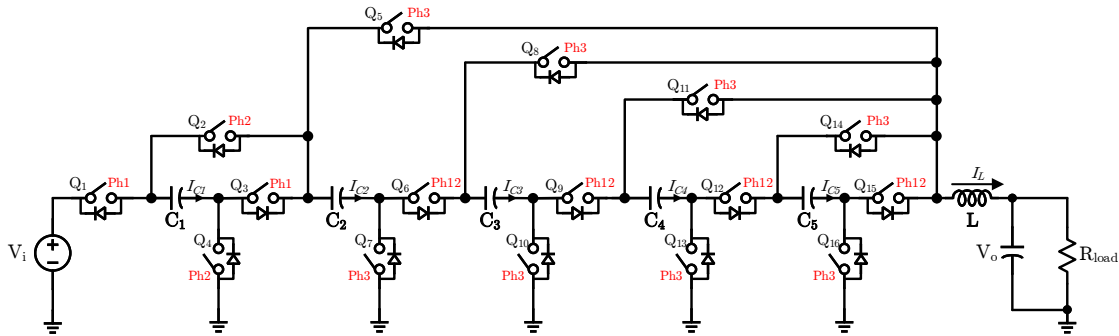


Figure 7.23: Schematic drawing of a 10-to-1 cascaded series-parallel converter (three-phase).

ratio.

A limitation of these multi-resonant SC converters is the high RMS current in the series-mode switches. For a desired  $N$ -to-1 conversion ratio, the duty ratio of the four switches in the first 2-to-1 doubler stage is  $\frac{1}{N}$ , and it gradually increases for the following switches. As discussed in Section 2.4, given fixed output current, the larger the duty ratio deviation from 0.5, the larger the switch RMS current and the resultant conduction loss. In comparison, the interleaved cascaded resonant converters in Chapter 6 always have a duty ratio of 50%, and may achieve higher efficiency under the same condition.



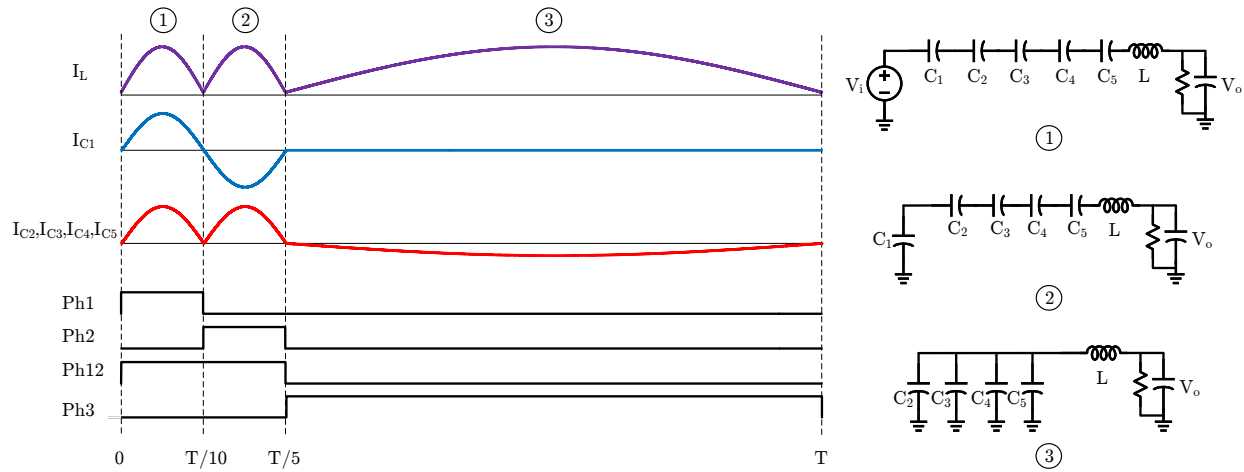


Figure 7.24: Inductor and capacitor current waveforms, control signals, and equivalent circuits of the 10-to-1 cascaded series-parallel converter.

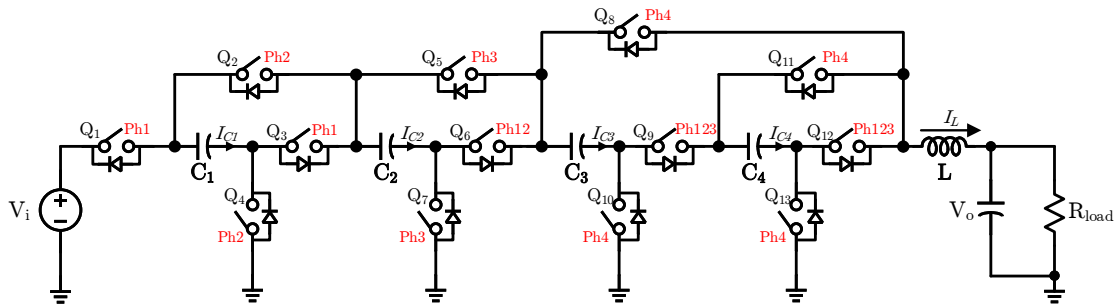


Figure 7.25: Schematic drawing of a 12-to-1 cascaded doubler series-parallel converter (four-phase).

## 7.7 Chapter Summary

In this chapter, the concept of multi-operating-phase is explored and applied to ReSC converters. Compared with two-phase operation, the multi-phase operation can achieve the same conversion ratio with significantly fewer capacitors and switches, leading to potentially better power density and efficiency performance. Two multi-resonant topologies, the 8-to-1 multi-resonant-doubler and the 6-to-1 cascaded series-parallel converter, are proposed and analyzed. Their superior performance is demonstrated by theoretical comparisons and hardware prototypes. At 48 V to 8 V, the cascaded series-parallel prototype achieves 99.0% peak efficiency (98.5% including gate drive loss), 97.1% full-load efficiency (97.0% including

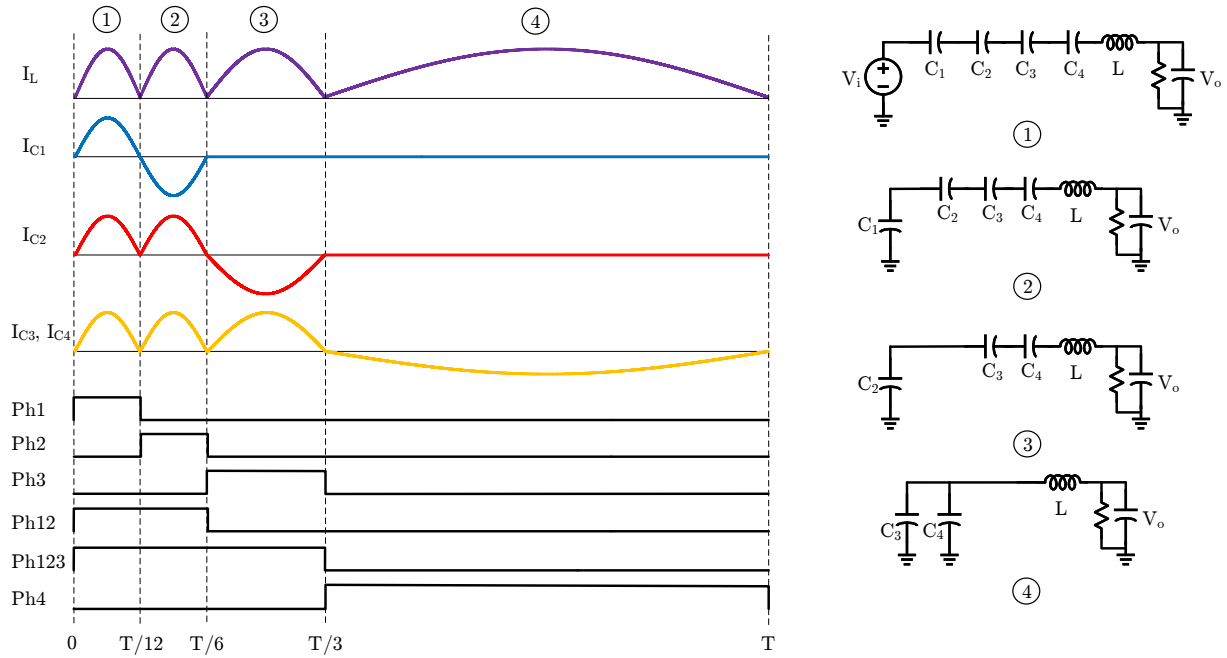


Figure 7.26: Inductor and capacitor current waveforms, control signals, and equivalent circuits of the 12-to-1 cascaded doubler series-parallel converter.

gate drive loss), and  $2230 \text{ W/in}^3$  power density. At 48 V to 6 V, the multi-resonant-doubler prototype achieves 98.6% peak efficiency (98.0% including gate drive loss), 96.0% full-load efficiency (95.9% including gate drive loss), and  $1675 \text{ W/in}^3$  power density. These results show great promise of using multi-resonant SC converters in high step-down (and step-up) applications such as two-stage power delivery from a 48  $V_{dc}$  bus in data centers.

## Chapter 8

# Multi-Level Binary Hybrid Switched-Capacitor Converter

This chapter presents a new hybrid SC topology to address the need of direct power conversion from  $48 V_{dc}$  to point-of-load (PoL) voltages in datacenters. The proposed hybrid converter carries *Multi-Level Binary* (MLB) voltages on the flying capacitors, which make it well-suited for PoL applications with very high conversion ratios. It can be viewed as an 8-to-1 multi-phase doubler SC converter merged with a two-phase interleaved buck converter [140]. Compared to two-phase hybrid SC topologies, multi-phase operation can achieve higher conversion ratio at the SC stage with an equal or fewer number of components, and thus reduce the switch and inductor stress of the following buck stage. In addition, the output inductors in the proposed topology benefit from a frequency multiplication effect similar to that of FCML converters. This can help further reduce the inductor size without increasing the switching frequency.

### 8.1 Background and Motivation

As discussed in Chapter 6 and 7, to address the challenge of very high conversion ratio from  $48 V_{dc}$  to the extreme low voltage and high current point-of-loads (PoL) in modern datacenters, a two-stage approach is commonly used. The  $48 V$  is first converted to an intermediate bus voltage (e.g., 12, 8, 6 V) through a bus converter, then stepped down to 1–2 V by PoL converters [33], [105], [138], [139], [141]–[143]. However, depending on application specifics, a number of recent works have demonstrated direct  $48 V$  to PoL conversion [109]–[113], and have shown promise for better overall efficiency, power density and reduced system cost. For such a high conversion ratio, a transformer-based converter is commonly used [110], [111]. Unavoidably, there is a trade-off between conversion efficiency and voltage regulation range. To address this challenge, the high step-down and the regulation requirements can be split between a highly efficient fixed-ratio LLC converter and an upstream buck-boost converter [112] or a series-stacked buck converter with partial power processing [113].

In addition to transformer-based solutions, recently proposed hybrid topologies comprising multi-phase buck converters merged with a fixed-ratio SC converter have also shown attractive features for direct 48 V to PoL conversion [18], [144], [145]. Similar to transformers, SC converters also have excellent performance at fixed-ratio conversions, thanks to their efficient utilization of active and passive components [7], [19], [25]. By combining the buck and the SC stages, the total number of components (e.g., switches and decoupling capacitors) can be reduced compared to cascaded two-stage solutions. More importantly, the inductors in the buck stage can greatly reduce or eliminate the capacitor charge sharing loss of the SC converter through soft-charging operation [16], [19], leading to very efficient fixed-ratio conversion in the SC stage. However, due to the fact that the circuit complexity of SC converters increases in proportion to the conversion ratio, the SC stage in the majority of existing hybrid works can only achieve a conversion ratio of 4-to-1 or 6-to-1, with the remaining conversion burden placed on the buck stage. Given a fixed output voltage, the efficiency of a buck converter generally decreases with increasing input voltage. If the first stage SC converter can achieve a higher conversion ratio without much extra loss, the input voltage of the buck converter can be decreased, and the overall 48V-to-PoL efficiency can be improved. References [104], [108] suggest that using a highly efficient 48 V to 6 V fixed-ratio converter in conjunction with a 6 V to PoL buck converter can provide improved overall efficiency.

This chapter proposes and explores a new hybrid topology with *Multi-Level Binary* (MLB) voltages on the flying capacitors that can simultaneously achieve high efficiency and power density for direct 48 V to PoL applications. The proposed MLB-PoL converter consists of an 8-to-1 SC stage and a two-phase interleaved buck stage with natural current balancing. By having multiple operating phases, the SC stage can achieve a conversion ratio of 8-to-1 with the theoretical minimum number of components (10 switches and 3 capacitors). The operation of the output buck stage is merged with the SC stage without the need for additional switches, thereby reducing the conduction loss. Furthermore, the inductors of the buck stage also benefit from a frequency multiplication effect similar to that of the FCML converter [45], [50]. This can further reduce the inductor size without increasing the switching frequency of the SC stage. A 48 V to 2.5–1.0 V converter prototype with 65 A output current is built and tested. At 48 V to 2 V, the prototype achieves 95.1% peak efficiency (94.3% including gate drive loss), 91.3% full load efficiency (91.1% including gate drive loss), and 395 W/in<sup>3</sup> power density.

## 8.2 Proposed Topology

The schematic drawing of the proposed MLB-PoL converter is shown in Fig. 8.1, with switch and capacitor voltage ratings labeled in red and operating phases labeled in blue. The voltage, current, and PWM waveforms of the converter and the equivalent circuit model of different operating phases are shown in Fig. 8.2. The proposed converter can be viewed as an 8-to-1 SC converter merged with a two-phase interleaved buck converter.

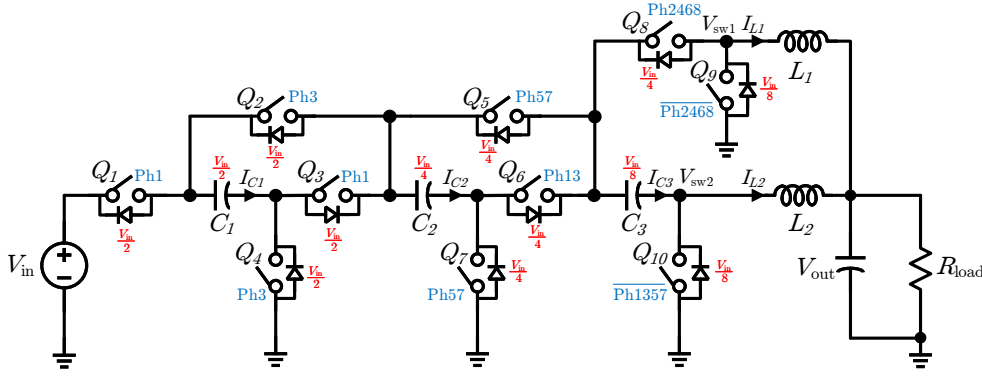


Figure 8.1: Schematic drawing of the proposed MLB-PoL converter. The device voltage ratings are labeled in red and the operating phases of the switches are labeled in blue.

The MLB-PoL converter employs multiple operating phases within each switching cycle. As discussed in Chapter 7, compared with typical SC converters that have two operating phases, multi-phase SC converters can achieve the same conversion ratio with significantly fewer switches and flying capacitors. The SC stage in the proposed topology is an 8-to-1 multi-phase voltage doubler (same as the multi-resonant-doubler ReSC converter in Chapter 7) [133], [142], which is one practical circuit implementation that achieves the theoretical maximum gain for an 8-to-1 SC converter (i.e., 10 switches and 3 capacitors). The flying capacitors carry binary voltages:  $C_1 = \frac{1}{2}V_{in}$ ,  $C_2 = \frac{1}{4}V_{in}$  and  $C_3 = \frac{1}{8}V_{in}$ , as do the switches:  $Q_{1,2,3,4} = \frac{1}{2}V_{in}$ ,  $Q_{5,6,7,8} = \frac{1}{4}V_{in}$  and  $Q_{9,10} = \frac{1}{8}V_{in}$ .

To maintain flying capacitor charge balance in multi-phase SC converters, the lower voltage capacitors must be charged/discharged for more time than the higher voltage ones [146]. Here, in order to merge the operation of the SC stage with the buck stage, the charge/discharge cycles of  $C_2$  and  $C_3$  are divided into multiple phases. As shown in Fig. 8.2,  $C_1$  is charged in Phase 1 and discharged in Phase 3,  $C_2$  is charged in Phase 1 and 3, and discharged in Phase 5 and 7, whereas  $C_3$  is charged in Phases 1, 3, 5, 7 and discharged in Phases 2, 4, 6, 8. The operation of the two-phase interleaved buck stage is merged with the SC stage without additional switches. This can help reduce the conduction loss compared to a two-stage approach, where the buck converter is directly cascaded with a SC converter. The two inductors are energized (i.e., current ramped up) alternately:  $L_1$  is energized by  $C_3$  during Phases 2, 4, 6, 8, and  $L_2$  is energized by the series combination of the flying capacitors during Phases 1, 3, 5, 7. Phase 9 is the freewheeling state for output voltage regulation where the current in both inductors ramps down.

There is an inherent current balancing mechanism between the two inductors. If  $I_{L1}$  is higher and over-discharges  $C_3$ , the switch node voltage of  $L_2$  will then become higher, inducing a higher  $I_{L2}$  that can charge  $C_3$  back to its nominal value. This operation is similar to the automatic current sharing behavior of the series-capacitor buck converter, which can

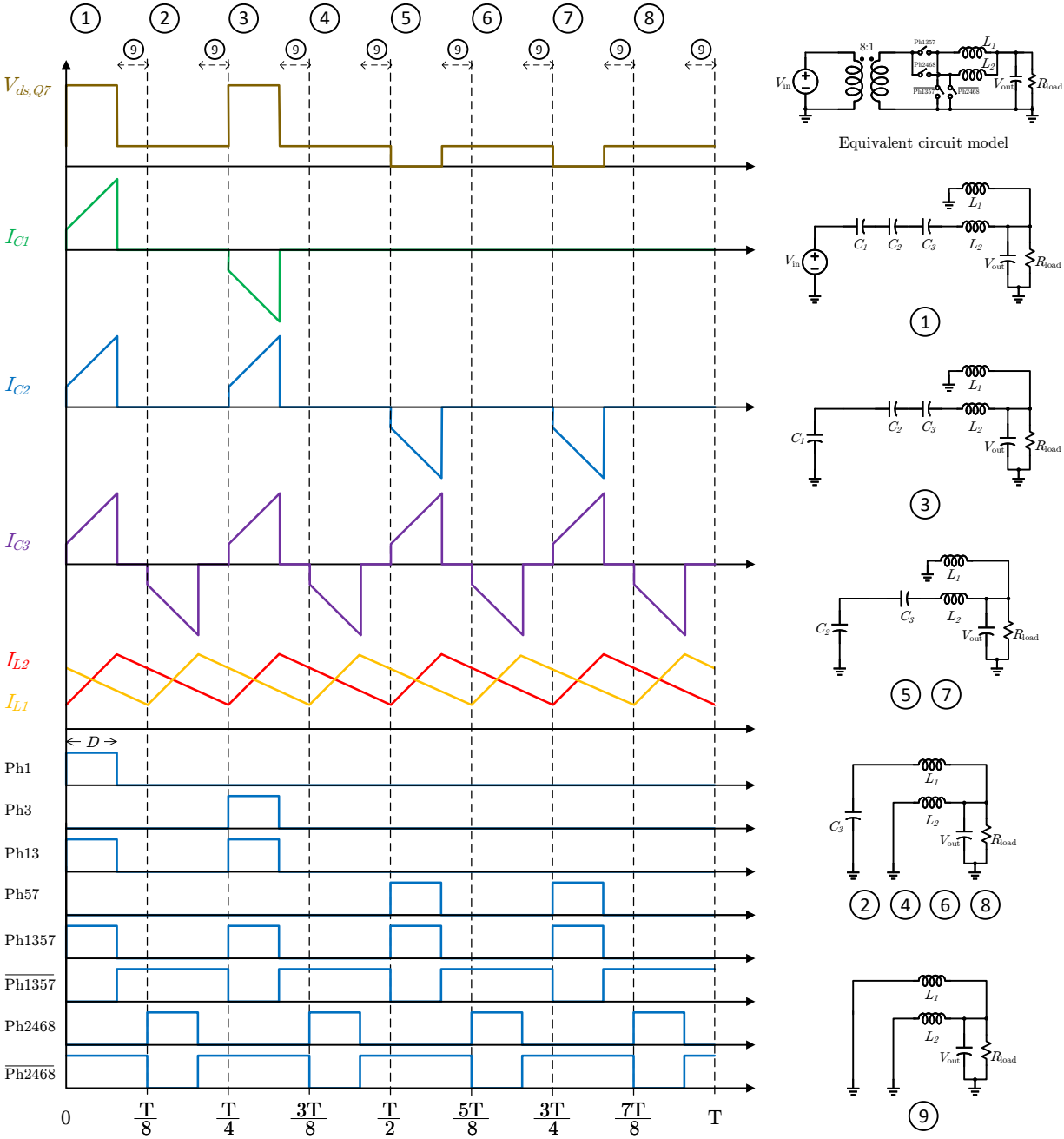


Figure 8.2: Voltage, current and PWM waveforms of the proposed MLB-PoL converter and equivalent circuit models.

be found in [147]. Here,  $C_3$  acts as the series capacitor that creates a negative feedback loop between the capacitor voltage and the average inductor currents. There is a caveat

Table 8.1: Voltage rating and operating frequency of the main active and passive components

	$V_{\text{blocking}}$	$f_{\text{sw}}$
$Q_1 - Q_4$	$\frac{V_{\text{in}}}{2}$	$f_0$
$Q_5 - Q_7$	$\frac{V_{\text{in}}}{4}$	$2f_0$
$Q_8$	$\frac{V_{\text{in}}}{4}$	$4f_0$
$Q_9 - Q_{10}$	$\frac{V_{\text{in}}}{8}$	$4f_0$ (ZVS)
$C_1$	$\frac{V_{\text{in}}}{2}$	$f_0$
$C_2$	$\frac{V_{\text{in}}}{4}$	$2f_0$
$C_3$	$\frac{V_{\text{in}}}{8}$	$4f_0$
$L_1, L_2$	$\frac{V_{\text{in}}}{8} - V_{\text{out}}$	$4f_0$

about negative inductor current. When operating in forced continuous-conduction mode, the inductor current may go negative at light load. When all switches are OFF during deadtime, the body diodes of  $Q_1$ ,  $Q_2$ ,  $Q_5$ , and  $Q_8$  will conduct to keep the current flowing, and therefore connect the switch node  $V_{\text{sw}}$  to the input. This will result in excess voltage stress on certain switches. In order to clamp the switch node voltage and protect the switches, zener diodes or transient-voltage-suppression diodes can be added to the switch nodes. Owing to similar fundamental SC structures, this phenomenon also appears in the cascaded series-parallel converter and the multi-resonant-doubler converter presented in Chapter 7, and the same mitigation method can be applied.

The MLB-PoL topology also benefits from an inductor frequency multiplication effect similar to that of the FCML converter. Defining  $f_0$  as the switching frequency of  $C_1$  and the associated switches  $Q_{1,2,3,4}$ , then  $C_2$  and  $Q_{5,6,7}$  operate at  $2f_0$  and  $C_3$ ,  $Q_{8,9,10}$ , and  $L_{1,2}$  operate at  $4f_0$ . Note that out of the three switches operating at  $4f_0$ , only  $Q_8$  is hard switched at  $\frac{V_{\text{in}}}{4}$ , while  $Q_9$  and  $Q_{10}$  operate with ZVS. In addition, the higher voltage rated switches operate at a lower frequency, reducing switching loss. This feature can provide inductor size reduction without increasing the frequency of all switches, particularly those with a higher voltage rating. The device voltage ratings and the corresponding switching frequencies are summarized in Table 8.1.

In order to derive the output voltage expression, we define  $D$  as the duty cycle of signal Ph1 as shown in Fig. 8.2. Since the inductors see four times the switching frequency, the effective duty cycle of the buck stage is  $D_{\text{eff}} = \frac{DT}{4} = 4D$ . The output voltage can then be derived by combining the conversion ratio of the fixed-ratio SC stage (DCX ratio) and the

Table 8.2: Comparison of the voltage conversion strategies of selected hybrid converters at 48 V to 2 V conversion

	DCX ratio	Buck ratio
This work	8:1	3:1
LEGO [18]	6:1	4:1
DIH [148]	6:1	4:1
MIH [144]	4:1	6:1
SC Buck [145], [149]	4:1	6:1

conversion ratio of the buck stage:

$$\begin{aligned}
 V_{\text{out}} &= V_{\text{in}} \cdot \text{DCX\_ratio} \cdot \text{buck\_ratio} \\
 &= V_{\text{in}} \cdot \frac{1}{8} \cdot 4D \\
 &= \frac{DV_{\text{in}}}{2}.
 \end{aligned} \tag{8.1}$$

As it is regulated with a duty cycle, the converter can share the same control techniques as that of conventional buck converters. Note that the maximum  $D$  is limited by the length of each operating phase to  $\frac{1}{8}$ . Thus, the highest output voltage of the proposed converter is  $\frac{V_{\text{in}}}{16}$ . With 48 V input, the maximum output voltage at the no-load condition is 3 V, making it incapable of supplying loads at 3.3 V. This reduced output range is a trade-off compared to other hybrid topologies with 4-to-1 or 6-to-1 SC stages. Nevertheless, if a lower output voltage is desired, the proposed converter with its 8-to-1 SC stage has the potential to achieve better performance compared to the 4-to-1 and 6-to-1 topologies. As shown in Table 8.2, for the desired conversion from 48 V to 2 V, the proposed converter can achieve the highest DCX ratio at the SC stage among all hybrid topologies, resulting in reduced stress at the following buck stage. This reduced stress can improve the buck stage efficiency, which can have a substantial impact on the overall system efficiency. Moreover, it is found that the total switch VA rating ( $\sum V_{ds}I_{rms}$ ) of the proposed converter can be as low as half that of a stand-alone buck converter, indicating better switch utilization in addition to reduced inductor stress.

### 8.3 Hardware Design and Experimental Results

A 48 V to 2.5–1.0 V hardware prototype with 65 A output current is designed and tested to verify the functionality of the proposed converter. The annotated photograph of the prototype is shown in Fig. 8.3, and the specifications of the key components are tabulated in Table 8.3. The main operating parameters are summarized in Table 8.4.



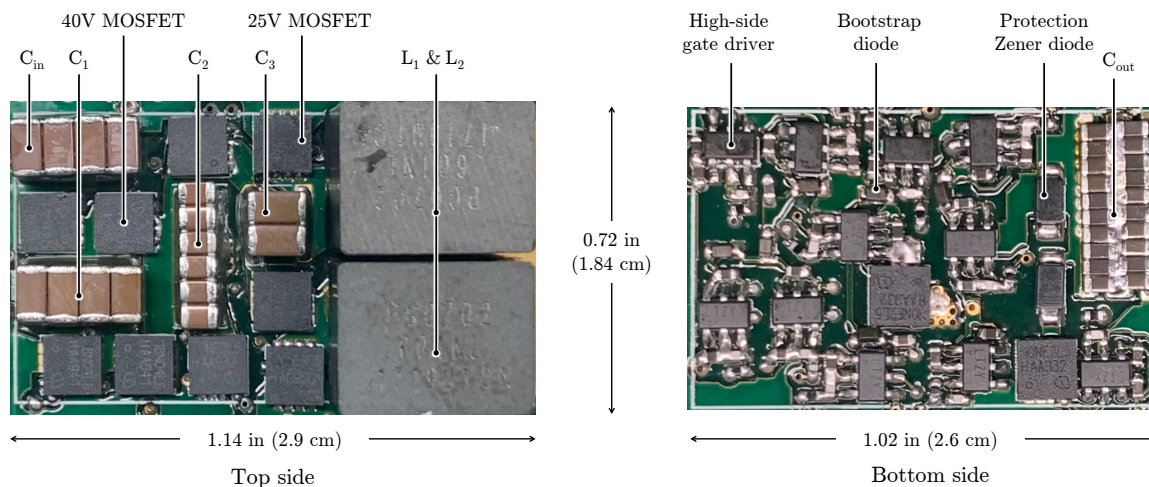


Figure 8.3: Photograph of the prototype. Dimensions:  $1.14 \times 0.72 \times 0.39$  inch ( $2.9 \times 1.84 \times 1.01$  cm).

In order to report a power/current density number by box volume and to compare directly with other commercial power modules, all main components are tightly placed within a 1.14 inch by 0.72 inch (2.9 cm by 1.84 cm) rectangular PCB area. The switches, flying capacitors, and the inductors are on the top side, while the gate drive circuits and other protection components are placed directly underneath on the back side of the board. Input and output capacitors are also included in the box area. Due to the reduced voltage stress of the doubler SC topology, low-voltage MOSFETs can be used (40 V for  $Q_{1-4}$  and 25 V for  $Q_{5-10}$ ). Since  $Q_{10}$  carries all of the output current, an additional switch is paralleled to reduce the conduction loss. High-side gate drivers with internal level-shifters are used to drive the switches, and a cascaded bootstrap circuit [73] is implemented to power the floating gate drivers. The PCB has 6 layers and is fabricated with 4 oz copper on the outer layers (where the critical conduction path is) and 2 oz copper on the inner layers.

The inductor selection is a critical design knob that affects the peak efficiency, the full-load efficiency, and the power/current density of the prototype. The Eaton HC1-1R0-R inductor used in [18] has high inductance ( $1 \mu\text{H}$ ) and low DCR ( $1.23 \text{ m}\Omega$ ), which may result in excellent peak and full-load efficiency. However, its bulky package size greatly limits the achievable box power/current density. The Coilcraft XAL7070-102 inductor has similar inductance and current rating, but comes in a smaller package size at the cost of higher DCR. It has the potential to achieve high peak efficiency and power density, though possibly at the expense of lower full-load efficiency compared to the Eaton inductor. Note that the peak efficiency of these hybrid converters usually appears at a very light-load condition, whereas the efficiency performance at middle to heavy load range might be more important in practical applications. Ultimately, the Pulse PG0702.601NL is selected, as it offers an

Table 8.3: Main component listing of the prototype

Component	Part number	Parameters
Switch $Q_1$ - $Q_4$	Infineon BSZ018N04LS6	40 V, 1.8 m $\Omega$
Switch $Q_5$ - $Q_8$	Infineon BSZ010NE2LS5	25 V, 1.0 m $\Omega$
Switch $Q_9$ - $Q_{10}$	Infineon IQE006NE2LM5CG	25 V, 0.65 m $\Omega$
Parallel $Q_{10}$	Infineon BSZ010NE2LS5	25 V, 1.0 m $\Omega$
Flying capacitor $C_1$	TDK C3216X5R1V226M160AC	X5R, 35 V, 22 $\mu\text{F}^* \times 8$
Flying capacitor $C_2$	TDK C2012X7S1E106K125AC	X7S, 25 V, 10 $\mu\text{F}^* \times 12$
Flying capacitor $C_3$	TDK C3216X5R1A107M160AC	X5R, 10 V, 100 $\mu\text{F}^* \times 4$
Inductor $L_1, L_2$	Pulse PG0702.601NL	600 nH, 0.91 m $\Omega$
Input capacitor $C_{\text{in}}$	TDK C3216X7S2A335M160AB	X7S, 100 V, 3.3 $\mu\text{F}^* \times 8$
Output capacitor $C_{\text{out}}$	TDK C1608X5R1A226M080AC	X5R, 10 V, 22 $\mu\text{F}^* \times 20$
Gate driver	Analog Devices LTC4440-5	80 V, high-side
Bootstrap diode	Infineon BAT6402VH6327XTSA1	40 V, Schottky

\* The capacitance listed here is the nominal value before dc derating.

Table 8.4: Key parameters of the prototype

Input voltage	48 V
Output voltage	1.0 - 2.5 V
Output current	65 A
Switching frequency (inductor)	250 kHz
Current density	198 A/in <sup>3</sup>

attractive compromise between size and low DCR with a nominal inductance of 600 nH and a DCR of 0.95 m $\Omega$ , all in an acceptable package size. Although the peak efficiency of the prototype with this inductor is nearly 1% lower than a prototype using either of the 1  $\mu\text{H}$  inductors, it achieves a good combination of high power/current density and full-load efficiency.

Compared to ReSC converters, the flying capacitor selection in these types of regulated hybrid SC converters is more relaxed, as the  $C$  and  $L$  values do not need to be tuned precisely so that the converter operates at the  $LC$  resonance point. The capacitance values have relatively minor effects on efficiency performance and flying capacitor voltage balancing. Nevertheless, it is important to make sure that the switches do not exceed their maximum voltage ratings and that the switch node voltage does not drop too low (i.e., to ground) due

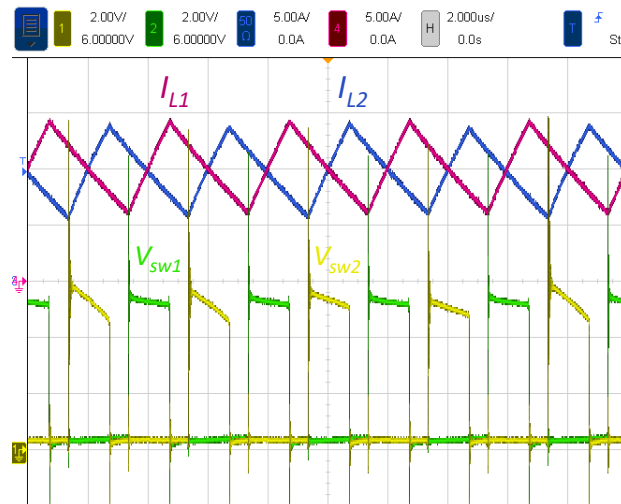


Figure 8.4: Balanced interleaved inductor currents ( $V_{out} = 2\text{ V}$ ,  $I_{out} = 20\text{ A}$ ).

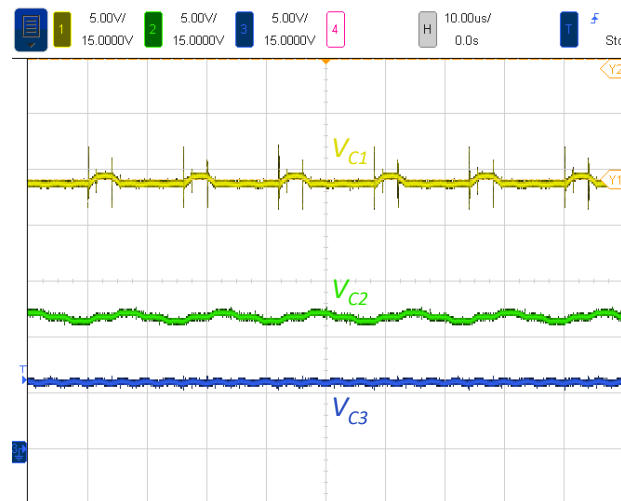


Figure 8.5: Flying capacitor voltages at  $V_{out} = 2\text{ V}$  and  $I_{out} = 20\text{ A}$ .

to the capacitor voltage ripple. Note that it may be possible to further reduce the amount of flying capacitance in the prototype, as the current design has not been fully optimized.

The two inductor currents and the corresponding switch node voltages are shown in Fig. 8.4, and exhibit good balancing. Fig. 8.5 shows the voltages across the  $C_1$ ,  $C_2$ , and  $C_3$  capacitors, which also exhibit good balancing, matching well with the theoretical values of 24 V, 12 V, and 6 V.

The performance of the prototype is measured with a Yokogawa WT3000E precision power meter. The converter is tested up to 65 A output current, resulting in a current density

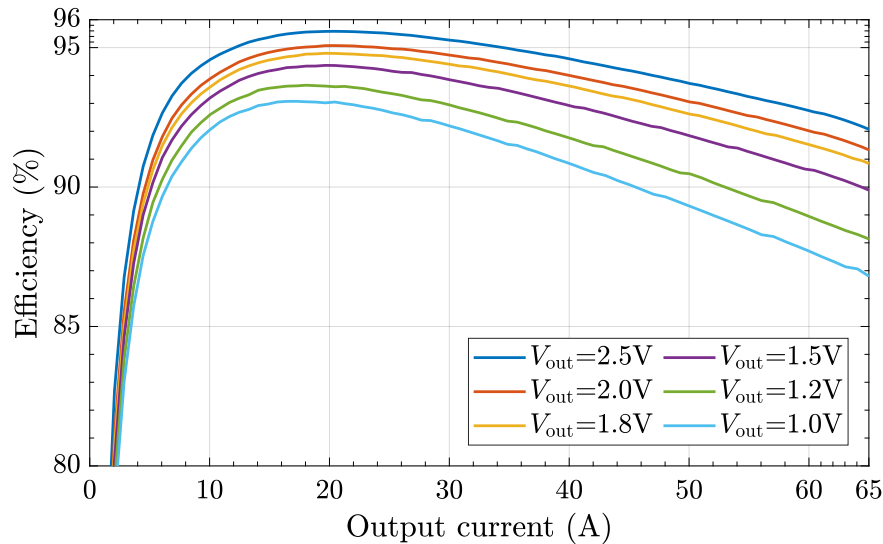


Figure 8.6: Measured power stage efficiency from 48 V to 2.5–1.0 V.

of 198 A/in<sup>3</sup> (as measured by the smallest rectangular box that can contain the converter). The measured power-stage efficiencies at various commonly-used output voltages are plotted in Fig. 8.6, and the corresponding system efficiencies with gate drive loss included are shown in Fig. 8.7. Table 8.5 summarizes the peak and full-load efficiencies of each output voltage, as well as the power density by box volume and surface area. The converter operates at an effective switching frequency of 250 kHz (as seen by the inductors). At 48 V to 2 V, the prototype achieves 95.1% peak efficiency (94.3% including gate drive loss), 91.3% full load efficiency (91.1% including gate drive loss), and 395 W/in<sup>3</sup> power density. As shown in Fig. 8.8, the maximum temperature of the board at thermal equilibrium is about 85°C, when operating at full-load with 110 CFM fan cooling only.

Table 8.6 compares this work with some of the best existing hybrid SC works with similar power ratings. As discussed previously, the proposed converter is designed to slightly trade peak efficiency at light-load for better heavy-load efficiency and power/current density. It can be seen that the proposed converter is able to carry the highest per-phase inductor current, while maintaining very good heavy-load efficiency. The comparison of current density is not straightforward, as different works use different calculation methods. Regardless, both the current density by box volume and by component volume reported in this work show the MLB-PoL’s great potential. Furthermore, not only is this converter well suited to deliver tens of amperes in a very compact form factor, but it can also be easily paralleled and scaled up for use in applications requiring hundreds of amperes.

Since all major components of the converter are packed into a small rectangular box, we are also able to directly compare with some of the best existing commercial power modules in this field. The results are summarized in Table 8.7. Although being the first proof-of-concept

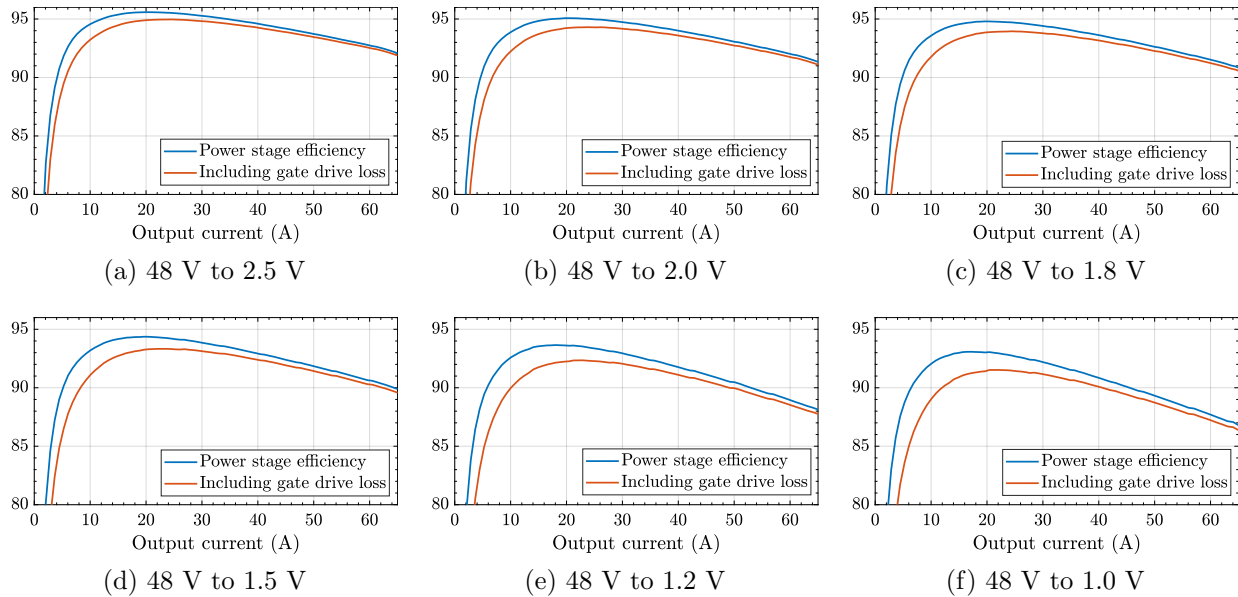


Figure 8.7: Measured efficiency at various output voltages.

prototype without advanced packaging technologies, this work shows very comparable efficiency and current density performance. Note that the efficiency sweep of this work is obtained by slowly ramping up the load currents, and thus the switch resistance increases at heavy load due to higher switch temperature. In contrast, industry products are commonly tested under pulsed load conditions where the switch junction temperature is equal to the ambient temperature. Therefore, a higher efficiency number can be expected if the proposed converter is tested under the same industry procedure. We also note that the current design has not been optimized, as the commercial off-the-shelf inductors (maximum height of 0.315 inch) are much taller than the other components (maximum height of 0.126 inch). Further optimization of the magnetic components (e.g., customized coupled inductors with PCB windings) and advanced 3D packaging technologies (e.g., board cutouts for recessing inductors) could dramatically improve the power/current density.

## 8.4 Alternative Topology Variation

The multi-operating-phase concept can also be applied to transform other SC converters to hybrid SC converters with merged buck stage at the output. Here, we demonstrate one hybrid variation of the 6-to-1 cascaded series-parallel SC converter presented in Section 7.4. The circuit schematic of the proposed hybrid converter is shown in Fig. 8.9, and its key operating waveforms and equivalent circuits are shown in Fig. 8.10. The core structure of the SC stage remains the same as that of the cascaded series-parallel converter, with a 2-to-

Table 8.5: Summary of measured efficiency and power density results at various output voltages

Output voltage	Power stage efficiency	System efficiency (including driver loss)	Power density
2.5 V	Peak: 95.6% Full load: 92.1%	Peak: 95.0% Full load: 91.9%	494 W/in <sup>3</sup> 196 W/in <sup>2</sup>
2.0 V	Peak: 95.1% Full load: 91.3%	Peak: 94.3% Full load: 91.1%	395 W/in <sup>3</sup> 157 W/in <sup>2</sup>
1.8 V	Peak: 94.8% Full load: 90.9%	Peak: 94.0% Full load: 90.6%	356 W/in <sup>3</sup> 141 W/in <sup>2</sup>
1.5 V	Peak: 94.4% Full load: 89.9%	Peak: 93.3% Full load: 89.6%	296 W/in <sup>3</sup> 118 W/in <sup>2</sup>
1.2 V	Peak: 93.7% Full load: 88.1%	Peak: 92.4% Full load: 87.8%	237 W/in <sup>3</sup> 94 W/in <sup>2</sup>
1.0 V	Peak: 93.1% Full load: 86.8%	Peak: 91.5% Full load: 86.4%	198 W/in <sup>3</sup> 79 W/in <sup>2</sup>

Table 8.6: Comparison of this work and existing hybrid SC works

Reference	Topology	Voltage ratio	Output current	Current Density	Efficiency	Notes
This Work	Hybrid 8-to-1 Multi-phase Doubler SC + two-phase Buck	48-to-1.5 V	65 A	198 A/in <sup>3</sup> (by box volume) 583 A/in <sup>3</sup> (by component volume)	System efficiency including driver loss: full load: 89.6% ( $I_{out}=32.5A/phase$ ) heavy load: 91.4% ( $I_{out}=25A/phase$ ) medium load: 92.4% ( $I_{out}=20A/phase$ ) peak: 93.3% ( $I_{out}=13A/phase$ )	Total volume of the main power devices (switches, capacitors, inductors) is used for the “by component volume” current density calculation
LEGO PoL [13]	Hybrid 6-to-1 Dickson SC + 12-phase Buck	48-to-1.5 V	300 A	114 A/in <sup>3*</sup> (by box volume)	Power stage efficiency: <sup>*</sup> full load: 87.7% ( $I_{out}=25A/phase$ ) peak: 96.0% ( $I_{out}=4A/phase$ )	Current density is estimated with optimum vertical inductor stack-up
MIH [14]	Hybrid 4-to-1 Dickson SC + three-phase Buck	48-to-1.6 V	40 A	213 A/in <sup>3*</sup> (by component volume)	Including <i>calculated</i> gate charge loss: <sup>*</sup> full load: 85.6% ( $I_{out}=13.3A/phase$ ) peak: 93.9% ( $I_{out}=3.3A/phase$ )	Total component volume of main power devices (switches, capacitors, inductors) is used for density calculation
Crossed-coupled QSD Buck [15]	Hybrid 4-to-1 SC + two-phase Buck	48-to-1.5 V	40 A	100 A/in <sup>3</sup> (by component volume)	Power stage efficiency: <sup>*</sup> full load: 92.7% ( $I_{out}=20A/phase$ ) peak: 95.1% ( $I_{out}=8A/phase$ )	The “by component volume” current density is estimated with the same method above

\* According to direct correspondence with the author.

1 front-end stage followed by a 3-to-1 series-parallel stage, and therefore a total conversion ratio of 6-to-1 at the SC stage. Besides the original inductor ( $L_3$  in Fig. 8.9) that is in series combination with all flying capacitors, two additional inductors are augmented to the positive terminal of each flying capacitor in the series-parallel stage. This way,  $C_2$  and  $C_3$  are softly discharged by  $L_1$  and  $L_2$  during the parallel mode, respectively. In order to have balanced and interleaved inductor currents, their discharging time are split to Phases 2 and 5 and Phases 3 and 6, respectively. Owing to this multi-operating-phase control strategy, the high voltage components ( $Q_1-Q_4$  and  $C_1$ ) only need to operate at half the frequency of the other components. Compared to the MLB converter, even though the conversion ratio of the SC stage is reduced from 8-to-1 to 6-to-1, the number of inductor phases increases from two

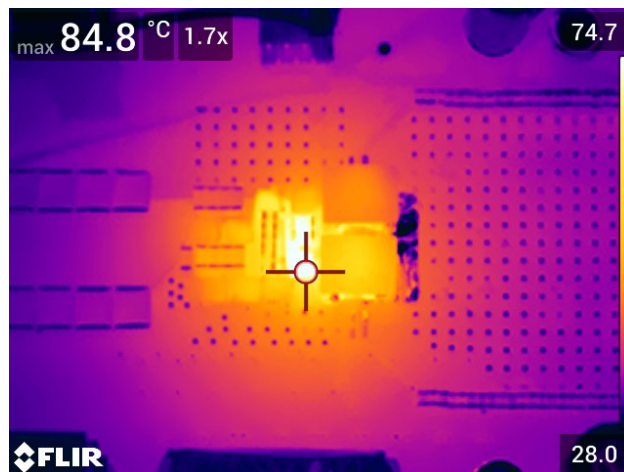


Figure 8.8: Thermal performance at equilibrium with 110 CFM fan cooling only ( $V_{\text{out}} = 2.0$  V,  $I_{\text{out}} = 65$  A).

Table 8.7: Comparison of this work and existing commercial products

Reference	Topology	Voltage ratio	Output current	Current Density	System Efficiency	Notes
This Work	Hybrid 8-to-1 SC + two-phase Buck	48-to-1 V	65 A	198 A/in <sup>3</sup>	full load: 86.4% 50 A: 88.7% peak: 91.5%	
ADI LTM4664 [109]	4-to-1 SC + two-phase buck	48-to-1 V	50 A	415 A/in <sup>3</sup>	full load: 88.0% peak: 90.8%	Highly integrated power module
TI [110] LMG5200POLEVM	Transformer-based	48-to-1 V	50 A	N/A	full load: 87.7% peak: 90.7%	GaN FET
bel power stamp [111]	Transformer-based	48-to-1 V	70 A	167 A/in <sup>3</sup>	Typical: 91%	Highly integrated power module, fixed output voltage
Vicor PRM [150] +2*VTM [151]	Buck-Boost + Sine Amplitude Converter	48-to-1 V	200 A	588 A/in <sup>3</sup>	Typical: 90%	Highly integrated power module

to three, leading to higher output current capability. Given that this topology has a very similar component number (one more switch, one more inductor) to the MLB converter, an even higher power density could be achieved.

## 8.5 Chapter Summary

This chapter presents a new hybrid topology with Multi-Level Binary (MLB) voltages on the flying capacitors that can simultaneously achieve high efficiency and power density for direct 48 V to PoL applications. The proposed MLB-PoL converter employs multiple operating

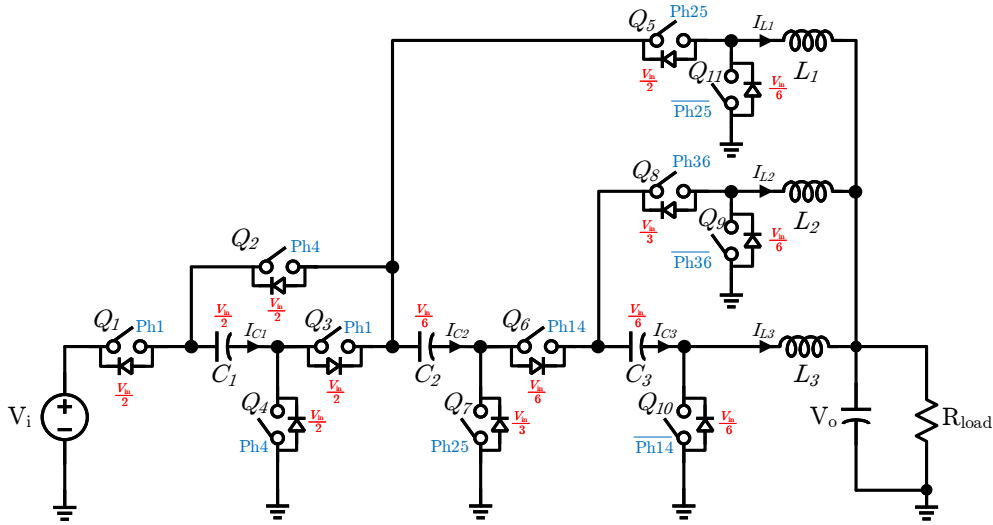


Figure 8.9: Schematic drawing of a proposed multi-phase hybrid converter with a 6-to-1 SC stage and three interleaved output inductors. The device voltage ratings are labeled in red and the operating phases of the switches are labeled in blue.

phases to achieve an 8-to-1 conversion ratio at the SC stage with the theoretical minimum number of components. This high SC conversion ratio can reduce the inductor volt-second stress of the following buck stage. Moreover, an inductor frequency multiplication effect is able to further reduce the inductor size without increasing the switching frequency of the SC stage. A 48 V to 2.5–1.0 V converter prototype with 65 A output current is built and tested. At 48 V to 2 V, the prototype achieves 95.1% peak efficiency (94.3% including gate drive loss) and 395 W/in<sup>3</sup> power density, demonstrating one of the best in-class performances. An alternative multi-phase hybrid converter with 6-to-1 SC stage and three interleaved output inductors is also proposed.



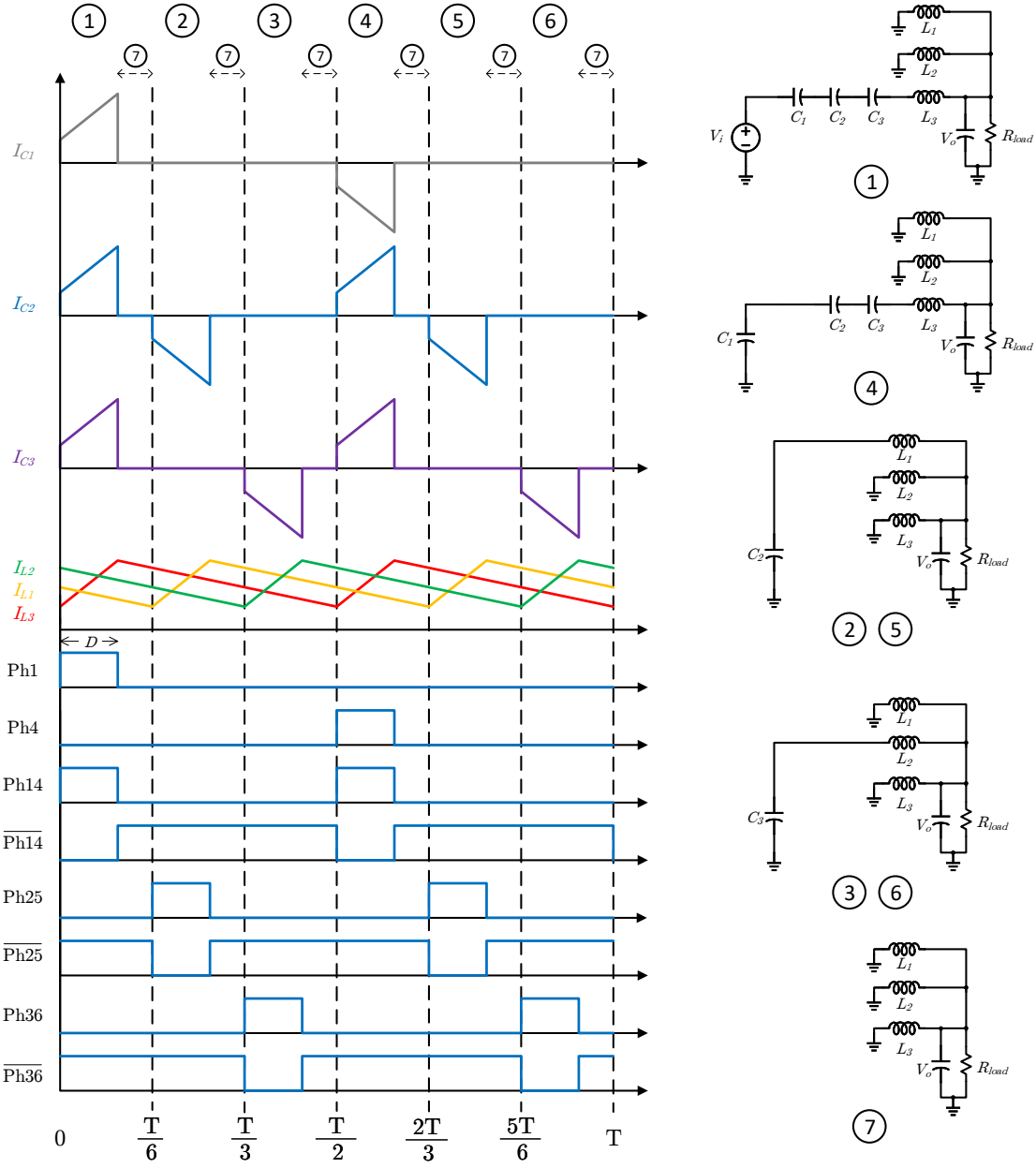


Figure 8.10: Voltage, current, PWM waveforms, and equivalent circuit models of the proposed hybrid SC converter with a 6-to-1 SC stage.

# Chapter 9

## Future Work

It should be recognized that hybrid and resonant switched-capacitor converter design remains an emerging topic in power electronics, with limited industry penetration to date. There is more theoretical work to complete and more practical implementation challenges to address. This chapter provides an outlook for hybrid and resonant SC converters and discusses some possible future work.

### Performance Wishlist

In order to outperform LLC converters in high-performance fixed-ratio conversions, ReSC converters need to demonstrate more favorable characteristics in the following areas:

- **High conversion ratio.** In existing discrete implementations, the performance advantage of ReSC converters diminishes with respect to the conversion ratio. At a 4-to-1 ratio, the cascaded resonant converter in Chapter 6 has efficiency and power density advantages over the latest high-frequency LLC converter with a highly optimized magnetic structure [122]. However, at an 8-to-1 ratio, the performance advantages of ReSC converters (such as the multi-resonant doubler converter in Chapter 7) is greatly reduced. For applications with even higher conversion ratios, such as the direct 48-to-1 V step-down for data center applications [112], ReSC converters cannot yet compete with transformer-based converters.
- **Flat efficiency curve and heavy load performance.** With similar power and voltage ratings, ReSC converters usually have better light-load efficiency than LLC converters, owing to less magnetic loss. However, their efficiency usually peaks at lighter loads compared to LLC converters, and then starts to drop at a faster rate, especially when the conversion ratio is high. This is because the switch count and the associated output impedance of ReSC converters typically increases proportionally with respect to conversion ratio, whereas the circuit structure and switch count of LLC converters remain unchanged. As a result, ReSC converters cannot achieve a low output impedance as easily as LLC converters at high conversion ratios.

- High output current. In LLC converters, the current and power rating can be easily scaled up by splitting the output current into multiple paralleled stages at the secondary side of the transformer. In comparison, as discussed in Section 6.6, because of the high circuit complexity, it is challenging for ReSC converters to achieve high conversion ratio and high output current simultaneously. To address this problem, strategic interleaving and cascading operations can be applied on selective topologies with simple basic structures.
- High operating frequency. Owing to the use of high energy density capacitors, ReSC converters can achieve high power density at a relatively low switching frequency. Most existing high-performance discrete implementations operate in the range of 50 to 350 kHz. To date, the ability of operating ReSC converters efficiently at higher frequencies has not been widely demonstrated. In fact, some frequency related loss mechanisms in practical implementations of SC converters have not been fully explored and understood. Through an experiment that was not included in the dissertation, an unclear frequency-dependent loss was discovered. A 2-to-1 SC converter prototype (with 25 V rated discrete MOSFETs) operating at 4-to-2 V exhibited a significant power loss increase with respect to switching frequency ( $P_{\text{loss},400\text{kHz}} \approx 3P_{\text{loss},100\text{kHz}}$ ), which was not expected at the heavy load condition tested, where conduction loss is usually dominant, especially when the voltage level and the associated switching loss of the switches are low.
- Full soft switching. In order to operate at a high frequency (in the MHz range) efficiently, it is essential to achieve full zero voltage switching and zero current switching on all switches, across the full load range. Among existing ReSC converters, the cascaded resonant converter and the Dickson converter can achieve full soft-switching on all switches, but the condition is load-dependent. For the multi-phase ReSC converters and the series-parallel converter, the single augmenting inductor at the output node is incapable of soft charging/discharging all switches, owing to the complex internal charge flow paths.
- New topologies with merged magnetic structures. The increasing use of capacitors in energy transfer is not meant to completely eliminate magnetic components. On the contrary, the hybrid approach itself demonstrates that a good combination of capacitors and inductors can yield a better overall performance. In addition to merging capacitors with inductors or buck converters, it is also worthwhile to explore the opportunity for merging capacitors with transformers, which may have potential benefits for applications with very high conversion ratios or isolation requirements. Some early works in this field include the MultiTrack architecture [79] and the multilevel structure with merged transformer-based current doublers [152].

## Practical Implementation Challenges

- **Start-up circuit.** When the input voltage of the hybrid resonant SC converter is not well controlled, a dedicated start-up circuit is needed. Alternatively, the switch connected to the input may need to be rated for a higher-than-nominal voltage to accommodate the worst-case scenario. This may penalize different topologies differently. For instance, the first switch in a series-parallel converter needs to block a high voltage regardless, therefore the penalty considering the start-up condition is relatively mild. In contrast, the first switch in a Dickson converter only blocks  $V_{\text{out}}$  during normal operation, but it has to be rated for  $V_{\text{in}}$  when the start-up condition needs to be considered. In applications where the input voltage can be slowly ramped up to the rated voltage, no additional start-up circuit is needed. For instance, in a cascaded two-stage architecture, the previous stage can serve as a soft-start circuit for the following stage.
- **PCB layout.** The complex circuit structure of hybrid and resonant SC converters complicates PCB design, which in return directly impacts the performance of the converter. Therefore, the ease of layout should be considered when comparing different topologies. A good PCB layout should have short interconnect traces (low parasitic resistance and inductance) and small switching node area (low parasitic switching loss), while being compact and power dense. The cascaded resonant converter is found to have unique advantages in terms of PCB design.
- **Gate drive loss.** As discussed in Chapter 5, hybrid and resonant SC converters have a large number of switches and the associated gate drive loss contributes a non-negligible portion to the overall loss. Therefore, the gate drive circuit should be designed to be as efficient as possible, and the gate drive loss should be included in the overall efficiency measurement.
- **Capacitor balancing.** This remains a crucial challenge for hybrid SC converters, especially for FCML converters. Many benefits of such topologies rely on the reduced voltage stress on the switches, and it is of great importance to ensure the voltages of flying capacitors are balanced and close to their nominal values.
- **Input and output capacitance.** For ReSC converters, the input and output capacitors participate in the resonant operation. Consequently, their values may have a direct impact on the conversion efficiency. There is a great value in analyzing the effects of input and output capacitance on the output impedance of ReSC converters, both theoretically and experimentally.

## Devices, Integration, and Packaging

While this dissertation mainly studies hybrid and resonant SC converters from a topological perspective, the other aspects in power converter designs should not be neglected. In

particular, device customization, power train integration, and advanced packaging have the potential to further improve the performance of hybrid and resonant SC converters.

- Discrete low-voltage power MOSFETs. For low-voltage high-current applications such as 48 V data center power delivery, the switch blocking voltage of many hybrid resonant SC converters can be as low as 6–10 V. However, the minimum rating of existing discrete power MOSFETs with the requisite on-resistance value is 25 V. If lower voltage rated devices are available, the theoretical performance benefits of these topologies can be better realized.
- Customized capacitor packaging. In practical implementations, multiple MLCCs may need to be paralleled to get the desired capacitance value. With standard assembly technology, these MLCCs have to be spaced apart in order to meet manufacturing component clearance tolerances, and they cannot be stacked in multiple layers. With customized capacitor arrays (a long row of capacitors packaged together by manufacturers), the reliability and power density of the converters can be greatly improved.
- FET and driver integration. From an industry perspective, a major challenge of these topologies is the complex structure and the large number of components, which translates to cost and reliability concerns. This problem can be addressed through better integration of the power device and the associated gate drive circuit. The LTC7820 from ADI [8] integrates four series-connected gate drivers on a single chip and greatly simplifies the design of the 2-to-1 SC converter. The EPC2152 [153] presents a monolithic half-bridge module with integrated power devices, gate drivers, level shifter, and bootstrap circuit. Through further efforts to improve integration, the design of hybrid and resonant SC converters can be expected to be as easy as that of buck and boost converters today.
- Magnetic components. For the hardware prototypes presented in this dissertation, commercial off-the-shelf inductors are used for ease of design. However, they have become the bottleneck of the entire system: the output current rating is usually limited by the inductor saturation current and the power density is limited by the height/volume of the inductor. For fixed-ratio ReSC converters, customized one-turn inductor shows great promise [154]. For regulated hybrid SC converters, coupled inductors may provide dramatic performance improvement [155]. In addition, innovative structures such as the merged LC resonator [156] and the piezoelectric resonator [157] maybe worth further attention.
- Advanced packaging. Packaging not only determines the power density, but also directly impacts the electrical and thermal performance of the converter. Most existing hybrid and resonant SC works are board-level designs. It would be interesting to see more demonstrations with advanced power module designs. Recently, the concept of vertical power delivery has emerged for very high current ASICs applications. Ref [158]

demonstrates a 3-D stacking concept for hybrid SC converters with good power density performance.

# Chapter 10

## Conclusions

This dissertation demonstrates the great performance potential of hybrid and resonant switched-capacitor power converters, through both theoretical analysis and experimental verification. With augmenting inductor(s), the capacitor charge sharing loss in SC converters can be eliminated, thereby increasing the energy utilization factor of the capacitors without sacrificing the efficiency performance. When operating in resonant mode, ReSC converters can behave as a dc transformer and achieve very efficient and power dense fixed-ratio conversion. When operating in PWM regulated mode, hybrid SC converters can achieve better performance than conventional buck and boost converters, thanks to the reduced inductance requirement and better utilization of the switches.

In order to evaluate the advantages of passive component utilization of hybrid resonant SC converters, a passive component modeling method is proposed, by fundamentally analyzing the reactive power processed by the passive components. It is shown that the total passive component volume can be expressed as a function of flying capacitor voltage ripple, and the optimum inductor and capacitor allocation that minimizes the total volume is dependent on their relative energy density and topology-dependent parameters. The analysis and the associated experimental results also showcase that a 2-to-1 ReSC converter can use significantly less passive volume than conventional SC and buck converters for the same power conversion, while maintaining the best efficiency performance. In addition, by combining the proposed passive utilization metric with the switch utilization metric (switch VA rating), a framework to compare the relative performances of different ReSC topologies is created.

To realize the excellent performance potential of hybrid and resonant SC converters, two important practical implementation challenges are investigated, and corresponding mitigation strategies are presented. The first is flying capacitor voltage balancing, which is particularly challenging for flying capacitor multilevel converters. It is found that the source impedance and the associated input capacitance can have a drastic impact on capacitor balancing, and an FCML converter with an even number of levels inherently has stronger immunity to such disturbance than a converter with an odd number of levels.

The second challenge is in regard to powering the large number of floating gate drivers

in these topologies. To make the gate drive power supply circuit more compact and efficient, five circuit techniques are presented: bootstrap at deadtime, cascaded bootstrap with LDO, double charge pump, gate-driven charge pump, and synchronous bootstrap. By leveraging the inherent properties of multilevel converters, these methods can overcome the limitation of the conventional bootstrap method (i.e., the diode forward voltage drop) and make it possible to transfer ground-referenced power to all of the floating switches for any FCML or hybrid SC converters.

The excellent performance of hybrid and resonant SC converters is also demonstrated by three hardware prototypes for 48 V data center power delivery applications. The first is a 48-to-12 V cascaded resonant converter. By cascading two standard 2-to-1 ReSC converters, a 4-to-1 conversion ratio can be achieved, while keeping the same simple operating principle and full zero voltage switching capability. To reduce the size of the interstage decoupling capacitor, a two-phase interleaving strategy is adopted. The prototype achieves 99.0% peak efficiency (with gate drive loss included) and 2500 W/in<sup>3</sup> power density.

In order to achieve higher conversion ratios with manageable circuit complexity, the concept of multiple-operating-phase is applied. Compared to ReSC converters with two operating phases, the proposed multi-resonant SC converters can achieve the same conversion ratio with significantly fewer switches and capacitors. For 48-to-8 V conversion, a cascaded series-parallel topology is proposed, and its prototype achieves 98.5% peak efficiency (with gate drive loss included) and 2230 W/in<sup>3</sup> power density. For 48-to-6 V conversion, a multi-resonant-doubler converter is developed, with 98.0% peak efficiency (with gate drive loss included) and 1675 W/in<sup>3</sup> power density.

For direct 48 V to point-of-load conversion, a regulated hybrid SC topology — the multi-level binary (MLB) converter, is presented. Owing to the multi-phase operation, the MLB converter can achieve 8-to-1 conversion ratio at its SC stage, which is the highest among all existing hybrid topologies. The two-phase interleaved inductors at the output buck stage have balanced currents due to an inherent balancing mechanism. Moreover, the inductors benefit from a frequency multiplication effect similar to that in FCML converters, which results in a higher effective inductor frequency without the need for increasing the operating frequency of all other components. A 48 V to 2.5–1.0 V prototype with 65 A output current is built and tested. At 48 V to 2 V, the prototype achieves 94.3% peak efficiency (with gate drive loss included), and 395 W/in<sup>3</sup> power density. All these hardware prototypes achieve the best in-class efficiency and power density simultaneously, reflecting the great potential of hybrid and resonant SC converters for future power conversion systems.

Last but not least, some possible future works are discussed. With more research into device customization, power train integration, and advanced packaging, the cost and reliability concerns of hybrid resonant SC converters can be alleviated. Combined with increased research into exploiting the topological potential and addressing the practical implementation challenges, a broader adoption of hybrid and resonant SC converters by the power electronics society can be expected.



# Bibliography

- [1] D. Reusch, S. Biswas, and Y. Zhang, "System optimization of a high power density non-isolated intermediate bus converter for 48 v server applications," *IEEE Transactions on Industry Applications*, vol. 55, no. 2, pp. 1619–1627, Mar. 2019.
- [2] C. B. Barth, T. Foulkes, I. Moon, Y. Lei, S. Qin, and R. C. N. Pilawa-Podgurski, "Experimental evaluation of capacitors for power buffering in single-phase power converters," *IEEE Transactions on Power Electronics*, vol. 34, no. 8, pp. 7887–7899, 2019.
- [3] S. Coday, C. B. Barth, and R. C. N. Pilawa-Podgurski, "Characterization and modeling of ceramic capacitor losses under large signal operating conditions," in *2018 IEEE 19th Workshop on Control and Modeling for Power Electronics (COMPEL)*, Jun. 2018, pp. 1–8.
- [4] M. S. Makowski and D. Maksimovic, "Performance limits of switched-capacitor dc-dc converters," in *Power Electronics Specialists Conference, 1995. PESC '95 Record., 26th Annual IEEE*, vol. 2, Jun. 1995, 1215–1221 vol.2.
- [5] J. M. Henry and J. W. Kimball, "Practical performance analysis of complex switched-capacitor converters," *IEEE Transactions on Power Electronics*, vol. 26, no. 1, pp. 127–136, Jan. 2011.
- [6] C. Pascual and P. T. Krein, "Switched capacitor system for automatic series battery equalization," in *Proceedings of APEC 97 - Applied Power Electronics Conference*, vol. 2, Feb. 1997, 848–854 vol.2.
- [7] M. D. Seeman and S. R. Sanders, "Analysis and optimization of switched-capacitor dc-dc converters," *IEEE Transactions on Power Electronics*, vol. 23, no. 2, pp. 841–851, Mar. 2008.
- [8] *Ltc7820 datasheet*, LTC7820, Linear Technology, 2017.
- [9] H. P. Le, S. R. Sanders, and E. Alon, "Design techniques for fully integrated switched-capacitor dc-dc converters," *IEEE Journal of Solid-State Circuits*, vol. 46, no. 9, pp. 2120–2131, Sep. 2011.
- [10] S. R. Sanders, E. Alon, H. P. Le, M. D. Seeman, M. John, and V. W. Ng, "The road to fully integrated dc-dc conversion via the switched-capacitor approach," *IEEE Transactions on Power Electronics*, vol. 28, no. 9, pp. 4146–4155, Sep. 2013.

- [11] P. Lin and L. Chua, "Topological generation and analysis of voltage multiplier circuits," *IEEE Transactions on Circuits and Systems*, vol. 24, no. 10, pp. 517–530, 1977.
- [12] J. W. Kimball, P. T. Krein, and K. R. Cahill, "Modeling of capacitor impedance in switching converters," *IEEE Power Electronics Letters*, vol. 3, no. 4, pp. 136–140, 2005.
- [13] Y. Lei, "High-performance power converters leveraging capacitor-based energy transfer," Ph.D. dissertation, University of Illinois at Urbana-Champaign, 2017. [Online]. Available: <http://hdl.handle.net/2142/97413>.
- [14] S. Pasternak, C. Schaef, and J. Stauth, "Equivalent resistance approach to optimization, analysis and comparison of hybrid/resonant switched-capacitor converters," in *2016 IEEE 17th Workshop on Control and Modeling for Power Electronics (COMPEL)*, 2016, pp. 1–8.
- [15] Y. Zhu, Z. Ye, and R. C. N. Pilawa-Podgurski, "Modeling and analysis of the effect of finite input and output capacitances on the output impedance of switched-capacitor converters," in *2021 IEEE Applied Power Electronics Conference and Exposition (APEC)*, Jun. 2021.
- [16] R. C. N. Pilawa-Podgurski, D. M. Giuliano, and D. J. Perreault, "Merged two-stage power converter architecture with soft charging switched-capacitor energy transfer," in *2008 IEEE Power Electronics Specialists Conference*, Jun. 2008, pp. 4008–4015.
- [17] R. C. N. Pilawa-Podgurski and D. J. Perreault, "Merged two-stage power converter with soft charging switched-capacitor stage in 180 nm cmos," *IEEE Journal of Solid-State Circuits*, vol. 47, no. 7, pp. 1557–1567, Jul. 2012.
- [18] J. Baek, P. Wang, Y. Elasser, Y. Chen, S. Jiang, and M. Chen, "Lego-pol: A 48v-1.5v 300a merged-two-stage hybrid converter for ultra-high-current microprocessors," in *2020 IEEE Applied Power Electronics Conference and Exposition (APEC)*, 2020, pp. 490–497.
- [19] Y. Lei and R. C. N. Pilawa-Podgurski, "A general method for analyzing resonant and soft-charging operation of switched-capacitor converters," *IEEE Transactions on Power Electronics*, vol. 30, no. 10, pp. 5650–5664, Oct. 2015.
- [20] Y. P. B. Yeung, K. W. E. Cheng, S. L. Ho, K. K. Law, and D. Sutanto, "Unified analysis of switched-capacitor resonant converters," *IEEE Transactions on Industrial Electronics*, vol. 51, no. 4, pp. 864–873, Aug. 2004.
- [21] Y. Lei, R. May, and R. C. N. Pilawa-Podgurski, "Split-phase control: Achieving complete soft-charging operation of a dickson switched-capacitor converter," *IEEE Transactions on Power Electronics*, vol. 31, no. 1, pp. 770–782, Jan. 2016.
- [22] T. Urkin, G. Sovik, E. E. Masandilov, and M. M. Peretz, "Digital zero-current switching lock-in controller ic for optimized operation of resonant scc," *IEEE Transactions on Power Electronics*, pp. 1–1, 2020.

- [23] S. Jiang, S. Saggini, C. Nan, X. Li, C. Chung, and M. Yazdani, “Switched tank converters,” *IEEE Transactions on Power Electronics*, vol. 34, no. 6, pp. 5048–5062, Jun. 2019.
- [24] W. C. Liu, Z. Ye, and R. C. N. Pilawa-Podgurski, “Comparative analysis on minimum output impedance of fixed-ratio hybrid switched capacitor converters,” in *2019 20th Workshop on Control and Modeling for Power Electronics (COMPEL)*, 2019, pp. 1–7.
- [25] Z. Ye, S. R. Sanders, and R. C. N. Pilawa-Podgurski, “Modeling and comparison of passive component volume of hybrid resonant switched-capacitor converters,” in *2019 20th Workshop on Control and Modeling for Power Electronics (COMPEL)*, Jun. 2019, pp. 1–8.
- [26] K. Sano and H. Fujita, “Improving dynamic performance and efficiency of a resonant switched-capacitor converter based on phase-shift control,” in *2009 IEEE Energy Conversion Congress and Exposition*, 2009, pp. 3509–3515.
- [27] Y. Li, M. John, Y. Ramadass, and S. R. Sanders, “Ac-coupled stacked dual-active-bridge dc–dc converter for integrated lithium-ion battery power delivery,” *IEEE Journal of Solid-State Circuits*, vol. 54, no. 3, pp. 733–744, 2019.
- [28] J. Zhu and D. Maksimović, “A family of transformerless stacked active bridge converters,” in *2019 IEEE Applied Power Electronics Conference and Exposition (APEC)*, 2019, pp. 19–24.
- [29] Y. Lei, W. Liu, and R. C. N. Pilawa-Podgurski, “An analytical method to evaluate and design hybrid switched-capacitor and multilevel converters,” *IEEE Transactions on Power Electronics*, vol. 33, no. 3, pp. 2227–2240, Mar. 2018.
- [30] S. R. Pasternak, M. H. Kiani, J. S. Rentmeister, and J. T. Stauth, “Modeling and performance limits of switched-capacitor dc-dc converters capable of resonant operation with a single inductor,” *IEEE Journal of Emerging and Selected Topics in Power Electronics*, vol. 5, no. 4, pp. 1746–1760, Dec. 2017.
- [31] J. A. Cobos, H. Cristóbal, D. Serrano, R. Ramos, J. A. Oliver, and P. Alou, “Differential power as a metric to optimize power converters and architectures,” in *2017 IEEE Energy Conversion Congress and Exposition (ECCE)*, Oct. 2017, pp. 2168–2175.
- [32] D. H. Wolaver, “Fundamental study of dc to dc conversion systems,” Ph.D. dissertation, Massachusetts Institute of Technology, 1969.
- [33] Z. Ye, Y. Lei, and R. C. N. Pilawa-Podgurski, “The cascaded resonant converter: A hybrid switched-capacitor topology with high power density and efficiency,” *IEEE Transactions on Power Electronics*, vol. 35, no. 5, pp. 4946–4958, May 2020.
- [34] M. H. Kiani and J. T. Stauth, “Passive component modeling and optimal size allocation for hybrid-resonant switched capacitor dc-dc converters,” in *2018 IEEE 19th Workshop on Control and Modeling for Power Electronics (COMPEL)*, 2018, pp. 1–8.

- [35] M. D. Seeman, "A design methodology for switched-capacitor dc-dc converters," Ph.D. dissertation, University of California, Berkeley, 2009.
- [36] Vicor Inc., *Redefining 48v to pol regulation for high-power processors and ai asics*. [Online]. Available: <http://www.vicorpower.com/industries-and-innovations/power-on-package#seeitinaction>.
- [37] Z. Ye, Y. Lei, and R. C. N. Pilawa-Podgurski, "A 48-to-12 v cascaded resonant switched-capacitor converter for data centers with 99% peak efficiency and 2500 w/in<sup>3</sup> power density," in *2019 IEEE Applied Power Electronics Conference and Exposition (APEC)*, Mar. 2019, pp. 13–18.
- [38] C. Schaef, J. S. Rentmeister, and J. Stauth, "Multimode operation of resonant and hybrid switched-capacitor topologies," *IEEE Transactions on Power Electronics*, pp. 1–1, 2018.
- [39] Z. Ye, Y. Lei, and R. C. N. Pilawa-Podgurski, "A resonant switched capacitor based 4-to-1 bus converter achieving 2180 w/in<sup>3</sup> power density and 98.9% peak efficiency," in *2018 IEEE Applied Power Electronics Conference and Exposition (APEC)*, Mar. 2018, pp. 121–126.
- [40] J. T. Stauth, M. D. Seeman, and K. Kesarwani, "A resonant switched-capacitor ic and embedded system for sub-module photovoltaic power management," *IEEE Journal of Solid-State Circuits*, vol. 47, no. 12, pp. 3043–3054, Dec. 2012.
- [41] C. Schaef and J. T. Stauth, "A highly integrated series-parallel switched-capacitor converter with 12 v input and quasi-resonant voltage-mode regulation," *IEEE Journal of Emerging and Selected Topics in Power Electronics*, vol. 6, no. 2, pp. 456–464, Jun. 2018.
- [42] S. R. Sanders, E. Alon, H. Le, M. D. Seeman, M. John, and V. W. Ng, "The road to fully integrated dc–dc conversion via the switched-capacitor approach," *IEEE Transactions on Power Electronics*, vol. 28, no. 9, pp. 4146–4155, Sep. 2013.
- [43] Y. Lei, Z. Ye, and R. C. N. Pilawa-Podgurski, "A GaN-based 97% efficient hybrid switched-capacitor converter with lossless regulation capability," in *2015 IEEE Energy Conversion Congress and Exposition (ECCE)*, Sep. 2015, pp. 4264–4270.
- [44] P. S. Shenoy, M. Amaro, J. Morroni, and D. Freeman, "Comparison of a buck converter and a series capacitor buck converter for high-frequency, high-conversion-ratio voltage regulators," *IEEE Transactions on Power Electronics*, vol. 31, no. 10, pp. 7006–7015, 2016.
- [45] T. Meynard and H. Foch, "Multi-level conversion: High voltage choppers and voltage-source inverters," in *Power Electronics Specialists Conference, 1992. PESC '92 Record., 23rd Annual IEEE*, 1992, pp. 397–403.
- [46] Z. Liao, Y. Lei, and R. C. N. Pilawa-Podgurski, "Analysis and design of a high power density flying-capacitor multilevel boost converter for high step-up conversion," *IEEE Transactions on Power Electronics*, vol. 34, no. 5, pp. 4087–4099, May 2019.

- [47] J. S. Rentmeister and J. T. Stauth, "A 48v:2v flying capacitor multilevel converter using current-limit control for flying capacitor balance," in *2017 IEEE Applied Power Electronics Conference and Exposition (APEC)*, Mar. 2017, pp. 367–372.
- [48] S. Qin, Y. Lei, Z. Ye, D. Chou, and R. C. N. Pilawa-Podgurski, "A high-power-density power factor correction front end based on seven-level flying capacitor multilevel converter," *IEEE Journal of Emerging and Selected Topics in Power Electronics*, vol. 7, no. 3, pp. 1883–1898, 2019.
- [49] Z. Liao and R. C. N. Pilawa-Podgurski, "Control and modulation of a bipolar multi-level active power pulsation buffer for single-phase converters," in *2019 20th Workshop on Control and Modeling for Power Electronics (COMPEL)*, 2019, pp. 1–7.
- [50] Y. Lei, C. Barth, S. Qin, W. C. Liu, I. Moon, A. Stillwell, D. Chou, T. Foulkes, Z. Ye, Z. Liao, and R. C. N. Pilawa-Podgurski, "A 2-kw single-phase seven-level flying capacitor multilevel inverter with an active energy buffer," *IEEE Transactions on Power Electronics*, vol. 32, no. 11, pp. 8570–8581, Nov. 2017.
- [51] N. Pallo, T. Foulkes, T. Modeer, S. Coday, and R. Pilawa-Podgurski, "Power-dense multilevel inverter module using interleaved gan-based phases for electric aircraft propulsion," in *2018 IEEE Applied Power Electronics Conference and Exposition (APEC)*, 2018, pp. 1656–1661.
- [52] A. Shukla, A. Ghosh, and A. Joshi, "Capacitor voltage balancing schemes in flying capacitor multilevel inverters," in *2007 IEEE Power Electronics Specialists Conference*, Jun. 2007, pp. 2367–2372.
- [53] M. Khazraei, H. Sepahvand, K. Corzine, and M. Ferdowsi, "A generalized capacitor voltage balancing scheme for flying capacitor multilevel converters," in *2010 Twenty-Fifth Annual IEEE Applied Power Electronics Conference and Exposition (APEC)*, Feb. 2010, pp. 58–62.
- [54] M. A. H. Broadmeadow, G. R. Walker, and S. M. Bulmer, "An fpga-based, single transducer, active balancing scheme for a 5-level flying capacitor converter with 1 mhz effective switching frequency," in *8th IET International Conference on Power Electronics, Machines and Drives (PEMD 2016)*, Apr. 2016, pp. 1–6.
- [55] D. Reusch, F. C. Lee, and M. Xu, "Three level buck converter with control and soft startup," in *2009 IEEE Energy Conversion Congress and Exposition*, Sep. 2009, pp. 31–35.
- [56] L. Lu, Y. Zhang, S. M. Ahsanuzzaman, A. Prodić, G. Calabrese, G. Frattini, and M. Granato, "Digital average current programmed mode control for multi-level flying capacitor converters," in *2018 IEEE 19th Workshop on Control and Modeling for Power Electronics (COMPEL)*, Jun. 2018, pp. 1–7.

- [57] A. Stillwell, E. Candan, and R. C. N. Pilawa-Podgurski, "Active voltage balancing in flying capacitor multi-level converters with valley current detection and constant effective duty cycle control," *IEEE Transactions on Power Electronics*, vol. 34, no. 11, pp. 11 429–11 441, 2019.
- [58] X. Yuang, H. Stemmler, and I. Barbi, "Self-balancing of the clamping-capacitor-voltages in the multilevel capacitor-clamping-inverter under sub-harmonic PWM modulation," *IEEE Transactions on Power Electronics*, vol. 16, no. 2, pp. 256–263, Mar. 2001.
- [59] B. P. McGrath and D. G. Holmes, "Analytical modelling of voltage balance dynamics for a flying capacitor multilevel converter," *IEEE Transactions on Power Electronics*, vol. 23, no. 2, pp. 543–550, Mar. 2008.
- [60] R. H. Wilkinson, T. A. Meynard, and H. du Toit Mouton, "Natural balance of multi-cell converters: The two-cell case," *IEEE Transactions on Power Electronics*, vol. 21, no. 6, pp. 1649–1657, Nov. 2006.
- [61] T. A. Meynard, M. Fadel, and N. Aouda, "Modeling of multilevel converters," *IEEE Transactions on Industrial Electronics*, vol. 44, no. 3, pp. 356–364, Jun. 1997.
- [62] T. A. Meynard, H. Foch, P. Thomas, J. Courault, R. Jakob, and M. Nahrstaedt, "Multicell converters: Basic concepts and industry applications," *IEEE Transactions on Industrial Electronics*, vol. 49, no. 5, pp. 955–964, Oct. 2002.
- [63] A. Ruderman, B. Reznikov, and M. Margaliot, "Simple analysis of a flying capacitor converter voltage balance dynamics for dc modulation," in *2008 13th International Power Electronics and Motion Control Conference*, Sep. 2008, pp. 260–267.
- [64] A. Ruderman and B. Reznikov, "Five-level single-leg flying capacitor converter voltage balance dynamics analysis," in *2009 35th Annual Conference of IEEE Industrial Electronics*, Nov. 2009, pp. 486–491.
- [65] S. Thielemans, A. Ruderman, B. Reznikov, and J. Melkebeek, "Improved natural balancing with modified phase-shifted pwm for single-leg five-level flying-capacitor converters," *IEEE Transactions on Power Electronics*, vol. 27, no. 4, pp. 1658–1667, Apr. 2012.
- [66] J. S. Rentmeister and J. T. Stauth, "Modeling the dynamic behavior of hybrid-switched-capacitor converters in state space," in *2018 IEEE 19th Workshop on Control and Modeling for Power Electronics (COMPEL)*, 2018, pp. 1–7.
- [67] Z. Xia, B. L. Dobbins, and J. T. Stauth, "Natural balancing of flying capacitor multilevel converters at nominal conversion ratios," in *2019 20th Workshop on Control and Modeling for Power Electronics (COMPEL)*, Jun. 2019, pp. 1–8.
- [68] R. H. Wilkinson, T. A. Meynard, and H. du Toit Mouton, "Natural balance of multi-cell converters: The general case," *IEEE Transactions on Power Electronics*, vol. 21, no. 6, pp. 1658–1666, Nov. 2006.

- [69] Z. Liao, N. C. Brooks, Z. Ye, and R. C. N. Pilawa-Podgurski, "A high power density power factor correction converter with a multilevel boost front-end and a series-stacked energy decoupling buffer," in *2018 IEEE Energy Conversion Congress and Exposition (ECCE)*, 2018, pp. 7229–7235.
- [70] N. Pallo, S. Coday, J. Schaadt, P. Assem, and R. C. N. Pilawa-Podgurski, "A 10-level flying capacitor multi-level dual-interleaved power module for scalable and power-dense electric drives," in *2020 IEEE Applied Power Electronics Conference and Exposition (APEC)*, 2020.
- [71] Analog Devices Inc., *ADuM5210/ADuM5211/ADuM5212 Data Sheet*, 2013, pp. 3–4. [Online]. Available: <http://www.analog.com/media/en/technical-documentation/data-sheets/ADuM5210.pdf>.
- [72] Texas Instruments, *Lm5113 data sheet*, 2016, p. 2. [Online]. Available: <http://www.ti.com/lit/ds/symlink/lm5113.pdf>.
- [73] Z. Ye, Y. Lei, W. Liu, P. S. Shenoy, and R. . Pilawa-Podgurski, "Improved bootstrap methods for powering floating gate drivers of flying capacitor multilevel converters and hybrid switched-capacitor converters," *IEEE Transactions on Power Electronics*, vol. 35, no. 6, pp. 5965–5977, 2020.
- [74] J. A. Anderson, E. J. Hanak, L. Schrittwieser, M. Guacci, J. W. Kolar, and G. Deboy, "All-silicon 99.35% efficient three-phase seven-level hybrid neutral point clamped/flying capacitor inverter," *CPSS Transactions on Power Electronics and Applications*, vol. 4, no. 1, pp. 50–61, Mar. 2019.
- [75] Z. Liao, Y. Lei, and R. C. N. Pilawa-Podgurski, "Analysis and design of a high power density flying-capacitor multilevel boost converter for high step-up conversion," *IEEE Transactions on Power Electronics*, pp. 1–1, 2018.
- [76] B. Stevanović, D. Serrano, M. Vasić, P. Alou, J. A. Oliver, and J. A. Cobos, "Highly efficient, full zvs, hybrid, multilevel dc/dc topology for two-stage grid-connected 1500v pv system with employed 900v sic devices," *IEEE Journal of Emerging and Selected Topics in Power Electronics*, pp. 1–1, 2019.
- [77] S. Qin, Y. Lei, Z. Ye, D. Chou, and R. C. N. Pilawa-Podgurski, "A high power density power factor correction front end based on seven-level flying capacitor multilevel converter," *IEEE Journal of Emerging and Selected Topics in Power Electronics*, pp. 1–1, 2018.
- [78] W. Qi, S. Li, H. Yuan, S. Tan, and S. Hui, "High-power-density single-phase three-level flying-capacitor buck pfc rectifier," *IEEE Transactions on Power Electronics*, vol. 34, no. 11, pp. 10 833–10 844, Nov. 2019.
- [79] M. Chen, K. K. Afridi, S. Chakraborty, and D. J. Perreault, "Multitrack power conversion architecture," *IEEE Transactions on Power Electronics*, vol. 32, no. 1, pp. 325–340, Jan. 2017.

- [80] W. C. Liu, P. Assem, Y. Lei, P. K. Hanumolu, and R. Pilawa-Podgurski, "A 94.2%-peak-efficiency 1.53A direct-battery-hook-up hybrid dickson switched-capacitor dc-dc converter with wide continuous conversion ratio in 65nm cmos," in *2017 IEEE International Solid-State Circuits Conference (ISSCC)*, Feb. 2017, pp. 182–183.
- [81] S. Park and T. M. Jahns, "A self-boost charge pump topology for a gate drive high-side power supply," *IEEE Transactions on Power Electronics*, vol. 20, no. 2, pp. 300–307, Mar. 2005.
- [82] J. C. Crebier and N. Rouger, "Loss free gate driver unipolar power supply for high side power transistors," *IEEE Transactions on Power Electronics*, vol. 23, no. 3, pp. 1565–1573, May 2008.
- [83] *Application note an-978*, International Rectifier, 2007.
- [84] *Application note an-6076*, Fairchild Semiconductors, 2008.
- [85] B. A. Welchko, M. B. de Rossiter Correa, and T. A. Lipo, "A three-level mosfet inverter for low-power drives," *IEEE Transactions on Industrial Electronics*, vol. 51, no. 3, pp. 669–674, Jun. 2004.
- [86] C. Klumpner and N. Shattock, "A cost-effective solution to power the gate drivers of multilevel inverters using the bootstrap power supply technique," in *Applied Power Electronics Conference and Exposition, 2009. APEC 2009. Twenty-Fourth Annual IEEE*, Feb. 2009, pp. 1773–1779.
- [87] K. Abe, K. Nishijima, K. Harada, T. Nakano, T. Nabeshima, and T. Sato, "A novel three-phase buck converter with bootstrap driver circuit," in *2007 IEEE Power Electronics Specialists Conference*, Jun. 2007, pp. 1864–1871.
- [88] *Epc2016c datasheet*, EPC2016C, Efficient Power Conversion, 2019.
- [89] S. Biswas and D. Reusch, "Gan based switched capacitor three-level buck converter with cascaded synchronous bootstrap gate drive scheme," in *2018 IEEE Energy Conversion Congress and Exposition (ECCE)*, Sep. 2018, pp. 3490–3496.
- [90] E. Candan, A. Stillwell, N. C. Brooks, R. A. Abramson, J. Strydom, and R. C. N. Pilawa-Podgurski, "A 6-level flying capacitor multi-level converter for single phase buck-type power factor correction," in *2019 IEEE Applied Power Electronics Conference and Exposition (APEC)*, Mar. 2019, pp. 1180–1187.
- [91] D. Chou, K. Fernandez, and R. C. N. Pilawa-Podgurski, "An interleaved 6-level gan bidirectional converter for level ii electric vehicle charging," in *2019 IEEE Applied Power Electronics Conference and Exposition (APEC)*, Mar. 2019, pp. 594–600.
- [92] *Fundamentals of gallium nitride power transistors*, Efficient Power Conversion, 2009.
- [93] D. Reusch and M. de Rooij, "Evaluation of gate drive overvoltage management methods for enhancement mode gallium nitride transistors," in *2017 IEEE Applied Power Electronics Conference and Exposition (APEC)*, Mar. 2017, pp. 2459–2466.



- [94] Z. Ye, “A power supply circuit for gate driver of flying capacitor multi-level converters,” M.S. thesis, University of Illinois at Urbana-Champaign, 2016. [Online]. Available: <http://hdl.handle.net/2142/93072>.
- [95] *Gs61004b datasheet*, GS61004B, GaN Systems, 2018.
- [96] *Si827x datasheet*, Si827x, Silicon Labs, 2016.
- [97] *Epc2038 datasheet*, EPC2038, Efficient Power Conversion, 2019.
- [98] Z. Ye, Y. Lei, W. c. Liu, P. S. Shenoy, and R. C. N. Pilawa-Podgurski, “Design and implementation of a low-cost and compact floating gate drive power circuit for gan-based flying capacitor multi-level converters,” in *2017 IEEE Applied Power Electronics Conference and Exposition (APEC)*, Mar. 2017, pp. 2925–2931.
- [99] Y. Lei, C. Barth, S. Qin, W.-C. Liu, I. Moon, A. Stillwell, D. Chou, T. Foulkes, Z. Ye, Z. Liao, and R. C. N. Pilawa-Podgurski, “A 2 kW, single-phase, 7-level, GaN inverter with an active energy buffer achieving 216 W/in<sup>3</sup> power density and 97.6% peak efficiency,” in *2016 IEEE Applied Power Electronics Conference and Exposition (APEC)*, 2016, pp. 1512–1519.
- [100] *Egan fet drivers and layout considerations*, Efficient Power Conversion, 2016.
- [101] *Gn001 application brief: How to drive gan enhancement mode hemt*, GaN Systems, 2016.
- [102] Y. Li, X. Lyu, D. Cao, S. Jiang, and C. Nan, “A 98.55% efficiency switched-tank converter for data center application,” *IEEE Transactions on Industry Applications*, vol. 54, no. 6, pp. 6205–6222, Nov. 2018.
- [103] A. Shehabi *et al.*, “United states data center energy usage report,” *Lawrence Berkeley National Laboratory, Berkeley, CA, Tech.Rep. LBNL-1005775*, Aug, 2016. [Online]. Available: [https://datacenters.lbl.gov/sites/default/files/DCDWebscale\\_Shehabi\\_072016.pdf](https://datacenters.lbl.gov/sites/default/files/DCDWebscale_Shehabi_072016.pdf).
- [104] A. Lidow, *Powering graphics processors from a 48-v bus*, 2019. [Online]. Available: <https://www.powerelectronicstips.com/powering-graphics-processors-from-a-48-v-bus/>.
- [105] R.Miftakhutdinov, “Improving System Efficiency with a New Intermediate-Bus Architecture,” in *Texas Instruments Inc. Seminar*, 2009. [Online]. Available: [http://www.ti.com/download/trng/docs/seminar/Topic\\_4\\_Rais.pdf](http://www.ti.com/download/trng/docs/seminar/Topic_4_Rais.pdf).
- [106] D. Reusch and J. Glaser, *DC-DC Converter Handbook - A Supplement to GaN Transistors for Efficient Power Conversion, A Supplement to GaN Transistors for Efficient Power Conversion*. Efficient Power Publications, 2015.
- [107] E. A. Burton, G. Schrom, F. Paillet, J. Douglas, W. J. Lambert, K. Radhakrishnan, and M. J. Hill, “Fivr — fully integrated voltage regulators on 4th generation intel® core™ socs,” in *2014 IEEE Applied Power Electronics Conference and Exposition - APEC 2014*, Mar. 2014, pp. 432–439.

- [108] M. H. Ahmed, F. C. Lee, and Q. Li, "Two-stage 48v vrm with intermediate bus voltage optimization for data centers," *IEEE Journal of Emerging and Selected Topics in Power Electronics*, pp. 1–1, 2020.
- [109] Analog Devices, *Ltm4664 data sheet*, 2019, p. 1. [Online]. Available: <https://www.analog.com/media/en/technical-documentation/data-sheets/LTM4664.pdf>.
- [110] Texas Instruments, *Lmg5200polevm-10 user's guide*, 2017, p. 11.
- [111] Bel Fuse Inc., *48 v-to-pol power stamp datasheet*, 2020, p. 1. [Online]. Available: <https://belfuse.com/resources/datasheets/powersolutions/ds-BPS-48-V-to-POL-power-stamp.pdf>.
- [112] Vicro Inc., *Factorized power architecture and vi chips white paper*, 2013, p. 1. [Online]. Available: <http://www.vicorpower.com/documents/whitepapers/fpa101.pdf>.
- [113] M. H. Ahmed, C. Fei, F. C. Lee, and Q. Li, "Single-stage high-efficiency 48/1 v sigma converter with integrated magnetics," *IEEE Transactions on Industrial Electronics*, vol. 67, no. 1, pp. 192–202, 2020.
- [114] J. Xu, L. Gu, E. Hernandez, and J. Rivas-Davila, "Effect of class 2 ceramic capacitance variations on switched capacitor and resonant switched capacitor converters," in *2018 IEEE 18th Workshop on Control and Modeling for Power Electronics (COMPEL)*, Jun. 2018, pp. 1–7.
- [115] *Epc2024 datasheet*, EPC2024, EPC Inc, 2019.
- [116] *Bsz025n04ls datasheet*, BSZ025N04LS, Infineon Technologies, 2014.
- [117] R. H. Wilkinson, T. A. Meynard, and H. du Toit Mouton, "Natural balance of multi-cell converters: The two-cell case," *IEEE Transactions on Power Electronics*, vol. 21, no. 6, pp. 1649–1657, Nov. 2006.
- [118] Z. Ye, Y. Lei, Z. Liao, and R. C. N. Pilawa-Podgurski, "Investigation of capacitor voltage balancing in practical implementations of flying capacitor multilevel converters," in *2017 IEEE 18th Workshop on Control and Modeling for Power Electronics (COMPEL)*, Jul. 2017, pp. 1–7.
- [119] Y. Li, L. Gu, A. Hariya, Y. Ishizuka, J. Rivas-Davila, and S. Sanders, "A wide input range isolated stacked resonant switched-capacitor dc-dc converter for high conversion ratios," in *2018 IEEE 19th Workshop on Control and Modeling for Power Electronics (COMPEL)*, Jun. 2018, pp. 1–7.
- [120] D. Serrano, V. Toral, M. Vasic, J. A. Oliver, P. Alou, and J. A. Cobos, "Advantages of gallium nitride over silicon transistors in softswitched resonant switched capacitor converters," in *CIPS 2018; 10th International Conference on Integrated Power Electronics Systems*, Mar. 2018, pp. 1–6.
- [121] M. Kasper, R. M. Burkart, G. Deboy, and J. W. Kolar, "Zvs of power mosfets revisited," *IEEE Transactions on Power Electronics*, vol. 31, no. 12, pp. 8063–8067, Dec. 2016.

- [122] M. Ahmed, M. de Rooij, and J. Wang, “High-power density, 900-w llc converters for servers using gan fets: Toward greater efficiency and power density in 48 v to 6v/12v converters,” *IEEE Power Electronics Magazine*, vol. 6, 2019.
- [123] M. H. Ahmed, C. Fei, F. C. Lee, and Q. Li, “48-v voltage regulator module with pcb winding matrix transformer for future data centers,” *IEEE Transactions on Industrial Electronics*, vol. 64, no. 12, pp. 9302–9310, Dec. 2017.
- [124] J. Glaser, J. Strydom, and D. Reusch, “High power fully regulated eighth-brick dc-dc converter with gan fets,” in *Proceedings of PCIM Europe 2015; International Exhibition and Conference for Power Electronics, Intelligent Motion, Renewable Energy and Energy Management*, May 2015, pp. 1–8.
- [125] D. Reusch, “High frequency, high power density integrated point of load and bus converters,” Ph.D. dissertation, Virginia Tech, 2012.
- [126] T. Ge, Z. Ye, R. A. Abramson, and R. C. N. Pilawa-Podgurski, “A 48-to-12 v cascaded resonant switched-capacitor converter achieving 4068 w/in<sup>3</sup> power density and 99.0% peak efficiency,” in *2021 IEEE Applied Power Electronics Conference and Exposition (APEC)*, Jun. 2021.
- [127] EPC Inc., *How to exceed 98% efficiency in a compact 48 v to 6 v, 900 w llc resonant converter using gan fets*, 2018, p. 2. [Online]. Available: <https://epc-co.com/epc/Portals/0/epc/documents/application-notes/How2AppNote014%5C%20Exceed%5C%2098%5C%20percent%5C%20Efficiency%5C%2048%5C%20V%5C%20to%5C%206%5C%20V%5C%20Resonant%5C%20Converter.pdf>.
- [128] M. S. Makowski, “Realizability conditions and bounds on synthesis of switched-capacitor dc-dc voltage multiplier circuits,” *IEEE Transactions on Circuits and Systems I: Fundamental Theory and Applications*, vol. 44, no. 8, pp. 684–691, Aug. 1997.
- [129] M. S. Makowski and D. Maksimovic, “Performance limits of switched-capacitor dc-dc converters,” in *Proceedings of PESC '95 - Power Electronics Specialist Conference*, vol. 2, Jun. 1995, 1215–1221 vol.2.
- [130] J. A. Starzyk, Ying-Wei Jan, and Fengjing Qiu, “A dc-dc charge pump design based on voltage doublers,” *IEEE Transactions on Circuits and Systems I: Fundamental Theory and Applications*, vol. 48, no. 3, pp. 350–359, Mar. 2001.
- [131] M. S. Makowski, “On performance limits of switched-capacitor multi-phase charge pump circuits. remarks on papers of starzyk et al.,” in *2008 International Conference on Signals and Electronic Systems*, Sep. 2008, pp. 309–312.
- [132] —, “A canonical switched capacitor dc-dc converter,” in *2014 IEEE 15th Workshop on Control and Modeling for Power Electronics (COMPEL)*, Jun. 2014, pp. 1–8.
- [133] I. Oota, F. Ueno, and T. Inoue, “Analysis of a switched-capacitor transformer with a large voltage-transformer-ratio and its applications,” *Electronics and Comm. in Japan, Part 2*, vol. 73, no. 1, pp. 85–96, 1990.

- [134] S. Ben-Yaakov and A. Kushnerov, "Algebraic foundation of self adjusting switched capacitors converters," in *2009 IEEE Energy Conversion Congress and Exposition*, Sep. 2009, pp. 1582–1589.
- [135] S. Ben-Yaakov and M. Evzelman, "Generic and unified model of switched capacitor converters," in *2009 IEEE Energy Conversion Congress and Exposition*, Sep. 2009, pp. 3501–3508.
- [136] EPC Inc., *Building the smallest and most efficient 48 v to 5 - 12 v dc to dc converter using epc2045 and ics*, 2018, p. 2. [Online]. Available: <https://epc-co.com/epc/Portals/0/epc/documents/application-notes/How2AppNote001%5C%2048%5C%20V%5C%20to%5C%205-12%5C%20V.pdf>.
- [137] S. Webb and Y. Liu, "12 switch zero-inductor voltage converter topology," in *2019 IEEE Applied Power Electronics Conference and Exposition (APEC)*, 2019, pp. 2189–2196.
- [138] W. C. Liu, Z. Ye, and R. C. N. Pilawa-Podgurski, "A 97% peak efficiency and 308 a/in<sup>3</sup> current density 48-to-4 v two-stage resonant switched-capacitor converter for data center applications," in *2020 IEEE Applied Power Electronics Conference and Exposition (APEC)*, 2020, pp. 468–474.
- [139] R. A. Abramson, Z. Ye, and R. C. N. Pilawa-Podgurski, "A high performance 48-to-8 v multi-resonant switched-capacitor converter for data center applications," in *2020 22nd European Conference on Power Electronics and Applications (EPE '20 ECCE Europe)*, 2020, P.1–P.10.
- [140] Z. Ye, R. A. Abramson, Y. Syu, and R. C. N. Pilawa-Podgurski, "Mlb-pol: A high performance hybrid converter for direct 48 v to point-of-load applications," in *2020 IEEE 21st Workshop on Control and Modeling for Power Electronics (COMPEL)*, 2020, pp. 1–8.
- [141] M. H. Ahmed, C. Fei, F. C. Lee, and Q. Li, "48-v voltage regulator module with pcb winding matrix transformer for future data centers," *IEEE Transactions on Industrial Electronics*, vol. 64, no. 12, pp. 9302–9310, Dec. 2017.
- [142] Z. Ye, R. A. Abramson, and R. C. N. Pilawa-Podgurski, "A 48-to-6 v multi-resonant-doubler switched-capacitor converter for data center applications," in *2020 IEEE Applied Power Electronics Conference and Exposition (APEC)*, 2020, pp. 475–481.
- [143] W. C. Liu and R. C. N. Pilawa-Podgurski, "Bi-lateral energy resonant converter (berc) with merged two-stage inductor for 48-to-12v applications," in *2020 21th Workshop on Control and Modeling for Power Electronics (COMPEL)*, 2020, pp. 1–8.
- [144] R. Das, G. Seo, D. Maksimovic, and H. Le, "An 80-w 94.6%-efficient multi-phase multi-inductor hybrid converter," in *2019 IEEE Applied Power Electronics Conference and Exposition (APEC)*, 2019, pp. 25–29.

- [145] M. Halamicek, T. McRae, and A. Prodić, “Cross-coupled series-capacitor quadruple step-down buck converter,” in *2020 IEEE Applied Power Electronics Conference and Exposition (APEC)*, 2020, pp. 1–6.
- [146] J. A. Starzyk, Ying-Wei Jan, and Fengjing Qiu, “A dc-dc charge pump design based on voltage doublers,” *IEEE Transactions on Circuits and Systems I: Fundamental Theory and Applications*, vol. 48, no. 3, pp. 350–359, Mar. 2001.
- [147] P. S. Shenoy, O. Lazaro, M. Amaro, R. Ramani, W. Wiktor, B. Lynch, and J. Khayat, “Automatic current sharing mechanism in the series capacitor buck converter,” in *2015 IEEE Energy Conversion Congress and Exposition (ECCE)*, 2015, pp. 2003–2009.
- [148] G. Seo, R. Das, and H. Le, “Dual inductor hybrid converter for point-of-load voltage regulator modules,” *IEEE Transactions on Industry Applications*, vol. 56, no. 1, pp. 367–377, Jan. 2020.
- [149] G. Roberts, T. McRae, and A. Prodić, “A multiphase series-capacitor buck converter with reduced flying capacitor volume and auxiliary start-up circuit,” in *2019 21st European Conference on Power Electronics and Applications (EPE '19 ECCE Europe)*, Sep. 2019, P.1–P.8.
- [150] Vicro Inc., *Prm48ah480x200a00 data sheet*, 2020, p. 1. [Online]. Available: [http://www.vicorpower.com/documents/datasheets/PRM48AH480T200A00\\_ds.pdf](http://www.vicorpower.com/documents/datasheets/PRM48AH480T200A00_ds.pdf).
- [151] ———, *Vtm48mp010x107aa1 data sheet*, 2017, p. 1. [Online]. Available: [http://www.vicorpower.com/documents/datasheets/VTM48M\\_010\\_107AA1.pdf](http://www.vicorpower.com/documents/datasheets/VTM48M_010_107AA1.pdf).
- [152] M. Choi and D. Jeong, “18.6 a 92.8%-peak-efficiency 60a 48v-to-1v 3-level half-bridge dc-dc converter with balanced voltage on a flying capacitor,” in *2020 IEEE International Solid-State Circuits Conference - (ISSCC)*, 2020, pp. 296–298.
- [153] *Epc2152 datasheet*, EPC2152, Efficient Power Conversion, 2020.
- [154] T. Ge, B. Carpenter, and K. D. T. Ngo, “Design methodology of a one-turn inductor with significant dc and ac fluxes—demonstration in a resonant cross-commutated buck converter,” *IEEE Transactions on Industrial Electronics*, vol. 66, no. 11, pp. 8424–8433, 2019.
- [155] D. Zhou, Y. Elasser, J. Baek, C. R. Sullivan, and M. Chen, “Inductance dual model and control of multiphase coupled inductor buck converter,” in *2020 IEEE 21st Workshop on Control and Modeling for Power Electronics (COMPEL)*, 2020, pp. 1–8.
- [156] P. H. McLaughlin, P. A. Kyaw, M. H. Kiani, C. R. Sullivan, and J. T. Stauth, “A 48-v:16-v, 180-w resonant switched-capacitor converter with high-q merged multiphase lc resonator,” *IEEE Journal of Emerging and Selected Topics in Power Electronics*, vol. 8, no. 3, pp. 2255–2267, 2020.

- [157] J. D. Boles, J. J. Piel, and D. J. Perreault, “Enumeration and analysis of dc-dc converter implementations based on piezoelectric resonators,” in *2019 20th Workshop on Control and Modeling for Power Electronics (COMPEL)*, 2019, pp. 1–8.
- [158] Y. Elasser, J. Baek, and M. Chen, “A merged-two-stage lego-pol converter with coupled inductors for vertical power delivery,” in *2020 IEEE Energy Conversion Congress and Exposition (ECCE)*, 2020, pp. 916–923.